

Université de Limoges
École Doctorale Sciences et Ingénierie pour l'Information,
Mathématiques (ED 521)
Institut de Recherche Xlim, Limoges.

Thèse pour obtenir le grade de
Docteur de l'Université de Limoges
Electronique des Hautes Fréquences, Photoniques et Systèmes

Présentée et soutenue par
Abhilash Amsanpally

Le 7 juillet 2017

Linear properties of inhibited coupling hollow-core photonic crystal fibers

Thèse dirigée par Fetah BENABID et Frédéric GEROME

JURY :

Président du jury

M. Dominique Cros, Professeur, XLIM – Axe RF Elite, Université de Limoges.

Rapporteurs

M. Géraud Bouwmans, Professeur, IRCICA - Laboratoire PhLAM, Université de Lille.

M. Yves Jaouen, Professeur, Telecom ParisTech, Université Paris Saclay.

Examineurs

M. Gilles Renversez, Professeur, Institut Fresnel, Université d'Aix-Marseille.

Fetah Benabid, Directeur de Recherche, GPPMM, XLIM Institut de recherche.

Frédéric Gérôme, Chargé de Recherche, GPPMM, XLIM Institut de recherche.



Acknowledgment

First and foremost, I would like to express my sincere gratitude to my supervisor Dr. Fetah Benabid for his continuous support of my Ph.D study, for his patience, motivation and sharing his immense knowledge. His guidance helped me in all the time of research and writing of this thesis. I could not have imagined having a better advisor and mentor for my Ph.D study. I would like to thank my co-supervisor Dr. Frederic Gerome for his insightful comments and encouragement and also for the hard questions which intended me to widen my research from various perspectives. Their advices on PhD thesis as well as on my career as a research scientist have been invaluable.

My sincere thanks also go to Dr. Benoit Debort, Dr. Meshal Alharbi, Dr. Assad Baaz, Dr. Benoit. B and Dr. Jean-Marc Blondy for their knowledge sharing and their precious support which taught me sufficient experimental skills in the laboratory to conduct this research. I would like to express my special appreciation and thanks to my collaborator, Dr. Luca Vincetti for his continuous and great support to my thesis by providing up to date FEM simulations on time and for his valuable instructions. Also, I thank my fellow lab mates of GPPMM research group members, Martin Maurel, Mathew Chefer, David Kergoustin, Ximeng Zeng and Frédéric Delahaye, all the GLO photonics team members for being in support at my experiment and also sharing many memorable moments and fun time over coffee.

In particular, I am very thankful to Dr. Eden Sorolla and his family for their immense love and moral support. My special thanks go to my dearest friends Muhammad Adnan and Dr. Foued Amrani for standing by me throughout my stay in Limoges and their brotherhood nature which stood me up in all my critical situations.



Last but not the least; I would like to thank my mother and father, LAXMI GOPAL for all of the sacrifices that you've made on my behalf. My special mentions to my brother Abhishek and my sister Kavitha Prasad and my guru Kalyan Chakravarthy for your confidence in me and for supporting me spiritually throughout writing this thesis and life in general.



Abstract

This thesis is aimed to explore experimental linear characterizations and salient features of recently fabricated state-of-the-art hollow-core photonic crystal fibers (HC-PCFs) based on inhibited coupling (IC) guiding mechanism. This original type of optical fiber outstands with the fact that guided core modes and radiative cladding modes co-exist in effective-index and frequency space without strongly interacting. Such a salient feature and the novelty of the guidance mechanism require specific protocols for the fiber linear characterization, which are explored in this thesis using state-of-the-art IC guiding HC-PCF.

First, the thesis reviews the historical evolution of HC-PCF technology development and draws the main differences between photonic band gap (PBG) guiding HC-PCF and IC guiding HC-PCF, using the theoretical models that have been developed in the last decade. In the second chapter, we explain and analyze the modal spectrum of IC guiding fibers using two different lattice designs namely Kagome and tubular lattices. We will then present the results of the optimization of structural parameters of the HC-PCF cladding such as strut thickness, hypocycloid core contour and pitches in order to enhance coupling inhibition between core and cladding modes. As part of this fiber design and fabrication, a 7-cell hypocycloid Kagome IC HC-PCFs has been experimentally used to unveil Fano resonances between guide core and cladding modes; thus giving further evidence that IC guidance is a fiber-photonic manifestation of quasi-Bound state in a Continuum (Q-BiC). This was done in Chapter 3 by examining a high resolution transmission spectrum around 1550 nm. The obtained loss spectra exhibit the distinctive Fano asymmetric-shaped profiles with a bandwidth of 30 GHz which



are found to fit with empirical Fano formula. These results were further corroborated by numerical simulations.

The thesis describes the experimental characterization of the optical properties of different state-of-the-art IC HC-PCFs that have been developed during the tenure of my doctoral work to reduce the transmission loss or to address particular applications. With the seminal introduction of a hypocycloidal (*i.e.* negative curvature) core-contour in 2010, IC HC-PCFs have proven to be ideal optical fibers that combine broadband guidance and low transmission loss in air-core. The interest in IC HC-PCFs is as growing as varied. For example, IC hypocycloid Kagome HC-PCF with loss figures below 50-30 dB/km, proved to be an excellent means for milli-Joule ultra-short pulse (USP) lasers, for pulse compression with outstanding results such as optical pulse compression down to the single-cycle regime, or as optical nonlinearity *booster* which is illustrated with supercontinuum generation in air-filled IC HC-PCF. Within this context, reducing further the transmission loss has both a fundamental interest in better understanding the light guidance in IC fibers, and a technological impact in applications such as UV-guidance, nonlinear optics, plasma photonics and high resolution spectroscopy. Chapter 4 of this thesis gives details about the structural parameters of IC-HCPCF to optimize and reports on several measurements related to their transmission loss, their output beam reconstructed near-field and far-field, their modal content and polarization properties of their guided modes. Among the optimized fibers that have been characterized we count, a 7-cell Kagome HC-PCFs exhibiting a record level loss of 8.5 dB/km at 1030 nm which represents a factor of two improvements over the current state-of-the-art along with a wider 3-dB bandwidth and lower bend sensitivity. The modal properties (S^2 and PER) measurements show a quasi-single mode operation, with an optical power extinction ration between the fundamental mode and the lowest-loss higher order



mode of more than 26 dB. Another 7-cell Kagome HC-PCFs with a much broader fundamental transmission band, spreading down to 670 nm, able to cover the entire Ti:Sa, Yb and Er spectral ranges, was fabricated and characterized. This fiber was made by further reducing the silica thickness of the silica strut so the transmission band blue-edge is shifted down to Ti:Sa spectral range while preserving hypocycloid core design. The fiber shows a record fundamental band propagation loss with a minimum value of 30 dB/km at 780 nm. The fiber shows a low bending loss sensitivity over a large part of the fundamental band combined with a polarization extinction ratio of up to 15 dB. A third hypocycloid Kagome HC-PCF based on 19-cell core has been designed, fabricated and characterized. Increasing the effective area of the core by removing on more cladding ring of the recent 7-cell design would further increase the laser induced damage threshold (LIDT) of this type of fiber. We report on theoretical and experimental analysis of several hypocycloid-core-contour 19-cell Kagome HC-PCF in order to assess the fiber suitability for transport of ultrafast laser beams. These fibers, for the first time with core diameter that exceeds 100 μm covers all the visible and IR spectral range according to the transmission spectra of each fiber. They exhibit low transmission loss of 100 dB/km (state-of-the-art for a 19-cell design), low dispersion and ultralow optical power overlap with silica cladding down to a ppm record level combined with low bending induced transmission loss. Therefore these fibers can be an excellent platform for high power handling, USP delivery with pulse energy that could possibly be as high as 100 mJ.

Another IC-HC-PCF design which consists of an arrangement of isolated thin glass tubes is another cladding structure that nicely fulfills these IC conditions provided they are operated at large pitch regime. The illustration of such design is theoretically discussed for optimum design parameters with an aim to fabricate several ultra-low loss single-ring tubular lattice HC-PCFs guiding in the UV-VIS

and NIR. The current realized fiber's cladding tubes were relatively thicker and the achieved record level transmission loss as low as 50 dB/km in 3-4 μm was limited to the mid-IR spectral range. By optimizing such a tubular cladding and operating with much thinner glass-tube we report on the fabrication of one of the fibers with a record transmission loss of 7.7 dB/km at ~ 750 nm (only 4 dB above the Rayleigh scattering fundamental limit in silica), and guidance down to 220 nm. A second one exhibits ultra-broad fundamental band with loss figures of less than 20 dB/km over one octave spanning from 600 to 1200 nm. Both fibers present a near-single modedness (>20 dB extinction between HE_{11} and the first HOM) and very low bend loss (0.03 dB/turn for a 30 cm bend diameter at 750 nm). The results show that the fibers are limited by confinement loss (CL) for wavelengths longer than 1 μm and by surface-roughness scattering loss (SSL) for shorter wavelengths.

Finally, in the last chapter and with the aim to bring down the losses of IC HC-PCFs at fundamental levels especially at shorter wavelength regions, we report theoretical analysis based on pointing vector study and a novel experimental platform to investigate scattering losses and its distributions due to surface roughness and confinement losses.



Table of Contents

Chapter 1

Background and introduction of HC-PCF.....	1
1.1 Historical overview of hollow-core photonic crystal fibers (HC-PCFs)	2
1.2 Applications of HC-PCF in gas-photonics	7
1.3 Light guiding principles of optical fibers	10
1.4 PBG HC-PCF Guidance.....	16
1.4.1 Photonic Tight Binding Model	16
1.4.2 Limitations of PBG HCPCF	21
1.5 Inhibited Coupling HC-PCF Guidance.....	23
1.6 Thesis Outline	26

Chapter 2

Enhancement of guiding in IC HC-PCF	29
2.1 Introduction	30
2.2 Principles and key design parameters in IC optical guidance	33
2.2.1 Basic IC guidance principles	33
2.2.2 Key design parameters to enhance IC guidance.....	35
2.2.3 Differences between IC and ARROW guidance.	38
2.3 Kagome latticed IC HC-PCFs.....	41
2.3.1 DOPS of Kagome lattice designs	41
2.3.2 Modal analysis of Kagome latticed IC HC-PCF.....	43
2.3.3 Enhancement of IC guidance in Kagome HC-PCF.....	45
2.4 Tubular latticed IC HC-PCF	54
2.4.1 DOPS of tubular latticed IC HC-PCFs.....	55
2.4.2 Modal analysis of SR TL IC HC-PCF	57
2.5 Summary	61

Chapter 3

Fano resonance in IC Kagome HC-PCF	63
3.1 Introduction	64



3.2 Physical and historical background of BiC	68
3.2.1 Bound State in Continuum (BiC).....	70
3.2.2 Fano Resonance: Spectral manifestation of QBiC and BiC.....	71
3.3 Universality of BiC.....	74
3.3.1 BiC in two coupled mechanical oscillators	74
3.3.2 BiC in electronic hetero-structures.....	76
3.3.3 BiC in IC HC-PCF	77
3.3.4 Fano resonance in polygonal tubular lattice fibers.....	78
3.3.5 BiC in photonic crystal slab.....	80
3.4 Understanding Fano Resonance in Kagome IC HC-PCF through toy model and coupled mode theory	82
3.5 Theoretical Simulations of CL spectral structure under a scattering perturbation	87
3.6 Experimental observation of Fano resonance in Kagome HC-PCF.....	91
3.7 Summary	96
Chapter 4	
Experimental linear characterization of IC HC-PCFs	97
4.1 Introduction	98
4.2 Experimental setups for linear characterizations of IC HC-PCF	100
4.2.1 Transmission studies by cut back method.....	100
4.2.2 Macro bending loss analysis	102
4.2.3 Polarization extinction ration (PER) and M^2	102
4.2.4 Spatial and spectral (S^2) imaging.....	105
4.3 Linear properties of ultra-low loss (8.5 dB/km at Yb-laser region) Kagome IC HC-PCF for laser beam delivery applications	106
4.3.1 Fiber design and fabrication	106
4.3.2 Transmission loss characterization	107
4.3.3 Bending Analysis.....	109
4.3.4 PER.....	110
4.3.5 S^2 imaging	112
4.4 Linear properites of low loss (30 dB/km at 780 nm) Kagome IC HC-PCF with ultra-broad fundamental band	114



4.4.1 Fiber fabrication and transmission	114
4.4.2 Bending Analysis.....	118
4.4.3 PER.....	119
4.4.4 S ² imaging.....	120
4.5 Ultra-low transmission loss (7.7 dB/km at 750 nm) SR-TL IC-HC-PCFs.....	122
4.5.1 Design parameters and fabrication.....	123
4.5.2 Transmission and Loss	128
4.5.3 Bending Analysis.....	133
4.5.4 S ² Imaging.....	134
4.5.5 PER.....	135
4.6 Summary	136
Chapter 5	
Experimental investigation of surface scattering losses in inhibited coupling HC-PCF	139
5.1 Introduction and origin of SSL in HC-PCF	140
5.2 Physics of surface scattering in HC-PCF	142
5.3 SSL of IC HC-PCF	144
5.3.1 Impact of surface roughness on CL of IC HC-PCF.....	147
5.3.2 Poynting vector study.....	149
5.4 Simulations of SSL and CL in SR-TL IC HC-PCF.....	152
5.5 Experimental set-up to measure scattering losses in IC HC-PCF.....	154
5.6 Results.....	157
5.6.1 Angular distribution of scattering due to surface roughness	158
5.6.2 Angular distribution of scattering due to confinement	160
5.7 Summary	165
Conclusion.....	167
Annexure A	
Numerical simulations of optimized Kagome IC HC-PCFs	169
A.1 Simulation of fiber #1 and results	170
A.2 Simulation of fiber #2 and results	172
A.3 Summary	173



Annexure B

Ultra-large core size hypocycloid-shape IC HC-PCFs for high-energy laser beam handling.....	175
B.1 Introduction	176
B.2 Designing the enlarged hypocycloid 19-cell core.....	177
B.2.1 Impact of negative curvature on confinement loss.....	179
B.2.2 Impact of negative curvature on modal content	180
B.2.3 Impact of negative curvature on optical overlap with cladding	181
B.3 Fabrication and linear characterization	183
B.3.1 Transmission loss analysis	183
B.3.2 Bending loss analysis	186
B.4 Investigation of high energy USP laser handling.....	188
B.4.1 Theoretical investigation of the IC mechanism for power-link potential	188
B.4.2 Experimental demonstration of high energy USP laser handling at 1 μm	190
B.4.3 Experimental demonstration of high energy USP laser handling at 780 nm.	191
B.5 Summary	193
REFERENCES	195
PUBLICATION LIST	207



List of figures

Figure 1-1 Summary of historical development of HC-PCF technology based on PBG and IC guidance. The area in gray color in the graph represents the years of theoretical developments from PBG guidance to first HC-PCF invention. The blue area represents development of HC-PCF based on PBG (in solid line borders) and inhibited coupling (dashed borders).-----	5
Figure 1-2 (a) SEM images of different types of PBG, Kagome IC HC-PCF. (b) and their FOM. -----	9
Figure 1-3 SEM images of (i) HC-PCF-based gas cell and cleaved ends at (ii) the spliced junction and (iii) away from the junction. (iv) The photograph of the cell to compare its size to that of a match stick [from [26]].-----	9
Figure 1-4 Left side: (A) schematic of fiber cross sections of (a) a uniform dielectric material (b) a fiber with a defect of high index material. (c) Uniform PCF and its unit cel. (d) PCF with a unit cell defect operated in low pitch regime for PBG guidance. (e) Uniform Kagome PCF and its unit-cell and (f) with a 1-cell defect operated in large pitch regime for IC guidance (IC HC-PCF). (B) Shows DOPS diagrams and n_{eff} at fixed $k\Lambda$ for fiber models presented in (A). (C) Presents field distributions of defect modes identified at fixed $k\Lambda$ in the figure (B).-----	12
Figure 1-5 Schematic illustration showing the analogy between (a) TBA and (b) P-TBM [30]. The regions 1, 2 and 3 in (a) represent insulator, semi conduction and conduction domains of the material respectively. (a) Waveguide system with effective index n_h spaced by Λ and is DOPS ($n_{eff}-k\Lambda$) diagram. Blue and red dotted lines on $n_{eff}-k\Lambda$ graph represent large and small pitch domains of the waveguide systems.-----	18
Figure 1-6 (a) SEM image of a PBG HC-PCF and inset shows its unit-cell. (b) Zoomed in unit cell. Green circle is a hole formed by six apices shown in red circles and connecting struts shown in white elliptical circles.-----	19
Figure 1-7 (a) Dispersion curves of the fundamental and first higher-order modes of (a) an isolated silica rod (b) an array of identical rods spaced by pitch Λ and the dispersion curves of array of rods broaden to form allowed bands [from [32]].-----	20
Figure 1-8 (a) Details of the calculated density of state plot around the PBG region falling below the vacuum line. (b) Zoom in of the DOPS showing surface modes and HOMs within the PBG region [from [32]].-----	20
Figure 1-9 Effective indices of cladding modes calculated at high symmetry points for the structures with (a) strut thickness $t = 0.05\Lambda$ and varying apex curvature radius $r = 0.20\Lambda$ and (b) $t = 0.10$ and $\Lambda r = 0.15\Lambda$ [from [33]].-----	21
Figure 1-10 (a) Trajectories of the fundamental core mode (black dotted line) and a surface mode (blue and red solid lines) as they interact around an anti-crossing event. (b) Wavelength dependence of attenuation for a PBG HC-PCF (blue circles) and operating bandwidth (red squares) of a HC-PCF as a function of their central operating wavelength [From [34]].-----	22
Figure 1-11 (a) SEM images of triangular lattice structure of PBG HC-PCF, (b) Kagome lattice structure of IC HC-PCF. (c) And (d) show cladding designs of the PBG and Kagome IC HC-PCFs respectively.-----	24
Figure 2-1 (a) SEM images of a single-cell core large-pitch Kagomé fibers. (b) Zoom in to the details of the cladding structure. (c) Core formed by 1-cell defect.-----	32



Figure 2-2 Summary of the historical development of IC HC-PCFs and their respective loss figures with SEM images.	37
Figure 2-3 (a) density of photonic states for the Kagomé lattice structure. The horizontal yellow line indicates the air-line. (b) Transmission spectrum of fabricated Kagomé lattice fibers of the same structure as that simulated to obtain the DOPS. I and III are bands of high-transmission in the core, and II is a band of low transmission in the core. (c) calculated real (thick black) and imaginary (thin red) parts of the neff of HE ₁₁ mode.	42
Figure 2-4 (a) SEM of a single cell Kagomé fiber. (b) & (c) Shows comparison of the optical images under the microscope for a Kagome fiber and triangular PBG fibers respectively.	42
Figure 2-5 Nature of the Kagomé -lattice HC-PCF cladding modes. (A) The core mode and a cladding mode for a frequency $k\Lambda=50$ in band (I) (top), and for a frequency $k\Lambda=100$ in band (III) (bottom). At each frequency, the effective indices of the core and cladding mode differ by less than $10 - 5$. The third column shows the mode of an infinite Kagomé lattice, which corresponds to the cladding mode in column 2, calculated for the same frequencies at the Γ -point of the Brillouin zone. (B) Same as in (A) but for $k\Lambda=68$ (in band (II)).	44
Figure 2-6 Intensity profiles of (a) the guided core-mode of a Kagomé lattice fiber, and (b) a cladding mode of the same fiber. The graph plots the transverse intensity variation of both modes over a distance equal to the cladding pitch along the dotted lines in (a) and (b).	44
Figure 2-7 Transformation of IC Kagome HC-PCF core shape from (a) circular contour ($b=0$) to a (b) hypocycloid-like core with $b=1$. Inset: Definition of the parameters quantifying the curvature of the core arcs [49].	46
Figure 2-8 Schematic representation of the IC enhancement for the case of hypocycloid core-contour relative to the circular-like core-contour. (a) A circular core Kagomé HC-PCF and (b) a negative curvature core-contour Kagomé HC-PCF supporting the same HE ₁₁ core mode. (b) Zoom-in to highlight the HE ₁₁ core mode, the silica core-surround mode with its fast transverse oscillations for both fibers. Circled region (1) is outer most cup, (2) is the inner most cup and (3) is the nodal point pushed away from the core mode of hypocycloid Kagomé HC-PCF.	46
Figure 2-9 (a) Evolution of HE ₁₁ mode profiles at $1 \mu\text{m}$ with b for a 7-cell 3 ring Kagome IC HC-PCF. (b) Calculated loss spectra and (c) fractional power in silica at $1 \mu\text{m}$ for the fundamental core-mode HE ₁₁ and for the first four higher order modes. (d) Evolution of the azimuthal-like number m and the perimeter of the silica core-surround contour with b . (e) The fractional optical power residing in the cladding silica, for a wavelength of $1 \mu\text{m}$, for the core fundamental mode HE ₁₁ (black trace) and for the first four higher order modes: the two polarizations of the HE ₂₁ mode, TE ₀₁ and TM ₀₁ (red curve) [49].	49
Figure 2-10 (a) Simulated loss spectra for four different cladding ring numbers; (b) Confinement loss versus the bend radius for two wavelengths at $\lambda = 1550 \text{ nm}$ for different ring numbers. (c) - (f) Simulated fundamental mode profile at bend radius 1.1 cm at $\lambda = 1550 \text{ nm}$ for 1, 2, 3, and 4 ring numbers in the cladding [53].	52
Figure 2-11 (a) SEM image of a single ring tubular latticed IC HC-PCF. (b) Zoom-in to the core-cladding design.	54
Figure 2-12 Cladding designs of a TL in a (a) triangular and (b) square arrangement along with the details of a unit cell of the lattice on their right. The corresponding DOPS of an infinite tubular lattice is shown right below. (c) (d) Transverse profiles of the electric field magnitude of the photonic state (modes).	55



Figure 2-13 (a) Schematic of HC-PCF with a single-ring tubular lattice (i), a section of a tubular lattice in a triangular arrangement (ii) and the details of a unit cell of the lattice (iii). (b) The density of the photonic state of an infinite tubular lattice in triangular arrangement. (c) Transverse profiles of the electric field magnitude of the photonic state (modes) for $F = 0.8$ (fundamental band) and for $F = 1.2$ (first higher order band). -----	58
Figure 3-1 Schematic of the modal contents of (a) TIR guiding fiber, (b) PBG and (c) IC-guiding HC-PCF. -----	65
Figure 3-2 Schematic of BiC (red) having ionization potentials greater than conventional bound states (green) embedded in continuum (blue background). -----	71
Figure 3-3 (a) Natural line shapes determined by Fano formula for different values of q . (Reverse the scale of abscissas for negative q). (b) Fit of Silverman-Lassetre measured He spectrum [from [69]]. -----	72
Figure 3-4 (a) Schematic of conventional ionization process. (b) auto-ionization process showing the coupling between discrete and continuum due to transition of ground state electron to continuum via discrete state. The red spheres represent electrons at ground level. White and blue spheres represent electrons in transition from discrete to continuum level. -----	73
Figure 3-5 (a) Coupled pendulum driven by a periodic force of frequency ω . (b) The resonant dependence of the amplitude of the forced oscillator $ c_1 $ and (c) of the coupled one $ c_2 $ [from [72]]. -----	75
Figure 3-6 Conduction band diagram of reference sample of AlInAs/GaInAs hetero-structure with 32/150 Å. (b) GaInAs quantum well (32Å) with super lattice of AlInAs/GaInAs [from [73]]. -----	76
Figure 3-7 (a) Cross sections of a circular tube fiber and (b) a polygonal tube fiber (on left) and their equivalent planar structure in cylindrical coordinates (on right) with cylindrical coordinates $r_{int}, p\phi$ and $r_{ext}, p\phi$ represent the distance between the center of the fiber and the internal or external edges of the circular and polygonal tubes, respectively; (c) Schematic of the $\Delta\epsilon, \phi$ in the case of $N = 6$. (d) Calculated n_{eff} and CL curves for the FM core mode of the circular (red triangles) and for a polygonal fiber with 24 sides (black circles) [from [81]]. -----	78
Figure 3-8 (a) Schematic layout of the fabricated structure. The device is immersed in a liquid, index matched to silica at 740nm. (b) Normalized radiative lifetime Q_r extracted from the experimentally measured reflectivity spectrum are shown by red crosses and the blue solid line shows the prediction from FDTD [from [74]]. -----	81
Figure 3-9 Schematic of the 1D waveguide array of N waveguides separated by Λ and provided a defect at the center of the chain with perturbed scattering feature. -----	82
Figure 3-10 Evolution of transmitted power changing from Lorentzian to Fano asymmetric profiles. -----	86
Figure 3-11 (a) Image of 7-cell IC Kagome HC-PCF model considered for the FEM simulations (b) its DOPS. (c) and (d) are core and cladding mode profiles of the fiber. -----	87
Figure 3-12 Images of the fiber models of (a) ideal and (b) perturbed fiber (scattered features are shown in yellow and red circles) considered for the simulations to compare their DOPS and CL spectra as shown in (c) and (d) for ideal and perturbed fibers respectively. -----	88
Figure 4-1 (a) Experimental set-up for to measure transmission and (b) for measuring macro-bending loss spectra of FUT (IC HC-PCF). -----	101
Figure 4-2 (a) Experimental set-up to measure PER and (b) and S^2 imaging. -----	104



Figure 4-3 (a) SEM image of the fabricated fiber and its arc curvature shown in red square is shown in (b) along with parameters. (c) Shows micrograph of its strut with thickness of 835 nm. -----	107
Figure 4-4 Transmission spectra for 106 m (black line) and 3.8 m (red line) lengths of the fabricated fiber of the fiber shown in black and red curves respectively. -----	108
Figure 4-5 (a) Loss spectra curves of the fabricated fiber (black solid line) and its comparison with the current state-of-the-art Kagome IC HC-PCF (red dotted line) [49]. (b) Shows the zoom of the experimental and loss spectra. (c) The near field image recorded at the fiber output at 1030 nm. -----	108
Figure 4-6 Evolution of transmission loss for different bending radii. -----	110
Figure 4-7 Evolution of experimental (solid black line) and theoretical (dashed black line) bend loss with bend radius at 1030 μm along with corresponding near fields bend radii at $R_c = 2.5\text{ cm}$, $R_c = 5\text{ cm}$ and $R_c = 20\text{ cm}$. -----	110
Figure 4-8 (a) Evolution of the PER versus fiber length. (b) Periodic variations of PER (blue line) versus input polarization angles at 1064 nm for a fixed fiber length at 19 m. Black and red lines represent power variations of x-axis beam and y-axis beam respectively. -----	111
Figure 4-9 Measured group delay curves of propagating modes through a 5 m long fiber. The reconstructed mode field profiles are indicated at the corresponding MPI. -----	113
Figure 4-10 (Left) Different fabricated fibers with reduced strut thickness and measured b parameters. (Right) Their corresponding loss spectra. Spectral windows shown in black and gray dashed lines indicate fundamental and first high order bands respectively for each fabricated fibers. -----	115
Figure 4-11 (a) SEM image of low loss broad band Kagome IC HC-PCF with its hypocloidal core shape as shown in (b). -----	116
Figure 4-12 (a) transmission curve from a 96.2 m (red solid line) and 8.2 m long piece (black solid line). (b) Corresponding measured loss curve (black color) of the fabricated hypocycloid-core Kagome HC-PCF. Both transmission and loss spectra are compared with the previous state-of-the-art Kagome IC HC-PCF [49] (dashed lines). -----	117
Figure 4-13 (a) Loss spectra of low loss broad band Kagome IC HC-PCF for different bend radii. (b) Bend loss evolution at fixed wavelength of 750 nm, where the fiber exhibits record loss value 30 dB/km on fundamental transmission band and corresponding NF images at bending radii are shown in the inset of the figure. -----	118
Figure 4-14 (Black solid curve) PER spectra of of the fiber showing 15 dB around 780 nm and loss spectrum of the same fiber is also included in black dashed line. -----	119
Figure 4-15 S^2 imaging of fabricated fiber with core radius $R_{in}/R_{out} = 51/57\text{ }\mu\text{m}$ with beam profile of fundamental mode. Mode profile in red inset is for LP_{01} and (a), (b) are for mode images and MPI levels corresponding to the various peaks at LP_{11} and (c)(d) at LP_{12} modes. -----	120
Figure 4-16 1D field amplitude profile along a gap line between the canter of two adjacent tubes for spacing varying from 2 to 8 μm for a tubular lattice (a) and for hollow-core with single ring tubular lattice cladding (b). -----	124
Figure 4-17 Four panel showing (a) CL for different tube numbers (N), (b) Ratio between TE_{01} and HE_{11} loss, (c) loss spectra versus tubular gap (δ), (d) loss and DO spectra for different tube thickness (t) values. -----	126

Figure 4-18 (a) SEM pictures of 4 fabricated HC tubular lattice fibers with corresponding geometrical parameters (δ , R_c , t , R_c). (b) Experimental evolution of the loss spectrum with the tubular gap. -----	130
Figure 4-19 Measured transmission and attenuation spectrum for Fiber #5 (left) (a(i)) and Fiber #6 (right) (b(ii)). Fiber #5 reaches a record of 7.7 dB/km (a(ii)), and Fiber #6 exhibits a loss in the range 10-20 dB/km over one octave (b(ii)). Bottom: Measured attenuation of a 2 m-long piece of of Fiber #5 (c) and of Fiber #6 (d) with purple-filled curve highlighting UV/DUV guidance. The blanked data around 1 μ m in b(i) and b(ii) are due to the supercontinuum stronger power at 1064 nm. -----	132
Figure 4-20 Bend loss spectra measured at different bend radius for (a) Fiber #5 and (b) Fiber #6; (c) Recorded near fields are added for the different bending radius used (left: Fiber #5 / right: Fiber #6).-----	133
Figure 4-21 Group delay curves of the HOM content propagating in the Fiber #6 for 5 m and 15 m long pieces. The reconstructed mode field profiles are indicated with the corresponding MPI. -----	134
Figure 4-22 Evolution of the PER versus the fiber length. -----	135
Figure 5-1 (a) schematic of a hollow tube fiber cross section with roughness surface on its core wall and ϕ and θ are angles in horizontal and transverse plane (b) Schematic of spherical scattered filed distribution due to induced dipole radiation of surface scattering features on hollow-core fiber. (c) Calculated (red line) and semi-analytical (blue line) normalized scattering power spectra at point P due to scattered field spherically radiating out of roughness features on the core wall of the fiber [from [93]]. -----	143
Figure 5-2(a) and (b) are SEM images of a SR-TL IC HC-PCF and 7-cell hypocycloid Kagome IC HC-PCF. (c) and (d) are their respective experimental and theoretical loss spectra. -----	145
Figure 5-3 (a) Schematic of SR-TL HC-PCF showing spatial periodic perturbations at inner and outer surfaces of cladding tube. (b) top: Spectra of fractional optical overlap with the cladding, F , and bottom: confinement loss, CL , for the unperturbed fiber (black dashed line) and for for spatial aperiodic perturbation with two different peak-to-peak oscillations ($h_{pp} = 1.5$ nm and $h_{pp} = 2.5$ nm). -----	148
Figure 5-4 Comparison between CL computed through the mode eigenvalue (solid black line) and through Pr (red points) of a fiber with $\delta = 5.0$ μ m.-----	150
Figure 5-5 Transverse distribution of prn for four fibers with $\delta = 2$ μ m, 4 μ m, 6 μ m, 8 μ m, and at two wavelengths: 530 nm (<i>lhs</i> column) and 1200 nm (<i>rhs</i> column). -----	151
Figure 5-6 Azimuthal distribution of prn in the silica surrounding the micro-structured cladding. The 8 tubes are placed at 0° and multiple of 45°. The position of the tubes along the considered perimeter (fixed at 40 μ m) is represented by black circles. -----	151
Figure 5-7 (a) SEM images of SR-TL IC HC-PCF and (b) its theoretical and measured loss spectra. -----	152
Figure 5-8 ADS due to confinement in Tr-plan at (a) wavelength 1550 nm and (d) at 1064nm. Red and green spectra shown in the figures represent scattering for x and y polarizations respectively. The transverse profiles of corresponding Poynting vectors are shown on the left panel of the figures. The triangular inset of (b) and (c) represent abrupt peaks in the spectra shown in (a) due to non-uniformity in tubular gap. -----	153
Figure 5-9 Experimental scheme to measure scattering distributions due to surface roughness of IC HC-PCF. -----	156
Figure 5-10 Scattered signal collection part of the experimental setup shown in yello square of Figure 5-9. H-plane in blue color represent scattering field due to surface roughness and Tr-plane in green color represent scattering field due to confinement. (b)	

Schematic showing fiber cross-section and measurement points to record scattered signals points in H-plane (blue dashed line) and Tr planes.	156
Figure 5-11 Measured angular distribution of scattering due to surface roughness at wavelength (a) 1550 nm and (b) 1064 nm. Numbers in the legend indicate the fiber position at which the scattered signal is collected is taken and H represent for measurements in horizontal plane.	158
Figure 5-12 Curves fitting of scattering data to deduce decay rate coefficient of scattered signal at (a) 1064 nm and (b) 1550 nm. Red curve shown in the figures represent exponential curve fits.	159
Figure 5-13 Measured scattering distribution (blue triangular curve) due to confinement loss in Tr-plane and comparison with numerical result (red for x – polarization and green for y-polarization).	161
Figure 5-14 (i) Curve fittings of measured scattered signals with fiber length at (i)1064 nm and (ii) 1550 nm in Tr-plane. (a) and (c) represent evolution of maximum signals. Similarly (b) and (d) represent minimum signal evolution..	162
Figure 5-15 Comparison of calculated total loss spectra (orange dashed curve) of the single ring IC HC-PCF and its measured transmission loss spectra (blue solid curve). Red dashed and pink dotted curves are theoretically calculated spectra. Black squares and red circles are measured scattering coefficients in horizontal plane and triangular points are measured scattering coefficients in Tr-plane.	164
Figure A- 1. (a) SEM image of fiber #1. (b) Ideal Profile created in FEM simulation tool. (c) overlapping of SEM image with FEM profile to create real fiber structure for simulation.	170
Figure A-2 Comparison of calculated and experimental loss of the fiber #1.	171
Figure A- 3 (a) SEM image of the 7-cell Hypocycloid Kagome fiber #2. (b) Semi cross section of fiber profile extracted for FEM simulations.	172
Figure A- 4 Measured and calculate loss spectra of the 7-cell hypocycloid Kagome IC HC-PCF (fiber #2).	173
Figure B-1 Process of enlarging hypocycloid core size from (a) 7-cell core to (b) 19-cell along definition of b parameter. Hypocycloid core is highlighted in green color and inset shows the definition of b .	178
Figure B-2 (a) Enlarged 19-cell three rings Kagome-lattice fiber designs with different b values. (b) Computed loss spectra for the fundamental HE ₁₁ mode for different arcs curvatures with an inner core diameter of 80 μm and 400 nm of silica strut. (c) its loss comparison with earlier 7-cell counterpart.	179
Figure B-3 (a) Computed HE ₁₁ mode profiles and (b) and (c) first four HOM mode profiles of 19-cell enlarged core with optimum b value.	180
Figure B-4 Impact of negative curvater parameter, b of 19-cell IC HC-PCF on CL at 1 and 2 μm for HE ₁₁ and HOMs and (b) its comparison with CL of earlier state-of-the-art 7-cell design at 1064 nm.	181



Figure B-5 (a) Evolution of the optical power overlap in 19-cell defect fiber with air-core with the silica cladding structure for different b parameters and (b) compares optical overlap between 7 and 19-cell designs with $b=1$. -----	182
Figure B-6 Transmission after 3 m propagation and loss spectra for a bending diameter of 50 cm of the IC hypocycloid-core 19-cell Kagome-latticed HC-PCFs with core enlarged to (a) 75/85, (b) 77/91, (c) 82/98 and (d) 103/120 μm . The high loss region delimiting the fundamental (I) and the first high-order (II) bands is added. Optical micrographs of the fiber cross section and recorded intensity near-field at 1030 nm are shown for the four IC hypocycloid-core 19-cell Kagome-latticed HC-PCFs for a 3 m-long length. -----	184
Figure B-7 (a) Fiber #1 measured bend-loss spectra in the visible and NIR bands for five different bend radii and (b) the corresponding calculations. (c) Computed intensity profile of the fundamental core-mode HE_{11} for $R_c = 15$ mm at a resonant coupling wavelength (noted 1) and out of it (noted 2). -----	186
Figure B-8 Bend-loss evolution with bend radius of band-I and II central wavelength (exact values indicated on the plot) for the four fabricated IC Kagome fibers. -----	187
Figure B-9 Computed energy residing in silica core contour compared with the silica LIDT reported in [106]. (b) Evolution of the dispersion curve around 1 μm for varying silica thickness ($t = 400, 600, 700, 850$ nm) for a typical 19-cell three rings IC Kagome-lattice fibers with an inner hollow-core diameter fixed to 80 μm and an arc curvature b equal to 1. -----	189
Figure B-10 (a) Measured transmitted energy with input energy at 1 μm for 19-cell fiber (blue color-coded) and 7-cell fiber (black color-coded) for the different cases of fiber-length and gas-filling pressure; (b) Far field beam profiles showing single mode transmissions at 1 mJ of input energy for both fiber designs. -----	191
Figure B-11 Evolution of the fiber output energy with the input energy (black curve) and corresponding coefficient transmission curves (blue curve) for 55 and 35 cm long piece of large core HC-PCF filled with He at 3 and 5 bar respectively [43]. -----	192
Figure B-12 Mappings of the measured output spectrum versus input energy for 55 cm long 3 bars He-filled (left) and 35 cm long 5 bars He-filled (right) fiber pieces. -----	193



List of tables

Table 5.1 Summary of measured scattering coefficients in horizontal and transverse planes-- -----163

Table B.1 Dispersion length, nonlinear length, self-focusing critical power and ionization threshold
intensity [99] for different HC-PCF configurations. -----175

Table B.2 Geometrical parameters of four fabricated hypocycloid-core 19-cell Kagome latticed IC
HCPCFs. -----181



Abbreviations

AI	Auto-ionization
ARROW	Anti-resonant reflecting optical waveguide
BL	Bending loss
BS	Beam splitter
CL	Confinement loss
CMT	Coupled mode theory
CTF	Circular tubular lattice
DOPS	Density of photonic state
ECDL	External cavity diode laser
EIT	Electromagnetically induced transparency
Er	Erbium
FDTD	Finite-difference time-domain method
FEM	Finite element method
FF	Far field
FM	Fundamental mode
FR	Fano resonance
FUT	Fiber under test
GDFT	Group delay of interference signal fourier transform
HC-PCF	Hollow-core photonic crystal fiber
HDR	High dynamic range
HOM	Higher order mode
H-plane	Horizontal plane
HWP	Half wave plate
IC	Inhibited coupling
IR	Infrared
LIDT	Laser induced damage threshold
MPI	Multipath interference



Nd:Yag	Neodymium-doped ytterbium aluminum garnet
NF	Near field
NIR	Near-Infrared
OSA	Optical spectrum analyzer
PBG	Photonic bandgap
PBS	Polarizing beam splitter
PD	Photodetector
PER	Polarization extinction ratio
PhC	Photonic crystal
P-TBM	Photonic tight binding model
PTF	Polygonal tubular lattice
Q-BiC	Quasi-bound state in continuum
RCWA	Rigorous coupled-wave analysis
S²	Spatial and spectral
SEM	Scanning electron microscope
SR TL	Single ring tubular lattice
SSL	surface scattering loss
TBA	Tight binding model approximation
T-CMT	Time dependent coupled mode theory
Ti:Sa	Titanium-sapphire; Ti:Al ₂ O ₃
TIR	Total internal reflection
TM	Transverse mode
Tr-plane	Transverse plane
USP	Ultra-short pulses
UV	Ultra-violet
VIS	Visible
Yb	Ytterbium



Definition of symbols

β	Axial component of wavevector k
c	Speed of light in a vacuum
h	Planck's constant
\hbar	Reduced planck's constant ($h/2\pi$)
k	Wavevector, $1/\lambda$
k_b	Boltzmann constant
$k\Lambda$	Normalized frequency
Λ	Fiber cladding pitch
λ	Wavelength mean-free-path
n	Refractive index
n_{eff}	Effective refractive index



Chapter 1

Background and introduction of HC-PCF

This opening chapter reviews on hollow-core photonic crystal fibers (HC-PCFs) and summarizes its historical development and basic principles of different light guiding mechanisms. The discussion will first focus on well-known photonic bandgap (PBG) HC-PCFs. In the next section, an introduction of inhibited coupling (IC) HC-PCF is presented in order to open the discussion for the rest of the thesis.



1.1 Historical overview of hollow-core photonic crystal fibers (HC-PCFs)

Conceptual transfer from quantum mechanics and solid state physics to optics began with the proposal of the photonic microstructures exhibiting bandgap in 1987, by Sajeev John [1] and E. Yablonovitch [2] [3]. In their seminal works, Maxwell equations were for the first time casted as an eigenvalue problem and showed that periodic arrangement of dielectric materials would lead to the formation of photonic band gap (PBG) in a given wave vector-frequency (\vec{k}, ω) space. This means that no photonic state is supported by the dielectric structure in this region of frequency (\vec{k}, ω) space, which is similar to the formation of electronic energy bandgaps in semiconductors. This work led to emergence of a new field, which can be coined as PBG physics, and triggered huge interest in various fields including laser spectroscopy, planar waveguides, all-optical transistors and circuits, quantum computers and more importantly optical fibers including solid-core and hollow-core photonic crystal fibers. PBG fiber based on hollow-core technology has become ideal waveguides for the research and applications including transmission of well confined mode over kilometer distance with low loss of 1.7 dB/km [4]. Also with the provision to host atoms and Raman active gases, these air core PBG fibers have interesting platform for metrology [5] and nonlinear optics, for example gas-laser systems [6, 7, 8].

Indeed, PBG physics led to the emergence of a new class of fiber called photonic crystal fiber (PCF) whose cladding is formed by two dimensional periodic or almost periodic dielectric structures extending over the entire length of the fiber. This photonic cladding structure allowed guiding light by several mechanisms. By engineering opto-geometric parameters of the fiber's core and cladding, it is possible to guide the light via modified total internal reflection (TIR)



with unprecedented control on the fiber dispersion, leading to the development of endlessly-single mode fiber [9], and subsequently to the development of large mode area (LMA) fibers that are the key components in the advance of high power fiber lasers [10] [11]. On the other hand, by nano- and micro-structuring the cladding, one can control its modal spectrum so it exhibits no propagating modes (*i.e.*, PBG in (n_{eff}, ω)) at effective indices that can be below the material cut-off, including that of the lowest material index. Remarkably, cladding structures can be designed so PBG exist below the air index [12], leading to the development of PBG guiding HC-PCF [13].

Finally, a third and more intriguing optical guidance emerged and coined inhibited coupling (IC) guidance [14]. This optical guidance was proposed by Fetah Benabid [14] in an attempt to investigate the inexplicable properties of Kagome-lattice HC-PCF [6], such as its low transmission loss over a large bandwidth. This is so despite the gapless of its modal spectrum at (n_{eff}, ω) of the core guided mode. Akin to Von Neumann-Wigner bound state in a continuum [15], the core guided mode in IC guiding HC-PCF co-exists with a continuum of cladding modes without strong interaction. This inhibition in coupling was further enhanced by introducing hypocycloid core contour [16] [17], which led to a dramatic reduction in transmission loss as we will see it throughout this thesis.

The interest in guiding light in HC-PCF is larger than the fundamental aspects of its optical guidance mentioned above. The ability of guiding light in air or in a chosen gas has transformative impact as well as on long haul telecommunications as on nonlinear optics or spectroscopy to mention a few. For example, the transmission loss about 0.15 dB/km [18] in step index fibers is a fundamental limit that cannot be improved on because it stems from the Rayleigh scattering due to silica thermal quantum noise. Thanks to the highly diluted



nature of gases, the magnitude of such a scattering effect is dramatically reduced in air core fibers. Moreover, when a HC-PCF is filled with a chosen gas, it can be functionalized into different and diverse photonic components and or systems. Today, and after 17 years since the first demonstration of HC-PCF, several of the predictions and aims were realized especially with regards to gas-laser applications pioneered by Fetah Benabid [6]. However the long sought-after HC-PCF long-haul telecommunications is yet to be realized.

The PBG guiding HC-PCF stems from the extension of the concept of photonic bandgap (PBG) within the photonic crystal materials suggested by S. John [1] and Yablonovitch [2] in 1987 to the out-of-plane of the periodic structure. This out-of-the-plane PBG concept was suggested by Philip. St. J. Russell and reported in 1995 [12], and consists of mapping the modes or photonic states whose propagation direction lies outside the periodicity plane. For example if the periodicity is in (x, y) plane, the problem of finding out-of-the-plane PBG entails finding electromagnetic field whose electrical components have the form $E(x, y, z) \propto E(x, y)e^{-i\beta z}e^{-ik_x x}e^{-ik_y y}$ and map it in the (n_{eff}, ω) space. Here, we have $\beta = n_{eff}k$ and ω is the angular frequency of the electromagnetic field. In this seminal work [12] Russell and co-workers numerically demonstrated that a silica structure made of a triangular lattice of air holes with air filling fraction of 45% exhibits narrow PBG that extend beyond the air-line, synonymous of possible guidance in a hollow core. Indeed, any supported core mode with a couple (n_{eff}, ω) that lies with these PBG regions cannot escape through the cladding because of absence of modes to couple to, and thus is restrained to be guided with no leakage.



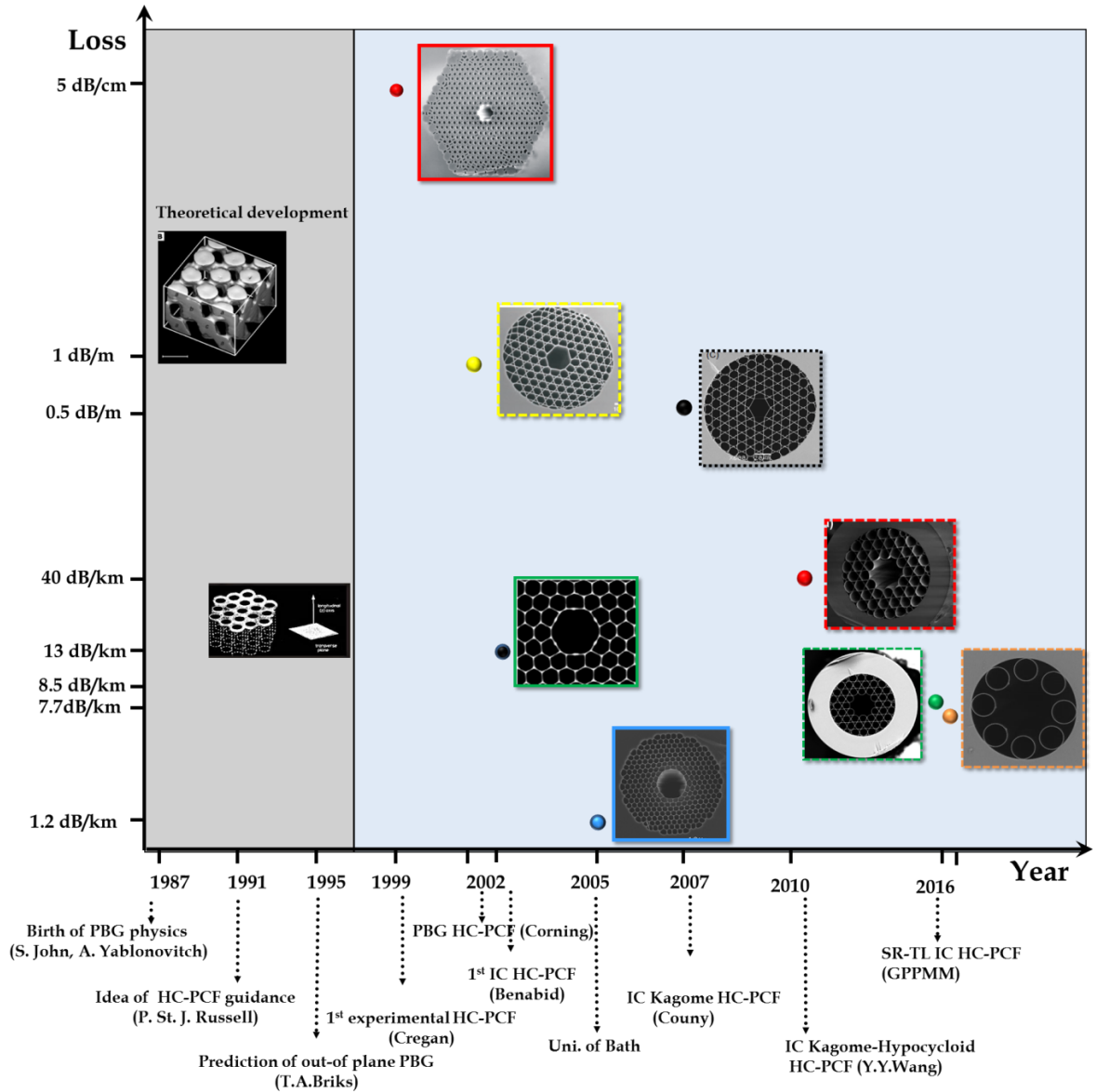


Figure 1-1 Summary of historical development of HC-PCF technology based on PBG and IC guidance. The area in gray color in the graph represents the years of theoretical developments from PBG guidance to first HC-PCF invention. The blue area represents development of HC-PCF based on PBG (in solid line borders) and inhibited coupling (dashed borders).

In late 1999, Cregan *et al.*, fabricated the first HC-PCF [19]. Whilst this work represented the triggering event in the experimental development of HC-PCF, it failed to demonstrate PBG guidance or low loss transmission. The undisputed PBG fiber guidance was demonstrated in late 2002 by Corning [13] using the same cladding structure as suggested in the original paper Birks *et al.* [12], but with a

larger air-filling-fraction. Here, the authors reported a HC-PCF with minimum loss value of few 13 dB/km at 1550 nm, which is shown in green inset of the Figure 1-1. In 2005, P. J. Roberts, *et al.* [20] improved its transmission performance by reporting the lowest loss of 1.2 dB/km at 1550 nm [20] with larger core diameter. This loss figure is set by surface scattering limit caused by surface roughness around core surround which is created by surface capillary waves (SCW) during the fabrication process [20].

In parallel to the development of PBG guiding HC-PCF, another class of HC-PCF was first reported by Benabid and co-workers in 2002 [6]. The reported fiber has a Kagome cladding lattice and guides over a broad spectral range and was the first reported HC-PCF to exhibit loss level in 1 dB/m before the then staggering figure of 13 dB/km in PBG HC-PCF reported by Corning few month later. The guidance of this class of fiber is not based on the formation of photonic bandgaps at the guiding wavelength, but upon coupling inhibition between cladding and core modes [14] due to transverse phase mismatch between them. This novel theoretical model was proposed by Fetah Benabid and first reported in 2007 by Couny *et.al* [14] and whereby they draw the analogy of this guidance mechanism with the bound state in continuum (BiC) predicted by Von Neumann and Wigner. The development of the IC model provided design tool and enabled the original introduction of fibers with hypocycloid core-contour, first reported in 2010 [16] and [17] which has the merit of dramatically enhance the IC. This work has also being the triggering event of rapid and succeeding results showing a continuous transmission loss reduction in IC HC-PCF for the last 7 years. For example, such fibers resulted in low loss transmission 40 dB/km at 1500 nm in 2011 [17] , then has been dropped to 17 dB/km at 1 μ m and 30 dB/km at 780 nm and later to a state-of-art fiber with 8.5 dB/km at 1 μ m by refining the fiber design parameters. The work of 2010 has also inspired the development of another new IC HC-PCF,



first reported in [21]. Its cladding design consists of an arrangement of isolated thin glass tubes called single ring tubular latticed IC HC-PCF. This fiber demonstrates record transmission loss of 7.7 dB/km at 750 nm (just 4 dB below the Rayleigh scattering limit) and an ultra-large transmission band covering one octave with losses ranging between 10 to 21 dB/km. IC HC-PCFs have become successor to PBG fibers in number of applications with their outstanding broadband guidance (over the visible and near-infrared spectral range) with relatively low attenuation.

This thesis is fully dedicated to study the guiding principles and linear properties of IC HC-PCFs with an aim to explore the salient features of inhibited coupling guiding mechanism and to develop optimized IC fibers with broadband and ultra-low loss. In this regard, section 1.3 will discuss about the guiding principles of different optical fibers with including conventional fiber, PBG fiber and IC HC-PCF. It is followed by more detailed review on photonic tight binding model theory [22] to understand the optical guidance in PBG HC-PCF. Final section of the chapter introduces IC HC-PCFs along with their main features and benefits over PBG HC-PCFs.

1.2 Applications of HC-PCF in gas-photonics

Thanks to the micro-meter scale core size and the low intrinsic loss, HC-PCFs provide a new fiber platform for long length light-matter interactions for both linear (such as laser-induced guidance of atoms and particles [23] [24]) and nonlinear applications. Efficiency of gas-laser interactions are generally quantified by figure-of-merit:

$$FOM = \frac{L_{eff}}{A_{eff}} \times \lambda \quad (1.1)$$



where L_{eff} is the effective interaction length, A_{eff} is the effective area of interaction and λ is the wavelength of the laser. Figure 1-2 shows evolution of FOM with core radius of different HC-PCF along with the free-space and capillary configurations. We can notice from the figure that HC-PCF enhances FOM in the order of magnitude 10^8 compared to conventional silica capillary and free space optics. Consequently, HC-PCFs allowed series of breakthroughs in nonlinear optics applications for example in gas-based photonics by introducing a Raman active medium such as H_2 gas into the hollow-core to generate optical frequency comb [6] and for electromagnetically induced transparency (EIT) in molecular gas [25] [7]. With the ability to host fluidic samples inside the air core, these fibers made it possible to diagnose and sense variety of samples. One of the major milestones of HC-PCF is the compact, stable and efficient all-fiber gas cell [26] which was demonstrated for enhanced simulated Raman scattering (SRS) [6] and exhibit excellent performance with long-term pressure stability. Figure 1-3 presents HC-PCF based micro gas cell made by splicing a SMF to HC-PCF. HC-PCFs with enhanced damage thresholds are used for high power laser delivery, pulse compression [27] and transmission of new frequencies which were not possible with conventional fibers.



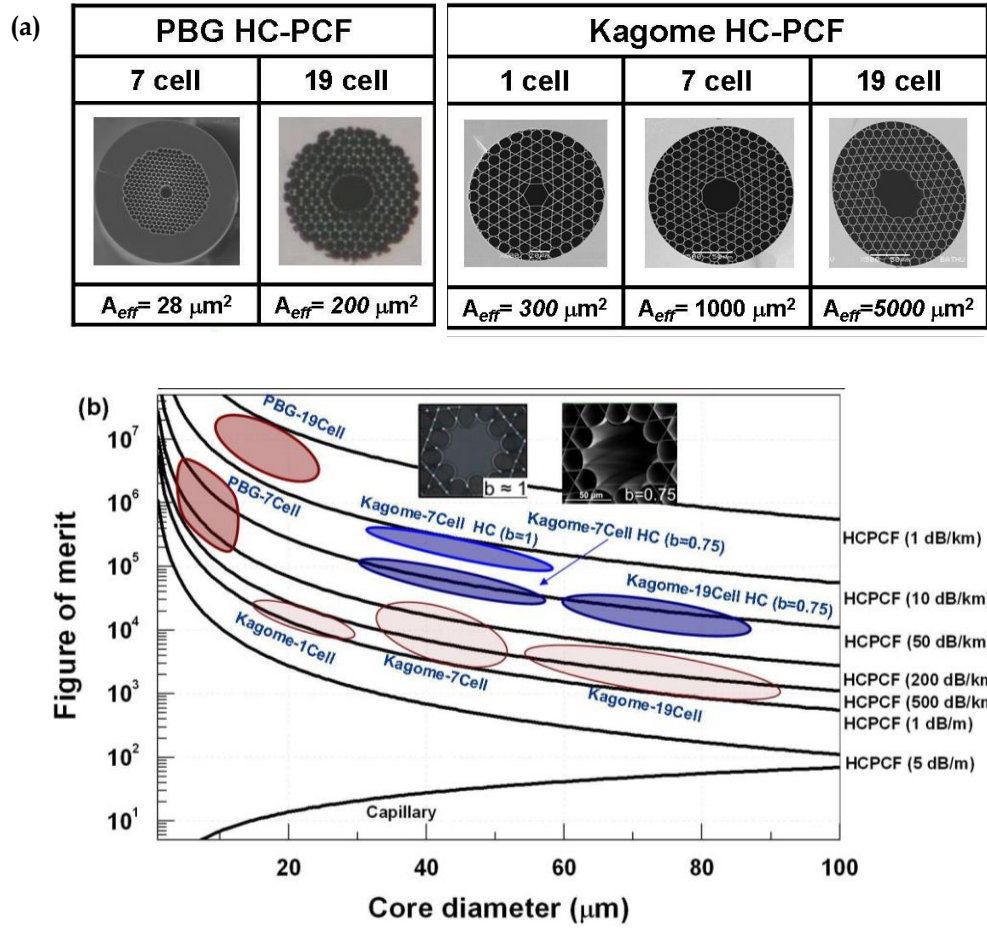


Figure 1-2 (a) SEM images of different types of PBG, Kagome IC HC-PCF. (b) and their FOM.

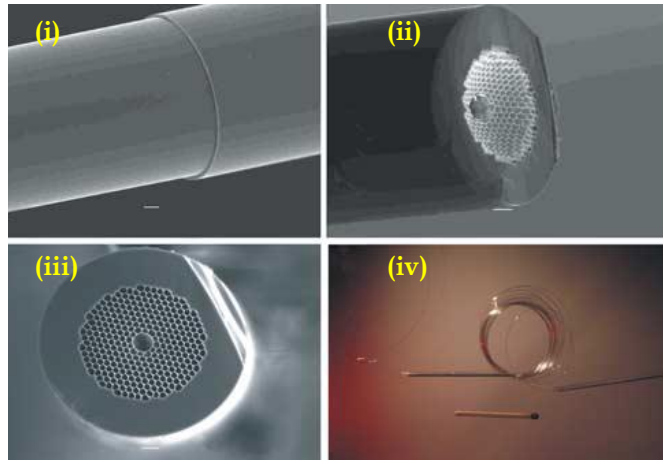


Figure 1-3 SEM images of (i) HC-PCF-based gas cell and cleaved ends at (ii) the spliced junction and (iii) away from the junction. (iv) The photograph of the cell to compare its size to that of a match stick [from [26]].

1.3 Light guiding principles of optical fibers

Akin to solid state physics approach, understanding the basic guidance mechanism of HC-PCF starts by considering the modal spectrum of the infinite form of its cladding structure in the $(\omega - n_{eff})$ space, and then introducing the fiber core as a defect to break the symmetry of the cladding lattice being it a periodic lattice or amorphous lattice. The modal spectrum is the mapping of different modes of cladding structure at different frequencies. This mapping of $\omega - n_{eff}$ gives density of photonic states (DOPS) which is defined by number of allowed states per unit of frequency and effective index. In guided photonics, the term photonic state relates to the mode propagating in the direction perpendicular to the periodic transverse plane of the medium. For example, when DOPS=0 at a given (ω, n_{eff}) that means no z-propagating modes are allowed at this (ω, n_{eff}) . We can identify allowed z-propagating photonic states in continuum of waveguides as guided modes and disallowed photonic states are photonic bandgaps (PBGs). By understanding this landscape in analogy with energy band diagram of condensed matter physics, we can define and design fibers of different guiding mechanisms. Similar to the electronic band gap formed between valance and conduction bands, the PBG is formed in the DOPS diagram between two consecutive modes from the photonic structure guiding features. The difference however is that the electrons naturally sit in a lower ground state energy level (potential well), while photons are guided in the highest refractive index material. The $\omega - n_{eff}$ mappings shown in Figure 1-4 illustrate the guiding principles of optical fibers of different geometrical configurations ranging from uniform dielectric material to a HC-PCF.

To begin with, let us firstly consider EM propagation out of the periodic plane in a uniform and infinite dielectric medium as shown on left side of Figure



1-4(a) with dielectric constant n_{cl} . The DOPS map of this dielectric medium (background material) can be found by casting Maxwell- Helmholtz equation as an eigenvalues problem [28]:

$$(\nabla^2 + k^2)H + \nabla(\ln n^2) \times (\nabla \times H) = \beta^2 H \quad (1.2)$$

here H is the transverse component of the magnetic field, n represents dielectric function of the cladding structure, k is the free-space wavenumber and $\beta (= n_{eff}k)$ is the propagation constant with effective index n_{eff} . The solutions of the above equation are eigen modes or photonic states which can be written in Bloch form: $H = e^{i\beta z} e^{ik_{\perp}r} u(z)$, where, k_{\perp} is wave vector in the plane of periodicity, r and z are unit vectors along transverse plane and propagation axis respectively and $u(z)$ is a Bloch wave propagating in z -direction with a propagation constant β . The DOPS of the uniform dielectric material is shown in the column B of the Figure 1-4(a). The gray region in this DOPS diagram indicates allowed photonic states with n_{eff} below its material index n_{cl} (i.e, $n_{eff} \leq n_{cl}$). These photonic states are called continuum of modes or extended Bloch modes that can be expanded as a combination of planar waves propagating in z -direction. In the black region above n_{cl} line (i.e, $n_{eff} \geq n_{cl}$) the material does not support any guided photonic state, thereby creates a photonic band gap. If we introduce a defect of dielectric constant n_c to create a core at the center of the continuum such that $n_c > n_{cl}$, and radius ρ , the continuous symmetry of the dielectric material structure is broken and defect can have its allowed photonic states or modes above the continuum as shown in dispersion diagram in the Figure 1-4(b). Therefore, above the continuum photonic states are now allowed and are localized within the defect. This situation represents TIR guidance of step index fiber in which core material of high effective index is embedded in background material of low index material. The number 01 in the Figure 1-4(b) represents fundamental mode and other numberings correspond to higher order modes.

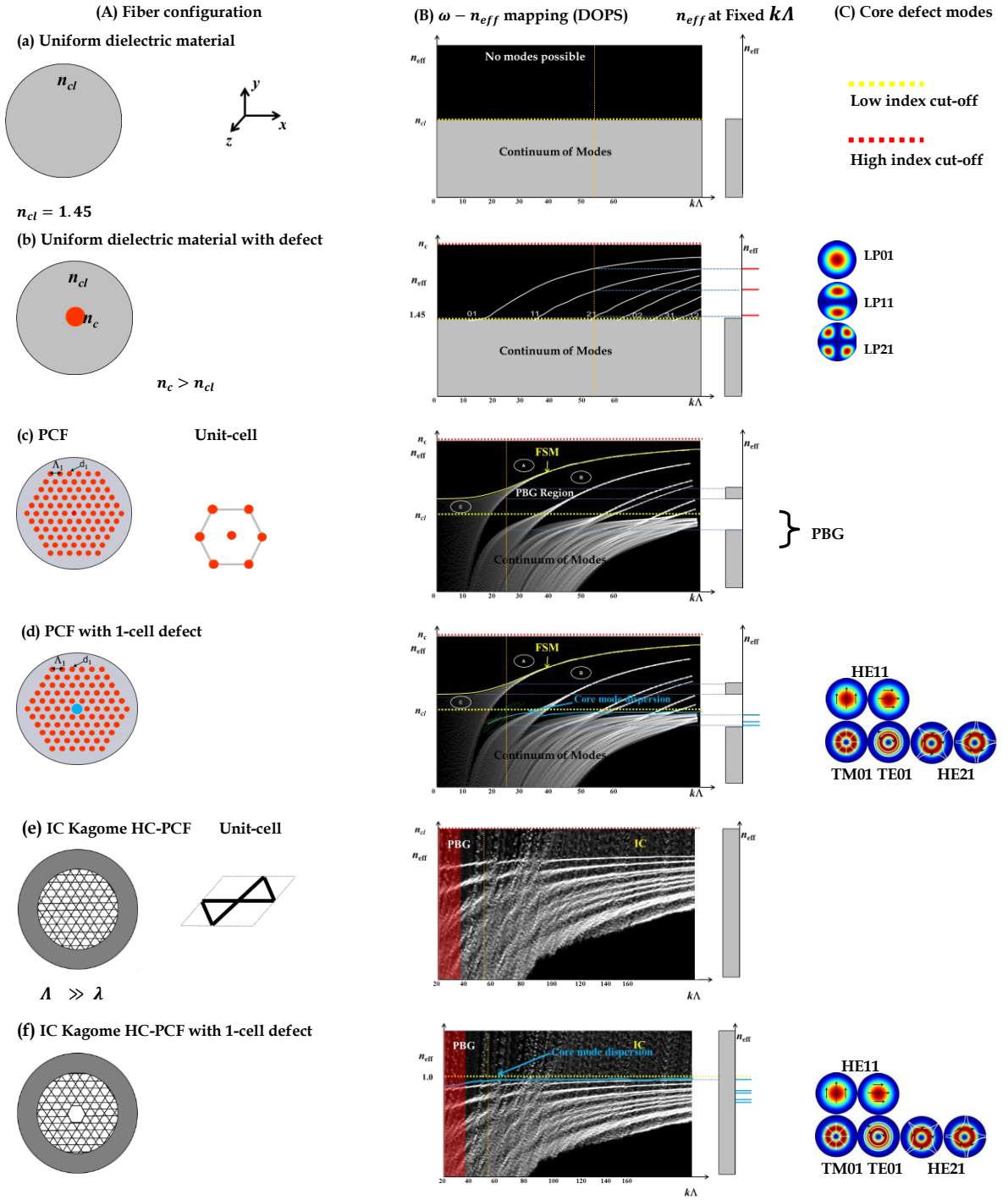


Figure 1-4 Left side: (A) schematic of fiber cross sections of (a) a uniform dielectric material (b) a fiber with a defect of high index material. (c) Uniform PCF and its unit cel. (d) PCF with a unit cell defect operated in low pitch regime for PBG guidance. (e) Uniform Kagome PCF and its unit-cell and (f) with a 1-cell defect operated in large pitch regime for IC guidance (IC HC-PCF). (B) Shows DOPS diagrams and n_{eff} at fixed $k\Lambda$ for fiber models presented in (A). (C) Presents field distributions of defect modes identified at fixed $k\Lambda$ in the figure (B).

This model of expressing guiding principle of optical fiber is so powerful in the sense that we can change n_{eff} by simply varying the properties of the defect for example by changing its radius, geometry and dielectric constant of the defect. Figure 1-4(b) (on right side) also shows allowed photonic states or allowed modes at a fixed frequency, $k\Lambda = 40$. Gray bars at its left represent continuum modes of the cladding and red lines at right side represent allowed photonic states or guided modes of the defect. The column C of the Figure 1-4 shows mode field distributions in the core defect. We can also notice a continuous band extended up to n_{cl} which is the continuum of dielectric modes and above it, until n_c the allowed photonic states belong to the defect.

Now, we can extend the above approach to explore the guiding properties of a PCF by considering micro-structured cladding such as the one shown in Figure 1-4(c). This fiber configuration is comprised of rods of material index n_c in a regular periodic triangular lattice with spacing Λ , and rods' diameter d which constitutes a uniform photonic crystal with periodic material index. The geometrical parameter (*i.e.* Λ and d) and the index contrast of the photonic crystal structure determine many of its optical properties in a similar fashion as it does for conduction properties of a semiconductor. Instead of a single dispersion line for each mode of the single rod as in the previous case, here due to combined effect of cladding structure formed by periodic rods, their dispersion curves get hybridized and open up allowed bands for a given cut off frequency. The DOPS presented in Figure 1-4(c) depicts this situation of broadening of dispersion curves for each mode as the distance between multiple rods is reduced. In other words, the dispersion of cladding broadens with decreased pitch ($k\Lambda$). The yellow line at top of fundamental band is called free space filling mode (FSM) which represents the fundamental mode (*i.e.* the mode with the highest effective index) of the

cladding structure when considered as a single waveguide. In other words, the propagative solution to Maxwell's equations with the largest n_{eff} is called the FSM [29], and the associated effective index value is represented by n_{FSM} . Therefore for the range $n_{FSM} < n_{eff} < n_c$, propagative fields exist in the core region but can only couple to evanescent fields of the cladding, which is exactly the same situation as in step-index fiber. Hence, we can conclude that if we introduce a defect with index higher than n_{FSM} (*i.e.* above FSM in $\omega - n_{eff}$ space), the optical guidance resembles total internal reflection (TIR) of step index fiber as represented by region A. This is a typical case in solid-core PCF. Therefore, with reference to Figure 1-4(c), we can say that step index fiber has a bandgap shown as the lowest open region below the FSM line. We also note that in region C with $(k\Lambda, n_{eff})$ propagative solutions do exist, but for solid-core PCFs these are mostly irrelevant and guidance properties are largely dominated by modes with $n_{FSM} < n_{eff} < n_c$, that is by modified total internal reflection (M-TIR). These modes are called guided modes of the cladding which are formed by the inclusion of high index material. Also, there exist several other regions represented by B where propagative solutions do not exist, and their widths depend on the geometrical parameters of the structure (in particular d and Λ). For lower frequency ranges or low pitch regimes, the guided modes of the cladding get hybridized and create PBG. If any light of specific frequency is allowed within this gap, it gets trapped and could not able to leak into cladding since there are no other allowed modes available to couple with. In other words, to confine or trap the light within the regions of PBG, a defect of proper index and geometry shall be introduced in the cladding so that its guiding frequencies fall within the PBG. As a result the defect modes would not resonate with cladding modes. Such a trapped state is shown in blue line in the Figure 1-4(d) at a fixed frequency $k\Lambda = 15$ within the bandgap of cladding continuum, especially by introducing a hollow-core defect ($n_c=1$).



As we can notice from the DOPS of Figure 1-4(d), PBG still exists below the airline ($n_{eff} = 1$). Hence, photonic states now can also be confined within the air-core; thereby it is called as PBG HC-PCF. The coupling of the core mode to the cladding is disallowed by micro-engineering the cladding structure such that its modal spectrum is void from any propagation modes (*i.e.*, $\{|\varphi_{clad}\} = \emptyset$, with φ_{clad} being the field wave function) at the core guided-mode effective index-frequency space, $n_{eff} - \omega$ or DOPS diagram calculated for infinite triangular latticed cladding structure. It is this absence of cladding modes which forces a core mode to be guided in a PBG fiber and restraints it from leaking out from the core. In the coming section 1.4.1 we review on photonic tight bonding model (P-TBM) theory to explain the guiding mechanism in a PBG HC-PCF.

However, the PBG guidance in low pitch regime is not the only guiding mechanism we can have in the PCF. As we increase frequency or pitch regime in $\omega - n_{eff}$ space ($k\Lambda > 50$) the dispersion bands get converged as in the case of individual rods. Such HC-PCF based for example on Kagome cladding design (see Figure 1-4) provides high air-fill fraction cladding or in high pitch regime ($\Lambda \gg \lambda$) enable higher-order gaps to open up relatively narrow and separated by wide spectral regions. The DOPS diagram shown in Figure 1-4 (e) is calculated for infinite Kagome cladding structure. Now, if we remove one of its unit-cell (see in the figure) from the center of the cladding, it forma a 1-cell defect Kagome HC-PCF. In this configuration the core guided photonic states co-exist with the continuum modes but will not be resonating with each other due to phase mismatch between both modes. The regions of steeper slopes in the figure represent resonances with cladding modes which leads to higher losses for guided core modes. In this way core modes *inhibit* their resonance with cladding modes and hence the guiding mechanism is called “*inhibited coupling (IC)*”. Therefore, HC-PCF based on this unconventional guidance mechanism is called as Kagome

latticed IC HC-PCF. We can notice that at fixed frequency ($k\Lambda=45$) the core defect mode (in blue line) is embedded within the continuum (gray rectangle), and at the same time no photonic band gap is observed around the defect state. Chapter-2 will review about the guidance of IC HC-PCF in analogy with bound state in continuum (BiC) [15].

1.4 PBG HC-PCF Guidance

In previous section we have seen that microstructure dielectric material compared to a uniform material exhibits a cladding modal spectrum which includes PBG and allowed states. Guiding mechanism of PBG HC-PCF can be better understood by using photonic tight binding model (P-TBM) which has been proposed by Benabid and co-workers reported by Couny *et al.* [22]. This model gives complete details about the formation of band structures and the origin of PBG along with prediction on other features like shifting of band and its width. P-TBM is explained on the strong parallelism with respect to the tight-binding approximation (TBA) [22] of solid state physics. Figure 1-5 shows an analogy between both models.

1.4.1 Photonic Tight Binding Model

Consider a crystal made up of symmetric, with well-defined energy levels and spacing between atoms. Such materials possess energy bandgap about which valance electrons shall cross in order to be conducted. When such atoms are subjected to any external force, their average inter-atomic spacing decreases and the electrons at the outer shell begin to overlap. If they are pushed even further closer, the inner most shells are also forced to overlap. In other words what was originally a single energy level is now split into number of energy levels above and below its original energy level such that it can still accommodate all the



electrons. For example, when N number of such atoms are brought in close proximity, their outer shell electrons begin to overlap and as a result their energy values get N -fold degeneracy. This process is called as tight binding approximation (TBA) and it is very important to study condition properties of any material that is subjected to external forces which would alter average inter atomic spacing that manipulates energy band gap of the material. This can be explained by the plotted graph for energy against inter atomic spacing (Figure 1-5(a)). When atoms are in unaltered position, the complete material possesses allowed eigen values of valance and conduction states defined by Schrödinger equation. In this situation, the material behaves as an insulator since the energy band gap (ΔE) is huge as identified in region 1 (dotted red line) Figure 1-5(a). Now, as the atoms are brought closer without altering its structure, dimension and symmetry, at a certain point, bands get closer where ΔE reduces further as shown in region 2 (dotted green line). In this configuration the material acts as semi-conductor. Further forcible decrease of inter-atomic distance results in complete disappearance of the energy gap where both valance and conduction bands get overlapped (shown in dark blue shaded region that begins at circle 3). As a result, the material would behave as a conductor.

Now, in order to explain HC-PCF guidance, in analogy with TBA, we consider each constituent feature of HC-PCF (which are cylindrical silica rods in Figure 1-5(b)) as individual atoms of TBA. Figure 1-5(b) shows photonic equivalence of TBA, *i.e.* P-TBM. As shown in scanning electronic micrograph (SEM) image of Figure 1-6, every unit cell of a HC-PCF can be approximated as a combination of three different constituent features. Firstly, a junction or an apex of the cladding structure (red circles) is similar to a single isolated silica rod. Secondly, every six of such rods are attached by a thin silica strut (shown in white



circles) forming a hexagonal unit cell. Finally, these two features form an air hole as shown in green circle in the same figure.

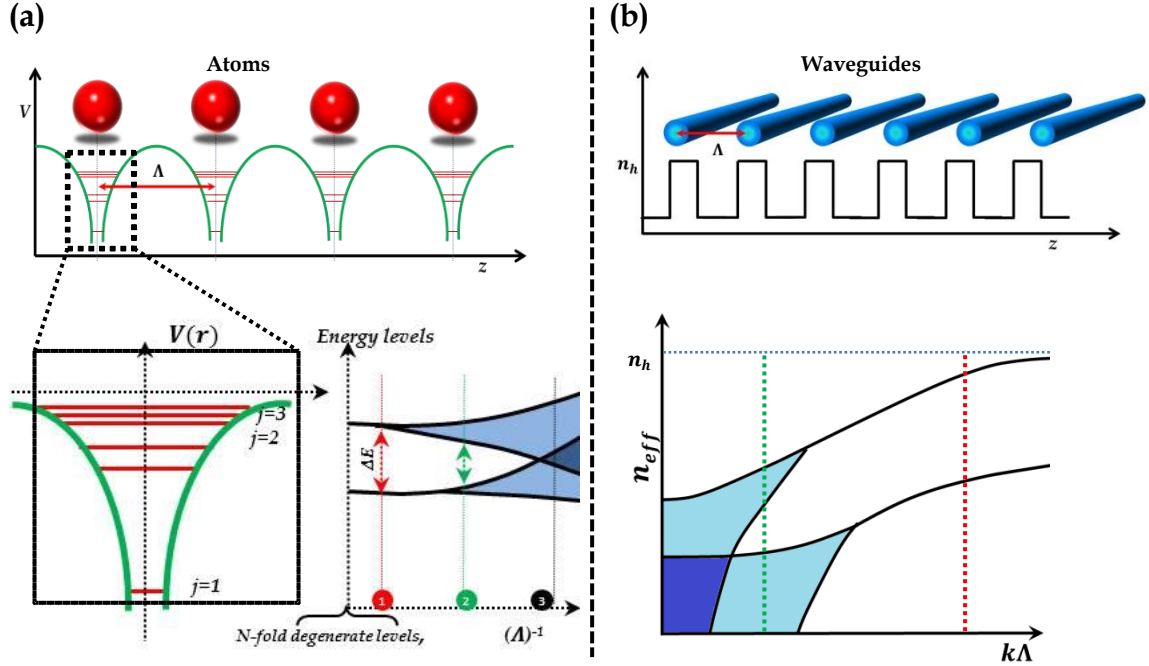


Figure 1-5 Schematic illustration showing the analogy between (a) TBA and (b) P-TBM [30]. The regions 1, 2 and 3 in (a) represent insulator, semi conduction and conduction domains of the material respectively. (a) Wavguide system with effective index n_h , spaced by Λ and is DOPS (n_{eff} - $k\Lambda$) diagram. Blue and red dotted lines on n_{eff} - $k\Lambda$ graph represent large and small pitch domains of the waveguide systems.

If we consider single isolated silica rod of diameter d , its dispersion spectrum will look like dispersion curve as shown in Figure 1-7(a). To illustrate T-BPM, let's introduce a toy model by making a 1D array of such N number of rods with pitch, $\Lambda = 0.45/d$. The rods assumed to have a Gaussian refractive index profile and to couple only with the nearest-neighbor rods. When the rods are far from each other, (i.e., $\Lambda \gg \lambda$), the allowed photonic bands of the system remain very narrow and do not deviate from the dispersion of a single rod. The situation is similar to atoms in TBA, as such N rods brought close enough (see Figure 1-7(b)), the allowed frequencies for a single rod splits and therefore their dispersion bands get broaden into allowed bands for the array. The red and green lines in the figure indicate evolution of band splitting as such rods or waveguides are brought closer

together from larger distances (large pitch regime to small pitch regime). The DOPS diagram shown in Figure 1-8(a) gives precise details of the continuum modes about the band gaps formed [31]. The upper edge of the bandgap shown in red color represents localized modes in the interstitial apex of the cladding, whilst the lower edge is formed by two modes of different symmetry, one being guided predominantly in the air holes (green line) and the mode guides within and close to the silica struts which join the neighboring apices (blue line).

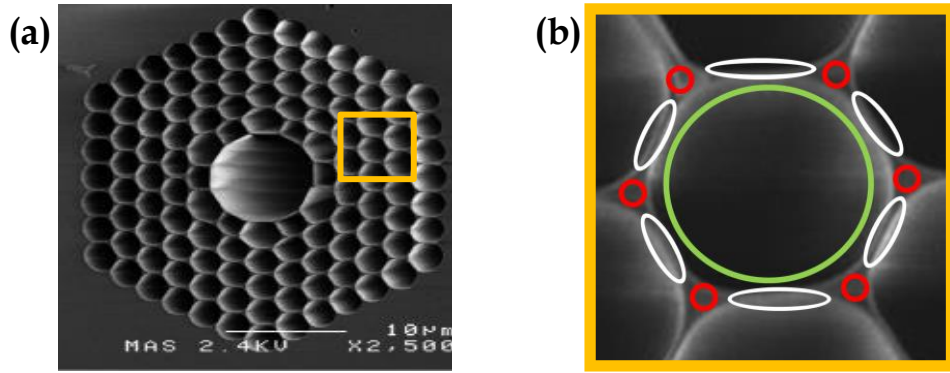


Figure 1-6 (a) SEM image of a PBG HC-PCF and inset shows its unit-cell. **(b)** Zoomed in unit cell. Green circle is a hole formed by six apices shown in red circles and connecting struts shown in white elliptical circles.

Therefore, as energy band gap of TBA depends on the inter-atomic spacing, the photonic band gap of HC-PCF is manipulated by the pitch, depth. The center frequency of the bandgap is dictated by the geometrical parameters of the apex and strut thickness. In other words, any changes to the resonators' geometry would alter its dispersion curves as we discussed in section 1.4 and if done properly, there could be a chance of having more than one PBG below the air-line. This fact triggered the idea of developing double PBG HC-PCF [33] below the airline simply by altering the structural features of its unit cell.

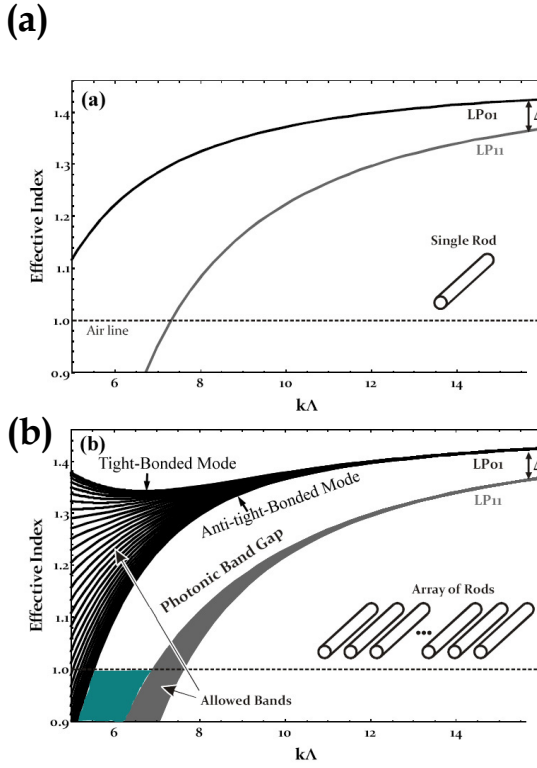


Figure 1-7 (a) Dispersion curves of the fundamental and first higher-order modes of (a) an isolated silica rod (b) an array of identical rods spaced by pitch Λ and the dispersion curves of array of rods broaden to form allowed bands [from [32]].

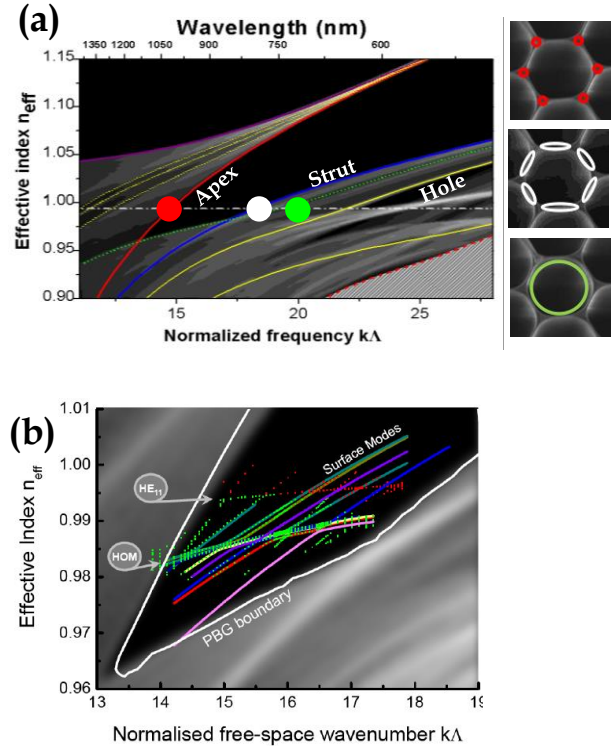


Figure 1-8 (a) Details of the calculated density of state plot around the PBG region falling below the vacuum line. (b) Zoom in of the DOPS showing surface modes and HOMs within the PBG region [from [32]].

Thanks PTBM for modelling the problem as the presence of resonators in the cladding; we can increase the width of the second PBG and its depth below the air-line by simply modifying its structural features for example, strut's thickness (t), apex radius (r) and pitch or AFF. As shown in Figure 1-9 the calculated dispersion curves for a typical triangular PBG HC-PCF show the opening of a second bandgap [33]. The left part of Figure 1-9(a) shows the DOPS for the cladding structure which is similar to apex curvature to that of a state-of-the-art HC-PCF with $t = 0.05$ and $r > 0.2\Lambda$. Such a structure results in the absence of the second bandgap (shaded region in Figure 1-9(a)). Whereas, by doubling t and decreasing the r by 25% the second bandgap will appear as shown on the right of the same Figure 1-9 (b).

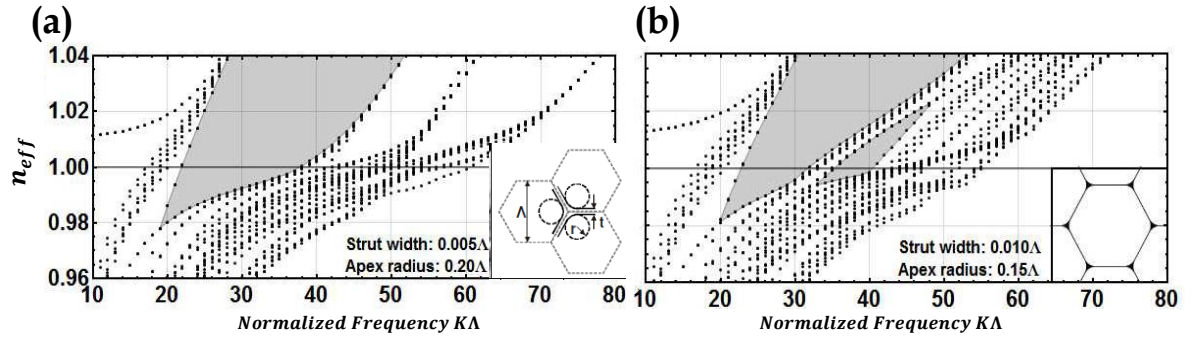


Figure 1-9 Effective indices of cladding modes calculated at high symmetry points for the structures with (a) strut thickness $t = 0.05\Lambda$ and varying apex curvature radius $r = 0.20\Lambda$ and (b) $t = 0.10$ and $\Lambda r = 0.15\Lambda$ [from [33]].

1.4.2 Limitations of PBG HCPCF

From the DOPS map shown in Figure 1-8(b), we can notice that along with flat dispersion line of HE_{11} modes there exist also surface modes and HOMs residing inside of the core-surround silica with steeper dispersion curves. This is the region where air-core guided modes resonate with the cladding modes by transferring most of the optical power into the silica cladding structure which leads to high loss and also increased dispersion. This limits the transmission band width of PBG HCPCFs typically less than ~ 70 THz which makes them ineligible for most of broadband applications. Another important core mode leakage is due to surface modes which originate at core-silica interface between the photonic crystal cladding and the core defect. Figure 1-10(a) reviews experimental studies about “anti-crossing” phenomenon in case of PBG HC-PCF [34]. If the surface and the core mode have the same frequency and propagation vector, an anti-crossing occurs where the dispersion curves of the modes repulse each other leading to an increase in the transfer of energy from the core mode to the high attenuation surface mode. These surface modes are problematic especially when we use these fibers for high energy laser beam delivery since energy residing by silica strut is beyond the capability of the material, results to strong damages of the material.

Therefore, despite of low loss guidance of 1.7 dB/km, the small core diameter of the PBG HC-PCF together with low laser induces damage threshold (LIDT) and strong ($\sim 1\%$) optical overlap of the core guided mode with the cladding limit their laser handling capabilities only up to pulse energy 7 μJ and high average power 0.7 W at 1.55 μm with ultrashort pulse duration less than 1ps) [35].

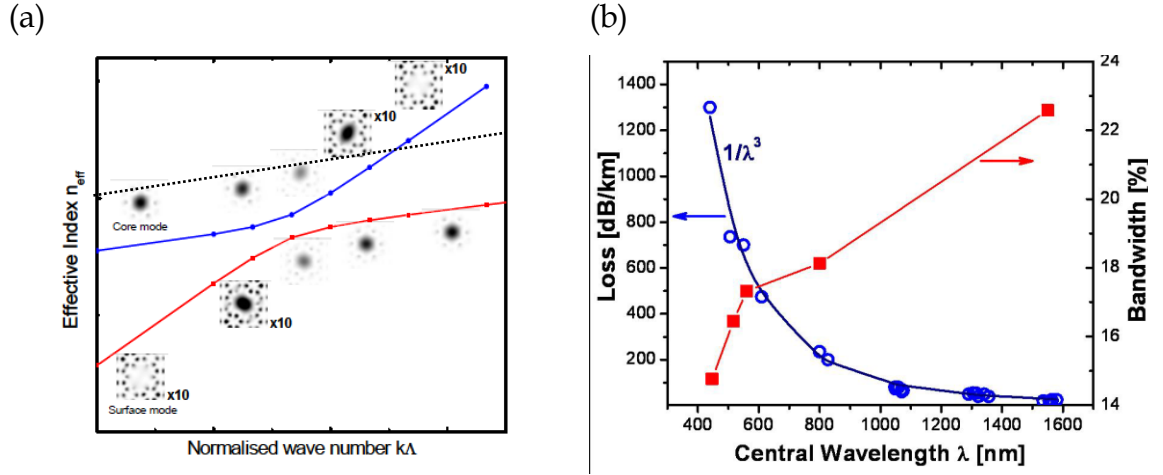


Figure 1-10 (a) Trajectories of the fundamental core mode (black dotted line) and a surface mode (blue and red solid lines) as they interact around an anti-crossing event. (b) Wavelength dependence of attenuation for a PBG HC-PCF (blue circles) and operating bandwidth (red squares) of a HC-PCF as a function of their central operating wavelength [From [34]].

Also, for atom-vapor applications the smaller fiber core size (between 5-10 μm and 10-20 μm in case of 7-cell and 19-cell defect air-core respectively) of these fibers renders the atom loading into the core very tedious and too slow. In addition large surface to volume area enhances the atom-surface interaction [36]. Enlarging the core size in order to either accommodate high power laser or to load efficiently atom would also require increasing cladding pitch. This process consequently affects shifting of transmission window from the required operating wavelengths, hence sets another limitation for the HC-PCF. Another important drawback of this class of fibers is the wavelength dependence of attenuation. Its measured transmission loss scales as $\alpha = (1/\lambda^3)$, due to surface roughness which imposes fundamental source of attenuation even in state-of-art HC-PCF [20]. As

shown in Figure 1-10(b), this scaling law sets losses exponentially increasing toward visible guidance (for example, up to 200 dB/km at 800 nm and 500 dB/km at 532 nm in case of 7-cell defect fibers) [34]. Also more practically and from fabrication point of view designing cladding pitch less than 1 micron is not possible to provide UV transmission. The losses of the fiber at UV regions as we can see in Figure 1-10(b) reach more than 1500 dB/km.

1.5 Inhibited Coupling HC-PCF Guidance

In parallel to the report of low loss PBG HC-PCF by Corning *et al.* [13], a new direction has been identified to optimize optical performances of the HC-PCF. Indeed, it is possible to optimise the bandwidth and the fiber attenuation of HC-PCF by increasing the air filling fraction (AFF) [32]. This intuition led to the development a novel class of HC-PCF which also stems from the conceptual transfer of semiconductor physics, called as inhibited coupling (IC) HC-PCF. This class of fiber was first reported by Benabid *et al.* [6] in 2002 with a 0.5-1dB/m loss-level. The guidance of IC HC-PCF is not based on the formation of photonic bandgaps at the guiding wavelength, but upon coupling inhibition between cladding and core modes [14]. Figure 1-11 shows SEM images of different in lattice structure of PBG and IC (Kagome) HC-PCFs respectively.

Thanks to salient optical properties, the IC HC-PCF has become successor to PBG fibers in number of applications. Firstly, low interaction of the core guided mode with the glass-confined cladding modes in Kagome lattice IC HC-PCF provides an uninterrupted transmission spectral range from the UV to the IR [6] which is not possible by PBG HC-PCF. With seminal introduction of a hypocycloidal (*i.e.* negative curvature) core contour [17], the optical overlap between core and cladding modes further reduced to 0.001%, which is about 3

orders reduction than PBG fiber (1%). As a result, IC coupling is further enhanced by demonstrating a record propagation loss of 17 dB/km around 1 μm . And during the tenure of this thesis, further optimization of core shape and cladding design new record Kagome fiber with losses 8.5 dB/km at 1 μm and SR TL IC HC-PCF with ultra-low loss of 7.7 dB/km at 750 nm over a broad spectral range have been developed. With its novel guiding mechanism and optical transmission characteristics, IC HC-PCF is dominating its place over PBG fibers in scientific and industrial applications. Figure 1-11(a) and (b) show SEM images of PBG and IC Kagome HC-PCFs with air-core formed by removing 7 unit cells from the center of the cladding structure. Figure 1-11(c) and (d) show the zoom into their corresponding cladding designs.

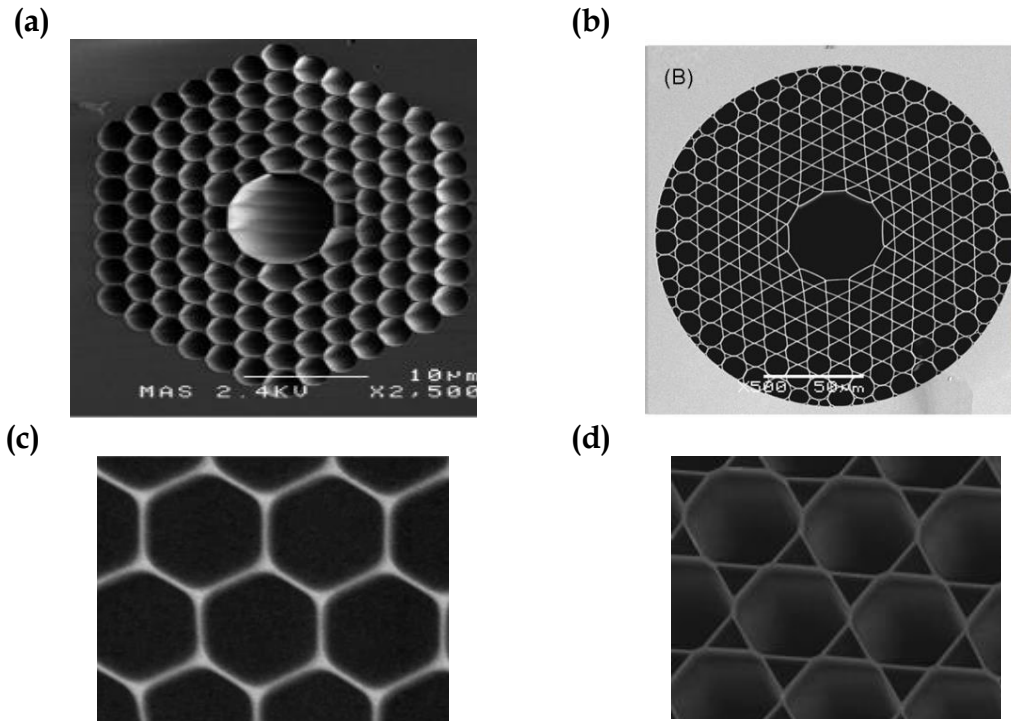


Figure 1-11 (a) SEM images of triangular lattice structure of PBG HC-PCF, (b) Kagome lattice structure of IC HC-PCF. (c) And (d) show cladding designs of the PBG and Kagome IC HC-PCFs respectively.

This thesis is fully dedicated to study in details about guiding principles and linear properties of IC HC-PCF with an aim to develop ultra-low loss, broadband

and high USP handlings along with flexibility and robust in nature. Further explanation of IC guiding mechanism with respect to $\omega - n_{eff}$ space mapping, modal analysis and optimization techniques will be addressed in chapter 2.



1.6 Thesis Outline

In this context, further analysis and optimization of IC HC-PCF designs is essential for its huge demand in several research domains. Therefore, this thesis is structured in the following way to cover complete study of linear properties of IC HC-PCF and new innovative designs.

- Chapter 2 presents in detailed theoretical and numerical explanation of IC HC-PCF guiding mechanism and various optical properties based on two cladding lattices: Kagome and tubular. This chapter reviews recent developments to enhance IC guidance including design, fabrication of ultra-low loss IC HC-PCF and the impact of cladding numbers and core shape.
- Chapter 3 experimentally demonstrates IC guidance as photonic manifestation of bound state in continuum by exploring Fano resonances in the transmission spectra of IC Kagome HC-PCF [37] [38, 39] which was proposed by Van Neumann and Wigner in 1929 [40]. This chapter also discusses about several examples of Fano resonance in various fields of physics to understand its basic phenomenon. A high-spectral resolution fiber-transmission shows the typical Fano asymmetric spectral signatures over 30 GHz bandwidth and a high dynamic-range near-field imaging resolves the core-cladding coupling.
- Chapter 4 presents our recent development of IC guiding HC-PCF designs by optimizing its structural features as will be discussed in chapter 2 and their linear characterizations. This chapter starts with presentation of several optimized fabricated 7-cell Kagome lattice IC HC-PCF design fibers



with record level losses down to 8.5 dB/km at 1 μ m and broad band transmission with 30 dB/km loss at 780 nm. These exceptional characteristics of IC HC-PCFs are not only limited to Kagome lattice designs but can also be observed in these alternative designs. Therefore, second part of this chapter presents a novel fiber design based on single ring tubular lattice (SR-TL) IC HC-PCF. Indeed, the fiber exhibits minimum loss of 7.7 dB/km at 750 nm and an ultra-large transmission band covering 1 octave spanning from 600 nm to 1200 nm with losses between 10 to 21 dB/km. The results indicate that the prospect of guiding light with transmission loss lower than the limit set by the ubiquitous silica Rayleigh scattering is now possible. Finally, UV/DUV guidance is also demonstrated with SR-TL IC HC-PCF.

- Chapter 5 discusses about new experimental procedure to investigate losses that are induced by surface roughness inside the core of the IC HC-PCF. This set up also measures angular distribution of scattering from which coefficients of surface scattering loss (SSL). The set-up also constructs the core mode leakage due to surface scattering in the transvers plane of the fiber to check the impact of SSL on confinement loss (CL).





Chapter 2

Enhancement of guiding in IC HC-PCF

In this chapter, we review guiding mechanism, optical characteristics and effect of structural features on transmission and modal properties of IC HC-PCF. Therefore, it provides sufficient knowledge to identify key design elements and physical parameters to optimize and engineer the IC HC-PCFs for ultra-low loss and broadband transmission.



2.1 Introduction

HC-PCFs with low intrinsic loss guidance and the ability to confine light in the hollow-core over larger distances demonstrated a number of breakthroughs in different applications ranging from quantum optics to light-matter interactions. HC-PCFs with micro-structured cladding designs provide platform for two new optical fibers based on their different guiding mechanisms. Firstly, PBG HC-PCF [20] in which light guidance is based on the formation of an out-of-plane bandgap of the micro-structured cladding. Owing to the structural features, these fibers ensure light confinement within the core formed by proper defect choice provided its effective index lies within the PBG of the cladding. Hence, the trapped light inside the hollow-core defect would have no access to radiate or decay into the cladding since it is bounded within the frequency range of PBG. We have summarized their optical characteristics in Chapter 1. This fiber has been exploited in many applications including soliton delivery [27], electromagnetically induced transparency (EIT) [25] [7] and Raman scattering [41] to mention a few. However, due to limited transmission bandwidth and the presence of surface modes, this class of fiber could not extend its scope to a large number of applications. For example, it would be desirable to bridge the wavelength ranges of Nd:YAG and Yb lasers at $\sim 1 \mu\text{m}$ with that of the Ti:Sapphire ($\sim 800 \text{ nm}$) or Er-doped lasers used in telecommunications ($\sim 1.5 \mu\text{m}$). This was illustrated in the achievement of double bandgap [33] HC-PCF, and whereby the photonic tight binding model (see Chapter 1) describes the difficulty with silica and air based HC-PCF to open up wide PBG below the air-line.

In parallel, we have seen that light can be guided in HC-PCF via IC mechanism such as Kagome-lattice HC-PCF (see Figure 2-1). These fibers proved to guide light with low loss over a broadband transmission window with *gapless*



cladding modal spectrum. This guidance was first demonstrated in a HC-PCF based on Kagome lattice cladding with large pitch and elongated silica web was reported for the first time by Benabid *et al.* [6]. The SEM image of cross section of such a fiber is Figure 2-1(a). The word “Kagome” comes from the Japanese “bamboo basket”, which is similar to the structure formed by a tessellated “star of David” as seen in the center of Figure 2-1(b). This class of fiber does not show any photonic bandgap in its modal spectrum of the cladding, instead it relies on coupling inhibition between core-guided modes and cladding modes. The two modes co-propagate along the fiber at same frequency and effective index with very negligible interaction. In other words, in case of IC guidance guided core modes are embedded within the continuum of the cladding and their coupling is strongly inhibited due to their transvers phase mismatch, whereas the core modes are trapped outside the continuum of cladding in case of PBG guidance. This fact makes the IC guidance very novel with its salient optical characteristics and gaining scientific attention because of its distinct guiding mechanism.

IC HC-PCFs with broadband transmission capability over the visible and near- infrared have broadened the scope of HC-PCF applications and becoming successor to the PBG class. The low chromatic dispersion of IC HC-PCF is paramount for achieving efficient non-linear applications such as Raman scattering or Raman sidebands. Also, IC Kagome fiber designs with low loss broadband transmission, filled with H₂ gas proved the ability to generate Raman frequency comb over-five octaves wide with high power picosecond-laser [42]. It's ultra-low light-in-glass fraction down to ppm level promises IC HC-PCF as an excellent means to deliver USP with low attenuation and with low temporal spectral distortion. This is further demonstrated by delivery of 600 fs pulses at 1 mJ or even more energy levels in a robustly single-mode fashion [43]. Finally, owing to its large core area, which benefits for atom trapping applications to load



the Rb or Cs atoms with ease and faster with low fiber loss figures around 780 nm, this class of fibers is preferred over PBG fibers [44]. A successful explanation of IC guiding mechanism is reported in [14], in analogy with von Neumann–Wigner bound states in a continuum (BiC) [40].

This chapter is divided into three main sections. The first section, section 2.2, reviews guiding principles of IC HC-PCF and the key design parameter to enhance IC guidance. Furthermore, in sub section 2.2.3 we give clarifications and distinctive properties of IC guidance from PBG and anti-resonant reflection optical waveguide (ARROW) model. The second section of the chapter reviews on modal analysis of the Kagome fibers and impact of its core optimization its optical performances. Finally, the chapter presents guiding and modal studies of a new IC HC-PCF design concept based on tubular cladding structure.

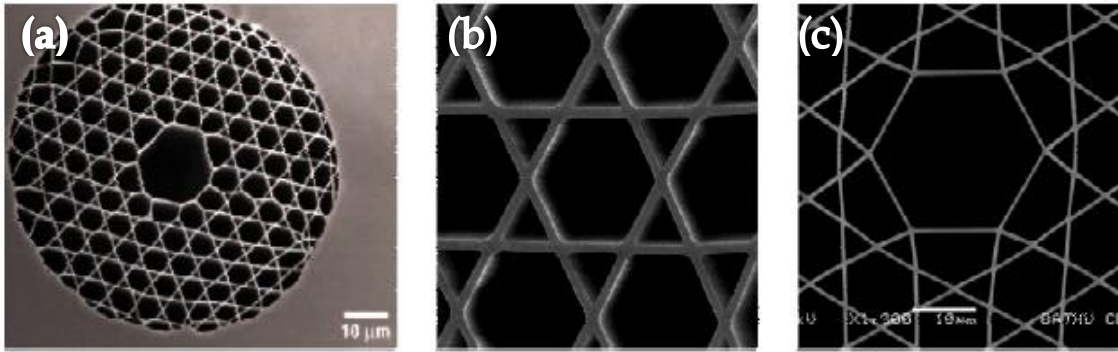


Figure 2-1 (a) SEM images of a single-cell core large-pitch Kagomé fibers. (b) Zoom in to the details of the cladding structure. (c) Core formed by 1-cell defect.

2.2 Principles and key design parameters in IC optical guidance

2.2.1 Basic IC guidance principles

Unlike PBG fibers, the guidance in IC HC-PCF does not exhibit bandgap in the DOPS diagram, but instead it relies on coupling inhibition between the guided core mode and cladding modes. In analogy with quasi-bound and bound state in a continuum (Q-BiC), a core guided-mode of IC HC-PCF (often leaky mode) cannot or strongly inhibited to channel out through the cladding by a strong reduction of coupling. In other words, dot product between the field of the core mode $|\varphi_{core}\rangle$ and the cladding mode $|\varphi_{clad}\rangle$ is strongly reduced (*i.e.*, $\langle\varphi_{clad}|\Delta n^2|\varphi_{core}\rangle \rightarrow 0$, with Δn being the photonic structure transverse index profile). This core-cladding coupling factor $\langle\varphi_{clad}|\Delta n^2|\varphi_{core}\rangle$ can be reduced either by having little spatial intersection between the fields of $|\varphi_{clad}\rangle$ and $|\varphi_{core}\rangle$ or by having a strong mismatch in their respective transverse spatial phase. Drawing on ideas from solid-state physics, the light leakage is reduced in IC HC-PCFs owing to symmetry incompatibility between the transverse phase of the core mode and those of the cladding modes. In this situation, core guidance can occur even with a dense continuum of cladding modes at its $n_{eff} - \omega$ space provided that the latter have a strong transverse-phase mismatch with the core guided-mode, and their intensity is concentrated in a cladding region with different material-index than that of the core. In the sense that a PBG fiber is defined by the absence of phase-matched cladding modes to transfer light outward from the core, the cladding continuum in IC guiding fibers effectively acts as a quasi-PBG over the core mode in $n_{eff} - \omega$ space.

A core guided-mode and cladding mode coexist at the same $(k\Lambda, n_{eff})$ and yet they propagate without strong interaction [45], but they do not hybridize. The



reason for this unconventional coupling inhibition is due to small spatial optical overlap and large transverse phase mismatch between slowly varying core modes and fast oscillating cladding modes with high azimuthal number (m). Therefore, the condition $\Delta\beta=0$ is not sufficient for the coupling of core and cladding modes in case of IC guidance. The high azimuthal number modes could have very close propagation constant with a core guided mode (*i.e.* $\Delta\beta \sim 0$) without strongly interacting. The figure of merit of coupled waveguides represented by $X = \Delta\beta/\kappa$. Here, $\Delta\beta$ is the longitudinal wavevector mismatch; κ is the coupling coefficient between the two waveguides. The maximum coupling between the waveguides takes place for $X = 0$, and the coupling becomes weaker as $|X|$ increases. This quantity is proportional to the scalar product between the electric field of the two modes (*i.e.* overlap integral over the transverse dimension of the electric field distribution of the two modes [46]). Applying this coupling figure of merit to IC HC-PCF, we notice that because of the extremely small κ (*i.e.* close to zero) between the highly localized and fast oscillating silica cladding modes and the air-core mode, they can co-exist with little interaction even when their n_{eff} are very close (*i.e.* $\Delta n_{eff} \approx 0$) [14]. Within this context, we note that the normal modes of each wave guiding features are not necessarily orthogonal, but their anti-crossing gap, which is indicative of the hybridization between modes, can be extremely small if $\kappa \approx 0$. Therefore, in order to increase IC one requires decreasing the spatial overlap of core mode with silica cladding modes. This in turn demands for a cladding structure with very thin and elongated glass web with no sharp bend or connecting nodes. Based on these guiding rules, optimal physical and geometrical parameters to achieve strong coupling inhibition for low loss and broader transmission IC HC-PCF will be discussed in the following section.



2.2.2 Key design parameters to enhance IC guidance

The design of micro-structured fiber relies more on the conceptual transfer from solid-state physics rather than guided optics. Understating the core guidance in HC-PCF by tracing transmitting wave through a complex photonic cladding is very tedious and time consuming. Instead, the better alternative conceptual tool is to construct DOPS diagram of cladding modal spectrum to identify the nature of the modes, it's symmetry and location. Understanding such a modal spectrum of the Kagome structure also requires the identification of its cladding as a combination of individual resonators formed by its thin membrane and silica nodes. This process of developing DOPS diagram for Kagome cladding structure is already well established as PTBM as we discussed in Chapter 1 in order to understand PBG guidance. In case of Kagome IC HC-PCF, for better inhibition with core modes, the cladding modes shall exhibit high azimuthal (m) number or high transverse mismatch in order to decrease optical overlap integral. The supported azimuthal number can be expressed as a function of the perimeter length l , and thickness t , of the silica membrane of the waveguide: $m = n_{\text{eff}} \left(\frac{1}{\lambda} \right) \left[1 - \pi \left(\frac{t}{l} \right) \right]$. Therefore, a glass micro-structure exhibiting a very thin and elongated glass-membrane network with a minimum number of sharp bends or nodes, and by operating in the large pitch regime ($\Lambda \gg \lambda$) would provide sufficiently large m that strengthens IC guidance. Index of the background material (1.45) provides larger n_{eff} with respect to air also contribute for high m . According to coupled mode theory, in large pitch cladding operation, the neighboring silica modes do not couple with each other [6]. Therefore, these two parameters serve as optimization tools to enhance IC guidance as will be discussed further in the following sections.



Figure 2-2 shows progress of IC HC-PCF technology. In 2002, the first of such fiber design with Kagome cladding with circular core shape was reported by Benabid *et.al*. This fiber was found to have most of optimum design parameters required for IC guidance by exhibiting transmission loss value 1 dB/m [6]. In order to achieve low loss and broadband transmission, its cladding structures should ideally have a topology with elongated and thin silica web to increase azimuthal-like number (m), thereby transverse phase mismatch between core and cladding modes [14]. Even after optimizing the cladding design up to the fabrication limit, residual connecting nodes or sharp corners, which are inherent to such cladding structures, imposed attenuation limits more than 0.5 dB/m in 2007 [47]. During the same period, another large pitch IC HC-PCF design based on square-latticed with thinner web cladding down to ~ 200 nm was fabricated and it demonstrated losses below 2 dB/m within the near-IR ranges [48]. Given the fact that most of the core-cladding field overlap occurs at the core-surround, its shape shows direct influence on the optical transmission of the fiber. This fact motivated to optimize Kagome IC HC-PCF's core with negative curvature [16] [17]. As shown in Figure 2-2, first negative curvature core shaped Kagome fiber was designed in 2010 which resulted in multifold reduction of optical overlap between core and cladding and became a breakthrough in IC fiber technology. This technique demonstrated hypocycloid core 7-cell Kagome IC HC-PCF with loss figure 40 dB/km, much lower than its circular core design [16]. Several other 7-cell and 19-cell low loss and broadband fibers were also fabricated and some of which could also sustain for USP laser delivery. This milestone encouraged the GPPMM group to look into further optimization of its core shape with careful fiber drawing techniques which resulted several record level fibers with losses down to 17 dB/km at $1\ \mu\text{m}$ reported in [49] and very recently to 8.5 dB/km which will be discussed in Chapter 4. However, it is found that rheological phenomena which



appear during fiber drawing imposed some limitations to bring loss figures down to the fundamental confinement limit of Kagome hypocycloid IC HC-PCF. This is due to the combination of limited control over various structural parameters (including strut thickness, core size and curvature) and the formation of the surface capillary waves.

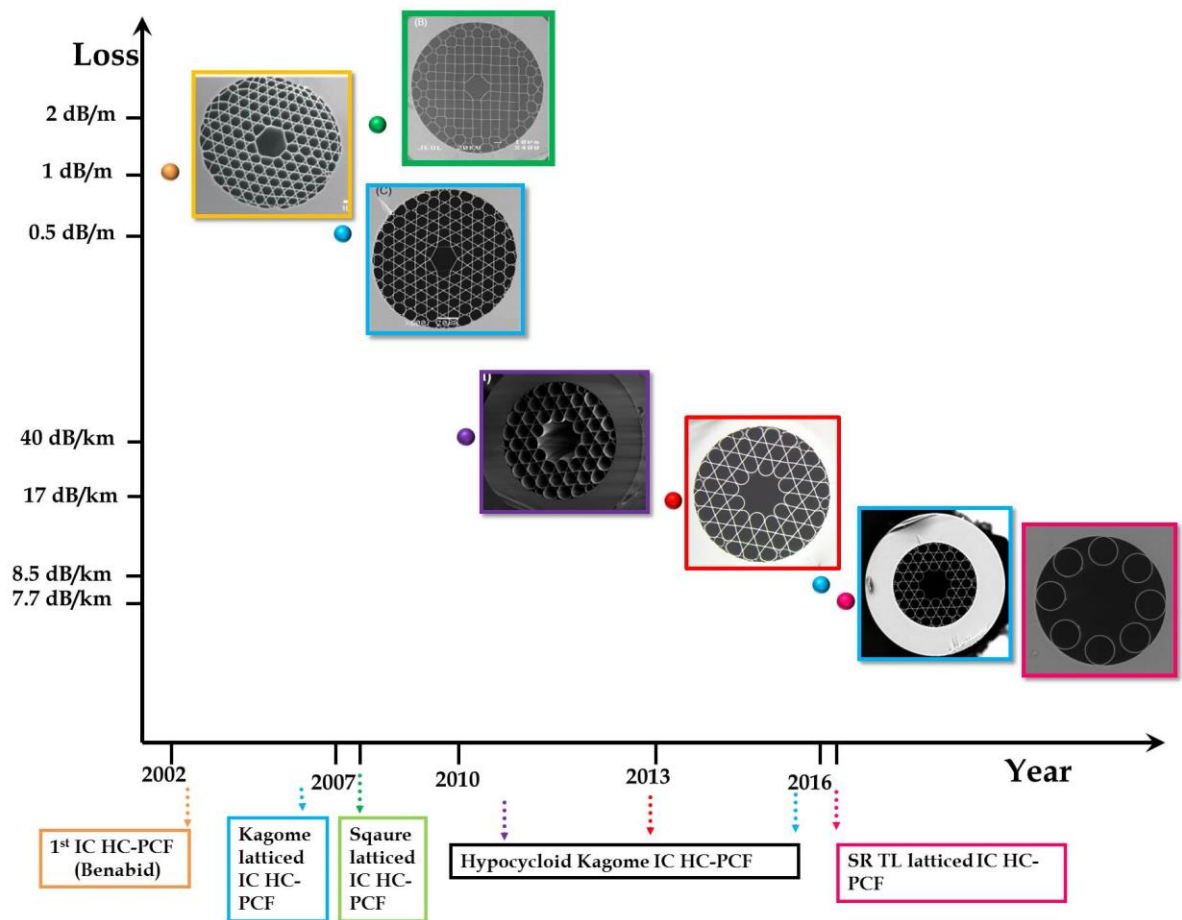


Figure 2-2 Summary of the historical development of IC HC-PCFs and their respective loss figures with SEM images.

The constraints imposed by structure of the Kagome lattice intrigued our GPPMM team to optimizing the design with respect to cladding. Such motivation and strong efforts resulted new IC fibers based on tubular lattice (TL) cladding. Such a fiber called single ring (SR) TL IC HC-PCF with thin elongated cladding

membrane when operated in large pitch regime, very recently demonstrated state-of-art performance in terms of loss record transmission loss of 7.7 dB/km at 750 nm. Though these fibers reach the limit of CL, but further losses are expected from fundamental limits imposed by surface roughness, which arise due to unavoidable surface capillary waves (SCW) during the fiber fabrication. Its experimental linear characterization will be discussed in Chapter-4 and Chapter-5 will discuss about the origin of surface scattering losses (SSL) and its impact on confinement loss (CL). In this regard, the rest of the Chapter will review modal analysis, optical characteristics and optimization techniques to enhance the IC guiding mechanism for ultra-broadband and low loss fibers.

2.2.3 Differences between IC and ARROW guidance.

The term of anti-resonant reflection was commonly used in interferometry to designate a Fabry-Perot cavity configuration when its reflectivity is maximized. Here, the reflection is enhanced compared to the Fresnel reflection by destructive interference of the optical wave inside the Fabry-Perot cavity. Dugay et al. (36) who coined the resulting waveguide ARROW have extended this effect to guided optics as early as 1986. Here, a planar waveguide with a low-index core layer is surrounded by higher-index thin dielectric layers to provide a transverse optical confinement in the core through the enhanced thin cladding-layers' reflectivity at the anti-resonant wavelength ranges. This ARROW picture was then used to derive the confinement loss of a hollow-core fiber whose cladding is comprised by one or several concentric anti-resonant dielectric rings (38). Among the findings of this work is an analytical expression of the HE_{11} mode minimum loss of a single anti-resonant hollow fiber for the case of $R_c \gg \lambda$, which is given by:

$$\alpha_{min} = \alpha_{HD}(2.405 \lambda) \left(2\pi R_c \sqrt{n_g^2 - 1} \right)^{-1}$$



$$= \frac{1}{2} (2\pi)^{-3} (2.405)^3 (n_g^2 - 1)^{-1} (n_g^2 + 1) \lambda^3 R_c^{-4} \quad (2.1)$$

Here, α_{HD} is the HE_{11} mode loss in a hollow dielectric fiber (*i.e.* tube thickness is considered infinitely large) deduced by Marcatili and Schmeltzer in the sixties (20). The HE_{11} minimum loss coefficient expression of equation (2.1) was written in this form to highlight the loss-decrease in an anti-resonant ring compared to a hollow dielectric fiber. It shows that the loss-decrease factor scales as λ/R_c .

Furthermore, using this expression for a core diameter of 15 μm , which is equal to that of the first reported Kagome HC-PCF in 2002 (6), one finds a loss range of 7-365 dB/m at 400-1500 nm spectral range. These loss figures were much higher than the measured loss in the aforementioned Kagome fiber, which was lesser than 3 dB/m over the same wavelength range, thus leading the authors of ref (6) to rule out the ARROW model as a possible comprehensive explanation for Kagome HC-PCF guidance. Nevertheless, the ARROW terminology was later found use to describe a class of PCF by Litchinitser et al. (33). The authors considered a PCF whose cladding entails isolated high-index inclusions in a lower index matrix, and coined the fiber ARROW PCF because for sufficiently large pitch relative to the high index inclusion diameter and to the optical wavelength, they found that the band edges of the fiber transmission spectrum depend very little on the pitch, and are strongly related to the optical feature of an individual inclusion. This PCF was then proved experimentally and theoretically by Argyros et al. (37) (12) to guide via PBG (*i.e.* the DOPS diagram of an infinite cladding does not support any propagating mode in the $n_{eff}-\omega$ space region of interest). Furthermore, it has been demonstrated later that the property of the non-dependence of the transmission band edges with the pitch can be explained by the photonic analogue of tight binding model (34), where for sufficiently large values



of the product between the lattice pitch and the optical frequency (*i.e.*, normalized frequency), the allowed photonic bands don't broaden from a single dispersion curve of an individual inclusion. In analogy with the strong tight-binding regime in solid-state physics, the large pitch regime corresponds here to a regime where the high-index material cladding modes are highly localized and do not strongly interact with their neighboring photonic sites. Thus, these modes are better represented by the maximally localized Wannier functions instead of extended overlapping Bloch states (18), and the DOPS diagram structure is close to that of dispersion curves from a single high index inclusion instead of photonic allowed bands. As a conclusion, the ARROW PCF in reference (33) is an example of a PBG guiding PCF in the large pitch regime. Also, similar to amorphous materials which can exhibit electronic bandgap, it is noteworthy to stress that the periodicity of a photonic structure is neither a necessary condition nor a defining feature for the existence of PBG.

In parallel, ARROW has also been extensively used very recently as a model to describe IC guiding fibers such as Kagome-lattice fibers or the present tubular lattice fibers. However, none of this recent reported literature on anti-resonant hollow fibers did justify the use of the ARROW terminology for such fibers or described their cladding modal spectrum, and seems to settle for the fact that the transmission band edges are located at cut off wavelengths defined by equation (2) being a sufficient and a defining feature for ARROW guidance. This feature or the reflection enhancement from thin dielectric cannot explain why fibers whose cladding have the same structure and the same glass thickness exhibit a dramatic difference in confinement loss depending on whether the fiber core-contour is hexagonal, circular or hypocycloid shape, and this is so despite presenting comparable core diameters (18) (26). This is expected because the original proposals of ARROW (36) don't treat the cladding modal structure and how they



couple or don't couple with the core mode in the anti-resonant bands. Instead, the model explains the core mode confinement through the cladding surface reflection enhancement which is in contrast with the much lower loss (<10 dB/km) observed in hypocycloid core-contour HC-PCF. Furthermore, one example that shows that the guidance in these optical fibers cannot be reduced to the difference in glass thickness, and highlights the role of the optical overlap and the azimuthal phase of the cladding modes is the CL behavior at the longer wavelength of the fundamental band. All this is unforeseen by the ARROW picture because it completely neglects the complexity of the cladding modal structure. In fact in the original proposals of ARROW (36; 38) only claddings with just one transverse coordinate dependence (*i.e.* multilayered structures in rectangular or cylindrical coordinates) and only the radial phase matching between core and cladding modes are considered. In fibers with a more complex cladding structure and core-cladding interface such as Kagome or tubular lattice fibers these approximations make it inadequate.

2.3 Kagome latticed IC HC-PCFs

2.3.1 DOPS of Kagome lattice designs

To understand the guiding mechanism of Kagome IC HC-PCF, we can follow its $n_{eff} - \omega$ space mapping or DOPS diagram as a function of the normalized $k\Lambda$ and the real part of the effective index (see Figure 2-3 (a)). The cladding structure presented here is operated at much larger frequencies ($k\Lambda \sim 100$) exhibits no bandgap as PBG triangular lattice ($k\Lambda \sim 15$), instead it passes through two low DOPS region I (for $k\Lambda = 20 \sim 60$) and III (for $k\Lambda = 80 \sim 140$) at the air line. In these regions resonance of cladding air holes are associated with relatively flat dispersion curves (red curves) and the optical transmission is expected to be high since the dispersion curves of air holes don't hybridized with connected network



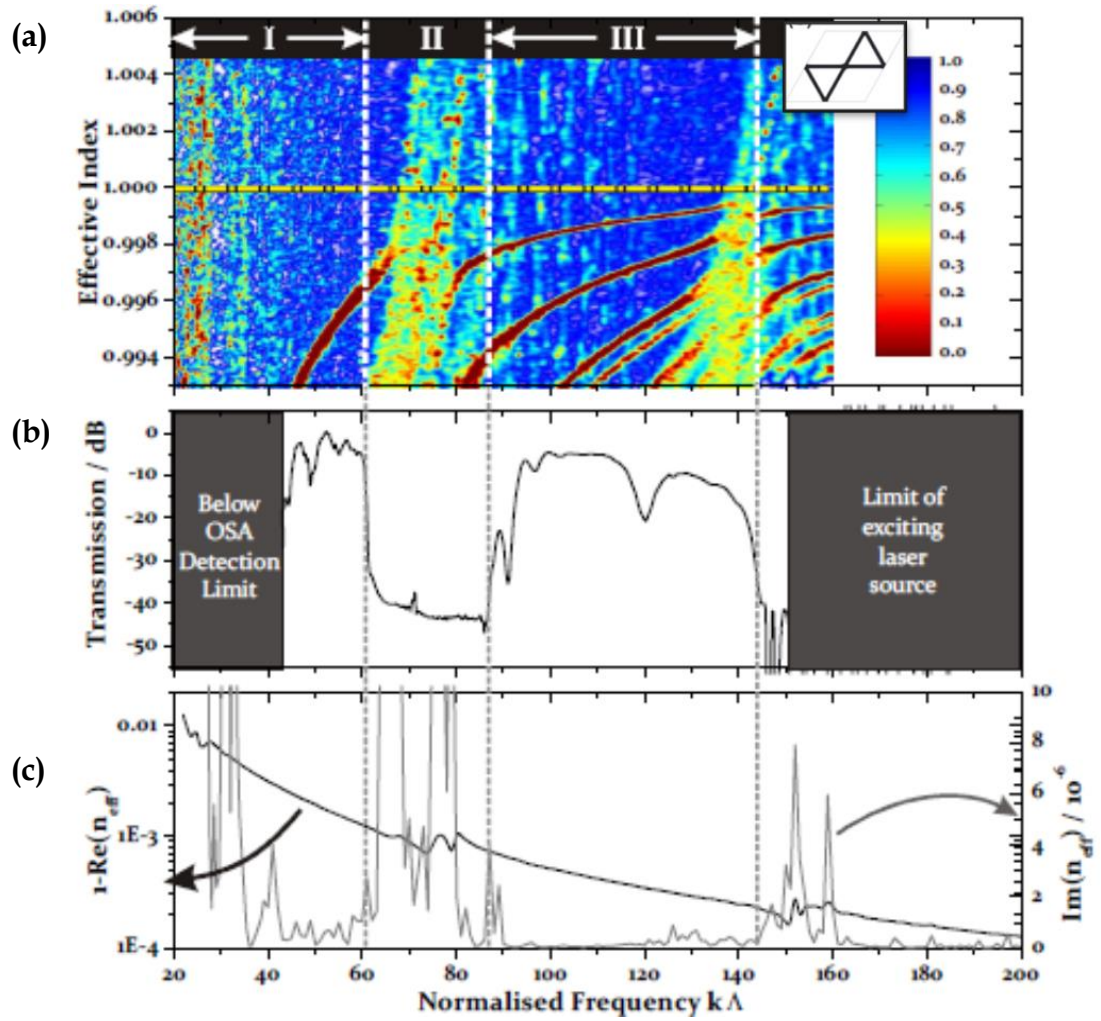


Figure 2-3 (a) density of photonic states for the Kagomé lattice structure. The horizontal yellow line indicates the air-line. (b) Transmission spectrum of fabricated Kagomé lattice fibers of the same structure as that simulated to obtain the DOPS. I and III are bands of high-transmission in the core, and II is a band of low transmission in the core. (c) calculated real (thick black) and imaginary (thin red) parts of the n_{eff} of HE_{11} mode.

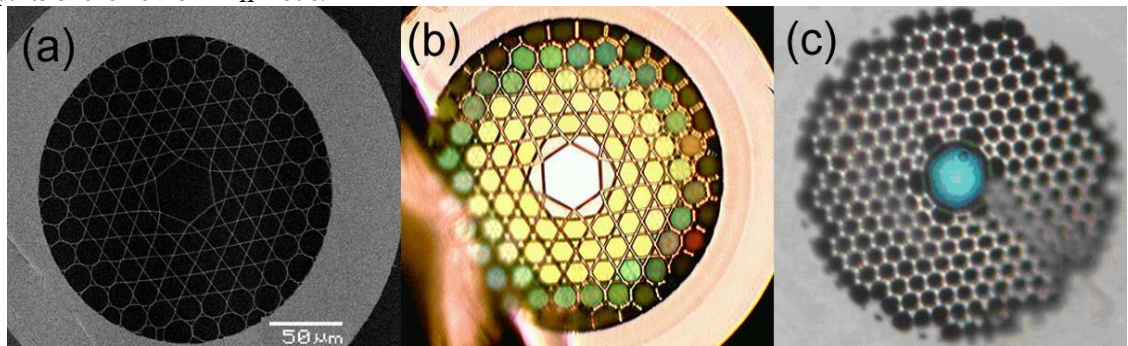


Figure 2-4 (a) SEM of a single cell Kagomé fiber. (b) & (c) Shows comparison of the optical images under the microscope for a Kagome fiber and triangular PBG fibers respectively.

of glass struts. Therefore, the coupling between core and cladding modes is "inhibited" and light is guided in the air-core with relatively low loss over the large spectral region of inhibition (band I and III). Besides, there exists a higher DOPS region in region II (for $k\Lambda=60\sim80$) which are associated with resonances of network of glass struts, hence the transmission in this band is low. As shown in Figure 2-3 (b), frequency edges of the high and low transmission bands measured in a single cell defect core Kagomé IC HC-PCF, match well with those inferred from the imaginary part of the n_{eff} of the "fundamental" HE_{11} -like guided mode calculated for unit lattice structure as shown in inset of the Figure 2-3 (a). The co-existence of quasi-bound core modes within a continuum of cladding modes at the same $(k\Lambda, n_{eff})$ indicates the presence of bound state in continuum (Q-BiC/BiC) that was predicted by Von Neumann and Wigner [40]. Therefore, IC is analogous to the problem of electronic bound states at energies above the potential barriers (*i.e.*, spatially confined within the continuum),

Fiber shown in Figure 2-4(a) experimentally demonstrates transmission of (see Figure 2-4(b)) white light through a few centimeters of a Kagome fiber which contrast to limited band width of the triangular PBG HC-PCF's confirms its limited bandwidth by transmitting only green light as shown by near-field image in Figure 2-4(c). Modal analysis in coming sections explains the origin of the interaction (or absence of interaction) between core and cladding modes.

2.3.2 Modal analysis of Kagome latticed IC HC-PCF

Figure 2.5 shows calculated modes at representative frequencies of the three transmission bands identified in Figure 2-3. High transmission bands (*i.e.*, band I and III) shown in first two rows of A are based on a finite Kagome lattice structure with a core defect by the removal of unit cell from the center of the infinite cladding, whereas modes in third column are for infinite Kagome lattice structure

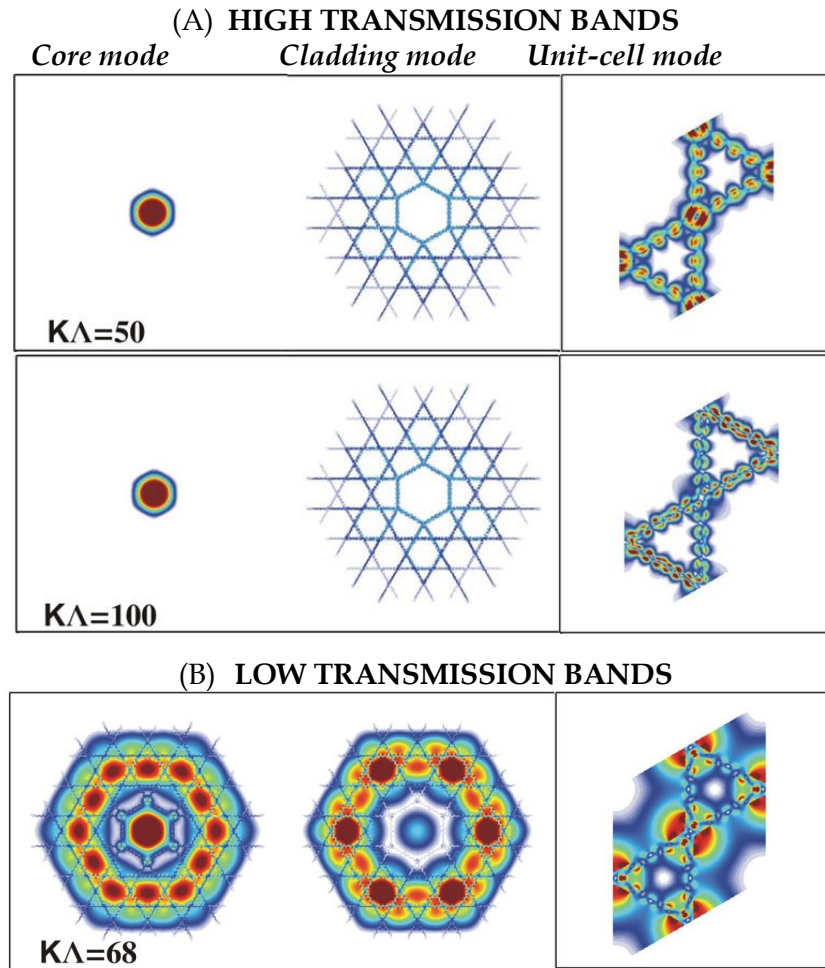


Figure 2-5 Nature of the Kagomé -lattice HC-PCF cladding modes. (A) The core mode and a cladding mode for a frequency $k\Lambda=50$ in band (I) (top), and for a frequency $k\Lambda=100$ in band (III) (bottom). At each frequency, the effective indices of the core and cladding mode differ by less than 10^{-5} . The third column shows the mode of an infinite Kagomé lattice, which corresponds to the cladding mode in column 2, calculated for the same frequencies at the Γ -point of the Brillouin zone. (B) Same as in (A) but for $k\Lambda=68$ (in band (II)).

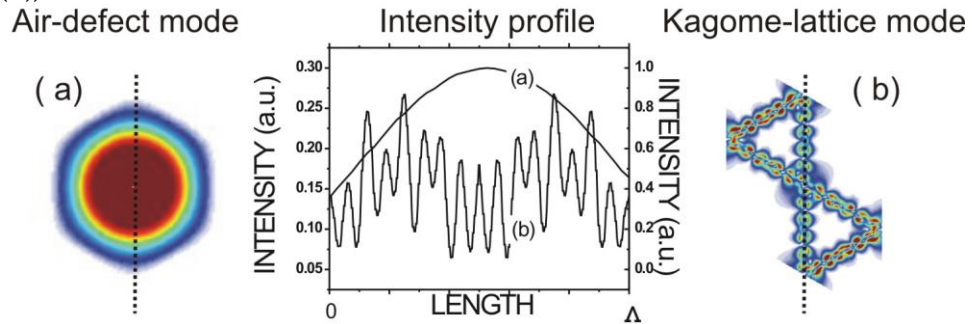


Figure 2-6 Intensity profiles of (a) the guided core-mode of a Kagomé lattice fiber, and (b) a cladding mode of the same fiber. The graph plots the transverse intensity variation of both modes over a distance equal to the cladding pitch along the dotted lines in (a) and (b).

without any defect. The second row B represents modes of low transmission band (*i.e.*, band II). Cladding modes in band I and III have n_{eff} values very close to the core mode and are mainly localized at silica strut with rapid decay into the surrounding air holes, which is evident also from dispersion curve with steeper slopes in the DOPS diagram. The cladding modes exhibit fast phase oscillations and support strong transverse-field mismatch leading to “washing-out” of the overlap with the slowly varying core-field distribution. The weak interaction between core and cladding mode that are phase-matched longitudinally is due to the large transverse field mismatch, as seen by the fast intensity oscillations of the cladding mode compared with the slowly varying intensity of the core mode in Figure 2-6.

2.3.3 Enhancement of IC guidance in Kagome HC-PCF

IC guidance can be enhanced by having a glass micro-structure exhibiting a very thin and elongated glass-membrane network with a minimum number of sharp bends or nodes. Since, it is operated in large pitch regime or at high normalized frequencies (*i.e.*, $\Lambda \gg \lambda$) [47], the silica modes of neighboring photonic sites do not interact. Such structural features ensure modes with strong confinement in the thin silica-web and with very fast transverse oscillation (*i.e.* high azimuthal-like number). Unlike PBG guidance, the criterion $\langle \varphi_{clad} | \Delta n^2 | \varphi_{core} \rangle \rightarrow 0$ for good IC guidance implies a strong dependence on the core mode profile, and thus the core-contour. This led to the seminal introduction of state-of-art hypocycloid core-contour design (*i.e.* negative curvature) in 2010 [16] [17], with the demonstration of dramatic reduction in transmission loss down to 17 dB/km at 1 μm [49] and its record level optical power handling up to 1 mJ. This section reviews the effect of negative curvature (hypocycloid) core on the confinement loss, bending losses of Kagome fiber.

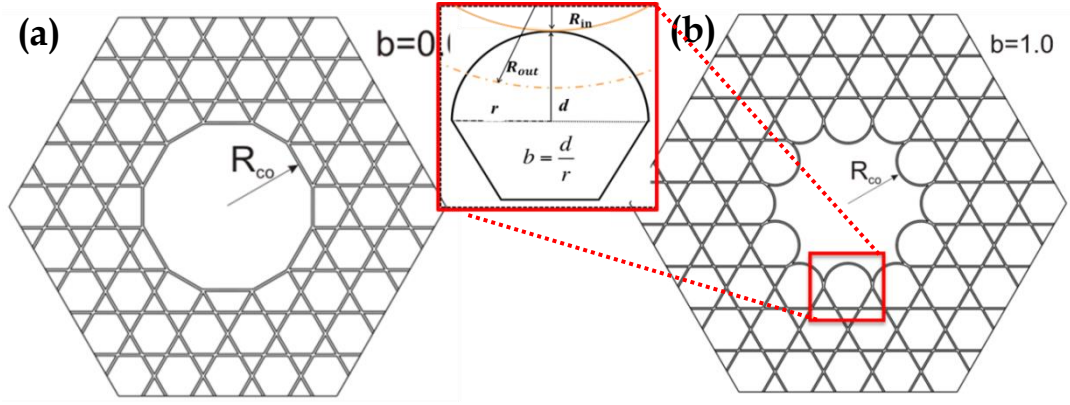


Figure 2-7 Transformation of IC Kagome HC-PCF core shape from (a) circular contour ($b=0$) to a (b) hypocycloid-like core with $b=1$. Inset: Definition of the parameters quantifying the curvature of the core arcs [49].

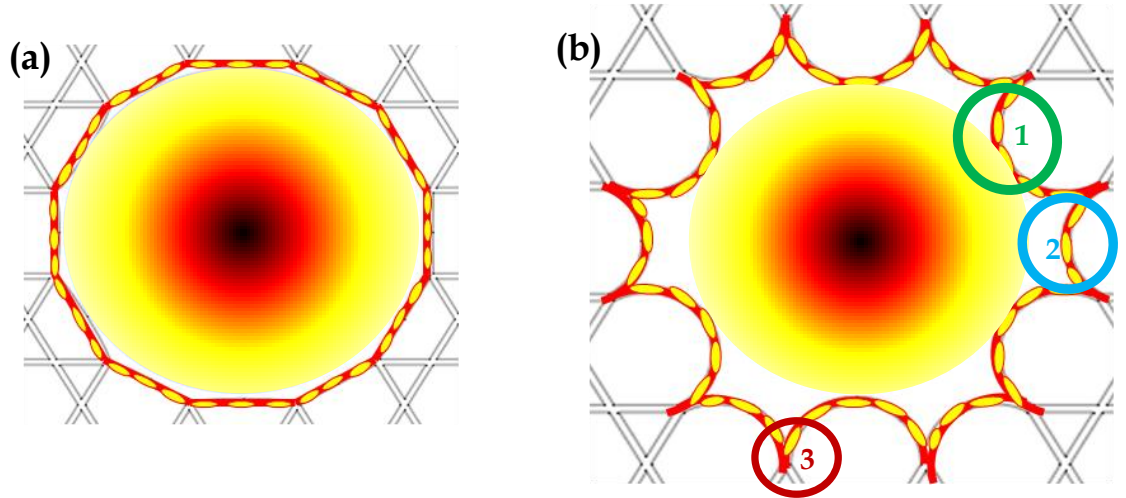


Figure 2-8 Schematic representation of the IC enhancement for the case of hypocycloid core-contour relative to the circular-like core-contour. (a) A circular core Kagomé HC-PCF and (b) a negative curvature core-contour Kagomé HC-PCF supporting the same HE_{11} core mode. (b) Zoom-in to highlight the HE_{11} core mode, the silica core-surround mode with its fast transverse oscillations for both fibers. Circled region (1) is outer most cup, (2) is the inner most cup and (3) is the nodal point pushed away from the core mode of hypocycloid Kagomé HC-PCF.

Figure 2-7 present the procedure to transform core-contour design from a circular-like to hypocycloid-like shape [49] with a set of alternating negative curvature cups with an inner radius R_{in} with the 6 most inward arcs and a larger circle with radius R_{out} that is tangent with the 6 most outward arcs. The parameter $b = (d/r)$ quantifies the curvature of the hypocycloid-like core (see Figure 2-7 (b)),

where d is the distance between the top of the arcs and the chord joining the nodes connecting the inward arc to its two neighboring ones and r is half the chord-length. By definition the conventional core contour designs are approximated as “quasi” circular core with $b=0$, whilst $b=1$ corresponds to circular shaped arcs core contour. The core with other than these values (*i.e.* $0 < b < 1$ and $b > 1$) have elliptical shape whilst the outward ones are set to have a circular shape. For this modified core contour, the fundamental mode of the hollow-core is of HE_{11} and whose mode-field diameter is that of a capillary or a circular core HC-PCF with a radius equal to R_{in} (see Figure 2-7 (b)).

With the seminal introduction of hypocycloid core shape in Kagome IC HCPCF, the overlap integral between the core-mode and the highly oscillating (*i.e.*, high azimuthal-like number m) silica core-surround mode (cladding-mode) is strongly reduced via following three avenues (see Figure 2-8).

Firstly, via a simple spatial overlap reduction argument. With modified hypocycloid shaped core, the perimeter of silica surrounding with which the core HE_{11} mode transverse profile intersects is now limited by only with tangents section of the six inner most cups (see green circle in Figure 2-8 (b), whilst it intersects with the whole circle perimeter in the case of the circular contour. As a result the spatial overlap of core mode with silica core surrounding is further reduced by 0.001%, which is three orders lesser than that of PBG HC-PCF [43].

Secondly, the IC is enhanced by symmetry argument. Owing to the hypocycloid shape with inward contour design the resultant core get larger perimeter that favors the silica core-surround modes to exhibit higher m (see blue circle in Figure 2-8 (b)). Consequentially by virtue of a stronger transverse phase-mismatch, *i.e.* $\Delta\beta_{\perp} \propto m$ [16], the overlap integral between the core-mode and the cladding-mode is further reduced which strongly favors IC.



Finally, connecting nodes, which are inherent in Kagome cladding structures, generally overlap with HE₁₁ mode in case of circular core. Thanks to the hypocycloid contour core designs, such connecting nodes are pushed further away from the core-mode, which reduces its optical overlap with the low azimuthal number modes residing at the connecting nodes (see red circle in Figure 2-8 (b)). By this simple and intuitive picture, one can expect further enhancement in IC and hence a stronger reduction in confinement loss. Following subsection discuss about consequential effect this new design concept on the performances of the fiber.

2.3.3.1 Hypocycloid core effect on confinement Loss (CL)

Several Kagome fiber designs with 7-cell defect and 3 cladding rings have been numerically analyzed* in [49] to check the impact of hypocycloid core shape on transmission loss. These fibers were assumed with strut thickness t equal to 350 nm with different core arcs varying from $b=0$ to $b=1.5$ and by keeping the R_{in} fixed at 60 μm . Figure 2-9(a) shows the evolution of HE₁₁ mode and its better confinement as b parameter is changed from 0 to 1.5. Figure 2-9(b) shows the calculated* loss spectra of the HE₁₁ core mode for fiber design with different arc curvatures which clearly show the strong influence of the inward arc curvature on the confinement loss (CL). The figure also confirms dramatic reduction of confinement loss by factor of 1000 as b parameter is increased from 0 to 0.5 ("quasi" circular core to hypocycloid core design). The higher losses at 700 nm (around 2 times the strut thickness) in the simulation correspond to the resonance of the fundamental core-mode with the glass struts, which occur at cut-off wavelengths: $\lambda_j = \frac{2t}{j} \sqrt{n_{gl}^2 - 1}$, where j is an integer, n_{gl} is the refractive index of the glass forming the cladding structure and t is the thickness of the glass web of the cladding [14]. Outside of these spectral regions where the silica cladding

structure is anti-resonant, the CL exhibits an exponential-like decrease with the increase of b parameter.

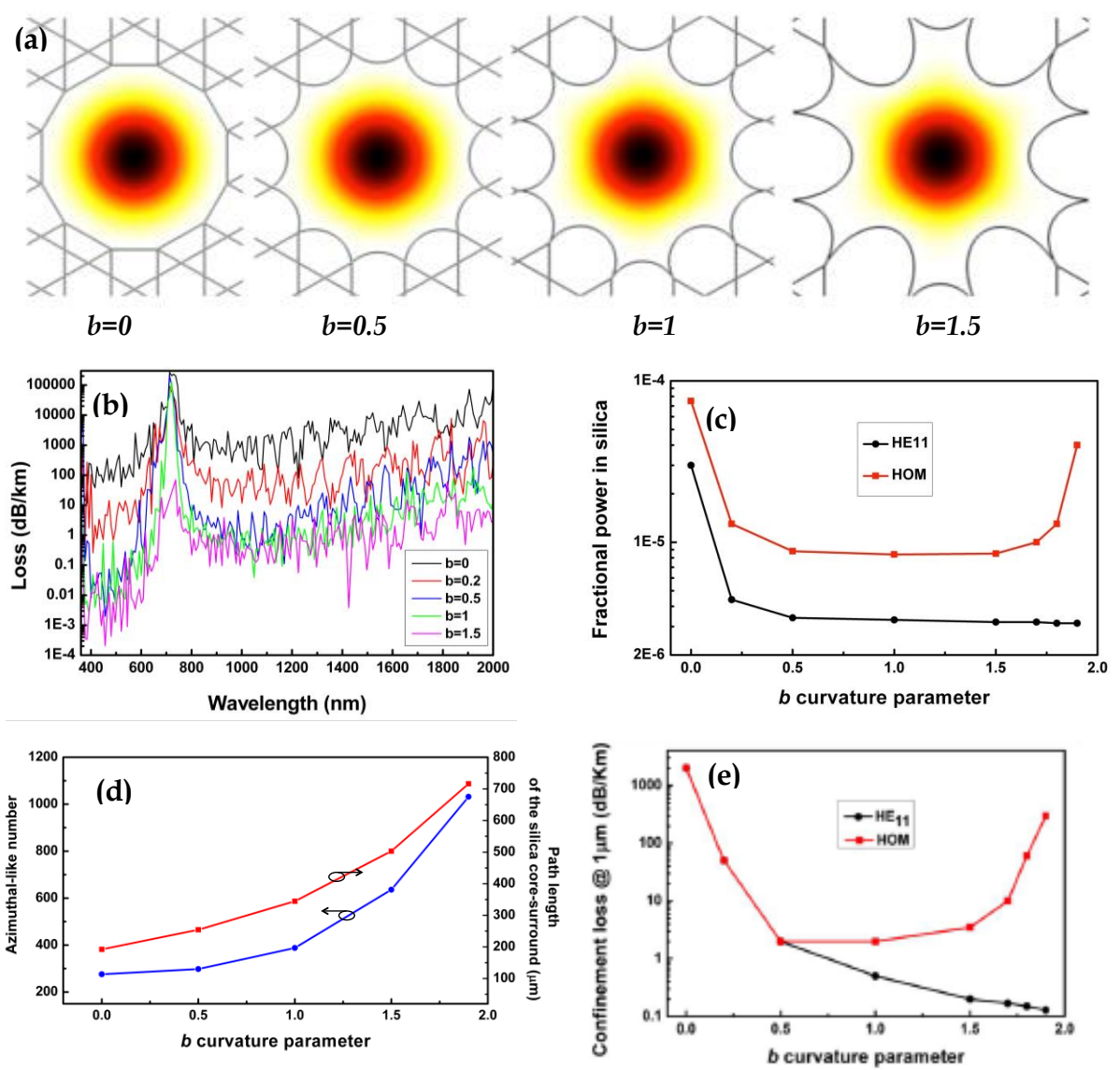


Figure 2-9 (a) Evolution of HE_{11} mode profiles at $1 \mu m$ with b for a 7-cell 3 ring Kagome IC HC-PCF. (b) Calculated loss spectra and (c) fractional power in silica at $1 \mu m$ for the fundamental core-mode HE_{11} and for the first four higher order modes. (d) Evolution of the azimuthal-like number m and the perimeter of the silica core-surround contour with b . (e) The fractional optical power residing in the cladding silica, for a wavelength of $1 \mu m$, for the core fundamental mode HE_{11} (black trace) and for the first four higher order modes: the two polarizations of the HE_{21} mode, TE_{01} and TM_{01} (red curve) [49].

2.3.3.2 Hypocycloid core effect on optical power overlap and modal content

The dispersion of the HE₁₁ mode shows almost very similar dispersion of the capillary with radius equal to that of the R_{in} of the hypocycloid and also it does not change much as b varies from 0 to 1.5 [49] [50]. This indicates the reduction of spatial optical power overlap (SPOP) with silica core surround in hypocycloid-core Kagome IC HC-PCF which is expected from a simple assessment of the geometrical overlap between the zero-order Bessel shaped HE₁₁ mode and the core-contour at radius R_{in} [16] [51]. Figure 2-9(c), shows the calculated evolution of fractional optical power residing in the cladding silica web for different b values for the core fundamental mode HE₁₁ (black curve) and HOMs (red curve). The fractional power in silica η was deduced numerically using the following expression:

$$\eta = \frac{\iint_{S_{si}} p_z ds}{\iint_{S_{\infty}} p_z ds} \quad (2.2)$$

where p_z is the longitudinal component of the Poynting vector, while S_{si} and S_{∞} indicate integration over the silica region and the whole cross section, respectively. Figure 2-9(c) shows that when b parameter is increased from 0 to 0.5, the relative power ratio for the HE₁₁ is decreased by a factor of ~10, but it decreases with slower rate for higher values of b . For the case of HOM, it follows the same trend for the b in the range of 0 - 1.5 whereas for b from 1 to 1.9, it increases since the whole size of the large arc increases, and thus the hole mode (HM) effective index increases and approaches to that of the fiber core. This condition favors coupling between them by virtue of phase matching and causes an increase in both the fraction of power in silica and the confinement loss of HOM, which is also indicative of the strong coupling inhibition between the core modes and the silica strut modes [14].



The decrease in the SPOP not the only reduces CL by increasing b above 0.5, but also reduces the overlap integral between the fiber core-modes and those of the silica core-surround via symmetry-mismatch (*i.e.* transverse phase-mismatch). Figure 2-9(d) indicates this situation by the exponential increase of m with b , which results from the increase in the perimeter of the hypocycloid core-contour and subsequent strong decrease in the overlap integral between the core mode and the silica core-surround. As a result, the azimuthal-like number increases to enhance IC between the core and cladding modes, and subsequently a decrease in the experimentally observed CL.

Figure 2-9(e) shows CL spectra at 1 μm for HE_{11} keeps decreasing with b , whereas for HOMs it starts increasing for the b values greater than 0.5 due to its coupling with the hole modes in the cladding as mentioned above. Therefore, HOMs are suppressed with stronger b , via propagation loss enhancement. Furthermore, the CL “extinction-ratio” between the HE_{11} mode and the HOM increases from 0 dB for $b < 0.5$ to 7 dB for $b = 1$, reaching the notable figure of >100 dB for $b = 1.9$. Therefore, it is clear that b shall be strong enough and higher than 0.5, to have single mode guidance. However, the highest achievable b parameter without altering the desired structure is a challenging task. In addition, designing thinner struts to increase the transmission window consequently exhibits higher losses in high order bands than what is numerically predicted [19]. It is believed that due to an enhanced capillary wave effect, the fiber core-wall get surface roughness during the fiber draws, which causes surface scattering losses (SSL). This effect will be theoretically and experimentally investigated in chapter 5.

2.3.3.3 Cladding ring number influence on confinement and bend loss

In order to review cladding ring effect on CL and bend loss, the Figure 2-10 shows numerical computations* of Kagome cladding-lattice HC-PCFs with

different cladding ring-numbers. The fibers considered for simulations are taken to have a hypocycloid-shape core with a constant $b=0.3$, a constant $R_{in}= 32.5 \mu\text{m}$, strut thickness $t=450 \text{ nm}$ and $\Lambda = 20 \mu\text{m}$. As we can notice from Figure 2-10(a) in case of a single ring structure the CL reaches a minimum of $\sim 50 \text{ dB/km}$ in the 1200-1400 nm spectral range, which is almost three orders of magnitude lower than that of a circular ring with comparable core-size and strut thickness [52] [17].

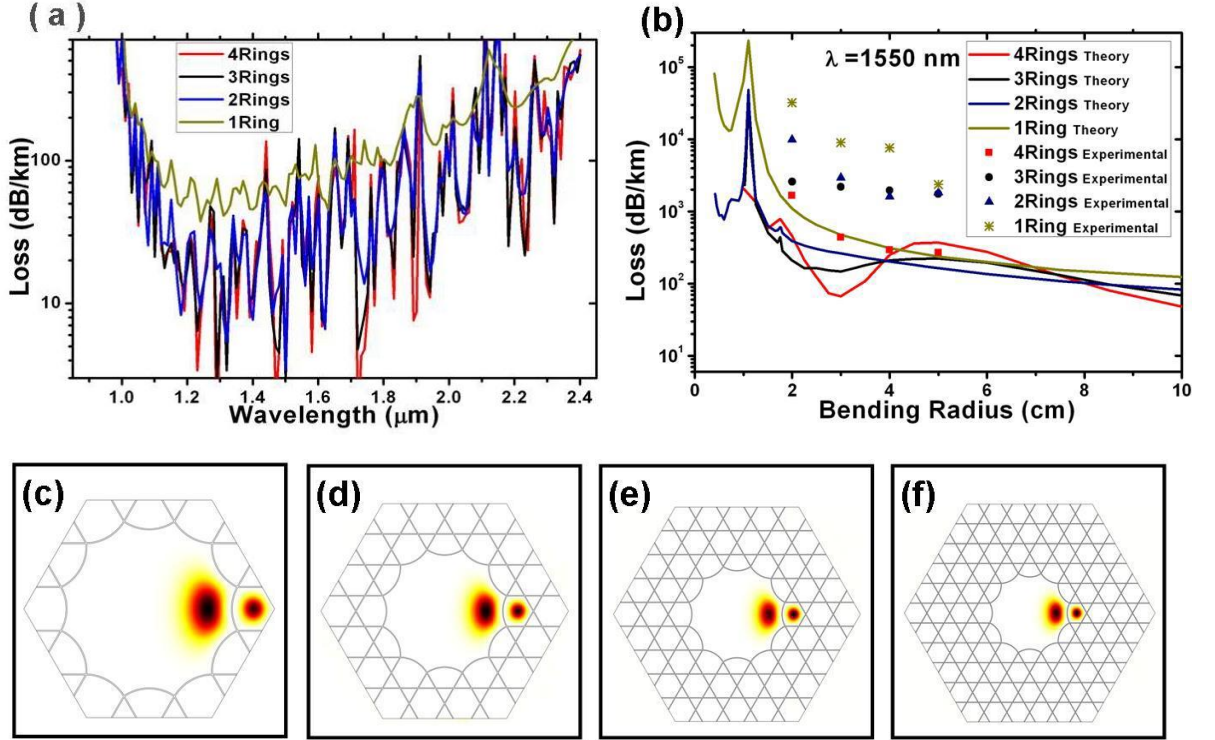


Figure 2-10 (a) Simulated loss spectra for four different cladding ring numbers; (b) Confinement loss versus the bend radius for two wavelengths at $\lambda = 1550 \text{ nm}$ for different ring numbers. (c) - (f) Simulated fundamental mode profile at bend radius 1.1 cm at $\lambda = 1550 \text{ nm}$ for 1, 2, 3, and 4 ring numbers in the cladding [53].

Numerical results in Figure 2-10(a) show two different trends in the CL evolution with the cladding ring number. Firstly, increasing cladding ring number from 1 to 4 brings only little overall variation in the CL which is similar to the one found with circular or hexagonal core Kagome HC-PCF [54]. In case of ring-number ≥ 2 for the same fiber, the average base line of the loss is around

20 dB/km between 1200-1400 nm spectral ranges. Secondly, the CL reduces significantly when the cladding ring number is increased from 1 ring to 2 rings fiber, with the average base-line loss figure dropping from 60 to 20 dB/km [53].

Figure 2-11(b) shows the computed** bend loss spectra for four fibers with different cladding ring-numbers, varying from 1 to 4 rings, by modelling bent fiber with refractive index $n(x, y)$ with a straight one having an equivalent index profile $n_{eq}(x, y) = n(x, y)e^{\xi/R_b}$ where $\xi = (x, y)$ is the transverse bending direction and R_b the bending radius [55] [56] [57]. Similar to the experimental results, CL is reduced significantly, when cladding rings are increased from 1 to 2, whereas a further increase in the number of cladding rings has a minor effect on the bend loss which can be observed in the figure by confinement loss versus the bend radius for wavelength 1550 nm. Due to the coupling between the fiber core HE_{11} mode and that of cladding hole, the evolution of the transmission loss with R_b exhibits a resonant loss instead of uniform decrease for a bend radius at 1.16 cm (see Figure 2-10(c)-(f)) [44] [57]. However, inherent structural features of the Kagome fiber designs such as connecting nodes and sharp corners of the cladding structure are unavoidable. Also, thinning silica strut to increase the transmission window by keeping hypocycloid core shape stronger is extremely challenging in fabrication perspective. These drawbacks of Kagome design impose limitation to bring confinement loss levels further down to its fundamental limits. These efforts have been continuing with the development of IC HC-PCF based on cladding design optimization to minimize the nodes in the structure. Following section discuss about IC HC-PCF based on tubular lattice cladding which inherently presents hypocycloid shaped core and absence of the connecting note. This new design is opening up new perspective in fiber design with recorded level lower attenuation over broadband transmission.



2.4 Tubular latticed IC HC-PCF

With the understanding of hypocycloid core contour Kagome IC HC-PCF design, we are now able to predict other cladding lattice structures with thin, elongated cladding and nodeless cladding membrane provided they are operated in high frequency regime. Tubular lattice which consists of an arrangement of isolated thin glass fulfills IC guidance requirement [58]. Thanks to TL's inherent cladding features, the elongated silica web, inherent hypocycloid core shape and completely void of connecting nodes fulfills possibility to realize fibers with stronger IC when it is operated in in high frequency ranges. Previously reported single ring hollow-core fibers by Pryamikov *et.al* [21] and F. Yu *et.al* [59] demonstrated transmission in the spectral regions greater than 3.5 μm . Very recently in 2016, by thinning the lattice tubes to 830 nm [60] and down to 360 nm [61] resulted the transmissions 30 dB/km at 1 μm and broad fundamental band respectively. Figure 2-11 shows SEM images of optimized state-of-art SR-TL IC HC-PCF that has been developed during this thesis.

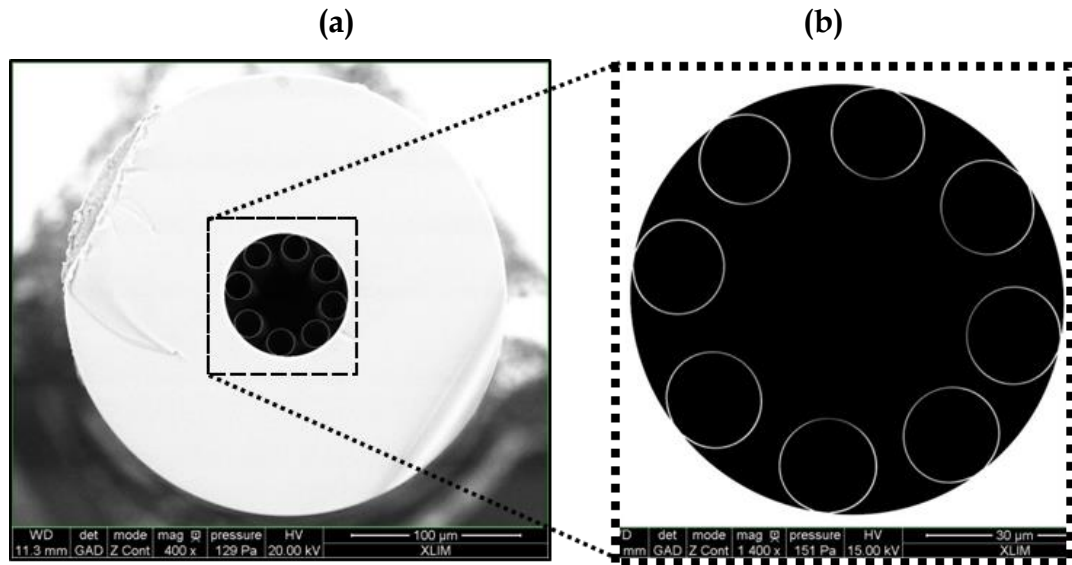


Figure 2-11 (a) SEM image of a single ring tubular latticed IC HC-PCF. (b) Zoom-in to the core-cladding design.

2.4.1 DOPS of tubular latticed IC HC-PCFs

To understand and determine the design parameters of single fibers for optimal guidance, we first examine the nature of its cladding modes. As presented in Figure 2-12, numerically calculated DOPS of tubular lattice for both triangular and square arrangements with different lattice spacing show that the structure and content of modal spectrum to depend very little on the tube arrangement or spacing when operated in large pitch regime.

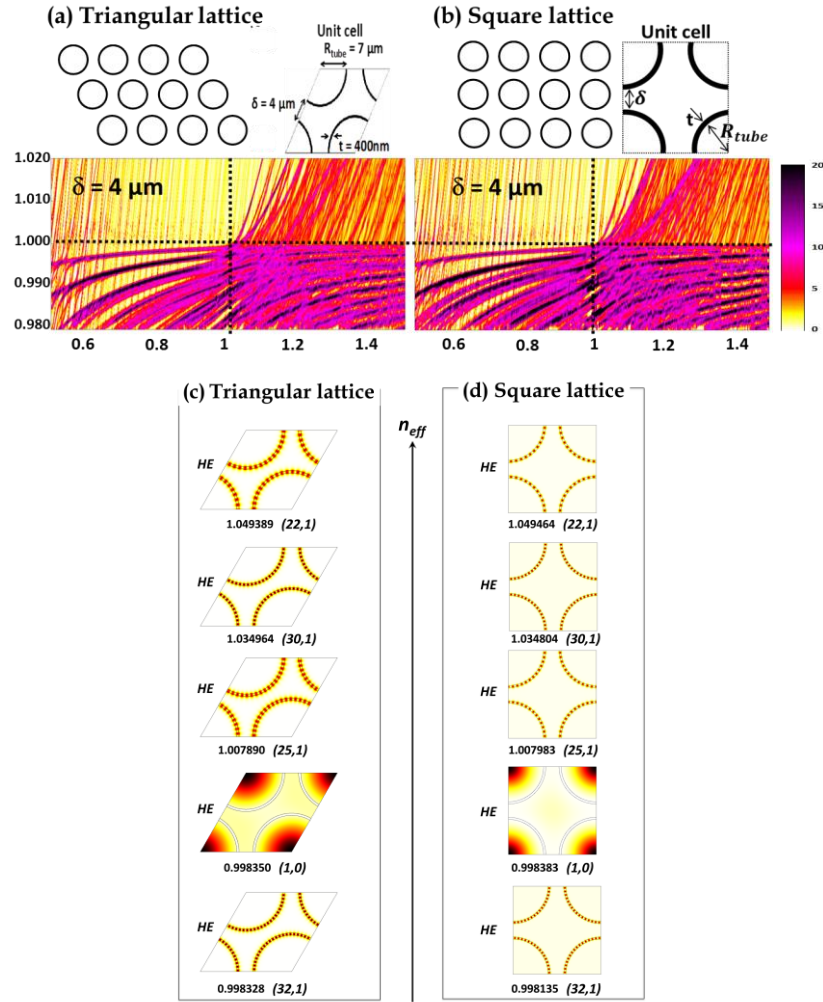


Figure 2-12 Cladding designs of a TL in a (a) triangular and (b) square arrangement along with and the details of a unit cell of the lattice on their right. The corresponding DOPS of an infinite tubular lattice is shown right below. (c) (d) Transverse profiles of the electric field magnitude of the photonic state (modes).

Figure 2-12(a) and (b) show different triangular and square cladding designs mentioned above and corresponding unit lattices of isolated glass tubes of refractive index $n_g = 1.45$ and with representative radius $R_t = 7 \mu m$, thickness $t = 400 nm$ and gap between two adjacent tubes $\delta = 4 \mu m$ (corresponding to a lattice pitch of $18 \mu m$, which is much larger than any of our operating wavelengths). Here, $F = (2t/\lambda)\sqrt{n_g^2 - 1}$ is a normalized frequency relative to the tube thickness and the refractive index of the glass and air. The figure also shows the DOPS#, defined to be the number of Maxwell equation mode solutions of the lattice at the normalized frequency F in the range of effective index between n_{eff} and $n_{eff} + \delta n_{eff}$, with δn_{eff} chosen to be 10^{-5} . The pitch is given by $\Lambda = 2R_t + \delta$. The nature of these modes is revealed in Figure 2-12 (c) by showing the transverse profile of their field magnitude for a given frequency from the fundamental band ($F = 0.8$). Within $n_{eff} - F$ range explored here, all the DOPS diagrams show a quasi-continuum of modes. Irrespective to the lattice geometry or the lattice pitch, the DOPS diagrams show similar overall landscape with very little variation between them. Figure 2-12(b) further corroborates this fact by showing the mode profiles at $F = 0.8$. These modes show the same transverse structure with the same azimuthal and radial numbers. The only difference is in their n_{eff} which exhibit a relative difference value of less than 0.01%. These results, which show very weak effect of the lattice pitch and geometry of the DOPS, are attributed to the fact that the modes are highly localized with little interaction with their close neighboring guiding sites. This fact has been first observed in PCF by Litchinitser *et al.* [62] and then explained using the photonic analogue of tight binding model by Couny *et al.* [63] in the context of investigating how photonic bandgap form in PBG guiding HC-PCF. Consequently, the optical fiber formed by introducing a core defect in a tubular lattice in a large pitch regime neither strongly depends neither on the lattice pitch nor on its geometrical symmetry.



2.4.2 Modal analysis of SR TL IC HC-PCF

As shown in Figure 2-13 we considered a triangular arrangement to calculate the modal spectrum of the SR-TL HC-PCF cladding (see central and right panel of Fig 2-13 (a)). For this purpose, we can consider the SR-TL HC-PCF cladding as a section from an infinite lattice of isolated tubes and where the fiber-core is introduced as a defect within the lattice. Furthermore, we operate in the large pitch regime, and thus the spectral characteristics of the photonic structure are primarily governed by the modal properties of the lattice single unit rather than their arrangement in the lattice [62]. This is explained by using the P-TBM [47] where for a lattice pitch much larger than the wavelength, the modes of each tube in its unit cell don't strongly interact with their close neighbors.

For example, the modal spectrum of a cladding with M tubes is comprised by M -degenerate modes from the individual tubes. Consequently, only the thickness and index of the unit cell individual wave guiding features (here silica tubes and air-holes) are relevant for the modal spectrum of the cladding photonic structure. In other word, under this large pitch regime the modal spectrum of the SR-TL HC-PCF cladding can be determined by considering an infinite lattice of any symmetry arrangement. The DOPS diagram shows no PBG regions in the mapped $n_{eff} - F$ space, but a quasi-continuum of photonic states. Within the explored F spectral range of 0.5-1.5, we can distinguish two bands at each side of $F = 1$. For $F < 1$, corresponding to the fiber transmission fundamental band, the modal spectrum exhibits a lower DOPS compared to the range $F > 1$, which corresponds to the fiber 1st higher-order band.



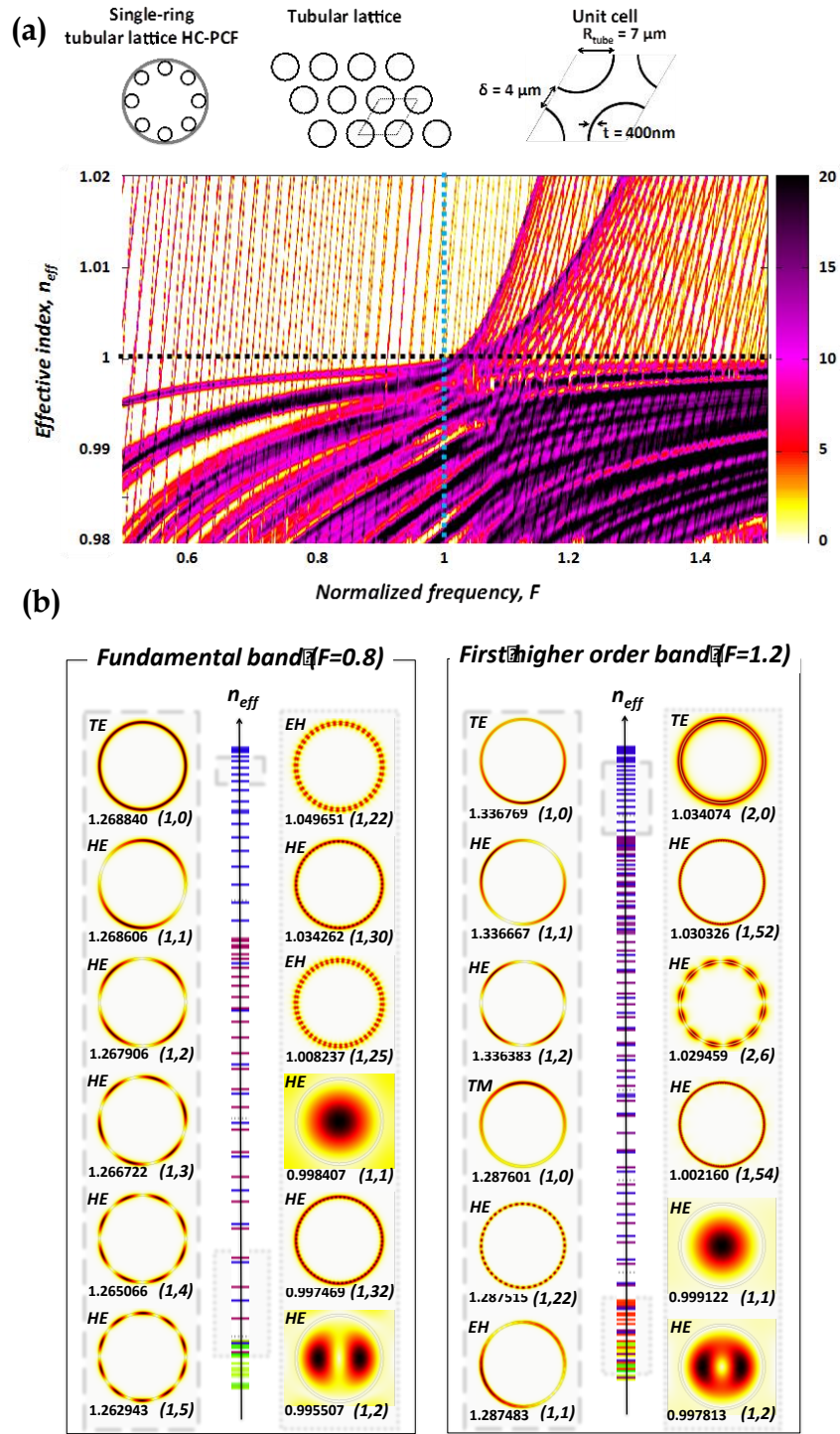


Figure 2-13 (a) Schematic of HC-PCF with a single-ring tubular lattice (i), a section of a tubular lattice in a triangular arrangement (ii) and the details of a unit cell of the lattice (iii). (b) The density of the photonic state of an infinite tubular lattice in triangular arrangement. (c) Transverse profiles of the electric field magnitude of the photonic state (modes) for $F = 0.8$ (fundamental band) and for $F = 1.2$ (first higher order band).

The color-map of these states highlights two classes of modes. The modes residing in the silica tube, which are identifiable with their steep dispersion curves (close to vertical), and those residing in air having flat dispersion curves (close to horizontal) and located below the vacuum-line (*i.e.* $n_{eff} = 1$).

The nature of these modes is revealed in Figure 2-13(c) by showing the transverse profile of their field magnitude for a given frequency from the fundamental band ($F = 0.8$) and from the 1st higher-order band ($F = 1.2$) at two representative sets of n_{eff} . The first set corresponds to $n_{eff} > 1$ and ranges from 1.2 to 1.3. Within this effective index range, the modes are all located in the silica tube as expected, and correspond to HE_{ml} (*i.e.* electric field direction is azimuthal) or EH_{ml} (*i.e.* electric field direction is radial) [64]. Here, m and l are the indices of the azimuthal and radial components of the transverse wavenumber respectively. The azimuthal and radial phases are commonly inseparable, however, given the fact that the radius of the tube is much larger than its thickness we can approximate the radial phase of these modes to that of a slab and apply the self-consistency condition on the azimuthal direction [64]. Consequently, for a fixed λ and for n_{eff} equal to that of HE_{11} fiber core mode (*i.e.* the silica cladding modes are longitudinally phase-matched with the core mode), we can relate the azimuthal and radial numbers to R_t , t and the fiber core radius R_c through the identity:

$$\left(\frac{m+1/2}{2R_t}\right)^2 + \left(\pi \frac{l+1/2}{t}\right)^2 = \left(\frac{2.405}{R_c}\right)^2 \quad (2.3)$$

From this simple identity, we can relate m to l and extract scaling laws such as $m \propto R_t/R_c$ when we fixed t and the wavelength.

By definition, all the silica modes in the fundamental band don't exhibit radial oscillations (*i.e.* $l=1$), and EH_{m1} can be distinguished from $HE_{m,1}$ by their slight lower dispersion slope in the DOPS diagram. In the 1st higher order band,



the radial number l can take either the value of 1 or 2, and the modes with $l=2$ can be distinguished by exhibiting two radial lobes in their field amplitude profile. The second set of n_{eff} corresponds to the modes below the vacuum-line ($n_{eff} < 1$), and ranges from 1.04 and 0.99 (see the dotted blue rectangle of Fig. 1(c)). Below the vacuum line, the photonic structure can support modes in silica and air. Here, the modal content comprises both the above silica tube modes and those residing in the air of the tube inner-region (air modes). We note that because m increases as n_{eff} decreases, all silica modes exhibit larger azimuthal number than those from the first effective-index set, which strongly favors coupling inhibition via enhanced transverse phase-mismatch between these silica modes and the low azimuthal number modes residing in air. This fact is exemplified by the easily distinguishable dispersion curve of the air modes in the DOPS. Indeed, the DOPS diagram shows that, apart from for frequencies near $F = 1$, where the dispersion of the air modes and the silica modes strongly hybridize (anti-cross), the dispersion of the two classes of modes are clearly distinguishable and they intersect with no meaningful anti-crossing, indicative of a strong coupling inhibition between them. The strong coupling between the air modes and the silica modes is practically limited to frequencies with integer values of F (*i.e.* $F = 1, 2, 3, \dots$), which stems from a radial transverse phase matching between silica and air modes when the azimuthal is nil or very low [58]. This air-glass modal coupling is manifested in the hollow-core fiber form of the photonic structure as high loss bands centered at wavelengths given by equation (2). On a side note, we highlight that this radial (here $m=0$) transverse-phase matching condition is used in some of the current literature as a defining feature of fibers guiding via anti-resonance reflecting optical waveguide (ARROW) [62] [65]. But ARROW picture does not give the physical mechanisms by which the core-guided modes are prevented from coupling to the cladding modes.



Therefore, the IC HC-PCFs we have discussed in earlier sections based on SR-TL HC-PCFs would enhance IC guidance guiding in the NIR-VIS-UV spectral range and showing ultra-loss. It is possible that by adjusting cladding properties it is possible to get optimum confinement loss and close-to-unity modal content using the IC formalism. Further optimization and linear characterization of several of such fabricated fiber will be discussed in Chapter 4.

2.5 Summary

In conclusion, this chapter has dealt with complete conceptual tools and numerical explanation on guiding principles of IC HC-PCF of two lattice designs, one with Kagome and Tubular lattice. The problem of guidance in IC HC-PCF has been treated in analogy of condensed matter physics and by describing its cladding modal structure and then consider the possible core modes that have no or limited coupling pathways to the cladding mode. Enhancement methods of IC guidance by the introduction of hypocycloid core contour design and with the design of SR-TL IC HC-PCFs are also discussed. As a conclusion, we could realize the salient features of IC guidance, its optimization parameters and scaling laws in order to develop long term waiting ambition of broadband and ultra-low loss IC HC-PCF.

* The numerical results have been obtained through the modal solver of the commercial software Comsol Multiphysics 3.5 based on the finite-element method, with an optimized anisotropic phase-matching layer (PML) [66].

** The numerical results were obtained through joint use of the FEM modal solver and of the conformal mapping technique [67].

The DOPS was computed by, using the commercial finite element modal solver COMSOL Multiphysics and by applying the Floquet-Bloch boundary conditions to the unit cell of the lattice. Here, we mapped the three symmetry points of the Brillouin zone. All simulations were performed by our collaborator Luca Vincetti at University of Modena and Reggio Emilia, Italy.





Chapter 3

Fano resonance in IC Kagome HC-PCF

This chapter reports on theoretical and experimental demonstration of Fano resonances in IC HC-PCF. Fano line shapes in transmission spectra of IC HC-PCF will be explained through coupled mode theory in order to prove that this fiber acts as a photonic manifestation of BSiC. A high-spectral resolution fiber-transmission spectra show typical Fano asymmetric spectral signatures and a high dynamic-range near-field imaging resolves the core-cladding coupling.



3.1 Introduction

As we discussed in the introductory chapter, light confinement in HC-PCFs is achieved either by PBG or by IC guiding mechanism. With respect to frequency spectrum, if we consider guided core and cladding modes as bound and continuum states respectively, in PBG guidance the guided core mode, akin to a defect bound state in solid state physics, lies outside the spectra of continuum. This absence of modes (*i.e.* $\{|\phi_{clad}\rangle\} = \emptyset$) in the cladding harboring the defect mode results in the lack of radiation channels that are accessible to the core mode through the cladding. Hence, the light is confined within the core along the fiber. Such a scheme of trapping or guiding waves is a well-established concept since the development of quantum mechanics and solid-state physics, and being implemented heavily in semiconductor technology. Also, from this perspective, the optical guidance via TIR can be seen as a form of PBG guidance as illustrated in Figure 3-1(a). Here, the conventional TIR guiding fiber relies on a core with a material index higher than that of the cladding n_{cl} .

As a result, and because $\beta < n_{cl}k$, meaning that β which is larger than $n_{cl}k$ is forbidden, a PBG in the (n_{eff}, ω) space is formed for $n_{eff} > n_{cl}$. On the other hand, for $n_{eff} < n_{cl}$, the modal content of the fiber is composed of cladding modes (low index material) and core radiation modes. From this stand point, the introduction of a micro-structured cladding instead of a uniform dielectric material has extended the existence of cladding PBG to regions in the (n_{eff}, ω) space where n_{eff} of the modes can be less than the cladding material index n_{cl} . This can be the case even for effective indices below 1; making thus air-core optical fiber possible (see Figure 3-1(b)).



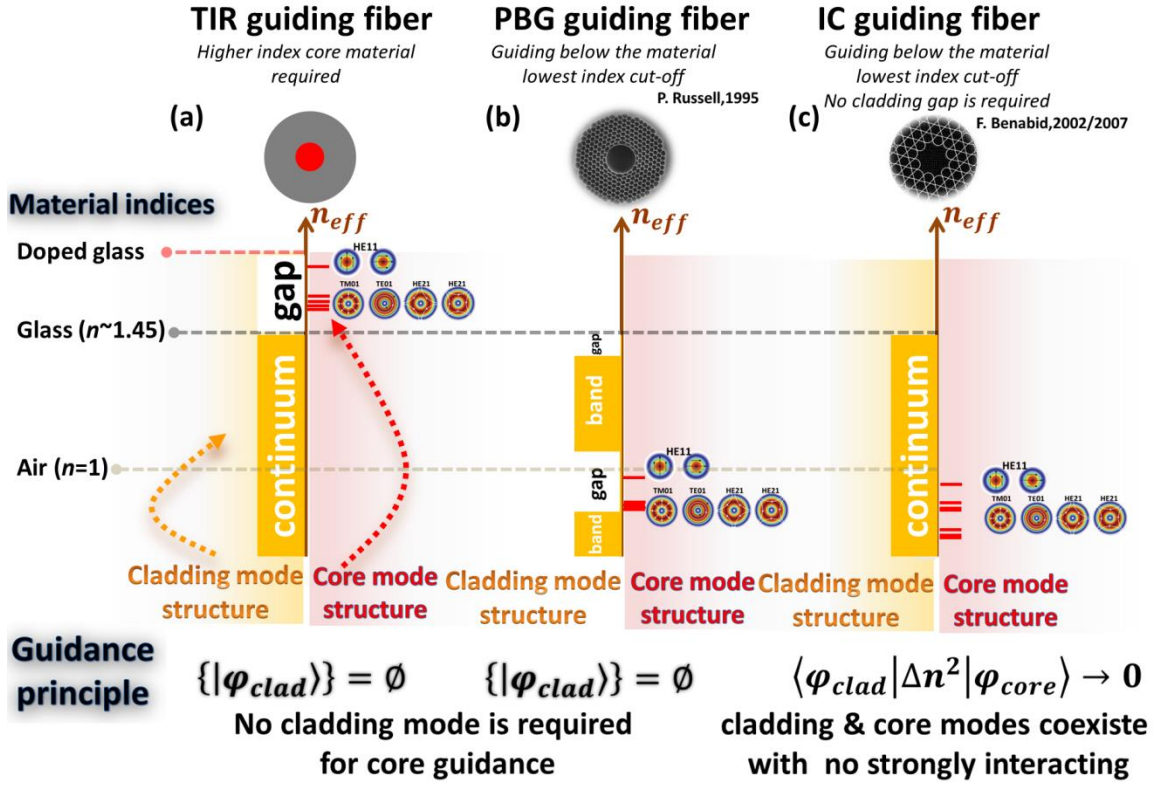


Figure 3-1 Schematic of the modal contents of (a) TIR guiding fiber, (b) PBG and (c) IC-guiding HC-PCF.

Here, the cladding modal content and structure (*i.e.*, those corresponding to $n_{eff} < n_{cladding}$) is made by allowed bands (cladding propagating modes) and the forbidden bands (PBG). Their formation can be described using the photonic tight binding model [22], which we mentioned in Chapter 1. In conclusion, guiding via PBG can be seen as the photonic analogue of semiconductors, and deciding whether a cladding photonic structure amenable for PBG optical guidance is done by the presence of a region in (n_{eff}, ω) of cladding modal spectrum that is void of any mode (*i.e.* DOPS=0).

Unlike for TIR and PBG fibers, the IC optical guidance no longer relies on the presence of a PBG in the modal spectrum of the cladding. This is illustrated by Figure 3-1(c) where guided core modes and cladding modes co-exist at the same (n_{eff}, ω) , and yet their coupling interactions are inhibited. This unconventional

guiding mechanism can be pictured as a bound state having its frequency embedded within the spectra of continuum. To be precise, in practice, there is always negligible residual radiation of core modes to the continuum; hence this guiding mechanism is referred as quasi-bound state in continuum (Q-BiC), otherwise, as perfect BiC for complete inhibition between both states.

This characteristic feature of core and cladding mode co-existence in IC guidance makes it difficult to determine with a microstructured cladding is suitable for IC guidance or not by simply examining its modal spectrum. Indeed, the PBG guidance can be determined by simply finding out in the DOPS diagram where $DOPS=0$. In the case of IC fibers such a criterion (*i.e.* $DOPS=0$ or $\{|\varphi_{clad}\rangle\} = \emptyset$) no longer holds. Instead, the suitability of a cladding microstructure for IC guidance is so far done by examining the profile of the continuum modes and/or engineering it so that overlap integral between the cladding modes and a core mode $\langle \varphi_{clad} | \Delta n^2 | \varphi_{core} \rangle$ as minimum as possible. Historically this was first done with Kagome lattice HC-PCF [47], where the authors demonstrated that the relatively low loss obtained with this type of HC-PCF is due to the cladding modes just below the air-line being highly localized in the silica cladding web and exhibiting fast transverse oscillations. Furthermore, such inhibition can become stronger provided stronger phase mismatch in their respective transverse spatial phase which is the characteristic of silica-core contour and directly linked to the reduction of the fiber confinement loss (CL) in IC guidance. This implies a strong dependence on the core-mode profile and led to seminal introduction of hypocycloid core-contour design (*i.e.* negative curvature) in 2010 [68] [17] to reduces optical overlap of core modes with silica and to increase azimuthal like number, which reduced transmission losses dramatically and enhance power handling capabilities at record level [49] [43].



From the above, one can see that it is very difficult to have an easy or direct means to determine whether a microstructured fiber is guiding via IC or not. It is thus desirable to have direct evidence of such guidance. Within the framework of atomic physics, Q-BiC or BiC states can spectrally manifest as Fano resonances [69].

The present chapter aims to *explore IC guidance mechanism as the photonic manifestation of Q-BiC or BiC by utilizing Fano resonance*. The chapter is organized as follows. In the next section 3.2, we first review about the origin and historical background of BiC and the necessity of manifesting guidance mechanism in IC HC-PCF with BiC. The subsection 3.2.2 gives another historical account, but focused on the Fano spectral signatures of auto-ionization (AI) which is the first observed BiC with unusual asymmetric profiles by Silverman-Lassette during measurement of helium (He) spectrum. This section is followed by a demonstration of the universality of BiC by discussing various simple physical systems such as mechanical oscillators, semiconductor hetero-structures and optical waveguides, and how in which Fano asymmetric spectral signatures can manifest. Finally, we report theoretically and experimentally Fano resonance in 7-cell Kagome IC HC-PCF. This was undertaken by first numerically simulating the effect of a small scattering perturbation on the confinement loss (CL) spectrum of the two polarizations of the core fundamental mode HE_{11} and by examining the spectral structure of the CL near resonant coupling between the core and the cladding modes. Secondly, we experimentally investigate Fano resonance in HC-PCF by set of experimental protocols, including: (i) examination of the fiber's transmission with high spectral resolution, (ii) spectral evolution of the Fano traces with input polarization, and (iii) reconstructed near-field imaging in high dynamic range for different wavelengths and input polarization.



3.2 Physical and historical background of BiC

Waves that remain localized even though they coexist with continuum spectrum of radiating waves which leak energy out of the system are called bound states in the continuum (BiC). Von Neumann and Wigner in 1929 proposed the concept of BiC by introducing Schrodinger equation for a single-particle that can have spatially localized states with energy lying above the asymptotic limit of the potential [40]. Such trapped states, especially in optical domain co-propagate with energies from continuum spectrum of leaky modes, but do not interact with other. A more detailed discussion about historical and physical account of BiC is presented subsection 3.2.1. A first physical manifestation of such a bounded state was encountered in the asymmetric spectral profile of auto-ionizing state transitions in atomic physics [70]. This profile is described by Fano resonances rather than the Lorentzian profile [71]. This section is followed by the discussion on first observation of S-shaped absorption spectra in auto-ionization of helium gas. Ugo Fano developed line shape formalism to fit such uncommon resonance profiles which were named after him (Fano resonances) [69]. Thereafter, such asymmetric profiles had been identified as characteristic of BiC. Development of Fano resonance concept provided verification tool for the BiC existence and many physical systems have witnessed this new wave localization schemes by exploring Fano signatures in their resonance profiles.

Though BiC remains uncommon scheme of trapping waves, it is universal [71], and has been reported in mechanical [72], electronic [73] and photonic crystal [74] systems. Its principle pertains to any physical system with a discrete mode close in energy to a continuum and BiC asymmetric lines can be observed by any mechanism that perturbs coupling between the discrete mode and the continuum. These asymmetric line-shapes are explained by interference



between two scattering pathways. The first scattering process occurs within a continuum of states (the background process) and the second from the excitation of a discrete state (the resonant process).

In photonics, the concept of co-habitation between discrete and continuum modes was first reported in 2007 by Benabid and co-workers [22] within the framework of fiber photonics. Here, the authors showed that despite the modal spectrum of a Kagome cladding exhibiting a continuum of propagation modes below the air-line, and thus having effective indices matching those of a hollow-core mode, the coupling of these modes to a defect mode (*i.e.* air-core mode) is strongly inhibited even when both modes exhibit very close effective index. Unlike in PBG fibers, whereby the effective index-frequency (n_{eff} , ω) pair of the core guided mode (*i.e.* bound state) lies outside that of the cladding continuum, and thus the core mode has no radiation channels via which light can leak out and couple to the cladding. In the case of IC HC-PCF, the guided core mode and cladding modes co-exist without strongly interacting by virtue of a strong reduction in their overlap integral. This unconventional guiding mechanism can be pictured as a bound state (core mode) having its index-frequency embedded within the spectra of continuum (cladding modes).

In this work, the authors showed that the mode continuum is comprised with modes that are strongly localized in the silica web and having a very fast oscillating transverse wave vector (*i.e.* high azimuthal-like number, m). Such properties mean that the overlap integral between these mode and an air-core mode exhibiting no or small azimuthal number is strongly reduced. This in turn results in an air-core mode with a very low transmission loss. It is noteworthy that the air-core mode is not a properly guided mode but leaky modes because of residual interaction with the cladding and leakage due to the finite size of the fiber



structure. As such it is more appropriate to talk about quasi-bound state in a continuum (QBiC) in the case of this IC optical guidance mechanism. Following this work [75], IC model has been used as a design tool to improve the performances of optical fibers, which led to the introduction of hypocycloid core-contour designs [68] in hollow-core fibers.

3.2.1 Bound State in Continuum (BiC)

As early as 1929, Von Neumann and Wigner introduced the concept of bound state in a continuum (BiC) by demonstrating that the single-particle Schrodinger equation possesses isolated eigenvalues embedded in the continuum of positive energy states [40]. In their seminal work they considered an artificial quantum potential to trap an electron with its energy lying below the continuum, but still would normally allow coupling to outgoing waves. This unconventional trapped state remains perfectly confined and cannot be decayed into continuum until and unless a generic perturbation to the potential breaks the symmetry of the system or binding of the trapped states. As a result, interaction between bound states and continuum takes place where their spectrum shows a destructive interference. Figure 3-2 represents such a state as shown in red circle with asymmetric profile as it couples with continuum. Such an interaction shows an destructive interference which is called as Fano resonance. The specific spectral profile of a Fano resonance makes it an experimental and theoretical tool for the BiC studies provided the system belong to the two configurations mentioned in Fano's original work [69]. One of the configurations is band of infinitely extended states and the other is bound states confined within the extended states. Furthermore, the spectral structure of Fano resonance can be used as an optimization tool to improve the performances of such physical applications, such as optimizing or engineering the performances of IC HC-PCFs.



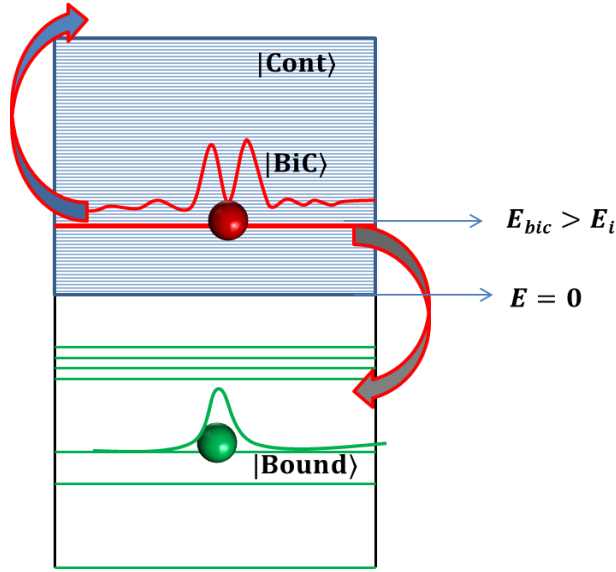


Figure 3-2 Schematic of BiC (red) having ionization potentials greater than conventional bound states (green) embedded in continuum (blue background).

3.2.2 Fano Resonance: Spectral manifestation of QBiC and BiC

Among the rare physical phenomena that exhibit BiC effect is that of auto-ionization (AI) with the unexplained Silverman-Lassette measured He spectrum above potential threshold and that was first observed by Beutler in 1935 [76]. Ugo Fano, for the first time in his theory of configuration suggested theoretical explanation for this effect and in 1961 [69] with the development of a line shape formula (see equation 3-1) in the context of inelastic electron scattering by the helium. His formula fitted well for the unusual asymmetric S-shaped sharp peaks of Silverman-Lassette measured He spectra (see Figure 3-3). These asymmetric line-shapes are explained by interference between two scattering pathways. The first scattering process occurs within a continuum of states (the background process) and the second from the excitation of a discrete state (the resonant process). The absorption lines in the ionization continuum of atomic (and molecular) spectra are represented by the Fano line shape formula [77] [70],

$$\sigma = \frac{(\epsilon+q)^2}{\epsilon^2+1} \quad (3.1)$$

here q is a shape parameter, ϵ is a reduced energy defined by $2(E-E_F)/\Gamma$ where E_F is a resonant energy, and Γ is the width of the auto-ionized state.

The lifetime of an atom in an auto-ionization state is large compared to typical atomic lifetimes. In other words, because of the possibility of its decay, the AI level is characterized by a width Γ , which is small compared to the excitation energy of this level ϵ (i.e., $\Gamma \ll \epsilon$), and we can consider the auto-ionization level as a quasi-discrete level. Therefore, such short-lived auto-ionizing states can be better explained by FR rather than normal bound states. If the radiative transitions in auto-ionization states are the dipole permitted ones, it creates the resonance structure of the photoionization cross section. This in turn, influences the absorption spectrum of atoms in the continuous region giving it asymmetric shape line as noticed by Beutler [76].

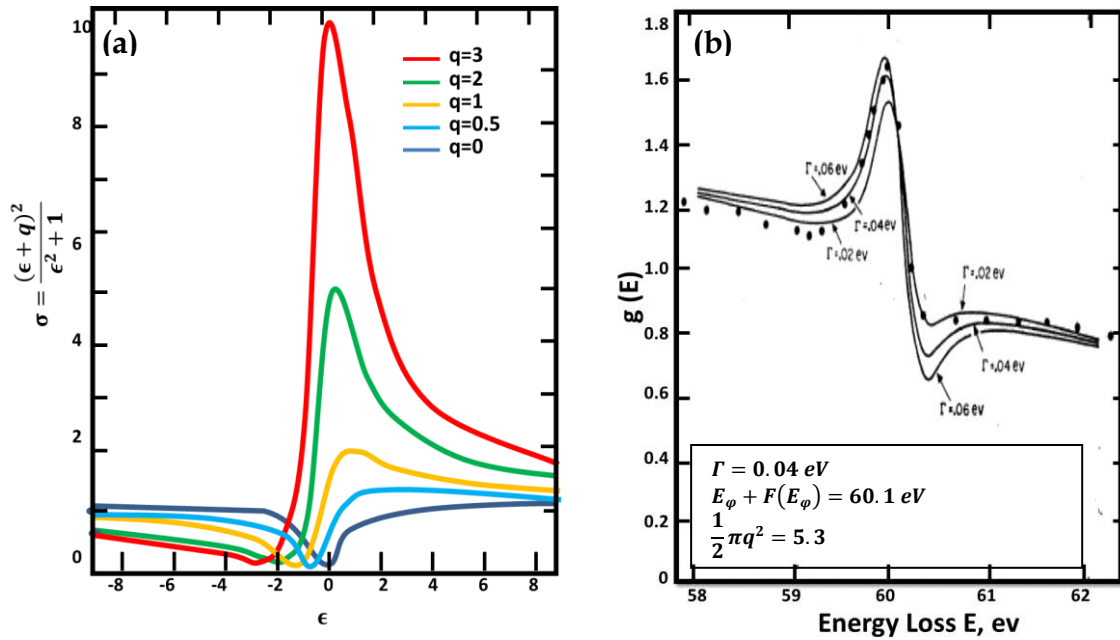


Figure 3-3 (a) Natural line shapes determined by Fano formula for different values of q . (Reverse the scale of abscissas for negative q). (b) Fit of Silverman-Lassetre measured He spectrum [from [69]].

The auto-ionizing (AI) state is the first physical manifestation of BiC and Q-BiC. AI state of atoms is a bound state whose discrete level lies above the boundary of continuous spectrum. As depicted in Figure 3-4 (a) general ionization process in which a discrete electronic state $|d\rangle$ raises into continuum $|c\rangle$. AI state results from the excitation of two atomic electrons (e^- s) whose total excitation energy exceeds the ionization potential of the atom. The interaction between electrons leads to the decay of this state so that one e^- transfer into a lower state and the second e^- takes an energy excess that causes its release (see Figure 3-4(b)). In this way AI phenomenon can be modelled as a perturbation which leads to destructive interference between discrete electronic state and continuum. Therefore, Fano resonances provide means for the light trapping studies in various physical systems provided they have a band of infinitely extended states and the other being bounded within the extended states [77] [78].

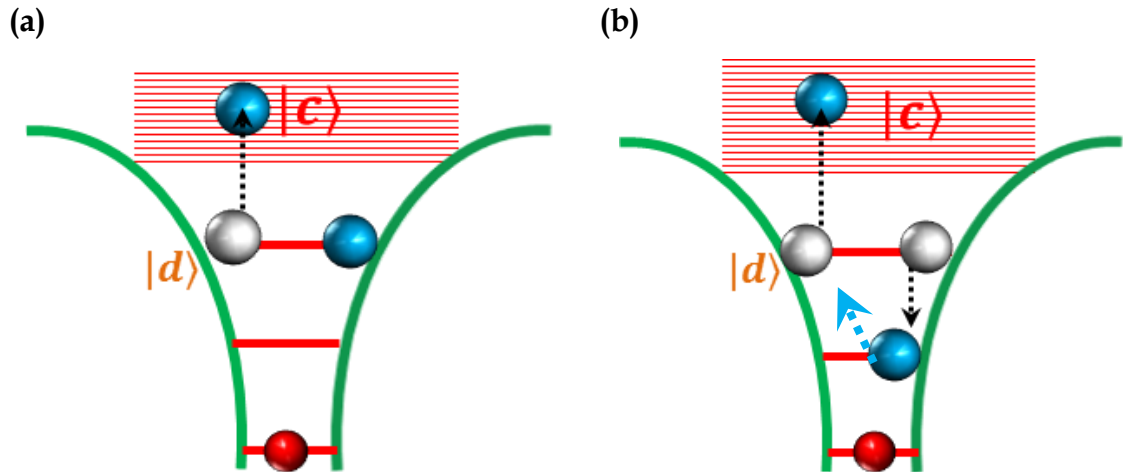


Figure 3-4 (a) Schematic of conventional ionization process. (b) auto-ionization process showing the coupling between discrete and continuum due to transition of ground state electron to continuum via discrete state. The red spheres represent electrons at ground level. White and blue spheres represent electrons in transition from discrete to continuum level.

3.3 Universality of BiC

Any physical system with a discrete mode close in energy to a continuum and with a means of a mechanism that perturbs coupling between both would encounter Fano asymmetric profiles of BiC. Surprisingly and despite BiC remains an uncommon scheme of trapping waves, it is universal [71] and has been reported in mechanical [37], electronic [73] [79] and photonic crystal [74] systems. Below we review such BiC manifestations in different configurations. Also experimental realization of BiC is more challenging than theoretical work. Though many research groups work on potential scientific and technological applications of BiC [74] [80], majority of works are being theoretical rather than experimental.

3.3.1 BiC in two coupled mechanical oscillators

One of such ideas of the FR manifestation can be explained by a pair of classical oscillators with natural frequency ω_1 and ω_2 , coupled by a weak spring, where one of them is driven by external force (see Figure 3-5(a)) [72]. The amplitude of driven pendulum (natural freq is ω_1) as we see in Figure 3-5(a), it is also resonant at ω_2 (not its natural frequency) and whose resonance spectral shape is not Lorentzian but has a Fano's asymmetric shape. The equations of motion for this system may be written as:

$$\ddot{x}_1 + \gamma_1 \dot{x}_1 + \omega_1^2 x_1 + v_{12} x_2 = a_1 e^{i\omega t} \quad (3.2)$$

$$\ddot{x}_2 + \gamma_2 \dot{x}_2 + \omega_2^2 x_2 + v_{12} x_1 = 0 \quad (3.3)$$

The above equations can have steady state solutions:

$$x_1 = c_1 e^{i\omega t}, \quad x_2 = c_2 e^{i\omega t} \quad (3.4)$$

here v_{12} describes the coupling of the oscillators with amplitudes

$$c_1 = \frac{\omega_2^2 - \omega_1^2 + i\gamma_2 \omega}{(\omega_2^2 - \omega_1^2 + i\gamma_1 \omega)(\omega_2^2 - \omega_1^2 + i\gamma_2 \omega) - v_{12}^2} a_1 \quad (3.5)$$

$$c_2 = \frac{v_{12}^2}{(\omega_1^2 - \omega_1^2 + i\gamma_1 \omega)(\omega_2^2 - \omega_1^2 + i\gamma_2 \omega) - v_{12}^2} a_1 \quad (3.6)$$

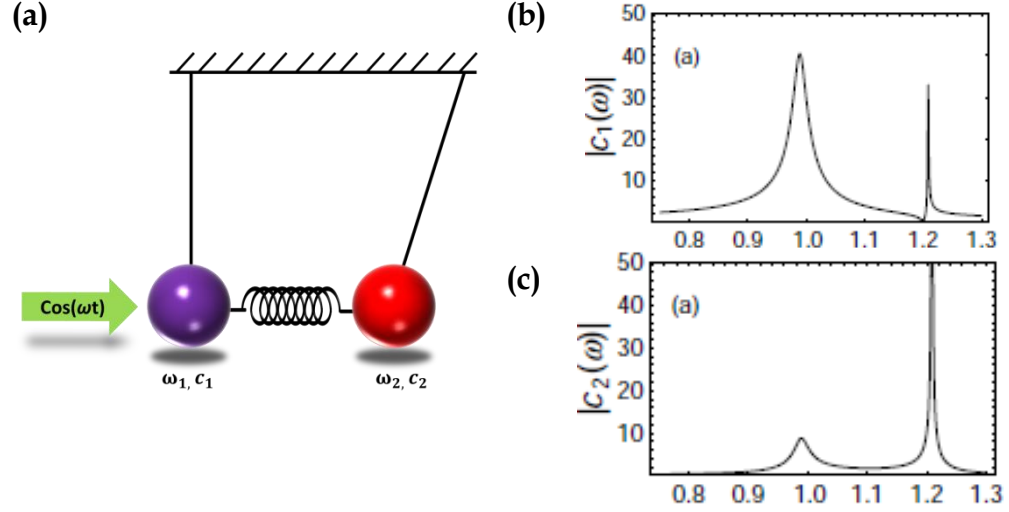


Figure 3-5 (a) Coupled pendulum driven by a periodic force of frequency ω . (b) The resonant dependence of the amplitude of the forced oscillator $|c_1|$ and (c) of the coupled one $|c_2|$ [from [72]].

The amplitudes of two oscillators respectively can have two resonances located close to Eigen frequencies ω_1 and ω_2 of the oscillators. As we can notice in Figure 3-5 (b), one of the resonances of the forced oscillator demonstrates the standard enhancement of the amplitude of symmetric Lorentzian function near its Eigen frequency ω_1 , while the other resonance exhibits an unusual sharp suppression of the amplitude near the Eigen frequency of the second oscillator ω_2 , due to existence of the zero frequency right near the peak position. This can be realized by observing equation (5) with assumption of zero friction for second oscillator at $\omega = \omega_2$. Therefore, amplitude of the first oscillator suddenly suppressed with this special condition called zero amplitude or anti-resonance condition which leads resonance shapes into Fano asymmetric profiles.

3.3.2 BiC in electronic hetero-structures.

The first direct evidence of positive energy bound states in semiconductor heterostructures was proposed in [73] by F. Capasso *et.al*, with the demonstration of a narrow, isolated transition from a bounded state within the quantum well to a bound state at higher energy than the height of the barrier. This work claims as first electronic manifestation of BiC. Figure 3-6(a) represents energy diagram of a 20 undoped GaInAs with 32 Å thickness separated by 150 Å thick layers of AlInAs barriers. Such a quantum well can have a single bound state energy E_1 , above which only scattering states exists. At energies corresponding to a semi-integer number of de Broglie wavelength across the well the transmission is enhanced. The coupling between wells form mini bands (band gaps in precise) at energies greater than E_1 (between E_{c1} and E_{c2}). But, the scattering and imperfections within the structure would not allow the confined states of the wells (E_1) to form mini-bands.

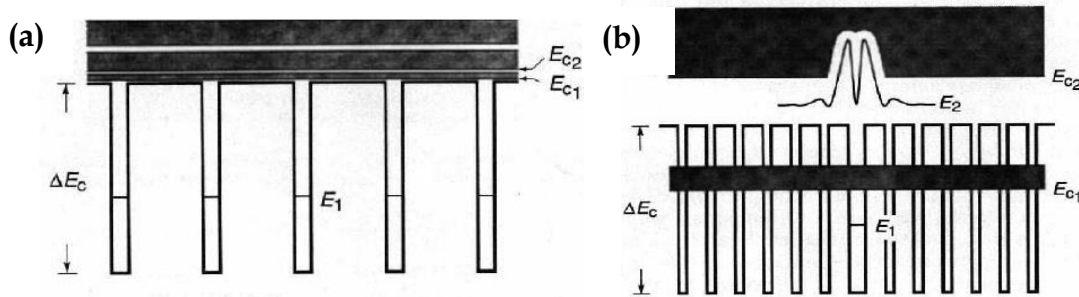


Figure 3-6 Conduction band diagram of reference sample of AlInAs/GaInAs hetero-structure with 32/150 Å. (b) GaInAs quantum well (32Å) with super lattice of AlInAs/GaInAs [from [73]].

Figure 3-6 (b), the super-lattice of AlInAs/GaInAs reported in [73] with thickness 16 Å and barrier with 39 Å thickness shows a localized bound state ($E_2=560$ meV) due to the interference of all the reflected waves from the super-lattice. Here E_2 represents spatial localization corresponding to first continuum resonance of the well and this state is localized above the well in the super lattice

minigap. E_2 can be understood as a deep level in the super-lattice bandgap, arising from the introduction of an artificial defect in the structure as shown in Figure 3-6 (b). Therefore, such an energy state E_2 is confined in the band gap formed between E_{c1} and E_{c2} . However, this study concerns the positive energy defect state E_2 lie within the bandgap formed by superlattice of semiconductor hetero-structure and such state cannot be manifested as BiC.

3.3.3 BiC in IC HC-PCF

The first fiber-photonic manifestation of BiC was reported using IC Kagome HC-PCF in 2007 by Couy, *et al.* [22]. In a Kagome IC HC-PCF, a central air core acts as a defect to trap the light. Such trapped guided light within the core are quasi-bound states embedded in infinite continuum of cladding of Kagome lattice structure. Therefore, one would expect that coupling inhibition between the core-mode and the cladding-mode would be affected by any perturbation that breaks the symmetry and results in Fano resonance in its transmission spectrum. The perturbation could be inherent to fiber structure due to the noise during the fiber fabrication by stack and draw method, while external perturbation is possible for example due to fiber bend. Also capillary scattering features are also possible during the fiber fabrication process which can change local index of the core, thereby creates perturbation to the configuration leading to FR. Then this chapter fully provides theoretical and experimental demonstration of BiC in 7-cell Kagome IC HC-PCF by exploring Fano resonance features in its confinement loss spectra provided a coupling channel through a scattering point on core contour.



3.3.4 Fano resonance in polygonal tubular lattice fibers.

A polygonal tube lattice fibers (PTF) made up of constituent tubular capillaries suffers from the extra losses due to the Fano resonance that arise due to imperfections in shape of each capillary. Noise during the fabrication of circular tubular fiber (CTF) creates asymmetric structural features which can be perturb fiber's core shape from circular to polygonal with N number of sides (Figure 3-7 (a)), while CTF can be considered with infinite sides.

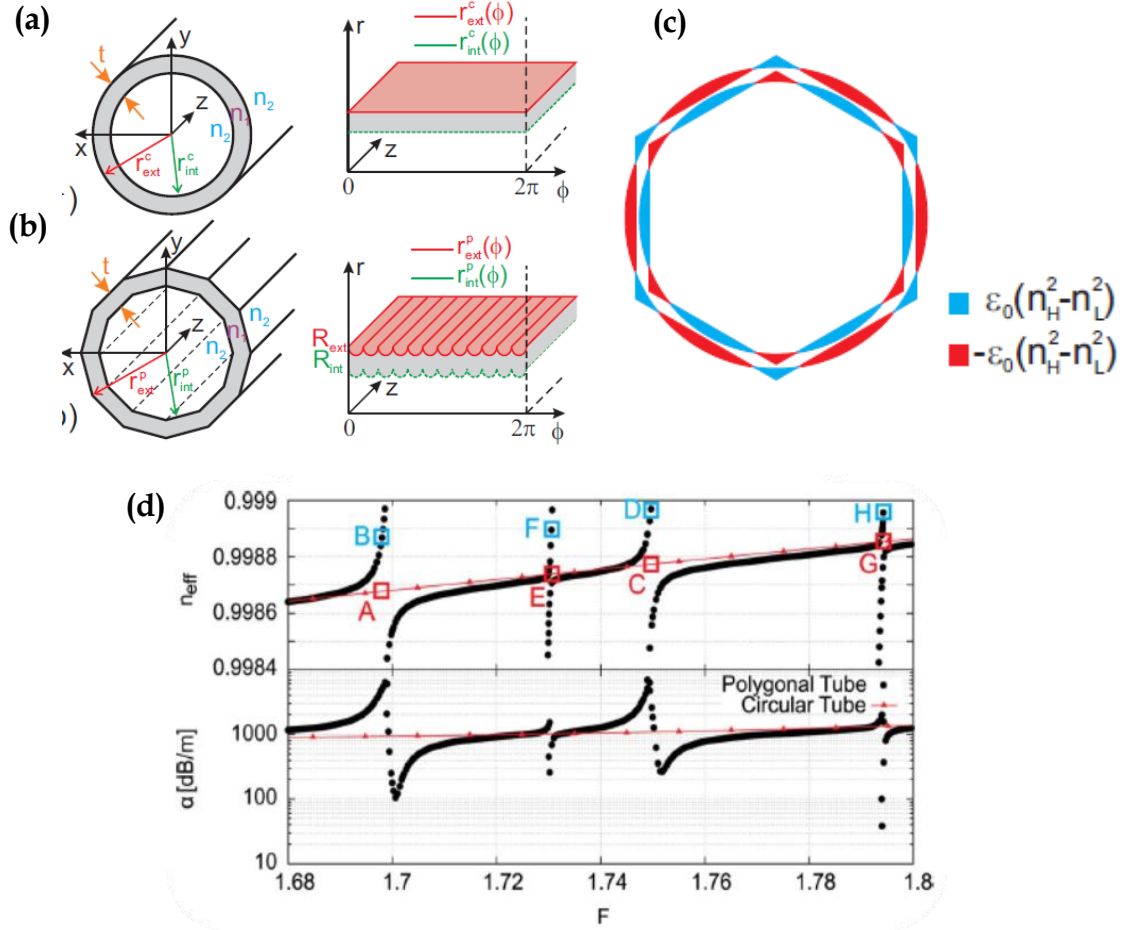


Figure 3-7 (a) Cross sections of a circular tube fiber and (b) a polygonal tube fiber (on left) and their equivalent planar structure in cylindrical coordinates (on right) with cylindrical coordinates $r_{int}^{c,p}(\phi)$ and $r_{ext}^{c,p}(\phi)$ represent the distance between the center of the fiber and the internal or external edges of the circular and polygonal tubes, respectively; (c) Schematic of the $\Delta\epsilon(r, \phi)$ in the case of $N = 6$. (d) Calculated n_{eff} and CL curves for the FM core mode of the circular (red triangles) and for a polygonal fiber with 24 sides (black circles) [from [81]].

In the work of Vincetti *et.al*, [81] it was reported that these perturbations create local change in effective index which perturb the symmetry of the system and breaks coupling inhibition between core mode and cladding modes lead to understand FR in IC HC-PCF. Consider an individual PTF from cladding which can be viewed as CT, but with a perturbed dielectric permittivity profile by N number of sides. This process can be described as the resonance between hollow core modes and high order dielectric modes which arise from the sharp edges of perturbed CTF. PTF can also be regarded as corrugated slab (Figure 3-7 (b)) since its radius varies in angle azimuthal direction about the center of the ring. Therefore, core modes consist in plane waves bouncing back and forth by dielectric slab and the reflection coefficients which determine CL oscillate slowly with frequency and its amplitude depends on n_1 and n_2 . But in corrugate slab model of PTF, the periodic variations increase the number of modes in transverse direction. The spectrum of reflection coefficient of the corrugated waveguide consists of a smoothly varying background as in planar slab and special kind of sharp oscillations due to extra coupling with the corrugated slab modes. The variations in the shapes of lattice tubes are the origin of extra coupling rising to FR in the fiber and also reason for extra losses [82]. As shown in Figure 3-7 (d), their spectral position depends on the dispersion curves of the slab modes, while the shape can be symmetric or asymmetric depending on the position of the background spectrum in which they appear. If they happen at a maxima or minima of the background spectrum they have symmetric Lorentz-line shape, in other cases they have asymmetric Fano-lines. Decrement in number of sides in the PTF would result in noisy CL spectra with more number of cut off regions and their shift towards lower frequencies.



3.3.5 BiC in photonic crystal slab

Recent report by Fan *et.al*, on trapping the light within the radiation continuum provides theoretical and experimental manifestation of BiC in a photonic crystal slab (PhC) [74]. The authors of the report observed BiC in a dielectric slab with square array of cylindrical holes that supports photonic band structures having frequencies within the continuum of radiation modes in free space with finite lifetime. The life time of these resonances goes to infinity at some k -points on certain bands where light is confined in the slab without any leakage. Such Eigen modes do not decay and exist within the continuum of radiation modes. The destructive interference of waves between several channels at slab-medium interface and at appropriate k - points suppress any leaky modes. Such phenomenon can be practically exploited by exploring Fano spectral features [83]. The fabricated PhC slab shown in Figure 3-8 with time-reversal and rotation symmetry excites the guided resonances and creates sharp Fano features in the reflectivity spectrum. As long as such a bound state does not couple with far field radiation, Fano features does not appear in its reflection spectrum. The lifetimes of resonances can be found by temporal coupled mode theory (T-CMT) [84] using Fano features described by:

$$f(\omega) = \frac{Q_r^{-1}(r_{slab} - t_{slab})}{\left(1 - \frac{\omega}{\omega_0}\right) + Q_r^{-1} + Q_{nr}^{-1}} \quad (3.7)$$

here ω_0 is the resonance frequency, Q_r and Q_{nr} are the normalized radiative and non-radiative lifetimes due to leakage into the free space, and r_{slab} and t_{slab} are coefficients of reflection and transmission of a homogeneous slab respectively. Normalized radiative lifetimes are investigated for different incident angles (θ) of light on PhC. Figure 3-8(b) shows measured and RCWA (rigorous coupled wave-analysis [85]) calculated evidence of disappearing leakage channels.



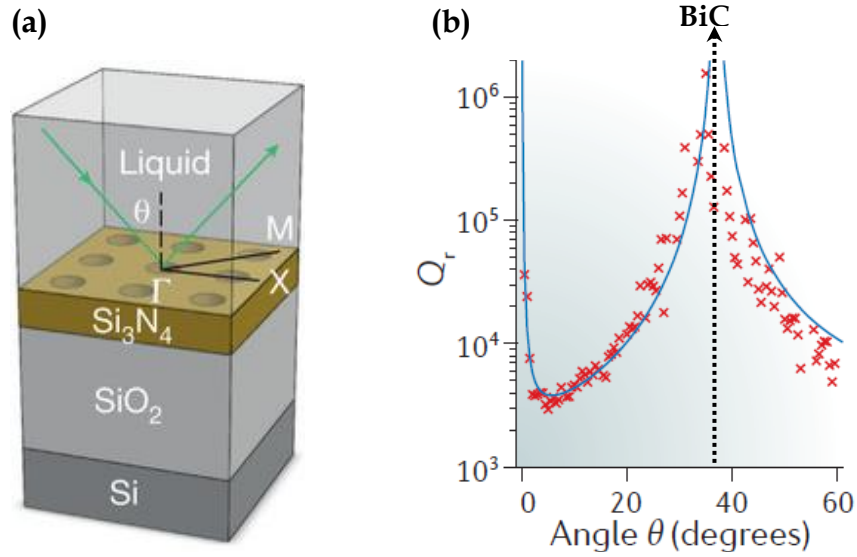


Figure 3-8 (a) Schematic layout of the fabricated structure. The device is immersed in a liquid, index matched to silica at 740nm. (b) Normalized radiative lifetime Q_r extracted from the experimentally measured reflectivity spectrum are shown by red crosses and the blue solid line shows the prediction from FDTD [from [74]].

The blue solid in Figure 3-8(b) represents calculated results of FDTD. The only difference between both the traces is the larger width of measured radiated lifetimes due to loss from material absorption, disorder scattering and in-plane lateral leakage. Both results show that about 35° incident angle of incoming light on PhC, Q_r reaches maximum values set by the instrument ($\gg 10^6$) as predicted by FDTD calculation. This situation indicates evidence of BiC with the demonstration of trapping the light for larger period life time within the continuous spectrum of radiation modes.

3.4 Understanding Fano Resonance in Kagome IC HC-PCF through toy model and coupled mode theory

In previous sections we have seen different physical systems including electronics, mechanical and photonic structures which manifested BiC and Fano resonances provided a discrete, continuum and a coupling pathway given by perturbation. Now this section focuses on how Fano resonances can be observed in optical waveguides. In order to observe Fano resonances in optical waveguides like IC HC-PCF, we have to consider perturbation by scattering channel provided by a surface roughness feature could either be inherent to structure that are formed due to noise during the fiber fabrication. Such perturbations provide means to couple discrete guided modes and continuum modes which results in asymmetric Fano profiles in transmission spectra. Also, recent report [86] relates Mie scattering as a cascade of Fano resonances by approximating Lorenz-Mie coefficient as infinite series of Fano resonances due to interference between the background radiation from an incident wave and modes from Mie scattering.

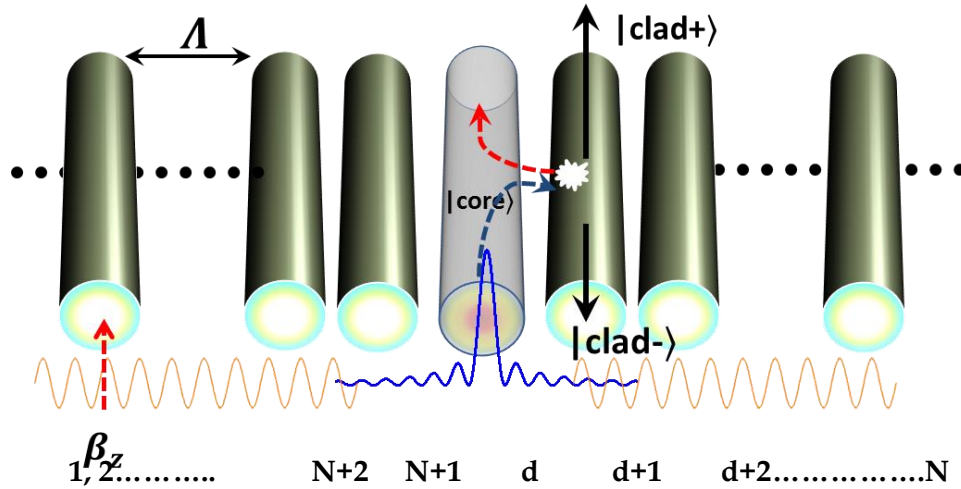


Figure 3-9 Schematic of the 1D waveguide array of N waveguides separated by Λ and provided a defect at the center of the chain with perturbed scattering feature.

In this regards we provide a toy model approach to mimic the configuration of Kagome IC HC-PC and to reduce the problem of BiC manifestation via scattering perturbation. Kagome fiber is basically consists of a micro structured cladding and a core defect. In this toy model we configure a one dimensional array of waveguides as cladding continuum and a defect core mode as discrete mode. Then, in order to provide coupling between both modes, we introduce a roughness feature on core-contour as a perturbation. Now, these modes spherically re-radiate out of roughness feature and couples back with z-propagating core mode in forward and backward direction. This scattering scenario can be simply modeled by using temporal CMT and very similar to the approach of scattering by a single obstacle reported in [87] by Fan *et.al*, in which they developed Fano formalism in in light scattering by a single obstacle. They considered an obstacle located at the origin which is uniform in z-direction and surrounded by air in x-y plane. When a wave with its magnetic field polarized along the z-direction impinges on the obstacle that supports the resonance for one of several channels. This result in the Fano effect due to interference of two pathways: the direct reflectance of the incoming wave that forms the background, and the outgoing radiation from the excited resonance.

We now can adopt the similar analytical approach and adopt it to our toy model of Kagome HC-PCF in order to understand Fano resonances caused by the destructive interference in transmission spectra due coupling of discrete core mode with continuum of cladding via scattering events. For this, we consider light with β_z propagation in z-direction in one-dimensional array of semi-infinite identical rods a radius ρ and spaced by a pitch Λ in x-y plane with translational symmetry and continuous symmetry in z-plane. This array is equivalent to the background or continuum of the system considered. When all such rods/ waveguides brought in close proximity, their transmittance shows sinusoidal

profile which resembles continuum spectra of cladding (see Figure 3-9). If we introduce a center waveguide by a capillary it will create a defect along z-direction. This represents the hollow-core of the Kagome fiber and the arrays of capillaries on its both sides represent cladding of the fiber. Therefore, this toy model mimics the configuration of IC Kagome HC-PCF. The presence of the core/defect will change the coupling coefficient with its nearest waveguides and will confine or trap the core guided modes inside the core as a result it will modify the transmission profile from sinusoidal to Lorentzian. These trapped core modes do not interact with cladding continuum due to the coupling inhibition.

This situation is nothing but embedding a discrete core mode within the continuum of the cladding, which exactly represents BiC. In order to prove existence of this BiC in the system, we introduce a scattering feature in the vicinity of core-cladding as represented by white dot in the Figure 3-9. The scattering perturbation breaks the symmetry of the system and creates coupling between scattering paths of core mode and other of cladding modes, which is schematically depicted in the same figure. The scattering feature re-radiates the incident light spherically with one of the component along with propagation direction ($|clad\rangle^+$) and other being backward ($|clad\rangle^-$) which especially couples back with core mode ($|core\rangle$) and is the reason for destructive interference which results in Fano asymmetric signatures in transmission spectra. For the sake of simple notations, let us replace discrete core state $|core\rangle$ by $|a\rangle$ with amplitude a and incoming and outgoing waves with cladding modes ($|clad\rangle^\pm$) by ($|c\rangle^\pm$) with amplitudes c^\pm for the forward (+) and backward (-) waves of the cladding modes. Now for this situation we can write the temporal coupled mode equation [87] as

$$\begin{aligned}\frac{da}{dt} &= -(i\omega_0 + \gamma_0 + \gamma)a + \kappa c_l^+ \\ c_l^- &= B c_l^+ + \eta a\end{aligned}\tag{3.8}$$



here ω_0 is the resonant frequency, γ_0 is the intrinsic loss rate due to material absorption, γ is the external leakage rate due to the coupling of the resonance to the outgoing wave, $B(=e^{i\phi})$ is the background reflection coefficient, and κ and η are coupling constants. The first expression in equation (3.8) represents coupling of discrete core-guided mode with forward cladding mode with coupling coefficient. The second expression represents coupling of core modes with backward cladding mode with coupling coefficient η .

Now, by assuming boundary conditions for lossless ($\gamma_0=0$) medium and in the absence of incoming wave $c^-=0$, along with energy conservation and time reversal arguments the relation between κ and η can be obtained.

According to energy conservation, the energy leakage rate must be equal to the power of outgoing wave, which bring the relation:

$$\eta\eta^* = 2\gamma. \quad (3.9)$$

According to time reversal symmetry consideration results in:

$$\kappa = \eta = \sqrt{2}\gamma e^{(\frac{\phi}{2} + \frac{\pi}{2} - n\pi)} \quad (3.10)$$

here n is an arbitrary integer and ratio between incoming and outgoing cladding amplitudes would give reflection co-efficient expressed by:

$$R = (c^- / c^+) = \frac{i(\omega - \omega_0) + \gamma_0 - \gamma(e^{i\phi})}{i(\omega - \omega_0) + \gamma_0 + \gamma} \quad (3.11)$$

Similarly we can get scattering coefficient:

$$\begin{aligned} S &= \frac{1}{2} \frac{(i(\omega - \omega_0) + \gamma_0)(e^{i\phi} - 1) - \gamma(e^{i\phi} + 1)}{i(\omega - \omega_0) + \gamma_0 + \gamma} \\ &= \frac{1}{2} \frac{(i\Delta\omega + \gamma_0)(e^{i\phi} - 1) - \gamma(e^{i\phi} + 1)}{(i\Delta\omega + \gamma_0 + \gamma)} \end{aligned} \quad (3.12)$$



Finally the scattering cross section defined by the fraction of the scattered power from the roughness feature to the total power. This can be expressed by

$$c_s = \frac{P_s}{I_0} = \frac{2\lambda}{\pi} |S|^2 = \frac{2\lambda}{\pi} \left| \frac{1}{2} \frac{(i\Delta\omega + \gamma_0)(e^{i\phi} - 1) - \gamma(e^{i\phi} + 1)}{(i\Delta\omega + \gamma_0 + \gamma)} \right|^2 \quad (3.13)$$

For lossless media (γ_0), the Equation (3-12) can be rewritten as:

$$c_s = A + \frac{\left(\frac{\Delta\omega}{\gamma}(e^{i\phi} - 1) + (e^{i\phi} + 1) \right)^2}{\left(\frac{\Delta\omega}{\gamma} \right)^2 + 1} \quad (3.14)$$

This equation resembles the modified Fano line shape formula. Here A is a frequency offset, and ϕ indicates the spectral response of the continuum which is equivalent to q parameter in Fano formula (see equation (3-1)) that quantifies the shape of the line.

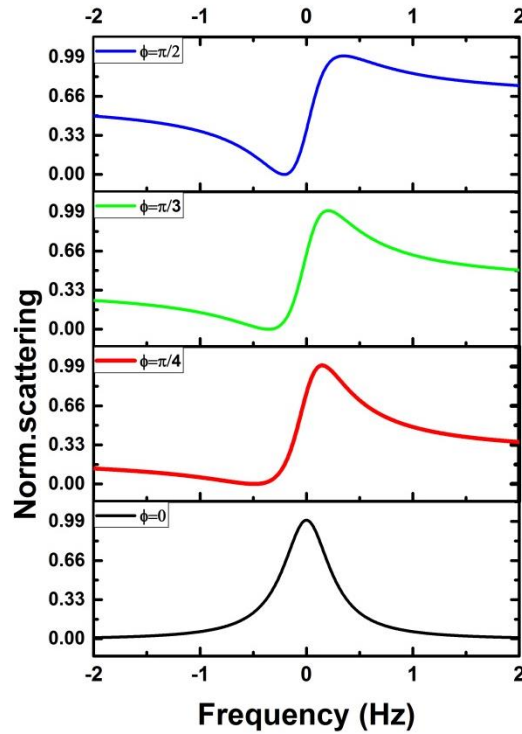


Figure 3-10 Evolution of transmitted power changing from Lorentzian to Fano asymmetric profiles.

The quantity γ and ϕ determine the coupling strength between the bound state (here core mode) and the continuum (here cladding modes). For a fixed value of the modified Fano expression (equation (3-13)) is now function of ϕ which is input polarization. Figure 3-10 shows evolution of scattering power profiles for different phase factors ϕ and at a fixed value of γ . The spectra for $\phi = 0$ Lorentzian profile and for any intermediate values, as shown in the figure, the profiles show typical asymmetric signatures of Fano resonance.

3.5 Theoretical Simulations of CL spectral structure under a scattering perturbation

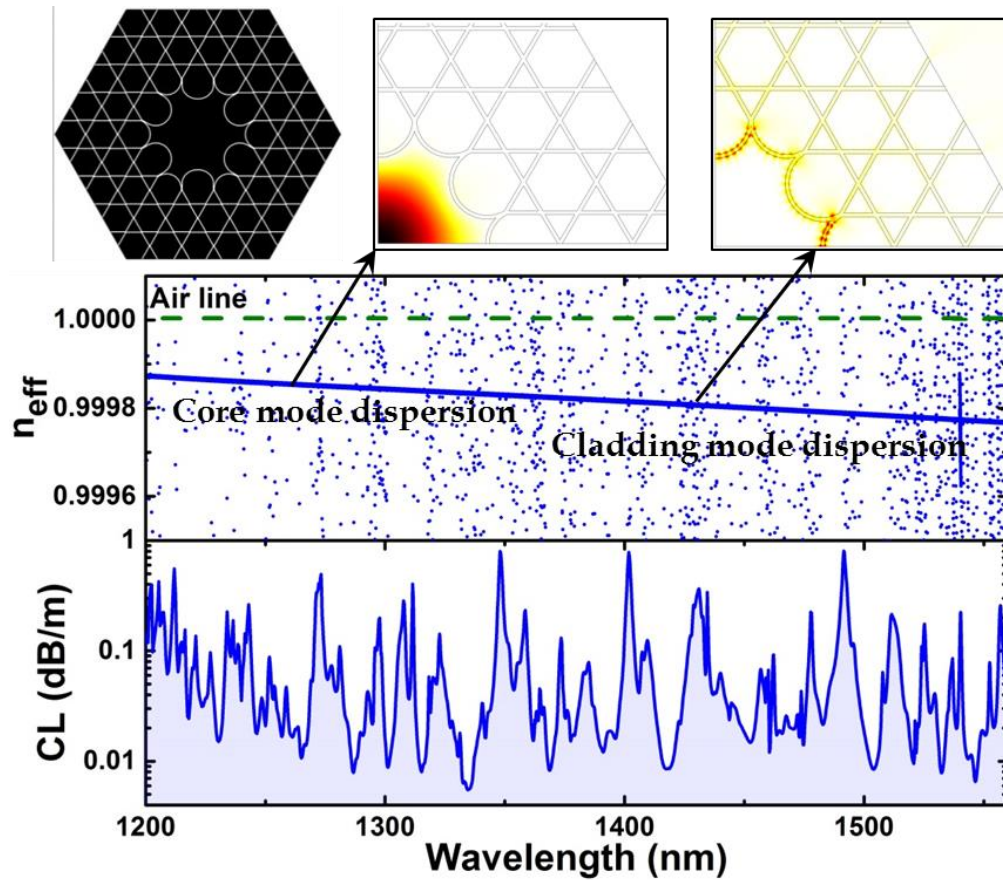


Figure 3-11 (a) Image of 7-cell IC Kagome HC-PCF model considered for the FEM simulations (b) its DOPS. (c) and (d) are core and cladding mode profiles of the fiber.

Numerical simulations were performed on 7-cell 3 ring cladding IC Kagome HC-PCFs, one with unperturbed and other with perturbed to verify Fano signatures. Then, spectral features of both fibers were compared in orthogonal polarization conditions. Figure 3-11 (a) shows SEM image of the fiber with unperturbed structural design with its DOPS and confinement loss (CL) spectra in Figure 3-11(c). DOPS reveals the coexistence of a (nearly horizontal line) core mode and highly dispersive (quasi-vertical) cladding modes. The transverse profiles of the modes of the ideal fiber confirm that the core and cladding modes do not couple at any frequency. Hence, it is once again confirmed by the transverse mode profiles as shown in the Figure 3-11 (c) and (d) that both core and cladding modes do not interact at any fixed frequency.

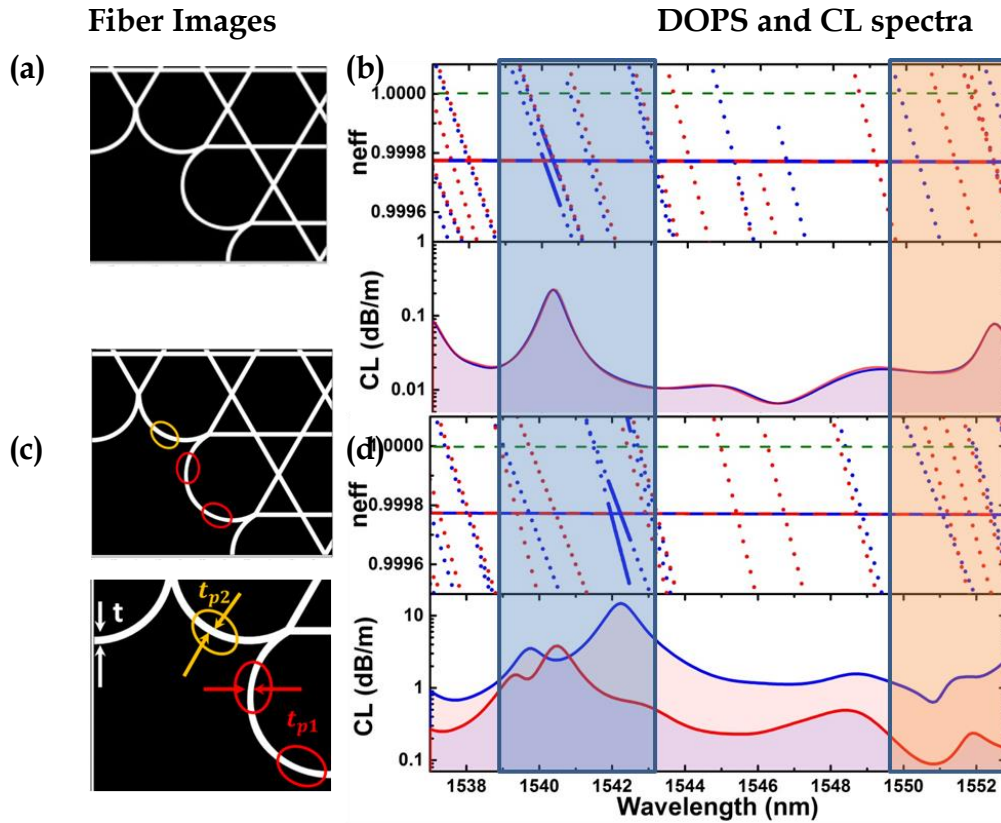


Figure 3-12 Images of the fiber models of (a) ideal and (b) perturbed fiber (scattered features are shown in yellow and red circles) considered for the simulations to compare their DOPS and CL spectra as shown in (c) and (d) for ideal and perturbed fibers respectively.

Spectra presented in Figure 3-12 compares DOPS and CL of the ideal as presented in the SEM image Figure 3-12 (a) along with its polarization dependence over a reduced spectral range. These simulations were then carried out for a structure described as "perturbed" (see Figure 3-12(b)), where diffusion zones were added to the vertices of the arcs of the contour of the core by changing the thickness of the silica struts as $t_{p1} = 920\text{nm}$ at $t_{p2} = 830\text{nm}$, to act as a coupling for the observation of Fano signatures.

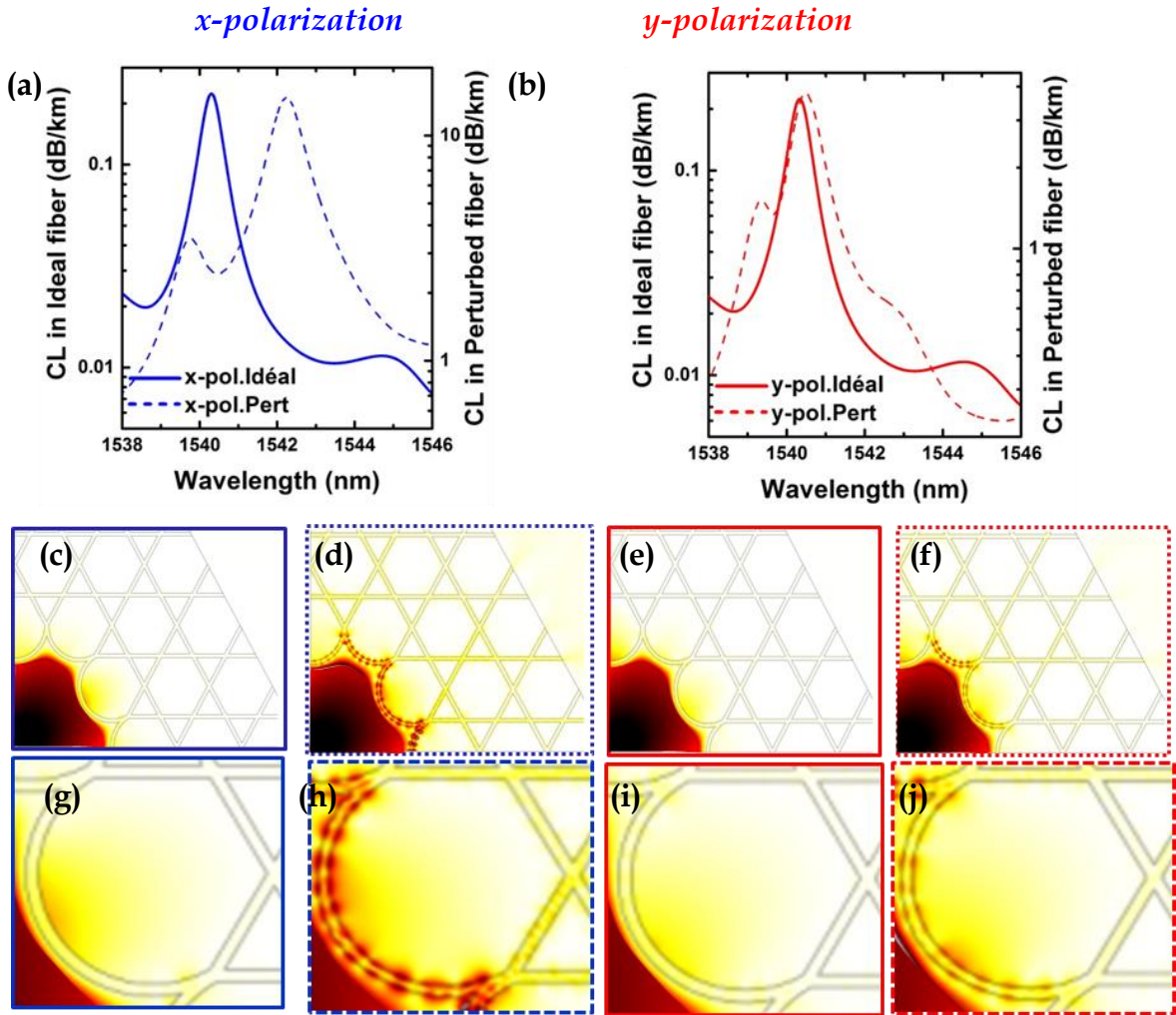


Figure 3-13 Zone-1: High-resolution spectra of the CL profiles for (a) x polarization on left (in blue color) and (b) y polarization (in red) on the right for the ideal (solid curves) and perturbed fiber (dashed curves) structures. Their corresponding core and cladding mode profiles are presented in (c)-(j).

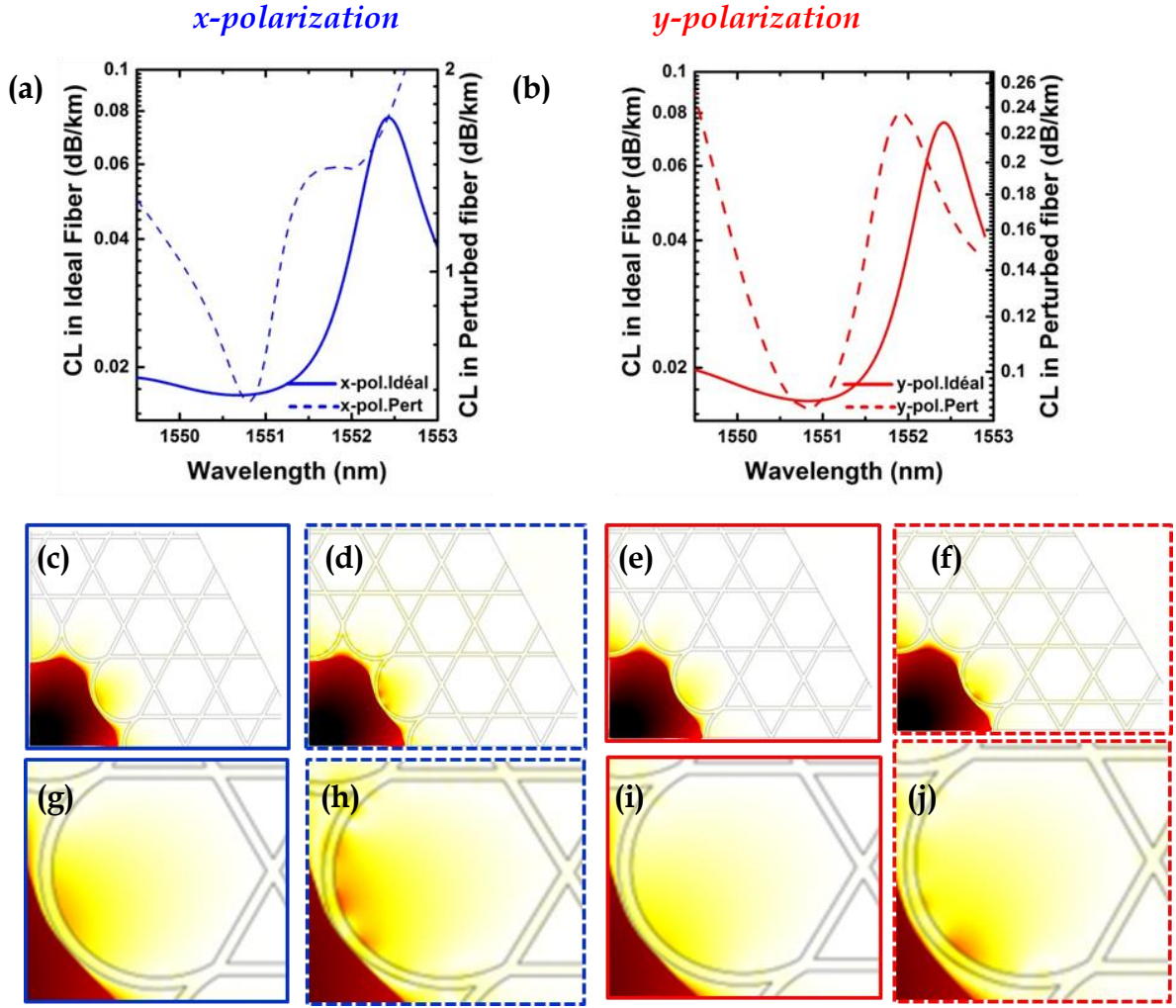


Figure 3-14 Zone-2: High-resolution spectra of the CL profiles for (a) x polarization on left (in blue color) and (b) y polarization (in red) on the right for the ideal (solid curves) and perturbed fiber (dashed curves) structures. Their corresponding core and cladding mode profiles are presented in (c)-(j).

The spectral characteristics (DOPS (dotted curves) and CL (solid curves)) of the two fibers are compared for two orthogonal excitation polarizations (*i.e.* polarization x in blue and polarization y in red). CL for ideal fiber has Lorentzian peaks corresponding resonance between core and cladding mode for y-polarization, whereas perturbed fiber shows relatively higher losses with asymmetric spectra which are nothing but Fano signatures showing BiC. Therefore, it is numerically confirmed that Fano asymmetric spectra arise due the

scattering perturbation and also dependent on polarization which predicts shape of the FR.

Figure 3-13 and Figure 3-14 summarize the spectro-modal contents for an ideal and perturbed Kagome structure compares the spectral characteristics with more resolution in Zone 1 (Figure 3-13) and in Zone 2 (Figure 3-14) on their left and right columns respectively. Loss spectra of the ideal fiber (solid curves), independent of polarization, have a Lorentzian shape, while those of the perturbed fiber (dashed curves) show typical characteristics of asymmetric Fano profiles. Fano shaped resonance of perturbed fiber exhibit shifts from 1540.3 nm (of ideal fiber) to 1542.2 nm in x-polarization, and to 1540.5 nm in y-polarization with comparatively weaker coupling than x-polarization. Their FM mode profiles for x-and y-polarizations are shown in blue ((c)-(d)) and red rectangles ((e), (f)). It is worthy to notice from Zoom in profiles ((g)-(j)) that the coupling between the discrete core mode and the cladding mode continuum takes place in case of perturbed fiber. These asymmetric spectral signatures Fano arise from the perturbation caused by the diffusion points and are dependent on the polarization.

3.6 Experimental observation of Fano resonance in Kagome HC-PCF

In order to proceed with experimental observation of the FR in the IC Kagome HC-PCF, high resolution fiber transmission technique is performed using a tunable and narrow linewidth external cavity diode laser (ECDL) source (see Figure 3-16). The ECDL is connected to a function generator with 10 Hz frequency and peak-peak voltage of $V_{pp}= 9V$ in order to fine tune the Littman configuration of ECDL for getting high resolution laser output.



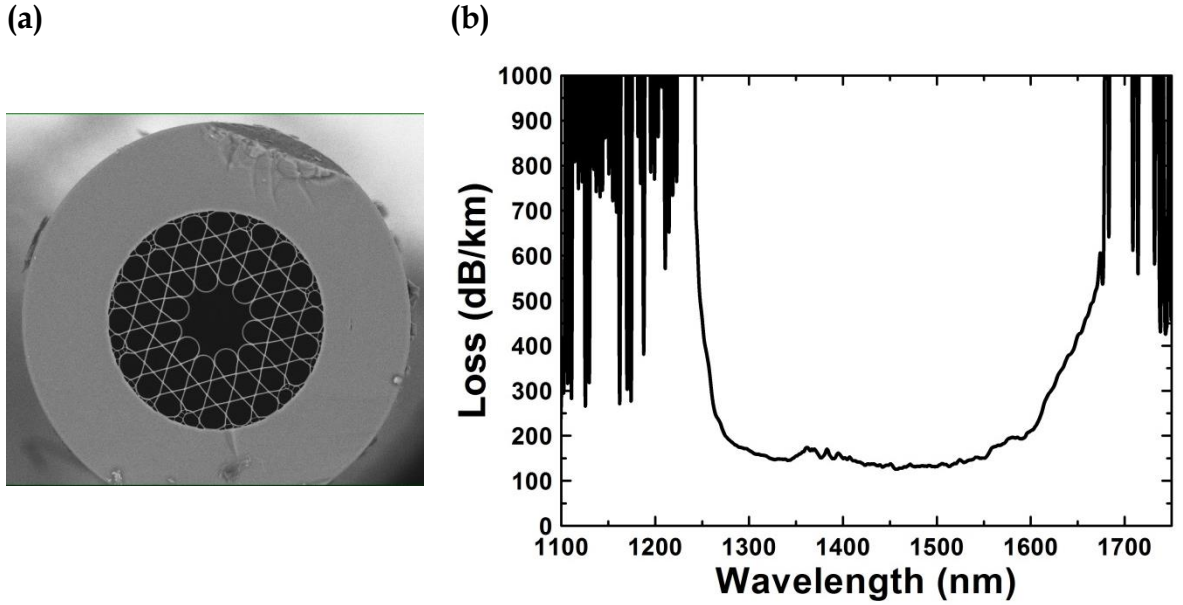


Figure 3-15 (a) SEM image of the 7-cell Kagome IC HC-PCF used for the experiment and (b) its loss spectrum.

Then, the output from laser head is split by 50/50 unpolarizing beam splitter. First beam is coupled into a 27m-long piece of Kagome fiber, after passing through the half wave plate (HWP) for input polarization control. The fiber used for the experiment is a hypocycloid-core Kagome fiber with a 7-cell core defect, presenting optimized propagation attenuation for 1550 nm region with average loss value of 150 dB/km as shown in Figure 3-15. Inset of the figure also shows the SEM image of the fiber which gives the following geometrical parameters: a pitch of 24 μm , inner and outer core diameter of 50 μm and 63 μm respectively, a curvature parameter of $b = 0.85$ and a strut thickness value of 1.2 μm . Output beam after 27 m length of the fiber is passed through GLAN polarizer to separate beams of fast and slow axis, followed by non-polarizing beam splitter to send one of the beams to high dynamic camera to record the reconstructed near-field (NF) or far-field (FF) profiles to resolve core-cladding coupling at FR whereas the rest of the beam is targeted on InGaAs photodetector-2 to record high resolution transmission spectra and its dependence on input polarization controlled by

HWP. The second beam of the input is sent to another InGaAs photodetector-1 (PD1), to be normalized with output power and hence removing any artifact in the transmission spectra due to laser source power fluctuations. Finally the output transmission spectra are normalized with respect any fluctuation at the input end.

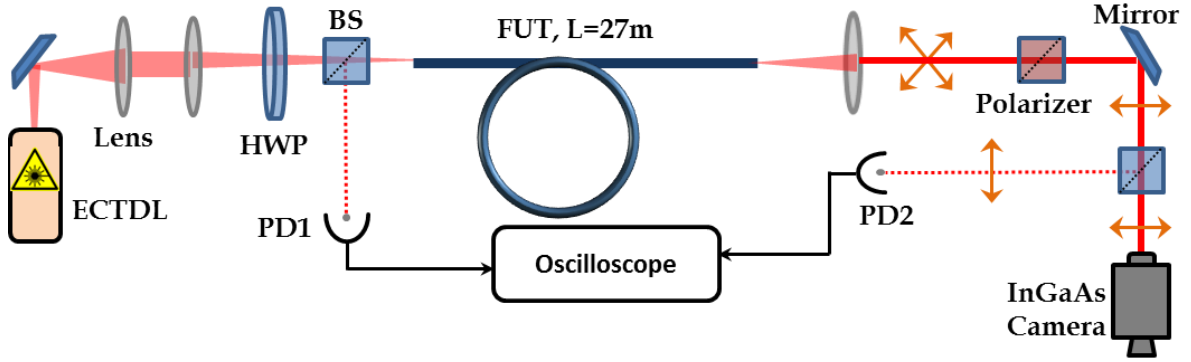


Figure 3-16 Experimental scheme with high resolution transmission set-up to explore Fano profiles in transmission spectra of 27 m length of 7-cell IC Kagome HC-PCF.

Figure 3-17 shows 50 GHz wide transmission-spectra for different input polarization states of the laser beam. The polarization is indicated by angle of the HWP. The spectra were centered at 1540.09 nm and normalized to the reference transmission spectrum. The curve clearly shows a polarization-dependent resonance-like spectral structure, and with an asymmetric-shaped as expected for the Fano resonance. The high typical contrast of $\sim 35\%$ of these traces, and as NF and FF profiles rule-out meaningful core inter-modal beating effect. Figure 3-17 (b) shows representative NF and FF for different points from the explored 50 GHz spectral span from the central wavelength. It clearly shows, within the 140 dB dynamic range of the imaging camera, that both NF and FF indicate no observable higher-order mode, and that any inter-modal beating with the core would have less than 2% oscillation depth in the transmission. Furthermore, the FF images at the frequency indicated by the label (2) clearly show the coupled power to the core surround.

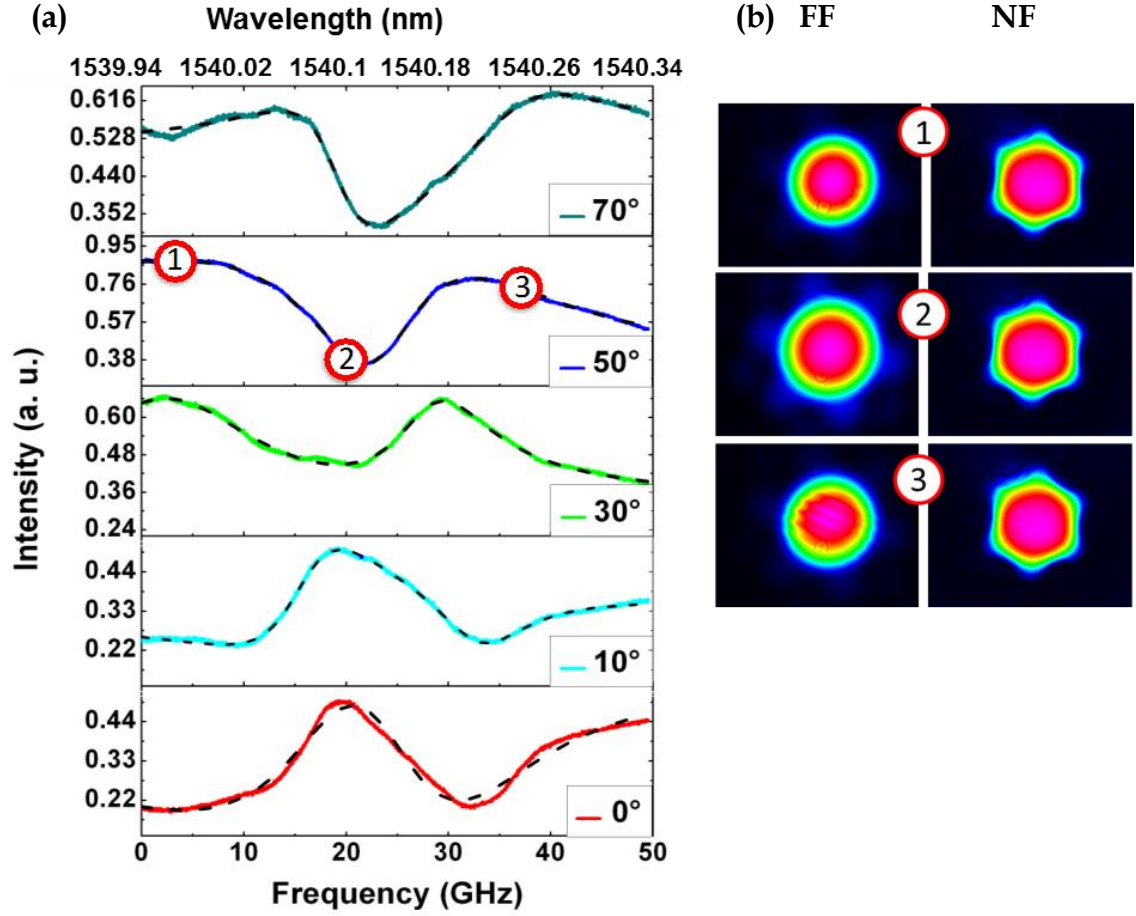


Figure 3-17 (a) Experimental transmission profiles recorded at the 15m-long fiber output at 1540.09 nm for different polarization angle. The fitting curves are superposed in dash curves; (b) NF and FF images recorded at the fiber output at three different points of the 50 GHz spectral span for the case of 50° angle;

A further investigation on the nature of these traces was done by fitting the logarithm of the traces to Fano modified Lorentzian equation:

$$\sigma = A + \left[\left(\frac{\omega - \omega_0}{g} + q \right)^2 / \left(\left(\frac{\omega - \omega_0}{g} \right)^2 + 1 \right) \right] \quad (3.15)$$

Here A is a frequency offset, ω_0 a resonant frequency, g is the width of the resonance and q indicates the spectral response of the continuum. Both g and q determine the coupling strength between the bound state (here core mode) and the continuum (here cladding modes). Furthermore, these parameters strongly

alter the spectral profile to go from a Lorentzian peak to S-shaped line by changing q from $|q| = \infty$ to $q = 0$. Interestingly, in our case this coupling strength can be altered by changing the polarization of the core mode, and thus giving further data. The fitted curves are presented in dashed lines in Figure 3-18.

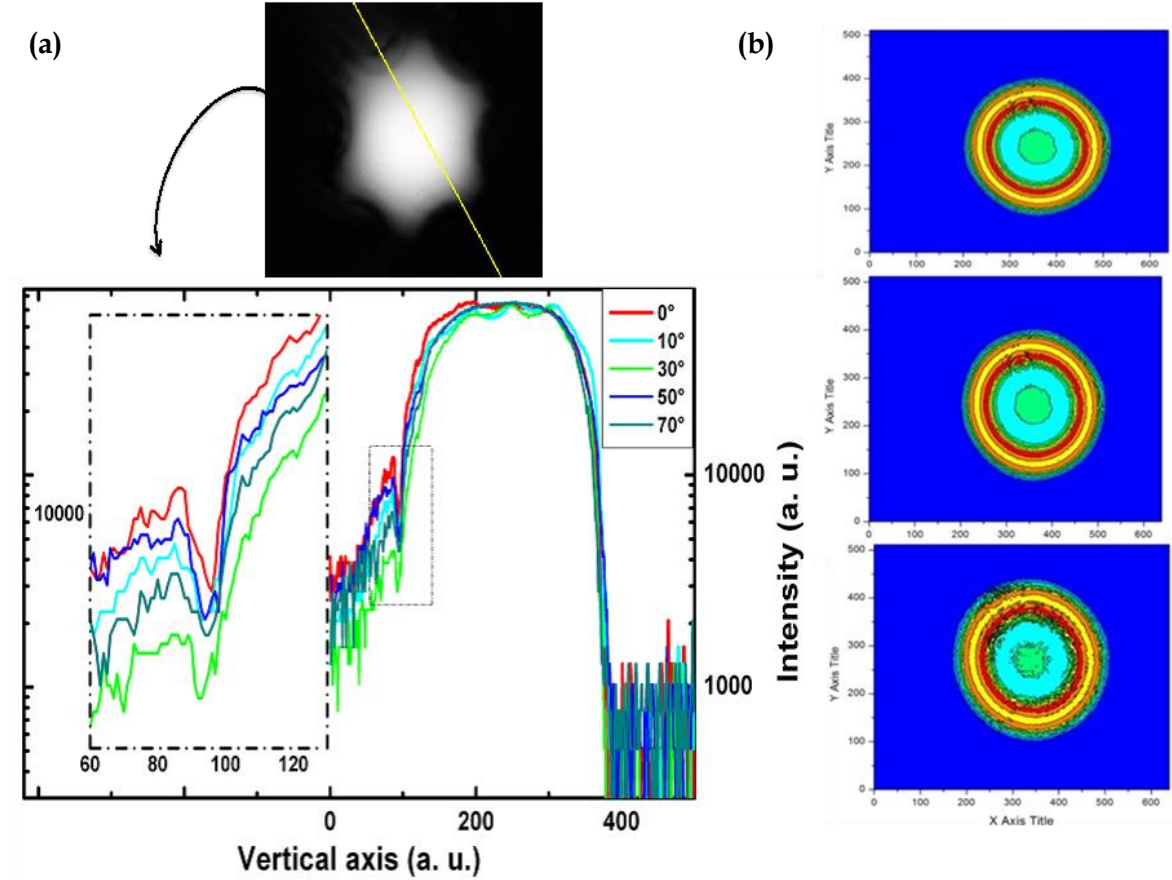


Figure 3-18 (a) Near field image and its profiles reconstruction in high dynamic range for different input polarizations. (b) Image profiling of far fields.

These high resolution transmission profile obtained around 1540.9 nm are well fitted to the scattering cross section profiles obtained by temporal CMT for each polarization as shown in Figure 3-10. Similar results were also observed at other wavelengths. In addition, near field images were processed to get information about interactions between the core modes (discrete) and cladding

modes (continuum) at the specified resonant wavelengths. Figure 3-18(a) shows one of the NF images recorded at the output beam for each input polarization states and their beam profiling along a given cross-line (yellow line in the inset of the NF). The zoomed-in profile in the inset gives the strong experimental evidence core-cladding resonance where the transmission spectra become more pronounced. As shown in Figure 3-18(b), intensity distribution of FF images resolves core-cladding coupling due to the perturbation.

3.7 Summary

To conclude, Fano resonance phenomenon was investigated in hypocycloid-core Kagome fibers and hence proved IC guidance as photonic manifestation of Q-BiC. Asymmetric-shaped Fano profiles were found with a bandwidth of 30 GHz in high resolution transmission spectra. Such experimental observation has been brought out by the accurate comparisons of the Fano profiles and NF evolution versus the polarization of the input.



Chapter 4

Experimental linear characterization of IC HC-PCFs

This chapter presents linear characterizations of IC HC-PCF design by optimizing its structural features as per guidelines outlined in Chapter 2. It firstly discusses improvements of guidance in Kagome HC-PCF based on silica struts and hollow-core shape optimizations in order to realize 7-cell Kagome HC-PCFs with reduced losses down to a level of 8.5 dB/km at 1 μm and 30 dB/km at 780 nm. The second section presents simulations, fabrications and characterizations of a new tubular lattice (TL) fibers based on cladding optimization. One of these fabricated sing ring TL IC HC-PCFs demonstrates record transmission loss of 7.7 dB/km at 750 nm (just 4 dB below the Rayleigh scattering limit) and second fiber with an ultra-large transmission band covering one octave with losses ranging between 10 to 21 dB/km. These results indicate that the prospect of guiding light with transmission loss lower than the limit set by the ubiquitous silica Rayleigh scattering is now possible and opens also a route to demonstrate low-loss guidance in the UV/DUV region.



4.1 Introduction

Since the development of hypocycloidal core shaped Kagome IC HC-PCF to further enhance IC between core and cladding resonances in 2010 [49], several fibers of this class have been realized and reported with dramatic loss reduction in different spectral ranges. For example, we have seen that (in chapter 2), hypocycloid core curvature dramatically reduces the loss and it can be further reduced by increasing negative curvature parameter b . As a result a hypocycloid core shaped Kagome IC HC-PCF with loss of 17 dB/km was demonstrated, but in a narrow operating 3 dB-bandwidth of 10 nm around 1 μm which is preferential wavelengths range in laser micro processing and high power applications [49]. High power laser handlings of IC HC-PCF could be raised by enlarging effective area of hypocycloid core with 19-cell defect design, but at the cost of increased higher order modes and bending sensitivity. In this context, it is desirable to reduce attenuation of such fiber further down, whilst keeping the same delivery performances. Also, Broadband and low-loss transmission HC-PCF guidance is also needed to address tuneable laser applications. Theoretically, and especially in opposition to the photonic bandgap HC-PCF, the IC guiding HC-PCF is the ideal means to cover with an uninterrupted transmission spectral range from the UV to the IR. However, the use of relatively thick silica struts for optimum hypocycloid core-contour resulted in several transmission bands delimited by poor-guidance cut-off regions and inherent fluctuations with thinner struts due to noise during the fabrication process imply the broadening of the cut-off regions and so an increase of the transmission loss [88]. Consequently, to extract the quintessence of the IC mechanism and to answer such a call, the ideal structure of IC HC-PCF will be to get the thinnest strut with the strongest curvature of the core.



As we have examined from the simulations in Chapter 2, and from the previous report [49], the hypocycloid shape parameter b , and strut thickness of the core contour play vital role in improving IC guidance. Firstly, larger parameter b supports the fiber for achieving high azimuthal like number. Secondly, thinner struts would shift cut-off wavelength towards shorter wavelengths thereby enlarge transmission windows. Therefore, combining and optimizing these two design parameters of IC fiber we would theoretically predict a fiber with low loss and broader transmission by making thinner struts below 700 nm and b nearly 1. But there is always a compromise when it comes to bring the idea into reality as the drawing of such thinner with stronger b is extremely challenging because of rheological limitations during fabrication. Also, thinner silica struts would not sustain for stronger b . Such limitations would hurdle the guiding properties more dominantly in high frequency regimes. Besides, connecting nodes of Kagome cladding design also limit the fiber performances. An alternative cladding design to get rid of such limitations has been inspired from previous works on single ring TL fibers [57] [58] [59] which provides absence of connecting nodes in the cladding and thanks to the design for well pronounced hypocycloid core shape that favours IC.

Each fabricated IC HC-PCF is intended to be used for specific applications at different wavelengths and in different scientific environments. For example IC HC-PCFs which are currently used in wide range of application including high power laser delivery has to be flexible and robust; meaning that it should be highly immune to any bending that occurs during the applications and to sustain for USP with minimum loss coefficients. Also in nonlinear applications like plasma generation and frequency comb generation IC HC-PCFs are used to host Raman active gases. Any disturbance in guiding properties of the fiber including laser beam quality, dispersion and polarization capability can affect the result of



the experiments. Therefore, after fabrication every IC HC-PCF shall be optically characterized to determine its suitability for desired applications. In this context, the first part of this chapter demonstrates fabrication and linear characterization of optimized 7-cell Kagome latticed fibers. Theoretical simulation of these fibers will be discussed in Annexure A and Annexure B will provide complete discussion about 19-cell enlarged core Kagome IC HC-PCF for high power laser delivery. The second part discusses about optimization of tubular cladding design and linear characterization of single ring tubular latticed IC HC-PCFs.

4.2 Experimental setups for linear characterizations of IC HC-PCF

This section describes measurement techniques to characterize the linear optical properties of IC HC-PCFs including their transmission loss, bending loss, polarization extension ratio (PER), spatial and spectral (S^2) imaging and M^2 measurements. The results obtained by these techniques will be presented in the coming section where we will analyze and assess the optical properties and capabilities of the fabricated fibers.

4.2.1 Transmission studies by cut back method

The most common linear characteristic of any optical fiber is the transmission spectrum and its loss spectrum. As presented in experimental set-up in Figure 4-1(a), a white light generated by injecting a monochromatic light at 1064 nm through a highly nonlinear supercontinuum (SC) fiber. Such SC source [89] provides sufficient spectral power density over broad spectrum to allow 0.05 nm wavelength resolution measurements with optical spectrum analyzer (OSA-Ando AQ-6315A) even with moderate fiber attenuation. The OSA records spectral ranges from 350nm to 1750nm with large power dynamic range (>100 dB) and



sensitivity (-90 dBm) a resolution of 1 nm. Firstly, a reference transmission spectrum is recorded at the output the test fiber by the OSA. Fibers under consideration must be of tens or hundreds of meters in length to get rid of any higher order mode (HOM) at the output end. Then, without altering input coupling part, the fiber is cut-back by few meters and transmission out of the remaining fiber is recorded. Let us consider the transmission amplitude of longer length (L_1) and shorter length (L_2) after cut-back recorded as P_1 and P_2 respectively. Then transmission loss per unit length of the fiber is measured by the following expression:

$$\alpha_{total} = \frac{10}{(L_1 - L_2)} \left[\log \left(\frac{P_1}{P_2} \right) \right] \text{ dB/m} \quad (4.1)$$

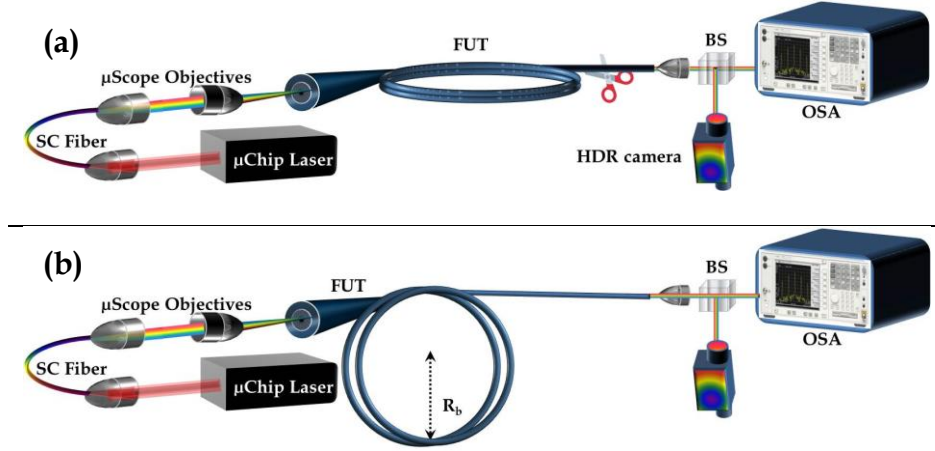


Figure 4-1 (a) Experimental set-up for to measure transmission and (b) for measuring macro-bending loss spectra of FUT (IC HC-PCF).

In general the measured transmission loss co-efficient α_{total} in hollow core fibers is a combination of confinement loss (CL), bending loss (BL) and surface scattering losses (SSL). Therefore, the measured loss can also be written as:

$$\alpha_{total} = \alpha_{CL} + \alpha_{BL} + \alpha_{SSL} + \alpha_{abs} \quad (4.2)$$

Here the subscripts represent respectively origins of the losses (*i.e.* bending and scattering loss) which will further be investigated in upcoming sections to

quantify their weights on total transmission loss. α_{abs} in the above equation represents absorption loss by silica material (in our case, it should be negligible).

4.2.2 Macro bending loss analysis

Core guided modes in IC HC-PCF are leaky by nature and sensitive to any sharp bends which deform the fiber structure. As a result local effective index vary sharply depending on the strength of the perturbation which is even more dominant at shorter wavelengths. Theoretical model predicts the bend losses increase at critical bend radius R_{cr} and follow exponential like trend with the radius at any specific wavelength within the transmission window. The experimental set-up as shown in Figure 4-1(b) investigates fibers' bending sensitivity. Firstly, transmission is recorded from the output a long section of FUT in almost straight configuration or in large bending state with radius $R_{ref}=80$ cm. Then, without altering the input coupling, the bending of the FUT is decreased which is then followed by recording the transmission spectra. Finally, the α_{BL} is deduced per each turn:

$$\alpha_{BL} = \frac{10}{N} \left[\log \left(\frac{P_{ref}}{P_b} \right) \right] \text{ dB/turn} \quad (4.3)$$

here N is number of turns of loop and P_{ref} and P_b are the powers at reference configuration and in bent state of the fiber.

4.2.3 Polarization extinction ration (PER) and M²

Conventional polarization maintaining (PM) optical fibers guide linearly polarized wave and maintain its polarization state throughout the fiber transmission length. This is done by having a preferred axis and thus creating a strong birefringence between the two orthogonally polarized states of the guided mode. In case of IC HC-PCF, there is no preferred axis, however, it can exhibit a



strong PM capabilities if the environmental perturbation (e.g. bends) or microstructural defects inherited during the fabrication are insignificant. PM is important properties in a number of applications where the polarization fluctuations are undesired. The PM property of IC HC-PCF can be quantified by measuring the extinction ratio which is defined as ten times the logarithm of the maximum light intensity along direction of polarization divided by the minimum light intensity perpendicular to the direction of polarization (see equation 4.4(a)). In this regard PER of IC HC-PCF has to be investigated using the optical scheme as shown in Figure 4-2(a). A GLAN polarizer and a half wave plate are placed between collimation and injection part of the input to allow a input laser in single polarization state. The FUT is looped with large bend radius around 40 cm to avoid bending effects on the measurements. Finally, the output beam of FUT is passed through polarizing beam splitter (PBS) to split into two orthogonal polarization compositions (fast axis and slow axis of the output beam). Beams from both orthogonal axes are directed to record its spectra and near field imaging for each polarization states. PER is measured by using the following expression:

$$\text{PER} = 10 \left[\log \left(\frac{P_x}{P_y} \right) \right] \text{dB} \quad (4.4(a))$$

where P_x and P_y powers of the beams along fast axis and slow axis respectively.

Apart from measuring PER, this experimental scheme also allows to assess beam quality factor, M^2 of output beam by using PHASICS camera. M^2 is a parameter that is often used to assess the transverse modal quality of a laser beam, and is calculated by taking the ratio of the measured beam mode field diameter to that of Gaussian TEM_{00} mode. For a Gaussian TEM_{00} laser transverse mode we have $M^2 = 1$.



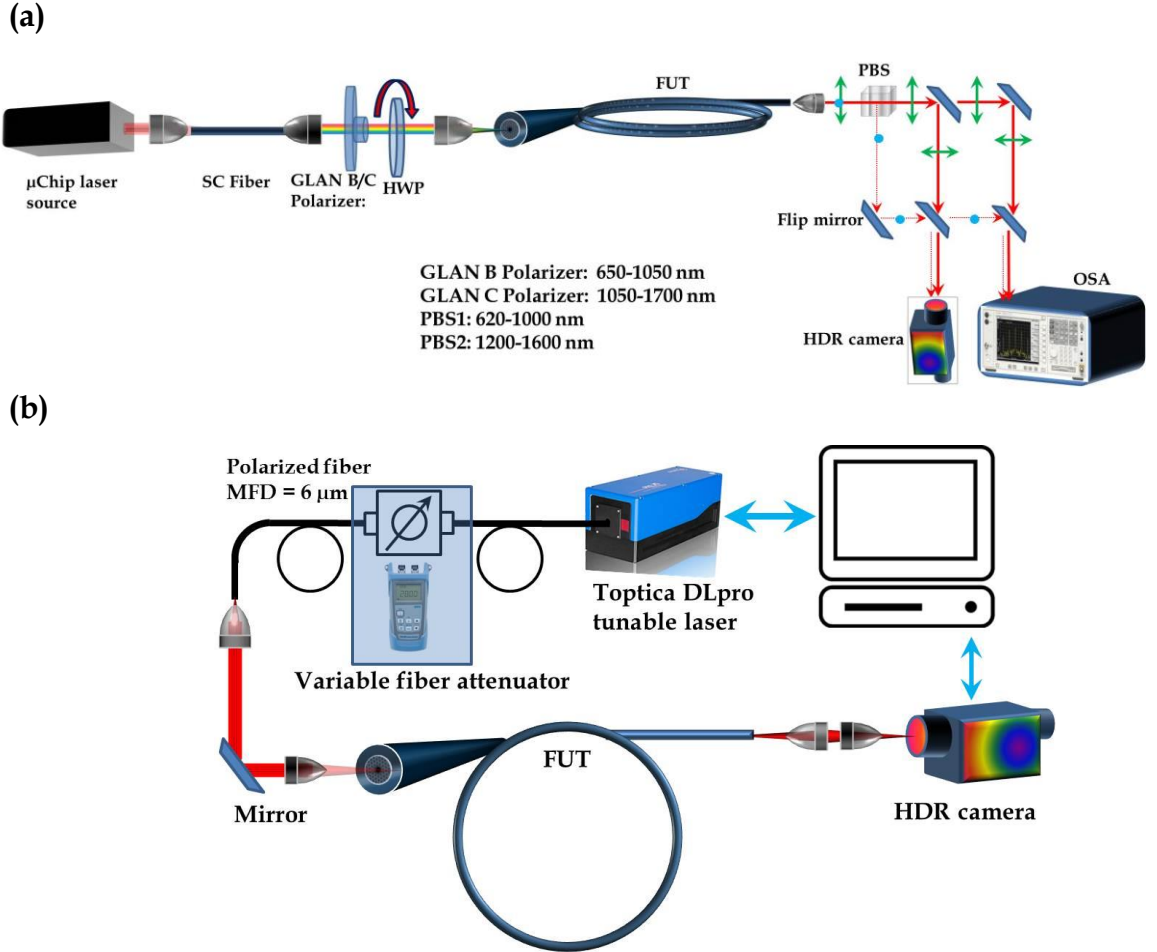


Figure 4-2 (a) Experimental set-up to measure PER and (b) and S^2 imaging.

In the case of a single mode fiber, the transverse mode of its guided mode is sufficiently close to a Gaussian, and thus we use M^2 to assess the modal content of the fiber guided laser beam. An approximate M^2 expression is given below:

$$M^2 = \frac{\omega\theta}{\omega_0\theta_0} \quad (4.4(b))$$

where ω and θ are the actual laser beam waist and divergence respectively. The quantities ω_0 and θ_0 are the expected waist and divergence when a Gaussian beam with a TEM_{00} transverse profile is used in the same experimental condition as the measured beam.

4.2.4 Spatial and spectral (S²) imaging

Increasing core size of IC HC-PCF is beneficiary in several ways: for example to reduce impact of scattering, to operate the fiber at high power USP and finally to mitigate nonlinearities. Consequently such large mode area (LMA) fibers increase higher order modes which travel at different group velocities and result in modal interference called multi-path-interference (MPI) [90]. This phenomenon degrades the output beam quality and thereby fiber's optical performances. Therefore, it is customary to characterize modal properties and total power distribution among the modes allowed inside the core of the fabricated IC HC-PCFs by quantifying relative power distributed among fundamental mode (P_1) and HOM (P_2) on a dB scale, which can be expressed as:

$$MPI = 10 \left[\log \left(\frac{P_1}{P_2} \right) \right] \text{ dB} \quad (4.5)$$

During the experiment FUT is coiled with 35 cm radius and the output is sent to a high dynamic range camera. The laser source and the camera are connected to a computer in order to trigger the laser and also for image processing and its Fourier transformation with specific code developed to compute MPI. These measurements of MPI are carried out based on spatially resolved measurements of the spectral interference among coherent modes propagating with different group delays in the FUT; hence it is called as spatially and spectrally resolved mode (S²) imaging. Figure 4-2(b) shows the experimental set-up of S² imaging to measure MPI between fundamental mode (HE₁₁) and higher order modes (HOMs) in FUT. Toptica DLpro tunable fiber laser with spectral ranging from 1010-1080 nm with wavelength step 40 pm is injected into FUT after passing through variable fiber attenuator (see Figure 4-2(b)).



4.3 Linear properties of ultra-low loss (8.5 dB/km at Yb-laser region) Kagome IC HC-PCF for laser beam delivery applications

Ultra-short pulse (USP) lasers with sub-picosecond and Giga-Watt peak-power level optical pulses are now available in compact tabletop and turn-key physical packages. IC HC-PCF has proved to be an excellent fiber for guiding USP with low attenuation and low temporal and spectral distortion. Previous state-of-the-art fiber with 7-cell, 3 cladding rings IC HC-PCF with the strut thickness $t = 1400$ nm, could transmit light at $1 \mu\text{m}$ with the loss figure down to 17 dB/km at $1 \mu\text{m}$ [49] in the second higher-order band. Since its strut was thick enough, it could withstand for arc curvatures as strong as $b = 1$. Thinning the struts for broadband transmission consequently induces surface roughness due to enhanced capillary waves due to noise at fabrication stage. This in turn creates a nonuniform struts which increase the cut-off regions and surface scattering losses (SSL) especially at shorter wavelengths, which again limits the transmission bandwidth.

The resulting fiber has demonstrated transmission for Yb and Nd:Yag laser beam delivery applications exhibiting record loss level of 8.5 dB/km at 1030 nm associated with a 225 nm wide 3-dB bandwidth and with low bending sensitivity. Compared to the current state-of-the-art fiber, this new loss of the fiber is decreased further down by a factor of 2. Finally, the modal properties (S^2 and PER) have been studied over the length of the fiber with a quasi-single mode operation.

4.3.1 Fiber design and fabrication

Because of growing demands of most of high power laser and tunability, we aim to increase the transmission bandwidth and to decrease loss levels of earlier state-of-the-art fiber further down by thinning struts and preserving its



stronger core curvature. But achieving both parameters at their best is challenging due to fabrication limitations. By maintaining the optimum drawing parameters, we could fabricate a 7-cell Kagome IC HC-PCF (see Figure 4-3 (s)) with negative core curvature as strong as $b=0.95$ and with possible thinner struts with $t= 835$ nm as shown in (b) and (c) of the same figure .

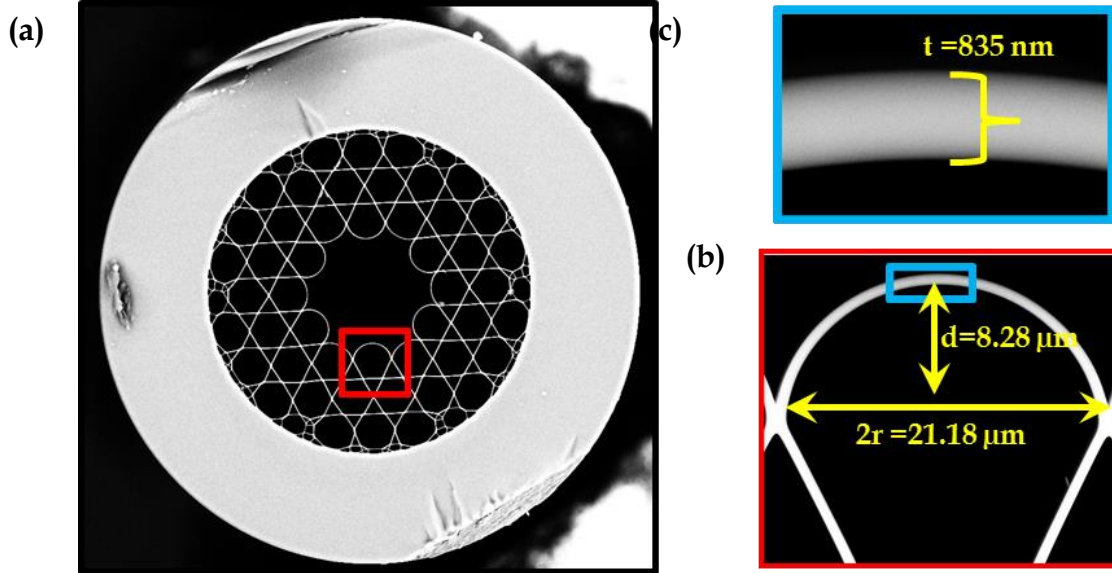


Figure 4-3 (a) SEM image of the fabricated fiber and its arc curvature shown in red square is shown in (b) along with parameters. (c) Shows micrograph of its strut with thickness of 835 nm.

4.3.2 Transmission loss characterization

The fabricated fiber is expected to have cut off regions as per the equation:

$$\lambda_j = \frac{2t}{j} \sqrt{n_{gl}^2 - 1} \quad (4.6)$$

where j is an integer related, n_{gl} is the refractive index of the glass forming the cladding structure and t is the thickness of the glass web which is assumed to be uniformly constant throughout the cladding structure. The equation (4.6) tells that thinner the struts smaller the cut off wavelength, *i.e.* the transmission band will be extended in the fixed visible-infrared windows.

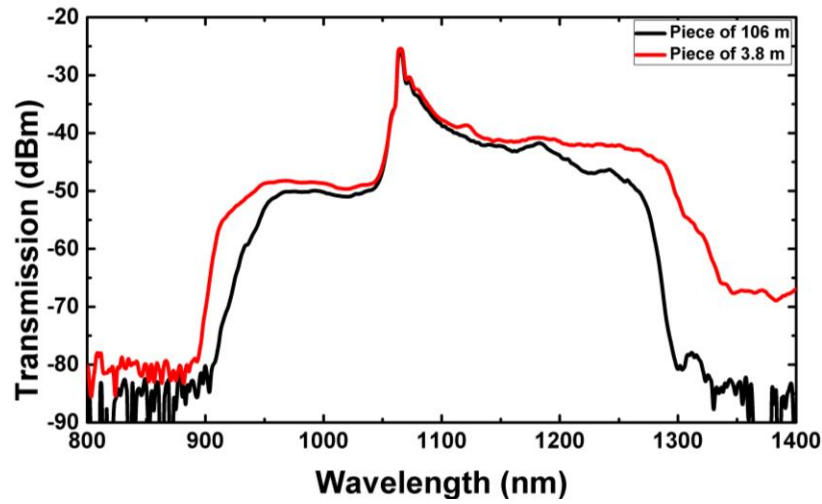


Figure 4-4 Transmission spectra for 106 m (black line) and 3.8 m (red line) lengths of the fabricated fiber of the fiber shown in black and red curves respectively.

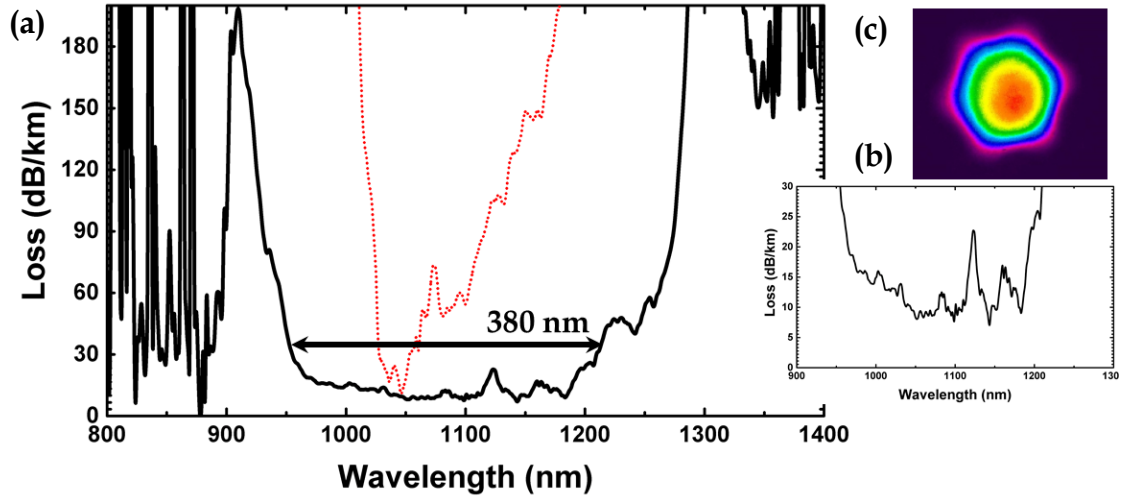


Figure 4-5 (a) Loss spectra curves of the fabricated fiber (black solid line) and its comparison with the current state-of-the-art Kagome IC HC-PCF (red dotted line) [49]. (b) Shows the zoom of the experimental and loss spectra. (c) The near field image recorded at the fiber output at 1030 nm.

Figure 4-4 shows broadband transmission through fabricated fiber pieces of 106 m as shown in black trace and a piece of 3.8 m in orange dotted trace. Measured loss spectrum in second band of the fiber (see Figure 4-5(a)) shows minimum loss levels below 10 dB/km at 1064 nm and especially record level loss 8.5 dB/km at 1030 nm with single mode guidance as shown in Figure 4-5 (b). It is also noteworthy that such low loss region extends up to larger range of wavelengths from 1000 nm to 1200 nm (3dB-bandwidth) which proves the fiber

suitable for Yb and Nd:Yag laser beam delivery applications. The loss spectrum also showed gray shaded spectrum to compare and highlight the improved performance of the present fabricated fiber with that of earlier record fiber of 17 dB/km losses at 1064 nm that was limited by 10 nm bandwidth.

4.3.3 Bending Analysis

Bending sensitivity of the fabricated fiber has been investigated especially at 1030 nm where the fiber is aimed to have record level transmission properties. Following the experimental procedure as discussed in section 4.2.2, a piece of 10 m long is used for macro bending analysis. First of all, the reference transmission spectrum is recorded to check the relative losses with bending cases. The fiber is looped with bend radius $R_{ref} = 40$ cm for reference spectra provided there are no noticeable losses with this configuration. Then measurements are followed by bending the FUT with $R_c = 2.5, 5, 7.5, 10, 15,$ and 20 cm and loss spectra relative to R_{ref} are presented in Figure 4-3. To avoid any uncertainties during the measurements, the fiber is coiled into multiple loops each time to increase the sensibility. More importantly, care is taken to carry out the experiment under single mode operation. Figure 4-6 shows the evolution of transmission loss spectra for different bend radius. Figure 4-7 shows minimum bend loss for different bend radius at a representative wavelength from the center of the transmission band chosen to be 1064 nm. The results show that when the fiber is bent with a bend radius of 20 cm, the noticed bend loss is 0.2 dB/turn, whilst it is exponentially increased up to 2.5 dB/turn for bend radius down to 2.5 cm as expected by the numerical analysis. Notice that these values are fully compatible for beam delivery applications. Near field images (Figure 4-9) confirm the stronger immunity of fundamental mode for bending by showing the persistence of single mode propagation of the fiber even at low bend radius.



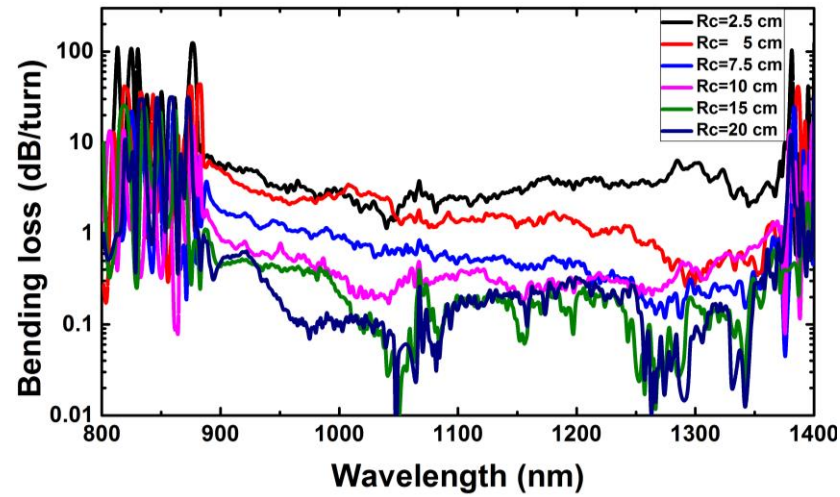


Figure 4-6 Evolution of transmission loss for different bending radii.

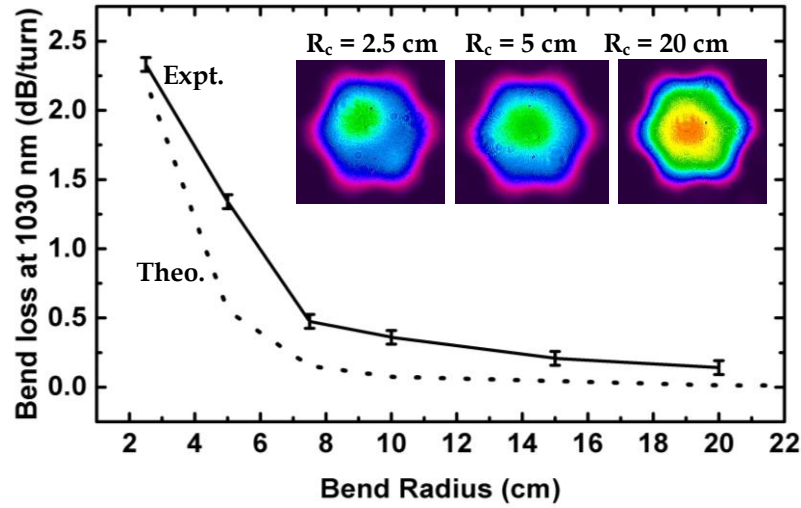


Figure 4-7 Evolution of experimental (solid black line) and theoretical (dashed black line) bend loss with bend radius at 1030 μm along with corresponding near fields bend radii at $R_c = 2.5$ cm, $R_c = 5$ cm and $R_c = 20$ cm.

4.3.4 PER

The modal performances of the fiber were investigated at 1030 nm. First, the polarization extinction ratio (PER) has been measured over the fiber length. For this part, a linearly polarized laser emitting at 1030 nm was launched into the fiber associated with a half-wave plate for polarization control. The output beam passes

through a polarizing beam-splitter (PBS) and each of its components *i.e.* x axis beam and y axis beam are recorded by a power-meter and by camera.

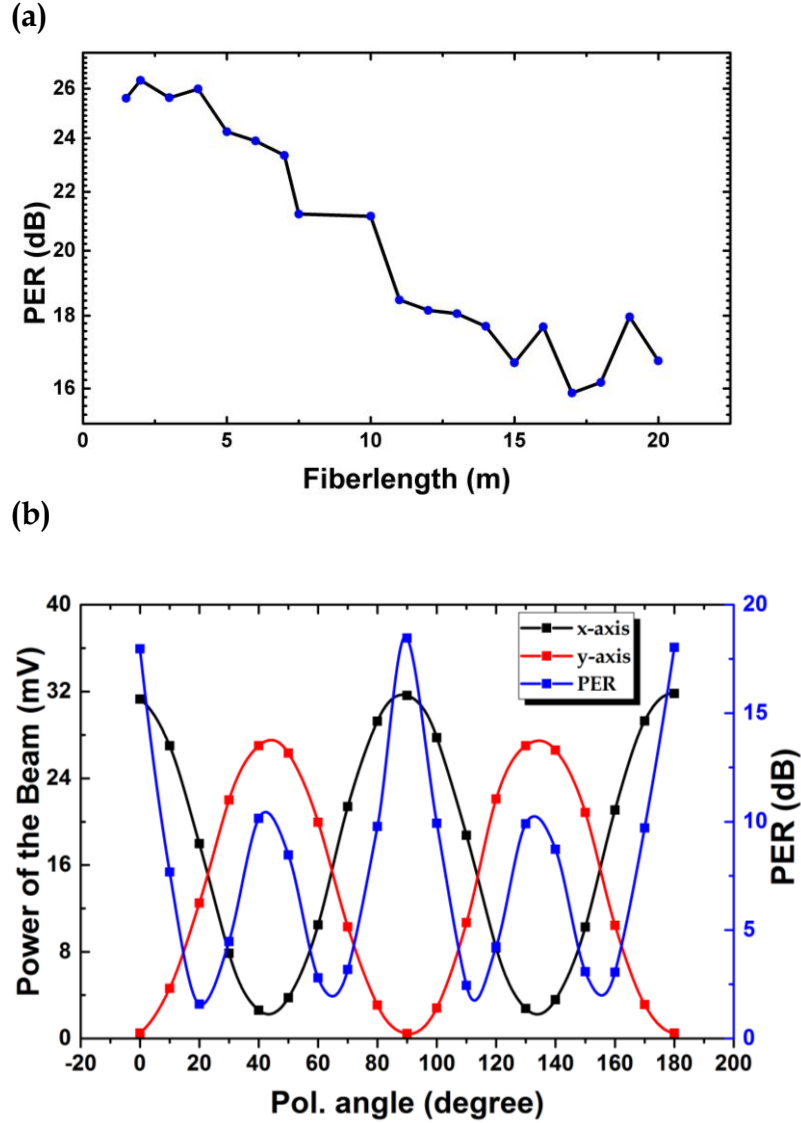


Figure 4-8 (a) Evolution of the PER versus fiber length. (b) Periodic variations of PER (blue line) versus input polarization angles at 1064 nm for a fixed fiber length at 19 m. Black and red lines represent power variations of x-axis beam and y-axis beam respectively.

PERs of the test fiber for different lengths are presented in Figure 4-8(a). The test fiber of 20 m is cut-back by every one meter and at the same time care has been taken to not alter input light launching during the measurement. We can notice that the evolution of PER is almost linearly reduced with increase of the

fiber length with the rate 0.6 dB/m. But as per the theory, PER must increase with the fiber length because of the suppression of HOMs. However, we suspect this uncommon trend of PER could arise because of the presence of additional surface scattering effect. Therefore, the evolution could be the result of back-coupling of surface scattering light from inner core surface roughness to HE_{11} core guided mode. Very importantly, the results indicate a maximum PER of 26 dB for a fiber length of 2 m which is not very far from a standard polarization maintaining fiber. The measured PER values are further confirmed by observing its periodic trend with input polarization. Figure 4-8 (b) shows that the fiber of 19 m length demonstrated the periodic variation of PER with maximum value of 18.5 dB with polarization angles of input light.

4.3.5 S² imaging

The S² imaging system comprises an InGaAs camera and a tunable laser source with a tuning range of 1010-1070 nm and a minimum step size of 40 pm. At the output of the fiber, a telescope is used to collect the light recorded by a camera, which is triggered directly from the laser and controlled by a computer. For a 5 m-long fiber spooled with a 25 cm bend radius, the LP_{11} mode presents a multi-path interference (MPI) of 20.2 dB which corresponds to a quasi-single mode operation (see Figure 4-9). Power contribution of the seventh mode (similar to the LP_{02}) is found slightly superior which is attributed to the direct impact of the input laser beam quality, whereas the power at the fiber output is found superior to 95% of the light injected. Reducing the loop radius of the fiber down to 7.5 cm permits to eliminate this LP_{02} while keeping the same MPI for the LP_{11} mode.



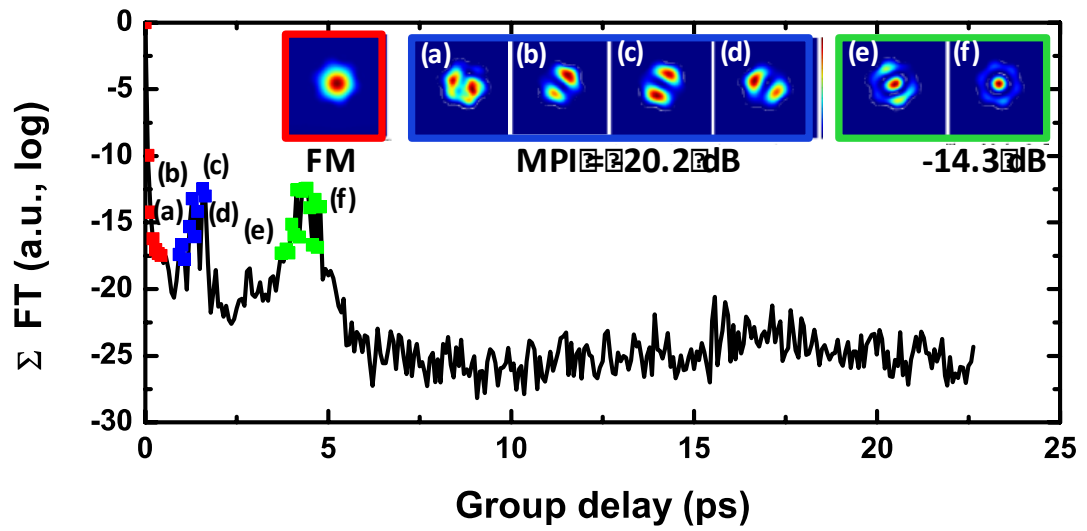


Figure 4-9 Measured group delay curves of propagating modes through a 5 m long fiber. The reconstructed mode field profiles are indicated at the corresponding MPI.

4.4 Linear properties of low loss (30 dB/km at 780 nm) Kagome IC HC-PCF with ultra-broad fundamental band

This section reports fabrication and linear characterization of a 7-cell hypocycloidal-core Kagome fiber exhibiting a larger transmission band (here working in the fundamental band) spreading down to 670 nm and able to cover the entire Ti:Sa, Yb and Er laser spectral ranges. A record propagation loss is demonstrated with a minimum value of 30 dB/km at 780 nm. The fiber shows a low bending loss over a large part of the fundamental band combined with a PER levels up to 15 dB.

4.4.1 Fiber fabrication and transmission

As shown in the left panel of Figure 4-10 cross sections of fabricated fibers with different b , core radius and with decreased strut thickness with an aim to extend the positions and to shift the cut-off wavelengths toward shorter regions, so that transmission band becomes broader in the fixed visible-infrared window. Few fibers were fabricated with different configurations in order to make a systematic study of transmission bandwidth together with low loss which can be achieved by optimizing b parameter of the core.

The reported 7-cell Kagome IC HC-PCF with 3 cladding rings was fabricated by stack and draw technique. With respect to equation (4.6), thinner struts would increase the transmission windows which are noticeable in the same figure. The first Fiber #1 exhibits a strut thickness $t = 700$ nm, a core radius $R_{in}/R_{out} = 53/67$ μm with $b = 0.93$ that has its fundamental transmission band extending only up to 1600 nm and minimum transmission loss 85 dB/km in this spectral region. This fiber is close to the previous state-of-art fiber [49] having



record loss at 1064 nm in its second band as shown in dashed line of Figure 4-11. Fiber #2 with thickness of 600 nm has $R_{in}/R_{out} = 49/62 \mu m$ with $b = 0.84$ has its first cut-off wavelength around 1500 nm with lowest loss of 65 dB/km at 1620 nm. Another fiber (labelled as Fiber #3) gets its fundamental band extended down to 1100 nm by decreasing its thickness further to 500 nm, with core radius $R_{in}/R_{out} = 48/59 \mu m$ and $b = 0.73$. Such fiber would have minimum loss around 1300 nm. Fiber #4 with thickness of 400 nm, $R_{in}/R_{out} = 44/55 \mu m$ and $b = 0.61$ is around 1000 nm with a minimum loss of 40 dB/km at 1064 nm.

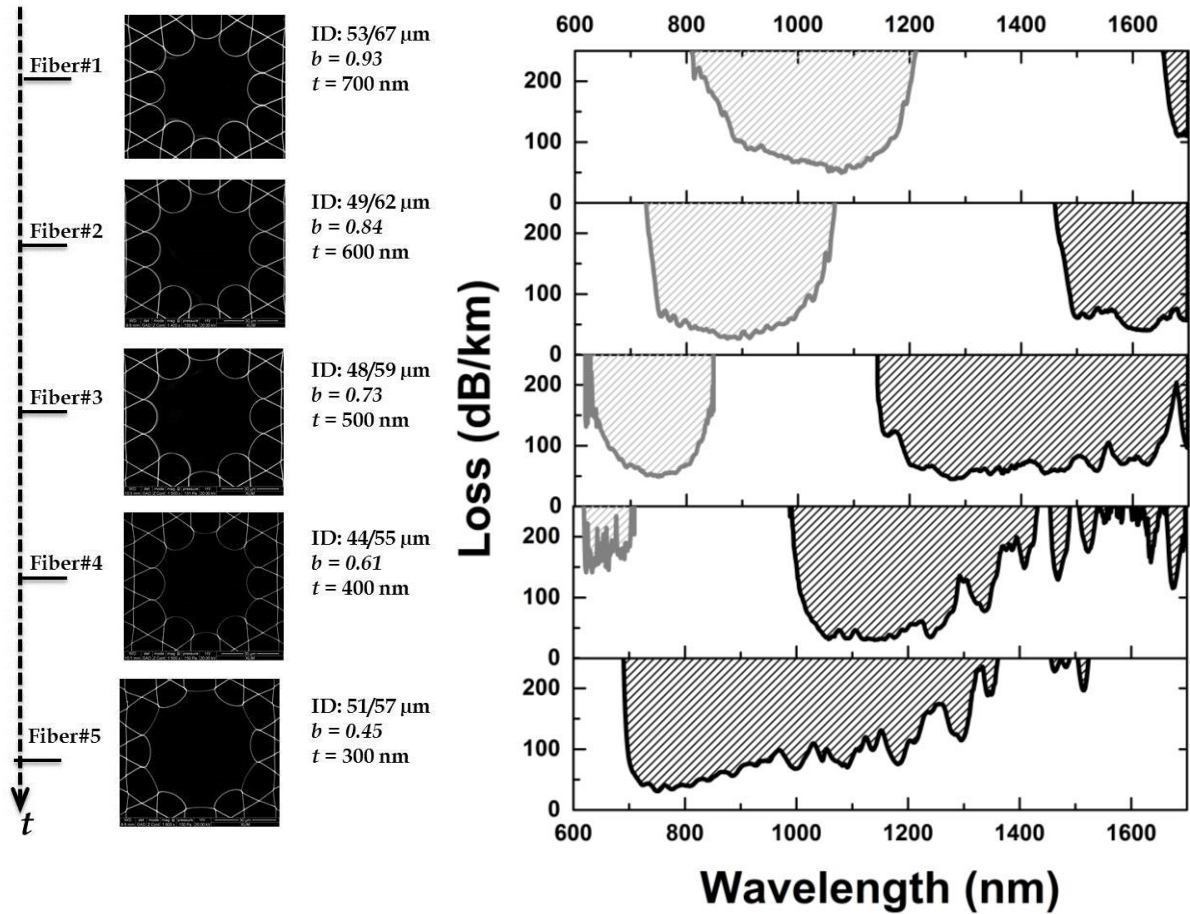


Figure 4-10 (Left) Different fabricated fibers with reduced strut thickness and measured b parameters. (Right) Their corresponding loss spectra. Spectral windows shown in black and gray dashed lines indicate fundamental and first high order bands respectively for each fabricated fibers.

Finally the last fiber (Fiber #5) fabricated with outer diameter set to $315\ \mu\text{m}$ keeping a hypocycloidal shape core with b curvature parameter equal to 0.45 and silica struts with a thickness of $300\ \text{nm}$ and core radius $R_{\text{in}}/R_{\text{out}} = 51/57\ \mu\text{m}$ (see inset of Figure 4-11 for the SEM image and its core curvature). Its loss spectrum plotted in Figure 4-12 has been measured by cut-back technique and shows a single transmission band ranging from $670\ \text{nm}$ to $1750\ \text{nm}$. Further transmission recording is limited by our detection system. For a comparison and to highlight performances, the transmission (Figure 4-11 (a)) and loss curves (Figure 4-11(b)) of the previous state-of-the-art in terms of absolute record loss level for an IC HC-PCF (dashed curve) [49] is added.

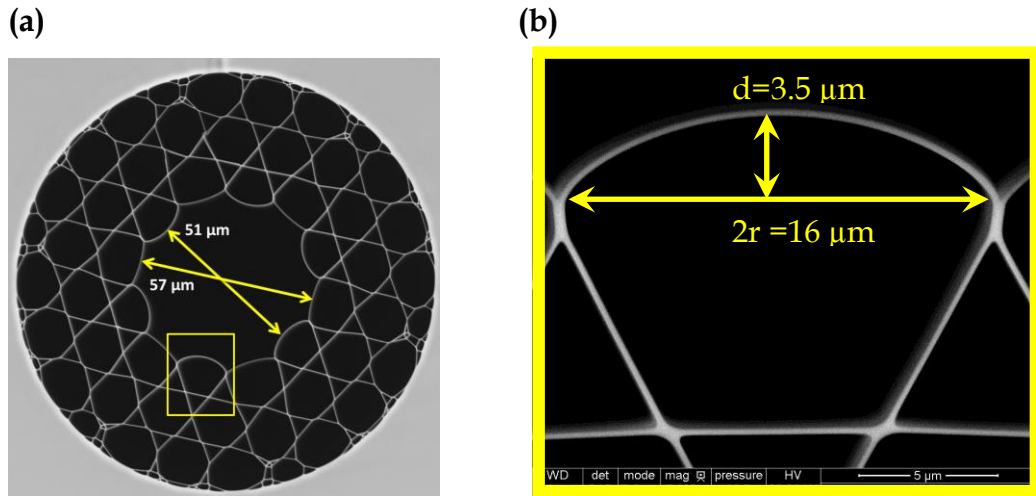


Figure 4-11 (a) SEM image of low loss broad band Kagome IC HC-PCF with its hypocycloidal core shape as shown in (b).

Also we can notice that the previous fiber presents drawbacks either by having strong loss increase at shorter wavelengths or by having multiple cut-off regions on the visible and IR ranges. In contrast, the presented fiber shows a broad fundamental transmission band, meaning that the first cut-off region is located at $670\ \text{nm}$. Therefore minimum and record value of loss $30\ \text{dB/km}$ is obtained at $750\ \text{nm}$ in this fundamental transmission band. The fiber also exhibits losses below $150\ \text{dB/km}$ over a large transmission spectral range from 670 to $1300\ \text{nm}$. That is,

to date, the first Kagome IC HC-PCF that combines such a thin and curved-arc core contour resulting in the demonstration of record transmission.

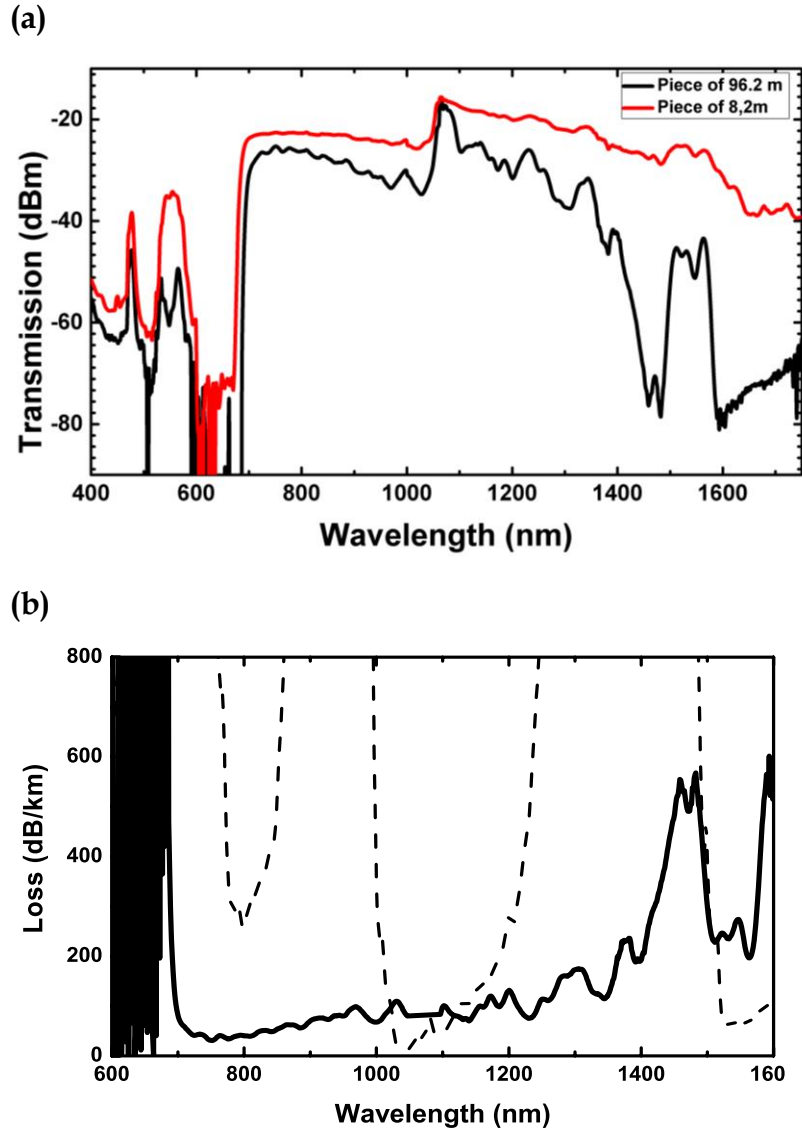


Figure 4-12 (a) transmission curve from a 96.2 m (red solid line) and 8.2 m long piece (black solid line). (b) Corresponding measured loss curve (black color) of the fabricated hypocycloid-core Kagome HC-PCF. Both transmission and loss spectra are compared with the previous state-of-the-art Kagome IC HC-PCF [49] (dashed lines).

4.4.2 Bending Analysis

The sensitivity of the fiber to bend was investigated. Bend loss spectra as shown in Figure 4-13(a) were measured from the output of the fiber at different bend radii over a 20 m long piece.

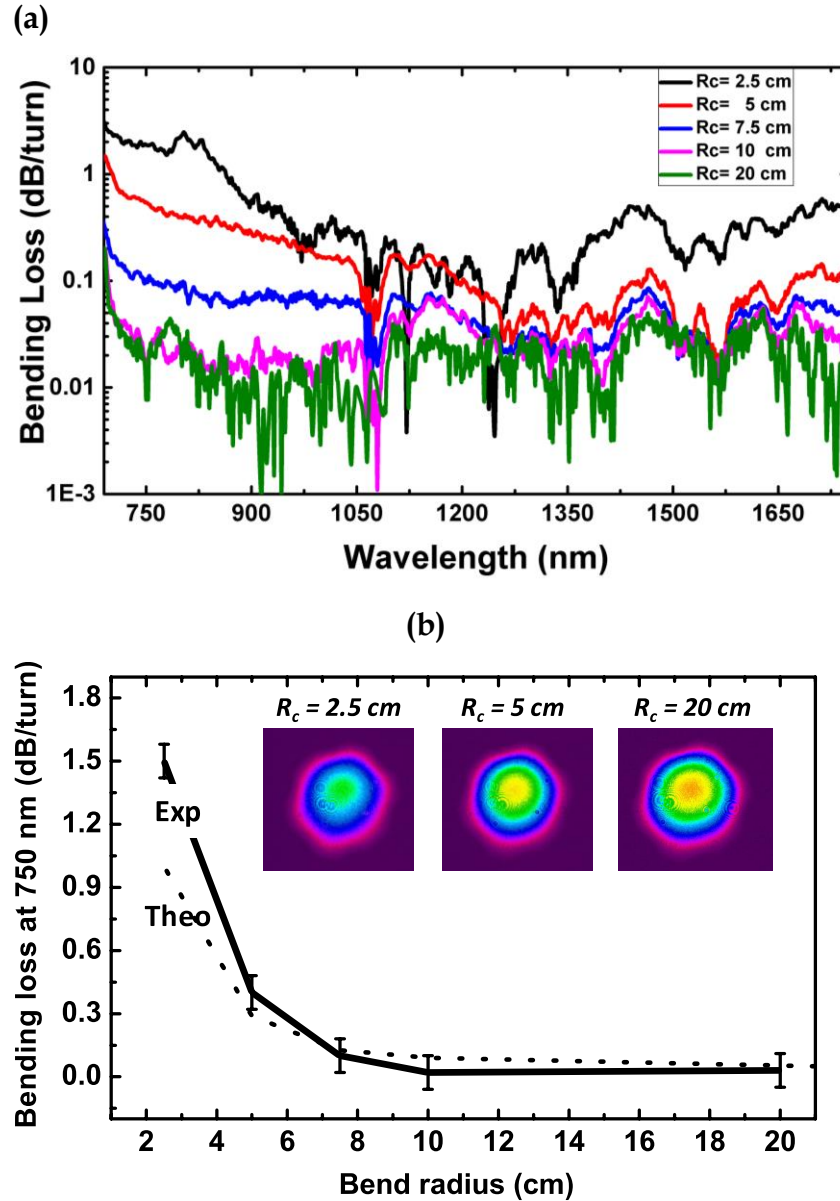


Figure 4-13 (a) Loss spectra of low loss broad band Kagome IC HC-PCF for different bend radii. (b) Bend loss evolution at fixed wavelength of 750 nm, where the fiber exhibits record loss value 30 dB/km on fundamental transmission band and corresponding NF images at bending radii are shown in the inset of the figure.

Typical bend radii (radius of curvature noted R_c) used were 20 cm, 10 cm, 7.5 cm, 5 cm and 2.5 cm. As expected, bend losses increase with the decrease in bending radius and show acceptable loss values with minimum of 0.1 dB/turn at 780 nm when R_c is superior to 7.5 cm (see Figure 4-13(b)). The M^2 parameters were also studied with values found inferior to 1.3 at the minimum loss wavelength, *i.e.* 1030 nm which confirms a quasi-single mode operation.

4.4.3 PER

Polarization extinction ratio (PER) of the fabricated fiber has been measured over the fundamental band using experimental set-up mentioned in Figure 4-2(b). A GLAN polarizer and half wave plates at input and polarizing beam splitters (PBS) (covering 650–1050 nm and 1200–1600 nm) at input and output respectively are used during the experiment. Laser beam from the output end of 8 m long FUT is passed through PBS and is decomposed into orthogonal components. Each beam is recorded by optical spectrum analyser and the PER is obtained by using equation (4.4).

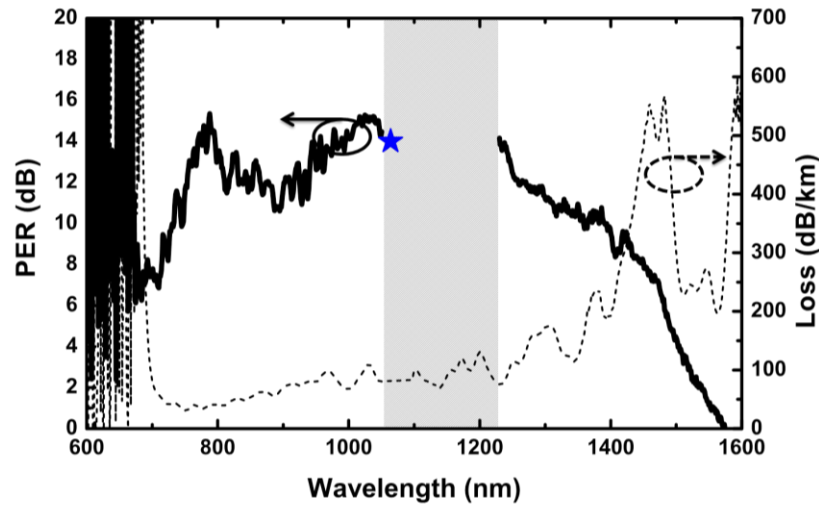


Figure 4-14 (Black solid curve) PER spectra of of the fiber showing 15 dB around 780 nm and loss spectrum of the same fiber is also included in black dashed line.

As shown in Figure 4-14 the fiber exhibits PER higher than 10 dB between 733 nm and 1390 nm and a maximum of 15 dB around 780 nm. Additional measurement has been performed by using a narrow bandwidth laser at 1064 nm (blue star symbol in Figure 4-14), which is consistent with the measured PER spectrum using supercontinuum. The dashed line in the same figure shows transmission loss of the fiber.

4.4.4 S² imaging

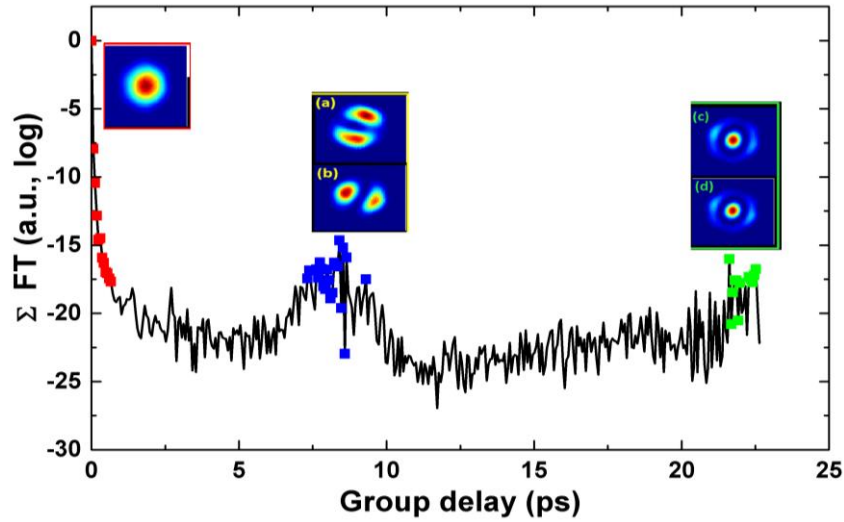


Figure 4-15 S² imaging of fabricated fiber with core radius $R_{in}/R_{out} = 51/57 \mu\text{m}$ with beam profile of fundamental mode. Mode profile in red inset is for LP₀₁ and (a), (b) are for mode images and MPI levels corresponding to the various peaks at LP₁₁ and (c)(d) at LP₁₂ modes.

Finally, the fabricated fiber with length of 5 m was investigated for modal analysis by S² imaging. The fiber is coiled with radius $R_c = 35 \text{ cm}$ and is injected with tunable laser that varies from 1010-1070 nm with minimum step size of 40 pm. Figure 4-15 shows the results obtained from the experimental set up as discussed in section 4.2.4. The results confirm the existence of HOMs propagate with different group velocities which are aimed to be further reduced. The near field images are collected by a computer and a high dynamic camera at the output of the fiber which are post-processed to measure real-time MPI. The relative power difference (MPI) between the first HOM and the fundamental mode was

more than -20 dB which confirms a quasi-single mode operation, whereas for second HOM it is -24 dB. Typical intensity profiles obtained with the S² imaging are also shown in the same figure.



4.5 Ultra-low transmission loss (7.7 dB/km at 750 nm) SR-TL IC-HC-PCFs

The optimized Kagome IC HC-PCF designs discussed above though have achieved losses at record level and broad transmission windows. Such designs inherently possess connected nodes at the core contour perimeter and to its cladding membrane which is expected (thanks to Inhibited guidance mechanism) to be one of the reasons limiting the losses to not reach down to fundamental limits. In this context, the cladding designs based on tubular lattice within large pitch regime as we discussed in Chapter 2, have further been numerically investigated and optimized, to avoid these limitations to enhance IC. It has also been noticed drop in loss levels further and better immunity to bending. These numerical studies further corroborated by experimental demonstrations with a hollow-core fiber having a single-ring of this cladding lattice [21] [59].

In this context, we report on several IC guiding HC-PCFs with a hypocycloid core-contour and a cladding structure made up of a single ring from a tubular lattice. These fibers guide in the UV-VIS and NIR, and among which we list one with a record transmission loss of 7.7 dB/km at ~ 750 nm (only a factor ~ 2 above the silica Rayleigh scattering loss (SRSL)), and a second with an ultra-broad fundamental-band with loss in the range of 10-20 dB/km spanning from 600 to 1200 nm. Both fibers present quasi-single mode guidance and very low bend loss. The results show that the limit in the transmission is set by confinement loss for wavelengths longer than ~ 1 μm and by surface-roughness for shorter wavelengths, thus indicating that transmission loss well below the SRSL in the visible is possible by reducing surface roughness and would open the possibility of the first UV low-loss light-guidance.



4.5.1 Design parameters and fabrication

In order to investigate the effect of triangular tubular lattice designs on IC guidance, numerical simulations were performed on several fibers of single cladding ring consisting of different tube numbers, tube parameters and spacing between adjacent tubes. Here, we use the IC formalism as a design tool to determine optimum tube radius (R_t), its thickness (t) and spacing between two adjacent tubes (δ) for best fiber transmission and for a fiber modal content that is close to single mode. In other words, we seek a cladding tubular arrangement, core size and shape such that the quantity $\langle \phi_{clad} | \Delta n^2 | \phi_{core} \rangle$ is reduced as much as possible [14]. Consequently, by simply recalling that cladding modes with a large azimuthal-number m favors IC guidance, which can be illustrated by the fact that the power overlap between a low-azimuthal number core mode (*i.e.* HE_{11}) and a high azimuthal-number cladding mode scales as m^{-2} , it is easy to note that increasing m implies thinning the silica tube and increasing its radius. Recently, an empirical study showed that the confinement loss scales as $\alpha_{CL} \propto t/R_t$ [91], which is consistent with the scaling of m with t/D , with D being the core contour perimeter [16] [17].

However, satisfying these rules is constrained by fabrication limitation and the fiber modal content. Indeed, keeping the circular shape of the tube, and minimizing its surface roughness during the fiber draw sets a limit on how small t one can tolerate. Moreover, because R_t is interconnected with the fiber core radius R_c , δ and the number of tubes in the cladding ring N through the identity $R_t = (R_c \sin(\pi/N) - \delta/2)(1 - \sin(\pi/N))^{-1}$, its increase can have reverse impact on both the confinement loss and the fiber modal content. In order to find the best trade-off between the above parameters, we start by finding out the optimal δ , then N and finally the R_c . Figure 4-16 summarizes the effect of δ on



both the cladding lattice modal spectrum and on the fiber core. Figure 4-16 (a) shows the evolution with δ of the electric field magnitude of a representative silica mode. The field is that of $EH_{9,2}$ at wavelength of 700 nm, for $t = 400$ nm (*i.e.* $F = 1.2$), and tube radius of $R_t = 7\mu\text{m}$. The results show that increasing δ from 2 to $8\mu\text{m}$ results in a decrease of the mode n_{eff} from ~ 1.00062 to 0.99993 , and in a stronger light confinement in the silica tube. This is readily shown in the 1D profile along a gap line joining the center of two adjacent tubes (z -line in Figure 4-16 (a), bottom panel), and where the field amplitude drops by a factor of more than 10 when δ is increased from 2 to $8\mu\text{m}$. This trend favors larger inter-tube gap for IC, however this would make sense only if the fiber core mode profile is not altered and kept its zero-order Bessel profile.

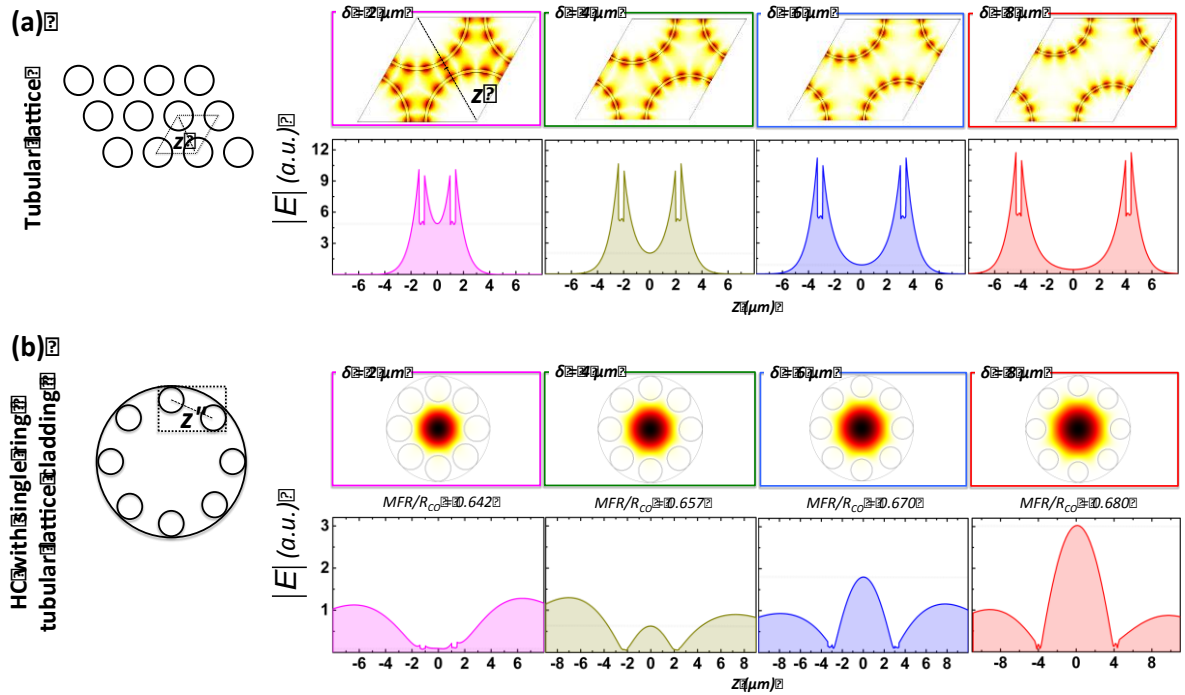


Figure 4-16 1D field amplitude profile along a gap line between the center of two adjacent tubes for spacing varying from 2 to $8\mu\text{m}$ for a tubular lattice (a) and for hollow-core with single ring tubular lattice cladding (b).

Figure 4-16 (b) shows the evolution of the HE_{11} core mode leakage of a single-ring tube lattice fiber when the gap is increased. Here, the single-ring cladding is comprised with 8 tubes. The results show that increasing δ from 2 to 8 μm leads to an increase of the mode-field radius relative to the fiber inner radius by almost 6%. This subsequently entails a stronger optical spatial overlap of the mode with the silica. Furthermore, the bottom panel of Figure 4-16 (b) clearly shows the increase with δ of field magnitude along the gap line between the centers of two adjacent tubes; indicative of stronger spreading of the core mode in the cladding. Consequently, and given the stronger impact of the core radius on the confinement loss ($\alpha_{CL} \propto R_c^{-4}$) [91] compared to that from the cladding modal change, the optimal δ will be a trade-off between a value that is sufficiently small to avoid a too high core mode leakage, and sufficiently large to avoid the formation of connecting nodes (which support low azimuthal-number modes) and a too strong coupling between the tubes. The top of Figure 4-17 summarizes the effect of cladding tube number N and δ on the fiber confinement loss. Figure 4-17 (a) shows the CL over a representative spectrum for different N and for fibers having $t = 400 \text{ nm}$, $R_t = 8 \mu\text{m}$ and $\delta = 5 \mu\text{m}$. The spectrum spans from 480 to 600 nm, and corresponds to F range of 1.4-1.75. The loss figure is expressed as $\alpha_{CL} R_c^4$ so to only keep the effect of N on the transmission loss trend with increasing N regardless of the fiber core radius. The results show that for the same core radius, the CL decreases with N increases. However, the decrease rate of the CL with N drops as it gets larger. For example and choosing a wavelength of 540 nm, $\alpha_{CL} R_c^4$ decreases by a factor of 3 when N is changed from 5 to 6. However, it decreases by only less than 20% when the tube number is increased from 8 to 9. This is due to the resonance between the core mode and the air modes of the tubes [44] [58]. On the other hand, the power-ratio of the higher-order core modes TE_{01} and HE_{11} , which is an indicator of how well the fiber can operate in a single mode manner,

increases as expected with decreasing N , thus favoring smaller number of tubes for single mode operation (see Figure 4-17 (b)). Consequently, and similarly to the finding of the optimal δ , the optimal N is the result of a trade-off between CL-decrease, which scales proportionally with N , and the fiber single modeness, which is inversely proportional to N , along with bend loss sensitivity which favors smaller fiber core size and thus smaller N .

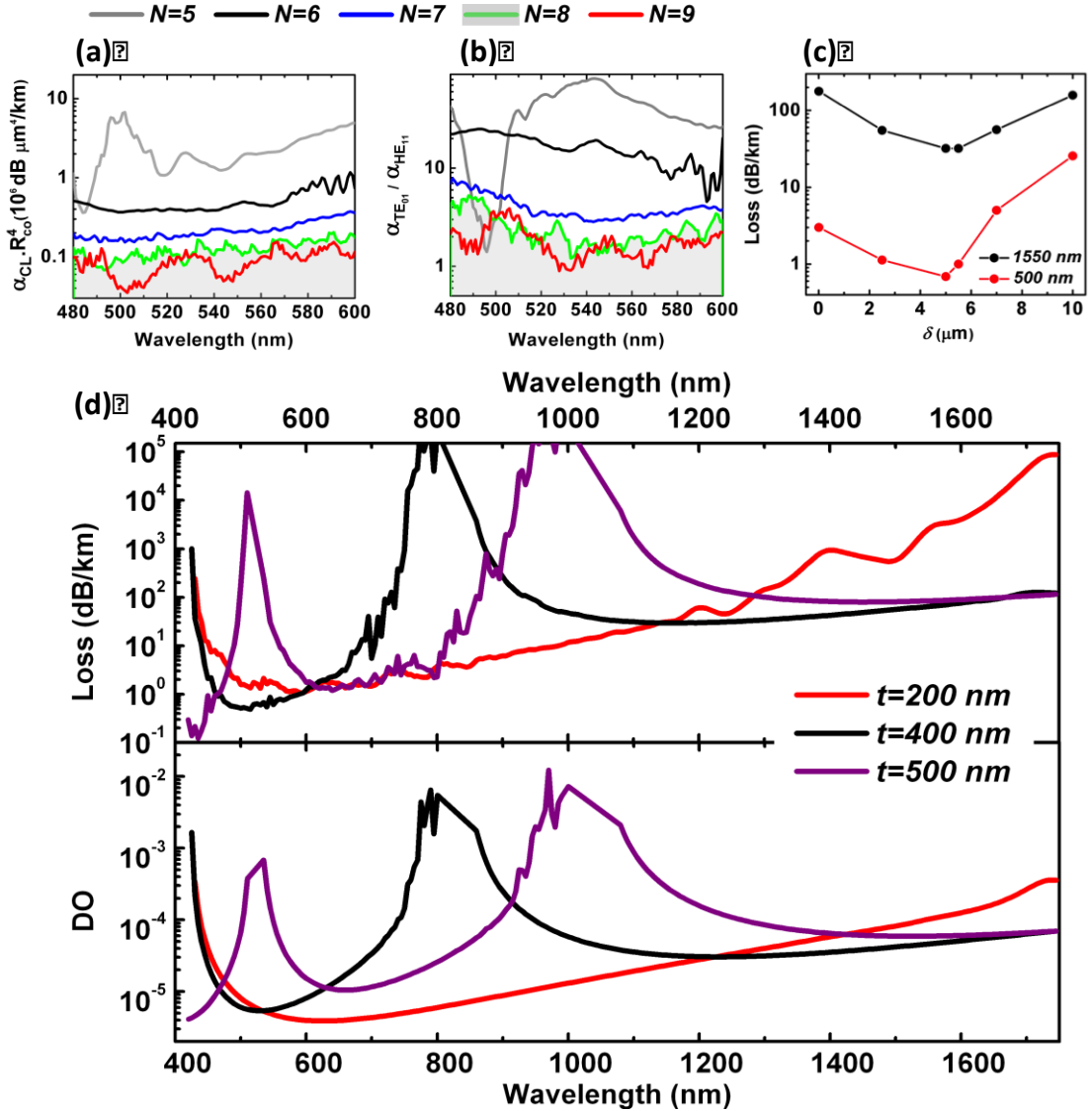


Figure 4-17 Four panel showing (a) CL for different tube numbers (N), (b) Ratio between TE_{01} and HE_{11} loss, (c) loss spectra versus tubular gap (δ), (d) loss and DO spectra for different tube thickness (t) values.

We found $N = 8$ to be a good compromise for a sufficiently low CL and a modal content that is dominated by the core fundamental mode HE_{11} . Figure 4-17 (c) shows the CL evolution with δ at 500 nm (red curve) and at 1500 nm (black curve) of a SR-TL HC-PCF with $N = 8$, $t = 400$ nm, and $R_t = 8$ μm which are optimum parameters to favor IC. The results show that the inter-tube gap range of 2-6 μm is suitable for low loss guidance.

Based on these design results, we calculated the CL spectra for different tube thicknesses. Figure 4-17 (d) shows the spectra of CL (top) and the optical overlap of HE_{11} core mode with the cladding dielectric (noted DO) (bottom) at different tube thicknesses ($t = 200$ nm, 400 nm and 500 nm) for a SR-TL HC-PCF with $N=8$, $R_t = 8$ μm and $\delta = 2.5$ μm . Within the explored wavelength range of 400-1750 nm, the $t = 200$ nm fiber exhibits one large transmission band corresponding to the fundamental band with a minimum loss of ~ 1 dB/km at wavelengths near 600 nm. For the $t = 400$ nm SR-TL HC-PCF, the spectrum exhibits two transmission bands separated by a high-loss band centered around 800 nm. Here, the lowest loss figure is 0.5 dB/km and occurs at wavelengths near 500 nm in the 1st higher order transmission band. For $t = 500$ nm SR-TL HC-PCF, we observe a spectrum with the 3 transmission bands, and lowest loss of 0.3 dB/km occurs in the 2nd higher-order band around 480 nm.

Below, we explore these results and scaling laws in the fabrication of several fibers with $N = 8$. The DO spectra show the same resonance structure as CL as expected by IC guidance which relies on the reduction of $\langle \varphi_{clad} | \Delta n^2 | \varphi_{core} \rangle$, which itself is proportional to the optical overlap DO. The spectra show that an overlap in the range of 10^{-6} is achievable with this type of IC guiding HC-PCF. The minimum obtainable can be reduced by further thinning the tube thickness and operating in the shorter wavelength. This trend results from the fact that the silica

cladding modes get more localized with the optical frequency increase. On a note relating to this fiber guidance mechanism it is significant to highlight the wavelength evolution of CL in the fundamental band which can only be explained by IC guiding concept. For $\lambda > 1600$ nm, we observe that the CL of the three fibers show different slope with increasing wavelength, and do not scale uniformly with the tube thickness. For example, at $\lambda = 1660$ nm, CL reaches 13480.6 dB/km for $t = 200$ nm, but is only 94.7 dB/km for $t = 400$ nm, and 98.4 dB/km for $t = 500$ nm. In order to explain such a trend, we recall that reducing CL implies reducing $|\langle \varphi_{clad} | \Delta n^2 | \varphi_{core} \rangle|^2$. Even though $\langle \varphi_{clad} | \Delta n^2 | \varphi_{core} \rangle$ entails expressions of core and cladding field with amplitude and spatial phase that are not separable, we can extract qualitative scaling law by making some approximations. For the case of HE_{11} core mode in the fundamental band (*i.e.* the radial phase number is $l=1$), the core-cladding field overlap is dominantly in the glass, and if we consider the cladding field amplitude to be constant over the whole glass regions, we can write the approximate proportionality identity $|\langle \varphi_{clad} | \Delta n^2 | \varphi_{core} \rangle|^2 \sim m^{-2} DO$. Consequently, the observed CL trend with the tube thickness can be explained by examining DO and the azimuthal number m of the cladding mode in the vicinity of the fiber-core HE_{11} effective index at $\lambda = 1660$ nm. The results show that the corresponding cladding modes are of the family of $EH_{6,1}$ for $t = 200$ nm fiber, of $EH_{12,1}$ for $t = 400$ nm, and of $EH_{15,1}$ for $t = 500$ nm, in consistency with the scaling law $m \propto 1/t$ mentioned above, and their respective $m^{-2} DO$ values follow the CL order as found numerically.

4.5.2 Transmission and Loss

After concluding optimum design parameters by simulations explained in earlier sections, several SR-TL IC-HCPCFs have been fabricated and linear characterized in order to assess their optical performances. Figure 4-18 (a) shows



the micrographs of four fabricated SR-TL HC-PCFs along with their physical properties. Here, we endeavored to vary δ whilst keeping R_t , t and R_c as constant as possible so to find out the optimal value from the stand point of fabrication and transmission performance. The table shown in Figure 4-18(a) summarizes these quantities values for the different fibers shows that δ spans from 2.7 μm (Fiber #4, pink colored micrograph frame) to 8 μm (Fiber #1, green colored micrograph frame). Within this δ span, the core radius R_c ranges from 13.75 to 18.5 μm , corresponding to a maximum relative difference between the different fiber core sizes of less than 35%.

Similarly, the cladding tubes radius R_t and t range from 5.1 to 6.15 μm and from 415 to 580 nm respectively and the relative difference of both quantities are also less than 20%. Figure 4-18 (b) shows the four fibers measured loss spectra versus λ/t . As expected over the measured wavelength range of 400-1750 nm and for tube thickness of 415-580 nm, the spectra show three transmission bands corresponding to the fundamental band ($\lambda/t > 2$), 1st order band ($1 < \lambda/t < 2$) and the second-order band ($\lambda/t < 1$). The different fibers loss curves in the fundamental and 1st order bands clearly demonstrate a dramatic reduction of the optical attenuation with δ decrease; from a near 1 dB/m loss-level for $\delta = 8 \mu\text{m}$ (green curve) down to only a few tens of dB/km for $\delta = 2.7 \mu\text{m}$. For the 2nd order band, the trend of the loss-decrease with δ is observed only for δ range of 8-5 μm . For smaller inter-tubes gaps, corresponding to tube thicknesses t smaller than 500 nm, the loss increases with δ decrease (*e.g.* orange curve compared to the blue curve). Furthermore, a comparison of the rate at which the loss decreases with the gap-shortening shows that the loss in the fundamental band decreases at a larger rate than that in the 1st order band. As a matter of fact it plateaus down to 15 dB/km for δ range of 3.7-2.7 μm (see pink and orange curves).



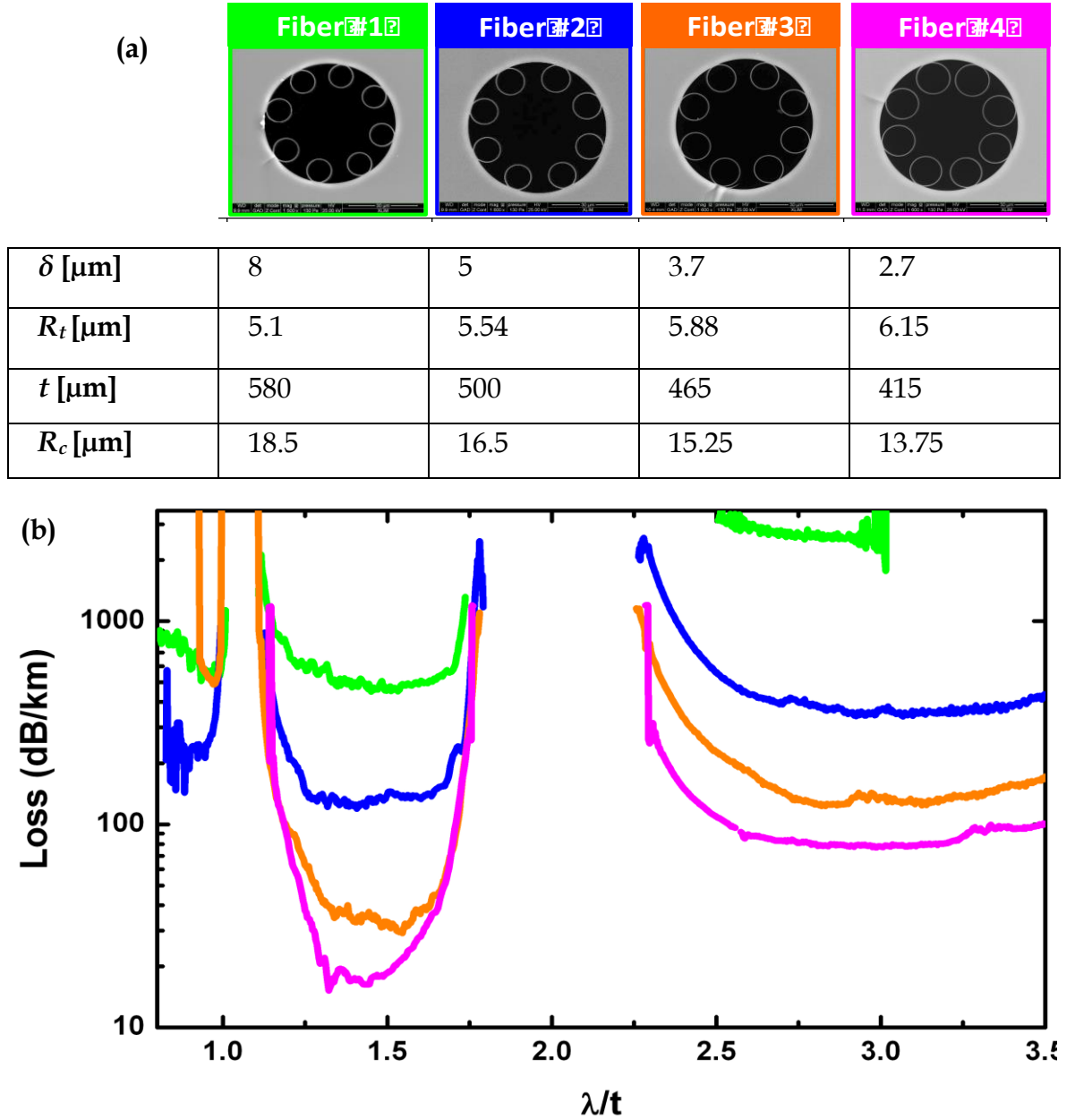


Figure 4-18 (a) SEM pictures of 4 fabricated HC tubular lattice fibers with corresponding geometrical parameters (δ , R_t , t , R_c). (b) Experimental evolution of the loss spectrum with the tubular gap.

Now that δ value impact on the transmission loss of fabricated fibers is demonstrated, we used $\delta \sim 2.5 \mu\text{m}$ as a parameter target and undertook two fiber fabrication campaigns with different aims. The first aim consists of the fabrication of fibers with the thinnest tubes possible so to have the broadest fundamental

band whilst having loss figures as low as the surface-roughness-induced transmission-loss could permit. The second aim is to have the lowest loss figure possible in the NIR-VIS spectral range. This was undertaken in an iterative process of several fiber draws. As mentioned above, having a too thin cladding tube (typically <250 nm) poses fabrication challenges in keeping the circular shape of the tubes but also increases the surface scattering through larger surface-roughness that results from enhanced surface capillary wave during the draw process. Consequently, reaching the lowest loss in the shortest wavelength will be a compromise between CL (*i.e.* design limited) and SSL (*i.e.* fabrication limited).

The results of this fabrication campaign are summarized in Figure 4-19. The figure shows the loss and transmission spectra of two fibers. The first one (Fiber #5) exhibits an average δ value of 2.5 μm , $t = 545$ nm and $R_c = 20.5$ μm . Its measured loss spectrum (cut-back between 293 m and 10 m long pieces) shown in Figure 4-19(a)(i) highlights ultra-low loss in the 1st order band with an absolute record transmission-loss for a HC-PCF of 7.7 dB/km at 750 nm. The second design (Fiber #6) presents thinner tubes ($t = 227$ nm), thus shifting the fundamental band blue edge to a wavelength as short as 515 nm Figure 4-19 (b) (i). An ultra-large low-loss window is demonstrated over one octave ranging from 600 to 1200 nm with loss between 10 and 21 dB/km (Figure 4-19 (b) (i)). This is to our knowledge the first time that a HC-PCF combines such a large bandwidth with such a low transmission loss. The measured transmission spectra of a 2 m-long sections from the two fibers are plotted in Figure 4-19 (a) (ii) and (b) (ii). Both fibers exhibit guidance in the UV domain. Remarkably, Fiber #5 shows three UV transmission-bands spanning down to 220 nm (purple filling color). Reliable measurements of loss spectra for wavelengths shorter than 350 nm were prevented from the limited dynamics of the photo-spectrometer.

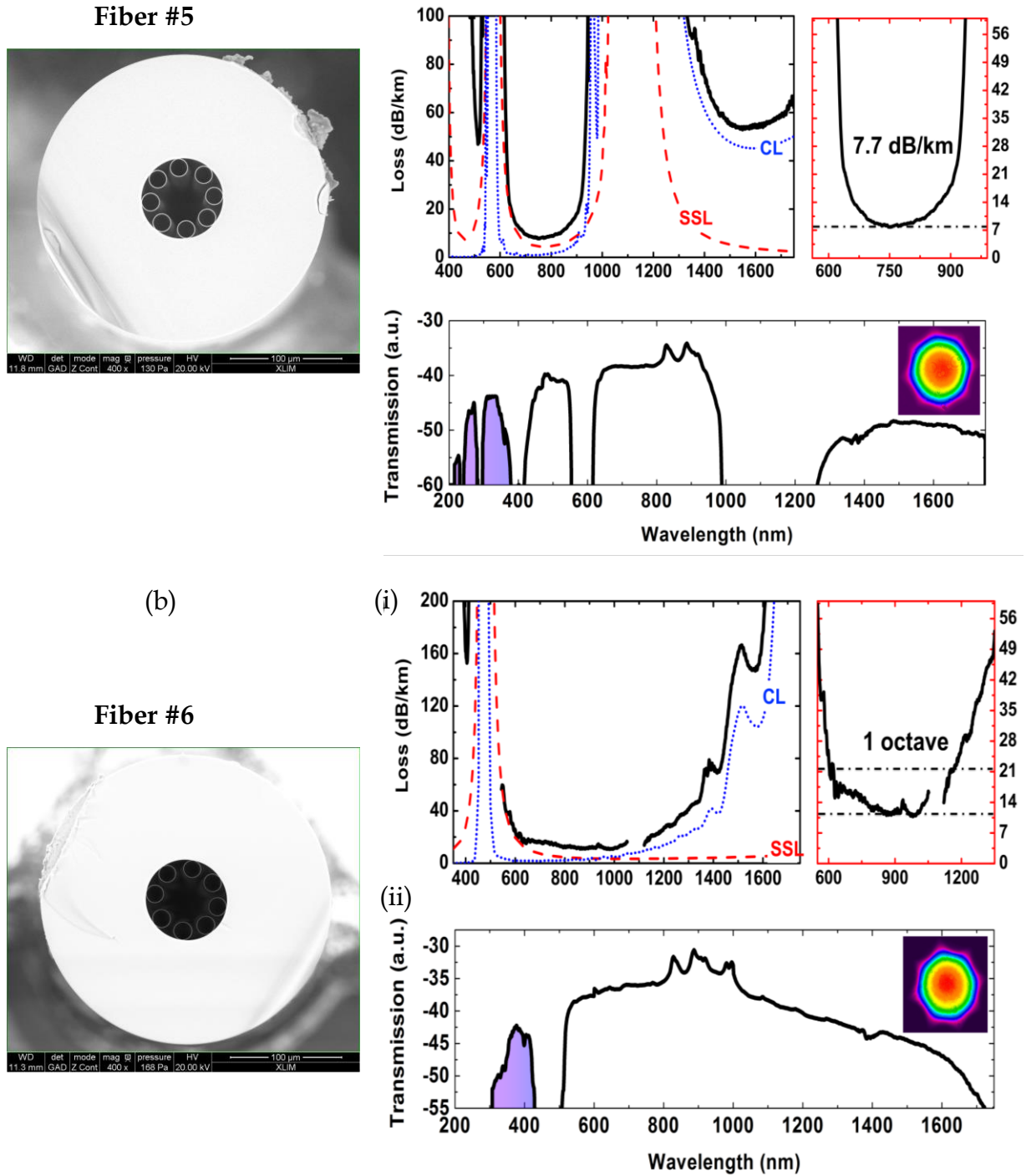


Figure 4-19 Measured transmission and attenuation spectrum for Fiber #5 (left) (a(i)) and Fiber #6 (right) (b(i)). Fiber #5 reaches a record of 7.7 dB/km (a(ii)), and Fiber #6 exhibits a loss in the range 10-20 dB/km over one octave (b(ii)). Bottom: Measured attenuation of a 2 m-long piece of of Fiber #5 (c) and of Fiber #6 (d) with purple-filled curve highlighting UV/DUV guidance. The blanked data around 1 μ m in b(i) and b(ii) are due to the supercontinuum stronger power at 1064 nm.

4.5.3 Bending Analysis

Bending sensitivity of both of these fibers (Fiber #5 & #6) was investigated. Transmission spectra were measured from the output of the fibers at different bend radii over a 20 m long piece. Typical bend radii (radius of curvature noted R_c) used were 20 cm, 15 cm, 7.5 cm, 5 cm and 2.5 cm. As expected, bend losses increase with the decrease in bending radius and with the decrease of the silica core contour thickness. At the wavelength where the minimum attenuation is reached, both fibers show acceptable values respectively of 0.03 dB/turn at 750 nm for Fiber #5 and 0.7 dB/turn at 1000 nm for Fiber #6 when R_c is superior to 15 cm as shown in Figure 4-20.

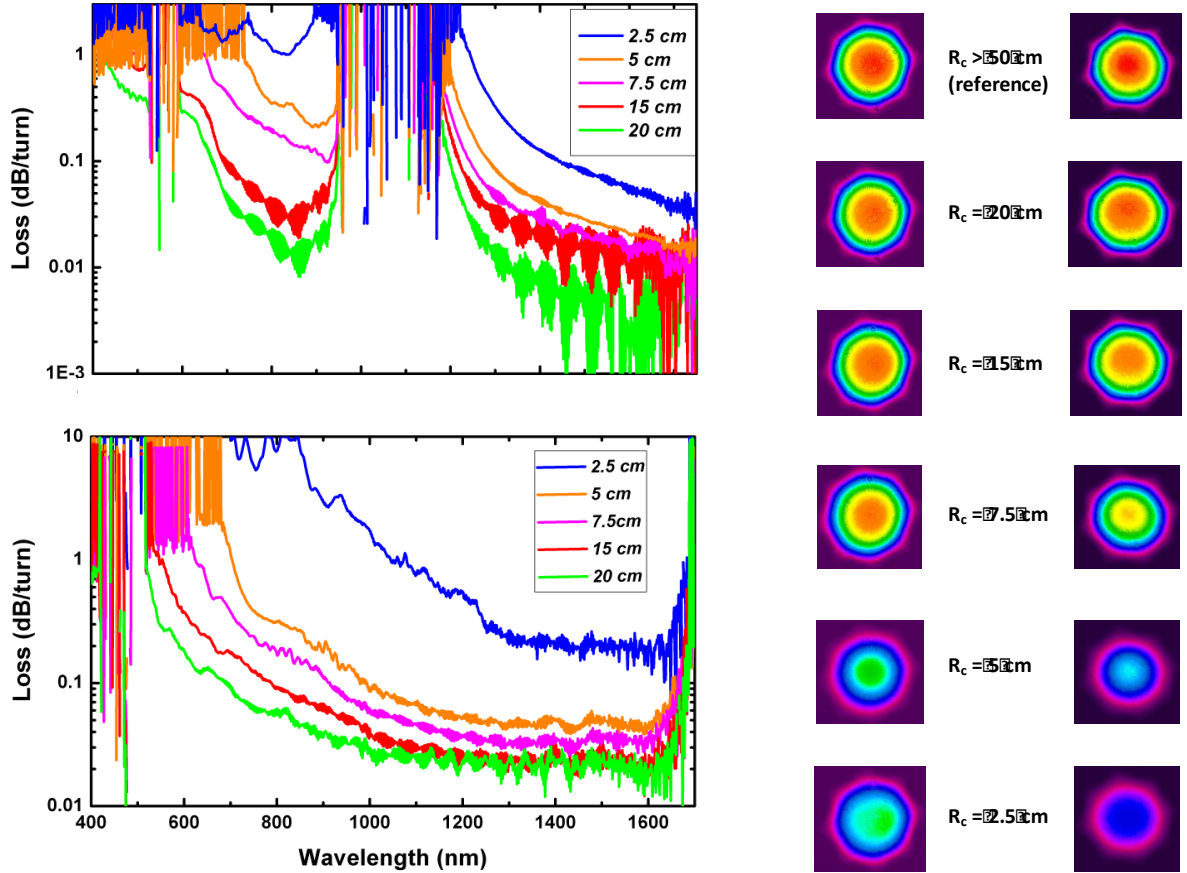


Figure 4-20 Bend loss spectra measured at different bend radius for (a) Fiber #5 and (b) Fiber #6; (c) Recorded near fields are added for the different bending radius used (left: Fiber #5 / right: Fiber #6).

4.5.4 S² Imaging

The modal studies of Fiber #6 has also been characterized using spectral and spatial (S²) imaging technique [90] [92]. Figure 4-21 shows the typical S² modal content and the evolution with the group delay of the interference signal Fourier transform (GDFT) for fiber-length of $L = 5$ m and $L = 15$ m from Fiber #6 that guides with low loss at 1030 nm.

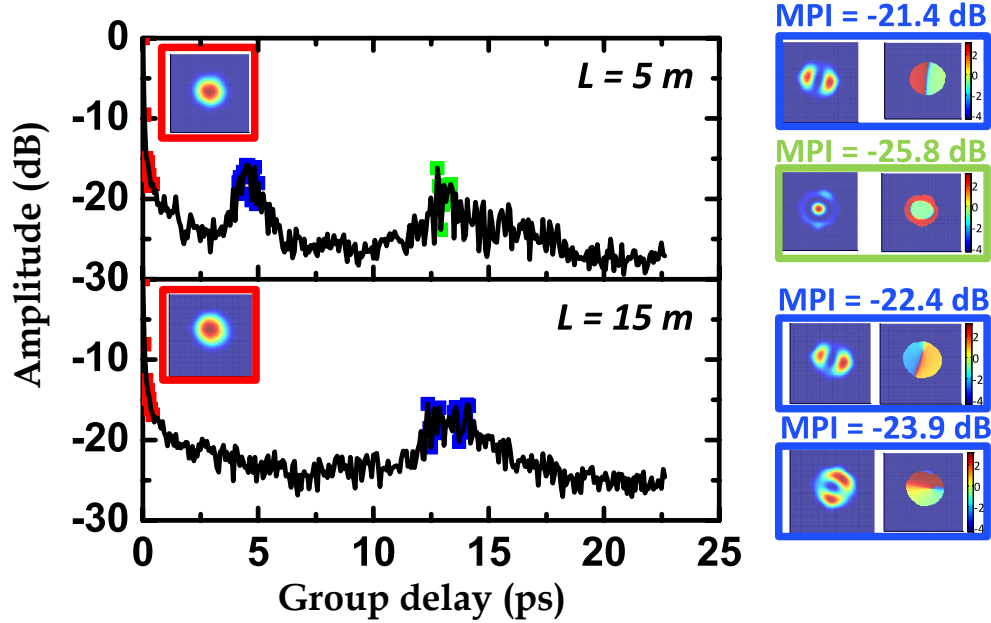


Figure 4-21 Group delay curves of the HOM content propagating in the Fiber #6 for 5 m and 15 m long pieces. The reconstructed mode field profiles are indicated with the corresponding MPI.

We recall that the S² imaging system comprises an InGaAs camera and a tunable laser source with a tuning range of 1010-1070 nm, and a minimum step size of 40 pm. Laser injection at the input end is optimized at 1035 nm. At the output of the fiber, a telescope is used to collect the light recorded through the camera, which is triggered directly from the laser and controlled by a PC. For 5 m long fiber, the LP₁₁ mode presents a multi-path interference (MPI) of 21.4 dB which corresponds to a quasi-single mode operation and increases to 23.9 dB for a length of 15 m.

4.5.5 PER

Finally, the fibers polarization maintaining properties were explored by launching into the fiber a linearly polarized laser beam at 1030 nm and a half-wave plate for polarization control. The transmitted beam is then passed through a polarizing beam-splitter (PBS) and each of its two output beams is recorded by a power-meter and a camera imaging its reconstructed near-field beam profile. Figure 4-22 shows the evolution of the polarization extinction ratio (PER) with the fiber length (Fiber #6 is used). The inset shows the fiber transmitted laser power from each of the 2 output ports of the PBS in function with the half-wave plate angle.

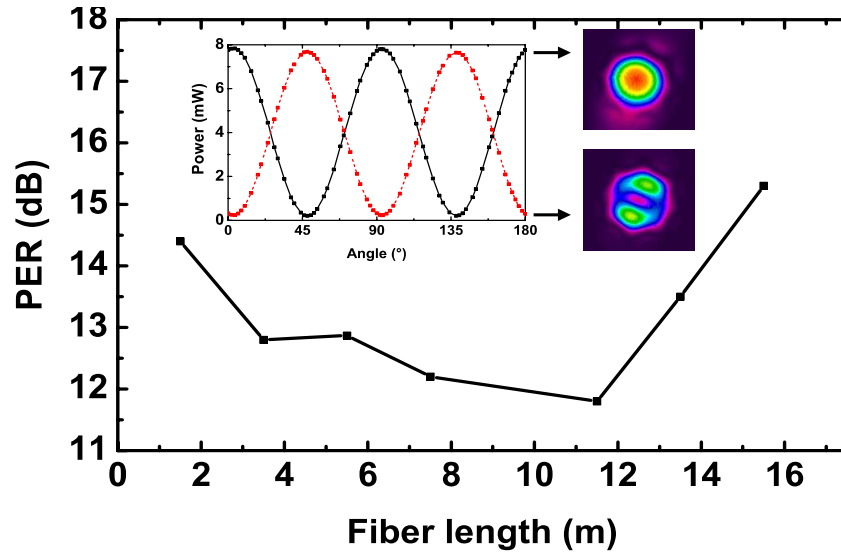


Figure 4-22 Evolution of the PER versus the fiber length.

The deduced PER was recorded for different fiber lengths. The results show a maximum PER of 15.5 dB achieved with a fiber length of 16 m, and an evolution with the fiber length which comprises a decrease in PER with the fiber length for length shorter than 12 m and then an enhancement in PER as the fiber length increases for length longer than 12 m. It is noteworthy that the profiles of the crossed-polarized beams show that for an input polarization corresponding to a

maximum PER, the mode of the dominant polarization orientation is mainly that of HE_{11} whilst the one with the crossed polarization shows a profile of that of the LP_{11} family (inset of Figure 4-22). We believe that this PER evolution with the fiber length and the fact that the mode of the crossed-polarized is that of LP_{11} results from the back-coupling to the core of the light scattering off the core inner surface. Indeed, by virtue of stronger optical overlap of the higher-order core modes with the core-contour, the light that is coupled back from the core-surround surface is likely to couple to higher order modes rather than the HE_{11} .

4.6 Summary

In summary, two optimized 7-cell hypocycloid core Kagome IC HC-PCFs presenting broad and low-loss fundamental band is reported. One of the fibers demonstrated record loss down to 8.5 dB/km at 1030 nm associated with a 225 nm wide 3-dB bandwidth and low bend sensitivity. This fiber can be used for Yb and Nd:Yag laser beam delivery applications. The loss figure achieve with this fibres is two times lower than current state-of-the-art 7-cell Kagome fiber (17 dB/km). Finally, the modal properties (S^2 and PER) have been studied, demonstrating a quasi-single mode operation. The fiber demonstrated maximum PER of 26 dB which is very closer value to the standard polarization maintaining fiber. The second Kagome fiber by virtue of thin silica struts of 300 nm and strong negative curvature of the core contour, demonstrated a record loss figure of 30 dB/km at 780 nm associated with good PER, and low bending sensitivity.

Connecting nodes of Kagome lattice which are inherent to the design have been removed by transforming lattice structure to tubular lattice. Finally, with large pitch and operating with much thinner glass-tube than has previously been achieved, we reported on the fabrication of several ultra-low loss single-ring



tubular lattice HC-PCFs (SR-TL HC-PCF) guiding in the UV-VIS and NIR. Among the fabricated fibers, we count one with a record transmission loss of 7.7 dB/km at ~ 750 nm, which is only 4 dB above the Rayleigh scattering fundamental limit in silica, and observed guidance down to 220 nm. A second one exhibits ultra-broad fundamental band with loss range of 10-20 dB/km over one octave spanning from 600 to 1200 nm. Both fibers present a near-single modedness, with ~ 20 dB extinction between HE_{11} fundamental core mode and the strongest first higher-order mode (HOM), and exhibit very low bend loss (0.03 dB/turn for a 30 cm bend diameter at 750 nm).





Chapter 5

Experimental investigation of surface scattering losses in inhibited coupling HC-PCF

The first part of this chapter discusses about further studies to understand the origin and effect of surface scattering losses (SSL) that are induced by surface roughness inside the core of the IC HC-PCF. In the second part a new experimental set-up is discussed to investigate angular distributions of SSL and confinement loss (CL) in horizontal and azimuthal directions respectively to find their loss coefficients and relation between them.



5.1 Introduction and origin of SSL in HC-PCF

Scattering has been a fundamental source of loss in optical fibers. In conventional silica fibers, the light scattering arises due to thermal noise in the fiber core bulk material, and represents the source of the current limit of about 0.15 dB/km in their transmission loss. For the case of HC-PCF, being it guiding via PBG or IC, such scattering losses are strongly suppressed because light is guided principally in air; highly diluted material. However, light scattering does affect the transmission in HC-PCF and is the limiting factor of state-of-the-art PBG HC-PCF [20]. Such scattering no longer originates from the core bulk materials but from the surface roughness of the fiber core silica surround, and is dependent of fiber design as well as operating wavelength. In particular, the optical overlap of core guided modes core-contour plays a major role in loss limitation for hollow-core fiber technology. The loss originating from this mechanism is named surface scattering loss (SSL) and is more dominant at higher frequencies, following a wavelength scaling law of λ^{-3} [91]. Furthermore, SSL is the limiting factor of the still lowest loss figures 1.7 dB/km achieved in PBG HC-PCF [4] and which is well larger than the confinement loss theoretical predictions. It was reported in [20] that the ultimate limit to the attenuation of such fibers is then determined by surface roughness due to thermally excited surface capillary waves (SCWs) present at the surface of molten glass which freeze-in as the glass goes through phase transition during the fiber draw. This inevitable thermodynamic origin of surface roughness makes the scattering loss mechanism as fundamental as Rayleigh scattering in solid core fibers. SSL can be reduced either by optimizing core design in order to decrease core mode overlap with silica surrounding or by careful fiber fabrication with minimal thermal noise to reduce the profile of SCWs.



In IC HC-PCF the guided core modes optical overlap with silica cladding is significantly suppressed. As results the impact of SSL should be reduced compared to PBG HC-PCF. For example with hypocycloidal core contour for Kagome IC HC-PCF [16] [17], the fraction of the core mode residing on the silica core-contour is of the order of ppm, which is several orders of magnitude than the lowest fraction obtained with PBG HC-PCF is slightly less than 1%. However, the calculated confinement loss in IC HC-PCF shows figures lower than the measured ones, including the very recent 7.7 and 8.5 dB/km obtained in the optimized IC HC-PCFs that we discussed in Chapter 4. Furthermore, the results show that the experimental loss spectra keep increasing towards shorter wavelengths, which is quiet opposite to theoretical prediction of loss spectra of IC HC-PCFs.

In this regard, it is very important to understand the nature and the fundamental limitations to the loss in IC HC-PCF. This chapter reports on systematic investigation of SSL, its impact on CL, its polarization dependence and as well its effect on modal conversion due to imperfections around the core contour of IC HC-PCF. The next sub section explains the origin and physics of SSL in HC-PCF. Then in section 5.2, based on Poynting vector study of core guided mode we discuss about how the SSL impacts CL of IC HC-PCF. We also report on the simulation of theoretical losses (CL, SSL) of one of the SR TL-IC -HC-PCFs discussed in Chapter 4, and compare them with its experimental transmission loss (TL). The final section of the chapter presents the experimental set-up designed to investigate angular distribution of scattering (ADS) from which coefficients of SSL and CL can be deduced.



5.2 Physics of surface scattering in HC-PCF

The roughness on the core-contour surface introduces sudden change in the local index of the material as its core surface departure from ideal boundary. When the core guided modes encounters such roughness, it is spherically diffracted away from the original direction and couples with other high order mode that do not guide through the core [93] [20]. According to coupled mode theory, this coupling can be described in terms of effective index $n = \beta / k$, where β is the propagation constant and $k = 2\pi / \lambda$. The coupling of light takes place between modes with effective indices n_0 and n component with spatial frequency $\kappa = k|n - n_0|$, here κ is spatial frequency of surface roughness. As a result the coupling of core mode and silica mode takes place and increases the optical overlap of the fundamental modes with the core-contour surface. The power fraction of core mode into cladding is quantified by the parameter F_{cc} which can be expressed by:

$$F_{cc} = \sqrt{\left(\frac{\epsilon_0}{\mu_0}\right)} \left(\frac{\oint_{core\ perimeter} dl |E|^2}{\oint_{core-area} dA E \times H \cdot \hat{z}} \right) \quad (5.1)$$

here E and H are the electric and magnetic field distributions respectively of the fundamental mode and \hat{z} is the unit vector along the fiber. Therefore, a portion of core guided mode is lost due to surface roughness. The loss coefficient of SSL due to surface roughness can be deduced using the formula [94]:

$$\alpha_{SSL}(\lambda) = \varsigma \cdot F_{cc}(\lambda) \cdot \lambda^{-3} \quad (5.2)$$

here α_{SSL} loss coefficients due to surface roughness and quantity ς is a fit parameter related to the surface roughness root-mean-square height.



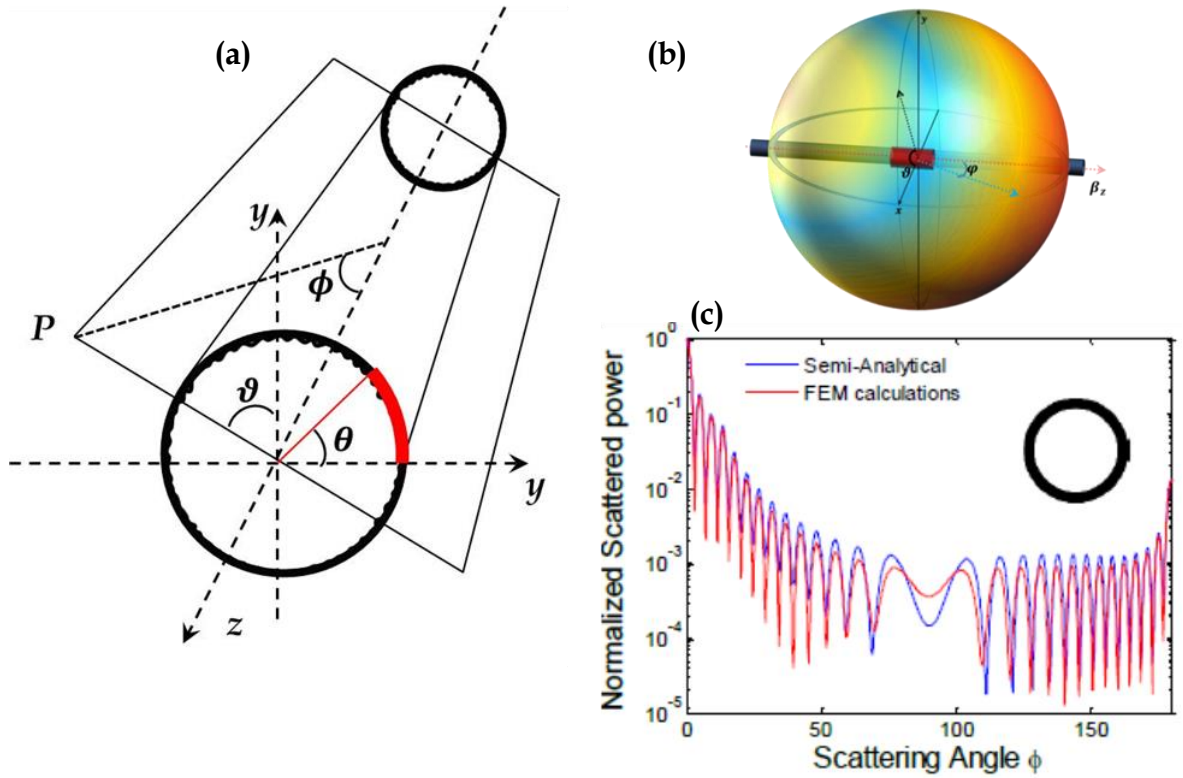


Figure 5-1 (a) schematic of a hollow tube fiber cross section with roughness surface on its core wall and ϕ and θ are angles in horizontal and transverse plane (b) Schematic of spherical scattered field distribution due to induced dipole radiation of surface scattering features on hollow-core fiber. (c) Calculated (red line) and semi-analytical (blue line) normalized scattering power spectra at point P due to scattered field spherically radiating out of roughness features on the core wall of the fiber [from [93]].

In a recent report [93] the statistical distribution of the surface irregularities was determined by a particular power spectral density function allowing calculating the total scattered power for an arbitrary input field. Figure 5-1 (a) shows schematically the coupling of the guided mode and Figure 5-1 (b) its spherical distribution due to surface roughness. Most of the light is scattered in the forward direction (shown in red) and backward directions close to the fiber axis, with only little amount of light being scattered in the transverse direction (shown in blue). As shown Figure 5-1 (c) the interference of scattered radiation and guided modes forms a characteristic scattering pattern in the far field and creates oscillations in scattering power spectra [95]. The distributed scattered light also



depends on the kind of guiding mechanism in the waveguide. IC HC-PCF with a completely different guiding mechanism than TIR or PBG, can exhibit different angular distribution trend in the transverse plane. In this regard, the next section would discuss about specific theoretical models to investigate the effect of surface roughness on confinement loss in case of IC HC-PCF.

5.3 SSL of IC HC-PCF

It has been observed that the experimental loss spectra of IC HC-PCF at shorter wavelengths increase strongly from visible to UV spectral ranges in the range of few tens to hundreds of dB/km which are in opposite to trends of theoretical simulations. To clarify this contradiction, we must examine all major loss sources namely CL and SSL by calculating their loss spectra and their combined effect on total transmission loss. Also, during the discussion about linear characterizations of IC HC-PCF in earlier chapters, we omitted the impact of surface roughness of the fibers which is the secondary source of propagation loss. Therefore, with an aim to reach the fundamental loss limits, these IC HC-PCFs have been further numerically and experimentally studied to find coefficients of SSL and its consequential effect on other optical performances.

In order to quantify the measured transmission loss and to compare with calculated loss, we considered the cases of recently fabricated fibers with record level performances. First of such IC HC-PCF is shown in Figure 5-2(a), with single ring tubular lattice (same as the fiber #5 of chapter 4) with loss levels just 4 dB above the Rayleigh scattering limit. The second fiber, shown in Figure 5-2(b), is the strut optimized Kagome latticed IC HC-PCF with record propagation loss is demonstrated with a minimum value of 30 dB/km at 780 nm (same fiber as we presented in section 4.4). The surface roughness of the core induces SSL and



degrades IC and is the reason for the discrepancy between the measured and simulated loss spectra of surface-roughness-free (ideal) fiber.

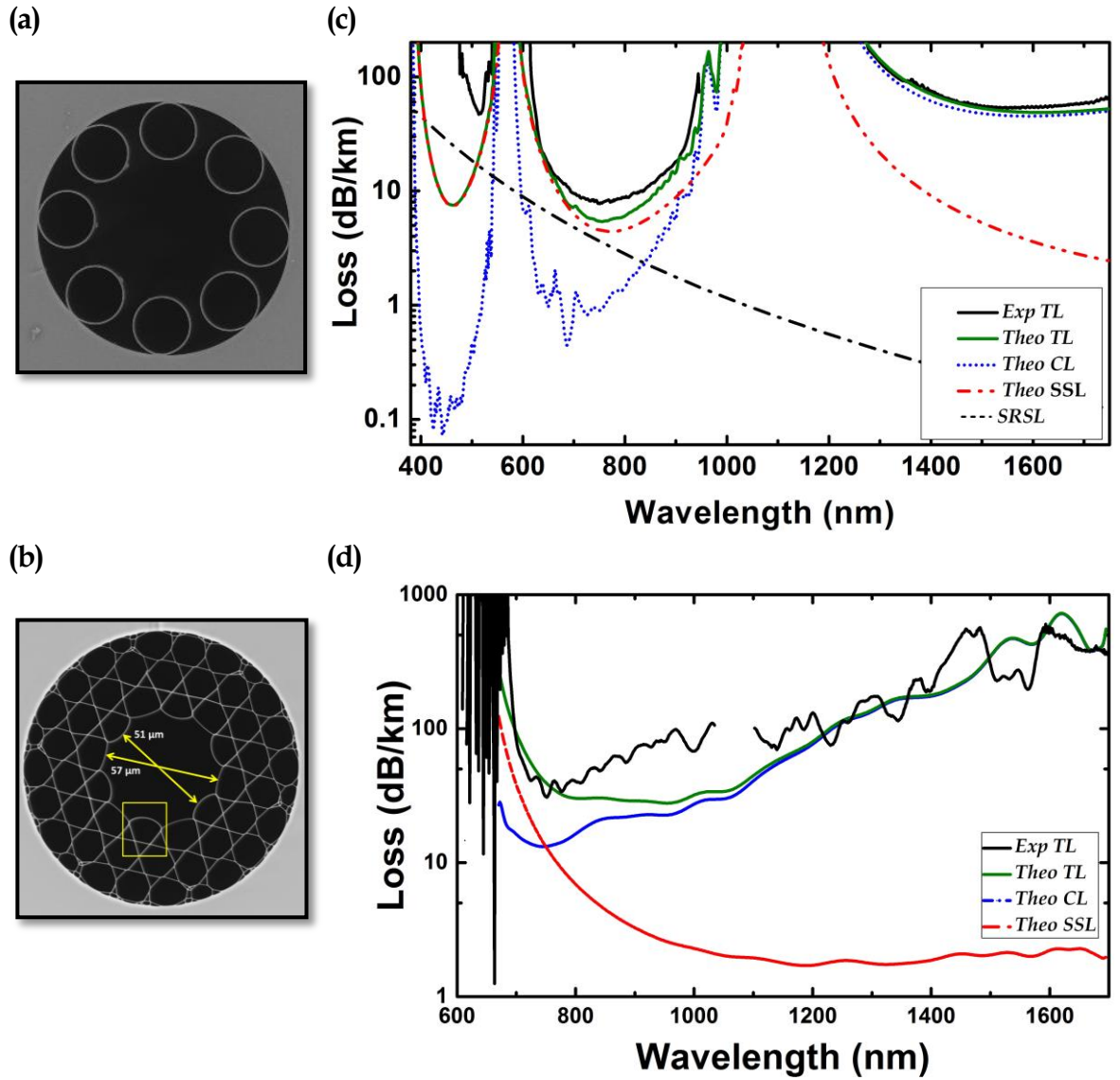


Figure 5-2(a) and (b) are SEM images of a SR-TL IC HC-PCF and 7-cell hypocycloid Kagome IC HC-PCF. (c) and (d) are their respective experimental and theoretical loss spectra.

As shown in equation 5.2, the wavelength dependence of the SSL for the typical small scale surface irregularities results from the fractional optical overlap with the core-contour $F_{cc}(\lambda)$ and its wavelength scaling of λ^{-3} [20] [91]. Figure also shows SEM images and corresponding theoretical CL and SSL loss spectra of the

SR TL and Kagome latticed IC HC-PCF considering no surface roughness. The fit was found to be better than 20% for both fibers and over the whole fundamental transmission band. Theoretical SSL spectra (dashed red curves) shown in the figure are calculated by using the expression shown in equation 5.2.

The loss spectrum of Fiber #5 (Figure 5-2(a)) shows that the measured total loss is dominated by CL in the range of 1300-1750 nm. Here, the CL is in the range of 80-45 dB/km, whilst the scattering loss is well below 20 dB/km. However, for the 1st and 2nd higher order bands the SSL is the dominating source of the transmission loss. The CL attains a minimum near 1 dB/km for the 1st band and 0.1 dB/km in the 2nd band, whilst the SSL level is above 4.4 dB/km for the 1st band, and above 7.4 dB/km for the 2nd band. It is noteworthy that the measured loss at these higher-order bands is found to be higher than the SSL limit, and this discrepancy increases as the wavelength shortens. The black dashed curve shown in figure is the calculated Rayleigh scattering loss (SRSL) of the silica material.

This is due to the fact that CL we are considering surface-roughness-free fibers for numerical simulations. Indeed, introducing surface roughness increases the CL for shorter wavelengths and the effect becomes stronger when the wavelengths get shorter in consistency with the measured loss spectra. The same trend is also observed for Kagome fiber as shown in Figure 5-2(b) where the CL dominates for wavelengths larger than 1000 nm, and the surface roughness induced SSL and CL increase becomes the dominant transmission loss for shorter wavelengths. Therefore, now it is more important to look into scattering effect on CL of the IC HC-PCF by considering the surface roughness of one of the constituent lattice tubes as aperiodic surface profile on the surface of the tube. Also in order to investigate leakage of HE₁₁ mode and to construct the far field distribution of scattered radiation out of a hollow-core of especially SR-TL IC HC-



PCF, the coming section provides more detailed theoretical analysis based on Poynting vector theory.

5.3.1 Impact of surface roughness on CL of IC HC-PCF

The effect of the surface roughness on CL in IC guiding fibers is less obvious, and in order to demonstrate its effects on CL, we considered the simulation of several SR-TL HC-PCFs with their cladding tube whose inner and outer radius exhibited spatial aperiodic perturbations $r_{p_i}(\theta)$ and $r_{p_o}(\theta)$ respectively to mimic a surface roughness along the azimuthal direction. The expressions of the radii can be written as:

$$\tilde{r}_{inn}(\theta) = r_{inn} + r_{p_i}(\theta) \quad (5.3)$$

$$\tilde{r}_{out}(\theta) = r_{out} + r_{p_o}(\theta) \quad (5.4)$$

here, r_{inn} and r_{out} stand for the inner and outer radius of a tube with no roughness. Figure 5-3(a) schematically shows the fiber and its constituent tube with modulated surfaces. Figure 5-3 (b) shows the spectrum of fractional integral of electric field intensity on the silica-air interface, F_{cc} and the calculated confinement loss (CL) for two values of peak to peak oscillation (h_{pp}) of 1.5 nm and 2.5 nm, being typical values of measured roughness in HC-PCF. Notice that in the CL calculation, the variation along fiber axis (z-axis) is not taken into account. Based on our experimental results we expect this variation along the z is of the same nature as in the azimuthal direction. Hence, our conclusion on transmission loss remains valid. The roughness profile was taken pseudo-random by considering the superposition of several aperiodic oscillating functions. Here, the SR-TL HC-PCF is taken to have $R_t = 7 \mu m$, $\delta = 2 \mu m$, $t = 400 \text{ nm}$. The results show that the effect of the surface roughness on F_{cc} is negligible for the different transmission bands.



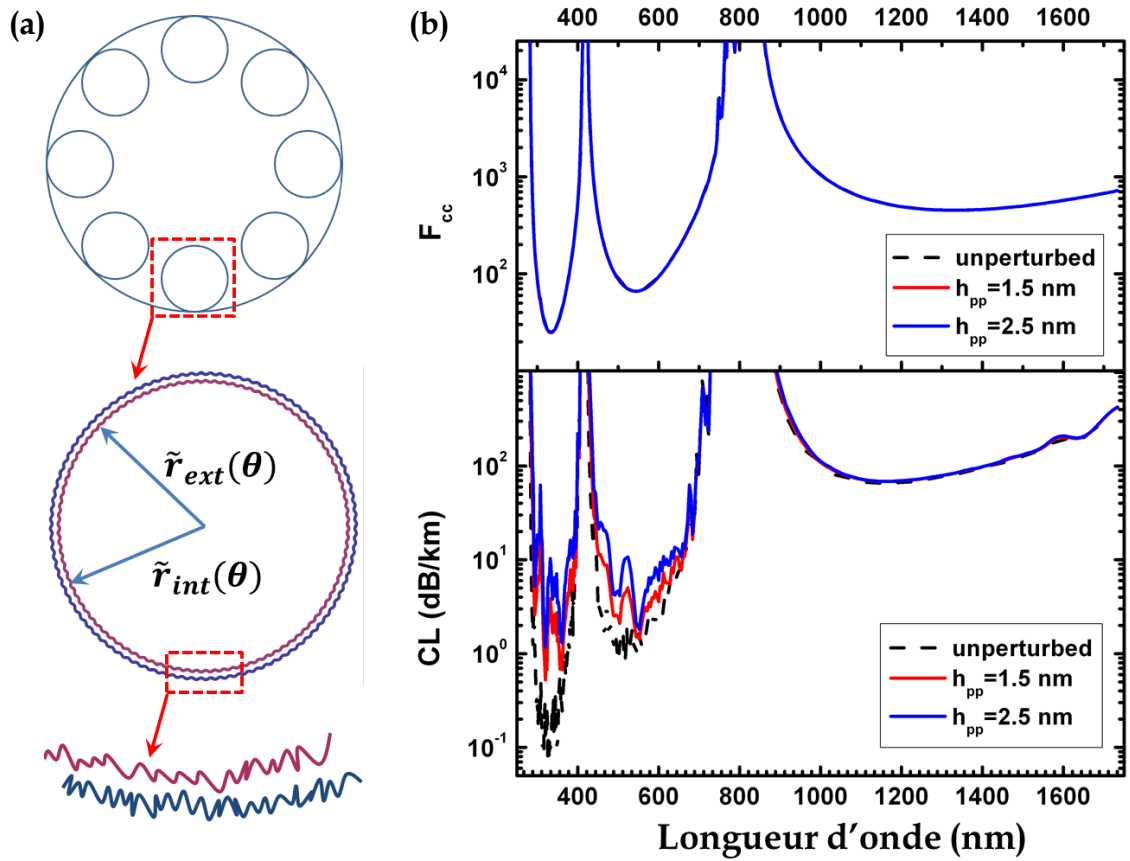


Figure 5-3 (a) Schematic of SR-TL HC-PCF showing spatial periodic perturbations at inner and outer surfaces of cladding tube. (b) top: Spectra of fractional optical overlap with the cladding, F , and bottom: confinement loss, CL , for the unperturbed fiber (black dashed line) and for for spatial aperiodic perturbation with two different peak-to-peak oscillations ($h_{pp} = 1.5$ nm and $h_{pp} = 2.5$ nm).

Furthermore, the CL spectra show an increase in CL only for higher-order bands (wavelengths shorter than 800 nm) while the fundamental band shows almost no change. The increase in CL gets stronger with decreasing wavelength where the loss is increased by a factor of more than 10 compared to a fiber with no roughness in the 2nd high order band. The observed CL increase in fibers with surface roughness at shorter wavelengths can be inferred by recalling the coupled-mode theory result which shows that a coupling coefficient of a waveguide with a perturbation is inversely proportional to the wavelength. Consequently, and because the IC guidance relies on decreasing the overlap integral between a core

mode and the cladding modes, a surface roughness creates a perturbation in the spatial index profile of the silica tube.

This perturbation and its periodicity affect the coupling between the cladding modes with the HE_{11} core mode, especially at short wavelengths [82]. This is also in consistence with the scaling law $|\langle \varphi_{clad} | \Delta n^2 | \varphi_{core} \rangle|^2 \sim m^{-2} DO$, where DO (dielectric overlap) is proportional to $F_{cc}(\lambda)$, and indicate that for the case of small surface roughness, the spatial overlap is much less affected than the modal transverse phase. Finally, this effect of the surface roughness explains the higher transmission loss at short wavelengths in the early IC guiding hypocycloid core-contour HC-PCF [16], [49, 53], [96].

5.3.2 Poynting vector study

The CL of identified fibers can be efficiently investigated by considering the imaginary part of the mode eigenvalue [97]. Unfortunately this approach doesn't give any information about the leakage mechanism such as the photonic structural components which are the dominant leakage channels. Here we propose to investigate the fiber leakage mechanisms by considering the power flux along the fiber radial direction. The density of power along this direction is given by the radial component of the Poynting vector:

$$p_r = \frac{1}{2} \vec{E} \times \vec{H} \cdot \hat{r}, \quad (5.5)$$

with \vec{E} , and \vec{H} being the electric and magnetic fields of the mode and \hat{r} the radial unit vector and p_r describes the modal power density flowing along the radial direction due to the leaky nature of the modes. The integration of p_r along a circle l surrounding the micro-structured region of the fiber gives the leaked power per unit of length:



$$P_r = \oint_l p_r dl. \quad (5.6)$$

Figure 5-4 compares the confinement loss computed by considering the imaginary part of the mode eigenvalue with that computed by starting from P_r through the formula:

$$CL = P_r/P_m \quad (5.7)$$

with P_m the power of the HE_{11} core mode. The figure clearly shows that the imaginary part of the mode eigenvalue and the formula of equation (0.8) give the same CL. We use the fact that p_r is an indicator of the core mode power leakage to investigate the effect of changing δ on the mode leakage and to analyze the azimuthal distribution of the confinement loss. Figure 5-5 shows the transverse profile of the normalized radial component p_{r_n} :

$$p_{r_n} = P_r/p_{z_{max}} \quad (5.8)$$

where $p_{z_{max}}$ is the maximum value of the longitudinal component of the Poynting vector on the fiber cross section. Four fibers having different δ at two representative wavelengths are considered: 530 nm, and 1200 nm, corresponding to the CL minimum in the fundamental and first transmission band.

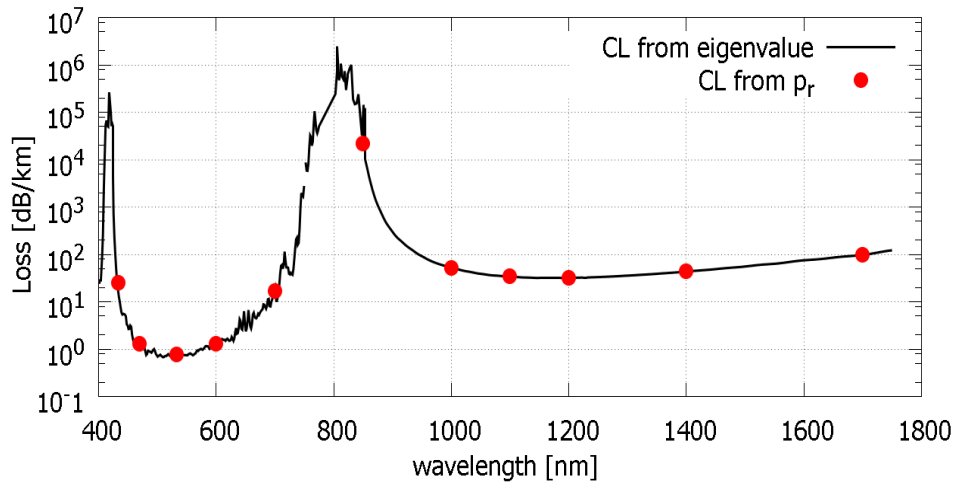


Figure 5-4 Comparison between CL computed through the mode eigenvalue (solid black line) and through P_r (red points) of a fiber with $\delta = 5.0 \mu m$.

Figure 5-5 clearly shows that for small inter-tube gap values (*e.g.*, $\delta = 2.0 \mu\text{m}$), the mode power mainly leaks out through the touching regions between the tubes and the surrounding silica, whereas for $\delta > 6.0 \mu\text{m}$ additional leakage through the inter-tube gaps takes place. This trend is further shown in Figure 5-6, which presents the angular distribution of p_{r_n} at a radius of $40 \mu\text{m}$. Tube-silica touching points correspond to an angle of 0° and multiples of 45° . The values of the maxima corresponding to the touching point do not significantly depend on δ . Lower values are observed at 530 nm than at 1200 nm , in agreement with CL spectra. Conversely, the values corresponding to the tube-tube gaps dramatically depend on δ . At 530 nm , with $\delta = 2 \mu\text{m}$ they are 20 dB lower than the touching points ones, whereas they are 10 dB higher with $\delta = 8 \mu\text{m}$. The dependence is a little bit weaker at 1200 nm , however the variation is about 20 dB .

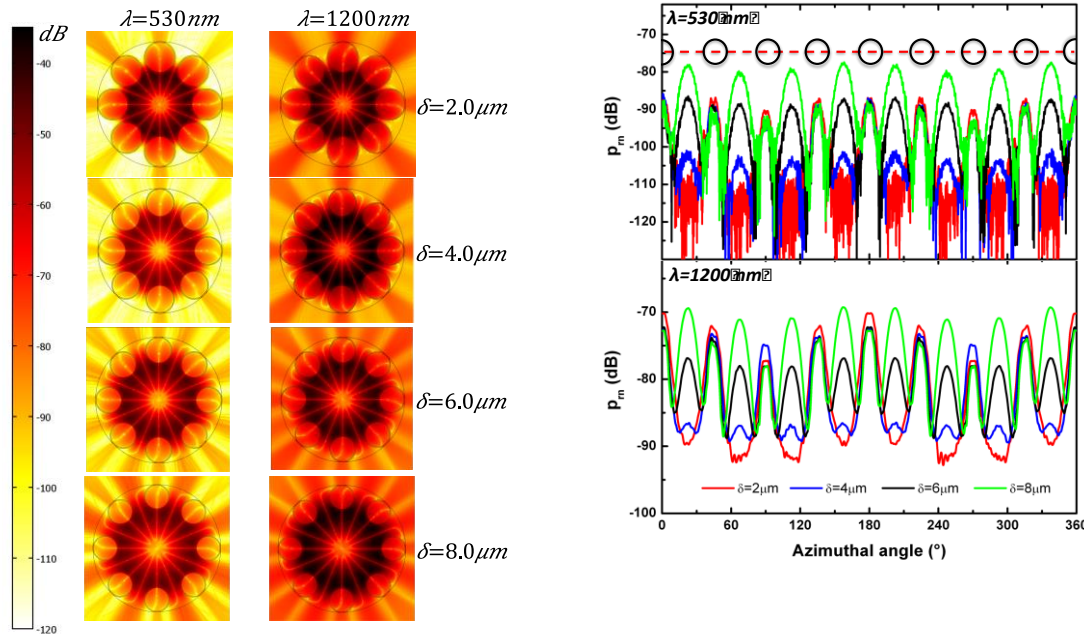


Figure 5-5 Transverse distribution of p_{r_n} for four fibers with $\delta = 2 \mu\text{m}$, $4 \mu\text{m}$, $6 \mu\text{m}$, $8 \mu\text{m}$, and at two wavelengths: 530 nm (*lhs* column) and 1200 nm (*rhs* column).

Figure 5-6 Azimuthal distribution of p_{r_n} in the silica surrounding the micro-structured cladding. The 8 tubes are placed at 0° and multiple of 45° . The position of the tubes along the considered perimeter (fixed at $40 \mu\text{m}$) is represented by black circles.

5.4 Simulations of SSL and CL in SR-TL IC HC-PCF

SR TL IC HC-PCF with average tubular gap of $2.5 \mu\text{m}$ and thickness $t=227 \text{ nm}$ that has been discussed in chapter 4 (Fiber #6) demonstrates an ultra large low loss window over one octave ranging from 600-1200 nm with loss between 10-21 dB/km (black solid line in Figure 5-7 (b)). Figure 5-7 (a) show the SEM image of the chosen fiber (SR TL IC HC-PCF). We can notice that in Figure 5-7 (b), the measured transmission loss is almost reaching its confinement limit of the design. But the loss trend still exhibits sharp increase at wavelengths shorter than 800 nm due to surface roughness on the tubes of the cladding ring. Therefore, in order to check the impact of surface roughness on performances, the chosen fiber has been numerically investigated for confinement loss and radial leakage of HE_{11} mode. Figure 5-7 (b) shows also the calculated SSL and CL in red dashed line and blue dotted curve respectively, and their combination gives total theoretical loss (green curve) to be compared with measured total loss (black curve).

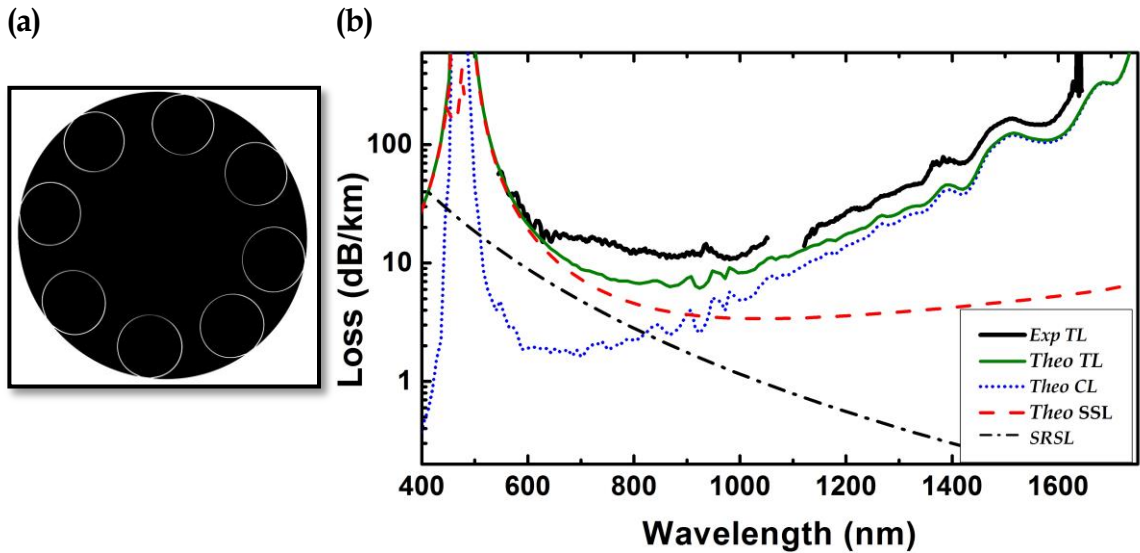


Figure 5-7 (a) SEM images of SR-TL IC HC-PCF and (b) its theoretical and measured loss spectra.

In case of tubular latticed IC HC-PCF, the gap between adjacent rings of the cladding determines the leakage of core modes. Also, as explained in the previous

section, CL is proportional to flux of Poynting vector that leaks radially outwards from the core mode. As shown in the Figure 5-8, this leakage has been investigated numerically for the real fiber structure.

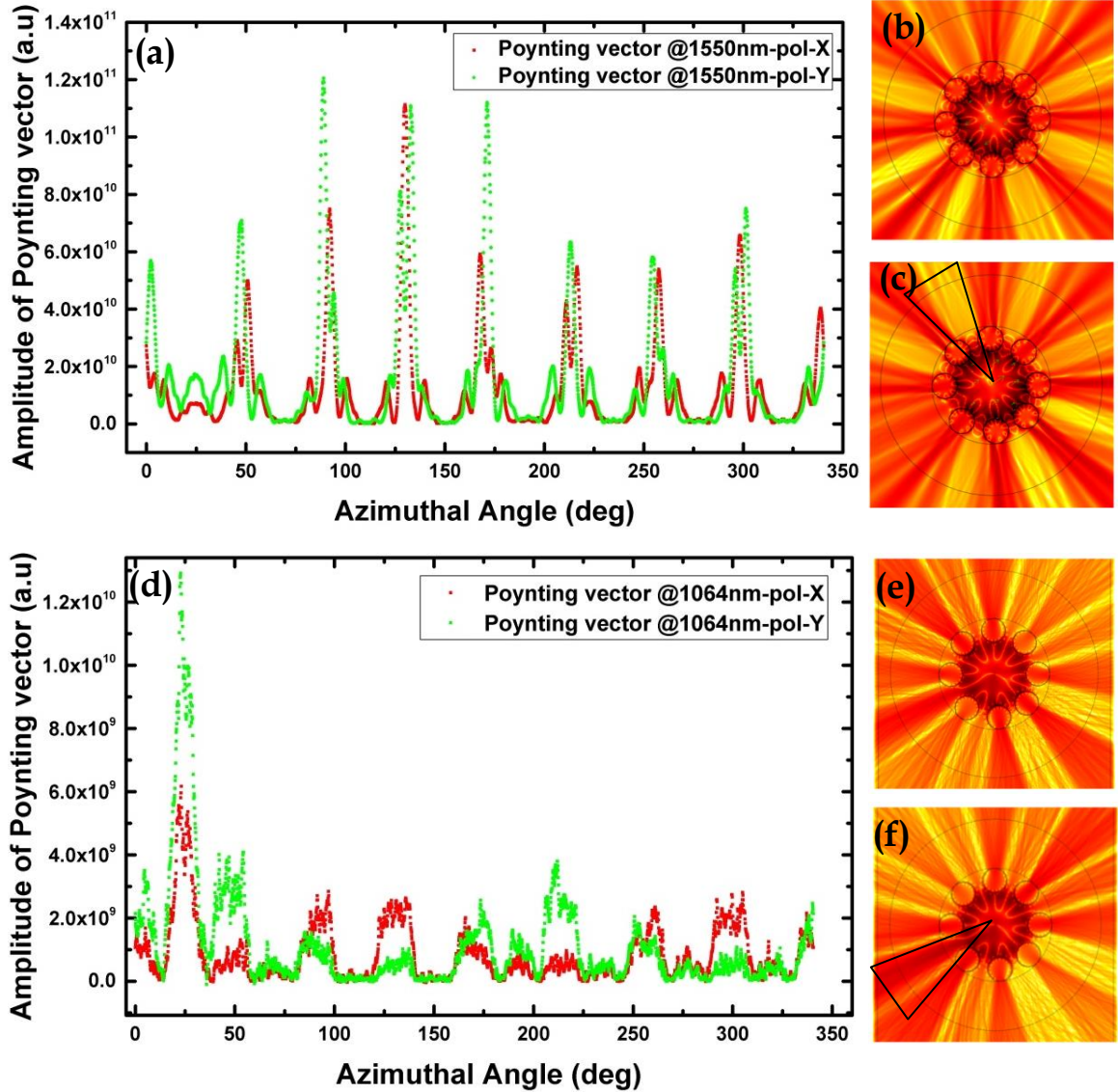


Figure 5-8 Angular distribution of scattering due to confinement in Tr-plan at (a) wavelength 1550 nm and (d) at 1064nm. Red and green spectra shown in the figures represent scattering for x and y polarizations respectively. The transverse profiles of corresponding Poynting vectors are shown on the left panel of the figures. The triangular inset of (b) and (c) represent abrupt peaks in the spectra shown in (a) due to non-uniformity in tubular gap.

Figure 5-8 (a) and (d) present angular distribution of scattering due to confinement which is measured in azimuthal plane, *i.e.*, perpendicular to

propagation direction. The spectra shown in red and green colors are for x- and y-polarizations respectively. The corresponding transverse profiles of p_r are also shown on the left of the Figure 5-8 (b) and (c) are for polarizations x and y respectively at 1550 nm, whereas (e) and (f) are for 10640 nm. The distributions are expected to have periodic peak and dip as in the case of an ideal fiber. But, for the real fiber scattering spectra as presented in the figures, are not the same as calculated ones, but are close to. This is due to imperfections in core-cladding structure in the real fiber. For example, the transmission loss shown in Figure 5-7, the test fiber (Fiber # 6) has lower values of CL at 1064 nm compared to 1550 nm, which is also evident from the simulations. The positions and amplitudes of p_r are dependent of the tubular gap of the cladding and also on operating wavelengths. As we can notice in Figure 5-8 (a), the peaks for both polarizations at 1550 nm represents severe leakage of p_r due to unequal tubular gaps in the cladding ring, which is also highlighted in the triangular insets of the Figure 5-8 (b) and (c). This same scenario of irregular peaks in amplitudes can also be noticed in Figure 5-8 (e) and (f) at 1064 nm.

5.5 Experimental set-up to measure scattering losses in IC HC-PCF

We have developed a new set-up to measure the scattering distributions due to surface roughness on the core-contour of IC HC-PCF. This setup not only measures the angular distribution of scattering in the plane of the fiber propagation or horizontal plane (H-plane), but also in transverse plane (Tr-plane). As shown in Figure 5-9, the set-up consists of a laser source, polarizer, beam splitters, photodetectors, lock-in amplifier set-up and 50 m length of SR-TL IC HC-PCF (Fiber #6). The input light from the laser source is split into two half beams by using a non-polarizing beam splitter in order to check any fluctuations from the



laser source. One part of the split beam is used as reference and second beam is injected into the test fiber with single mode excitation. Two highly sensitive InGaAs photodetectors are used in the experiment, one photodetector (PD1) to measure signal near the input of the fiber as a reference for the purpose of normalizing the scattering signal along various test points of the fiber measured at output by second photodetector (PD2). The output beam of the fiber is also divided by a 50/50 beam splitter in order to check the near field imaged with a high dynamic InGaAs sensor camera and measure output of the fiber.

In general, the scattered signal to be collected is very weak and could be influenced by any external noise; stray light in general could influence the experimental data. Therefore, to avoid the effect of any such noise on the measurements, the complete experimental set up is kept away from any stray light from outside. For precise measurement of scattering signal without noise or to increase the signal to noise ratio, a lock-in amplifier has been used. For this purpose, the input signal prior to coupling is chopped by sinusoidal voltage signal of 10 volts with a frequency of 100 Hz monitored with a function generator. Lock in amplifier (AMTEK signal recovery systems) has generally two ports on the front panel. One of the port is called reference to which chopped input signal has to be supplied, while the other port is supplied with the signal collected at the scattering point by the second photodetector (PD2). Lock-in amplifier is a device that “locks-in” on a signal of a particular frequency and amplifies it and rejects all other unwanted frequencies. Therefore, it can recover signals in the presence of an overwhelming noise background or, alternatively, it can provide high resolution measurements of relatively clean signals over several orders of magnitude and frequency. By adopting this technique to the experiment it is possible to reach signal to noise ratios up to 1000:1, which confirms better signal collection from the second photo detector.



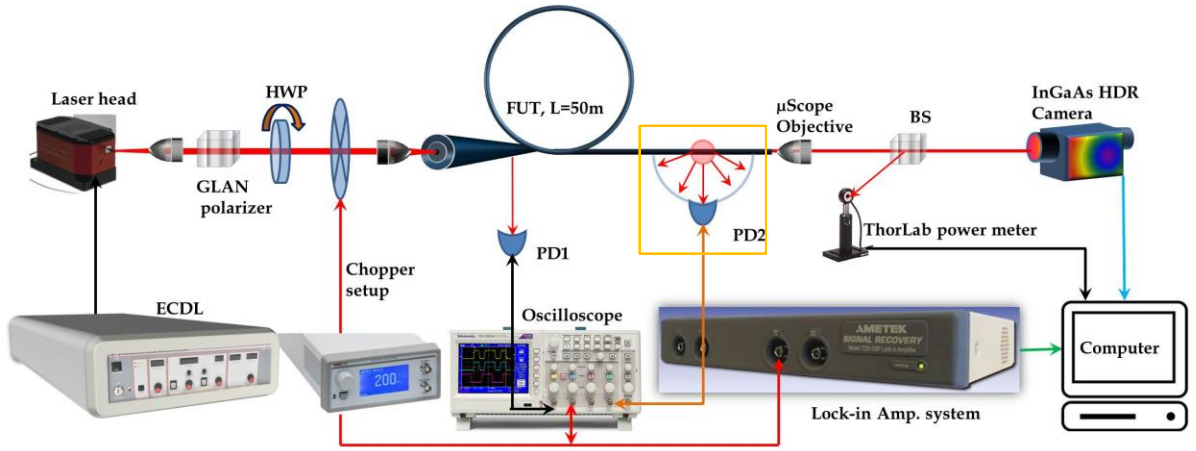


Figure 5-9 Experimental scheme to measure scattering distributions due to surface roughness of IC HC-PCF.

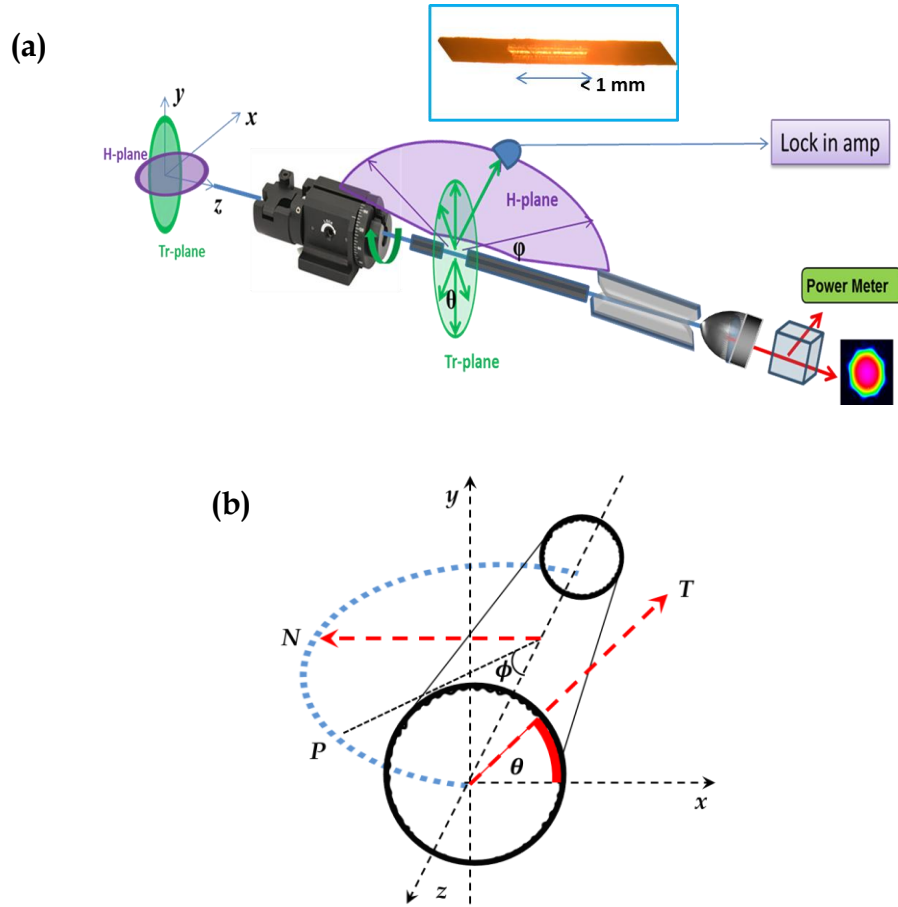


Figure 5-10 Scattered signal collection part of the experimental setup shown in yellow square of Figure 5-9. H-plane in blue color represent scattering field due to surface roughness and Tr-plane in green color represent scattering field due to confinement. (b) Schematic showing fiber cross-section and measurement points to record scattered signals points in H-plane (blue dashed line) and Tr planes.

As shown in the inset of the Figure 5-9, the segments of the test fiber to collect signal from are coated by black paint and a small opening is left about 1 mm that has to be exposed on to the photodetector. Firstly, the FUT is fixed in its position and the PD2 is rotated in the horizontal plane (H-plane) or in-plane of fiber axis so that it collects scattered signal majorly due to surface scattering. In second plane, in order to collect scattered signal due to confinement of the propagated light through it, the photodetector is fixed normal to the fiber axis and the fiber is rotated in its transverse plane (Tr- plane). Finally, lock-in amplifier gives the noise free scattered signals due to the surface roughness and as well due to confinement.

Figure 5-10 highlights the scattered signal collecting part of the experiment. The H-plane shown in blue is where the scattered signal mostly due to the surface roughness of the fiber core is distributed. A rotatable mechanical arm is included in the set up in order rotate the PD2 in H-plane to collect scattered signal by surface roughness. Also a fiber rotator in set-up used to rotate the fiber in Tr-plane to reconstruct scattering profile of HE_{11} mode that is radiated out of the fiber core. Figure 5-10 (b) schematically represents measurement positions of the PD2 in order to record scattering signal in H and Tr-planes.

5.6 Results

Following the experimental protocol, angular scattering distributions from test fiber due to surface roughness and confinement have been measured. Because of the limitations with experimental set-up, the scattering distributions were measured between 25 degrees to 165 degrees in H-plane, whereas in Tr-plane on a span of 155 degrees. The following sections present experimental results in both planes of the study.



5.6.1 Angular distribution of scattering due to surface roughness

Experimental results of scattering distributions in H-plane have been presented in Figure 5-11 showing the similar trends identified in [95] at different positions of the test fiber of 50 m length. All the spectra at 1064 nm and 1550 nm are presented in Figure 5-11 (a) and (b) respectively. Each of the measured spectra presented in the figure is normalised by the reference signals captured by the detector (PD1) placed at the input in order to remove any input fluctuation at the coupling end or from the laser source.

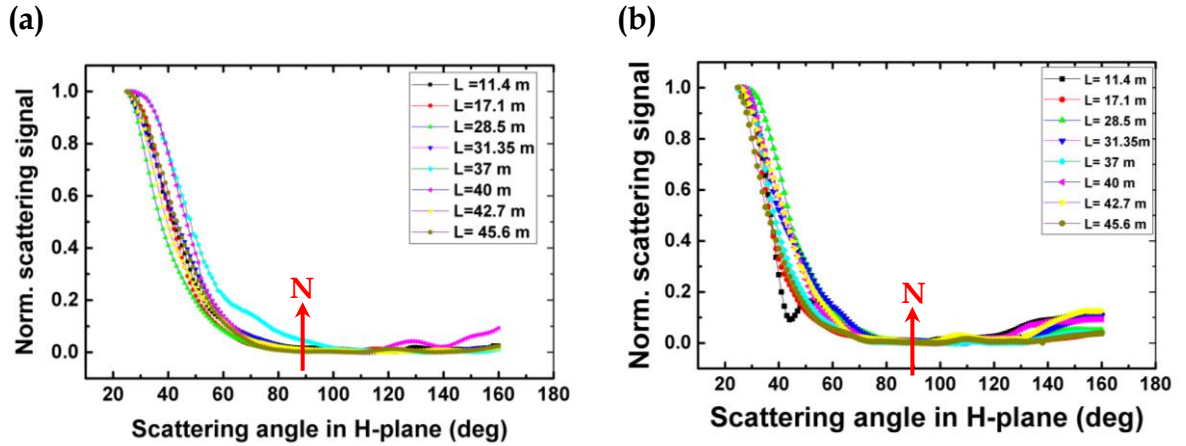


Figure 5-11 Measured angular distribution of scattering due to surface roughness at wavelength (a) 1550 nm and (b) 1064 nm. Numbers in the legend indicate the fiber position at which the scattered signal is collected is taken and H represent for measurements in horizontal plane.

It is worthy to observe that scattered radiation is dominant in forward direction and drops exponentially by an order of 100 at a point normal (point N) to the fiber. Again the scattered signal strength is raised by the factor of 10 from a point in Tr-plane to the backward direction of the propagation. This situation is demonstrated at 1064 nm and 1550 nm (see Figure 5-11). This confirms good agreement between experimental and calculated [95] distribution of scattering due to surface roughness. However, the calculated spectra of capillary waveguide

reported in [95] considered the core of the tube waveguide whereas experimental spectra presented here are for the IC HC-PCF. The difference in guiding mechanisms between both wave guides shows the spectral difference but in agreement with respect to the spherical distribution of surface scattering distribution of [93]. The non-zero scattered signals observed at the point of transverse plane explains the existence of distribution of scattering due to confinement in Tr-plane. The values of signal strengths at normal to fiber and forward as well as backward direction are also dependent on the operating wavelengths. For the FUT, we used for the experiment is SR-TL-IC HC-PCF has more confinement loss than the surface scattering at 1550 nm, but at 1064 nm the surface scattering dominates the other. As shown in Figure 5-11, at 90 degrees, the scattered signal strength at 1550 nm (red circled curve) is greater than that of 1064 nm (blue squared curve). This is expected due to contribution of scattering due to confinement on surface scattering.

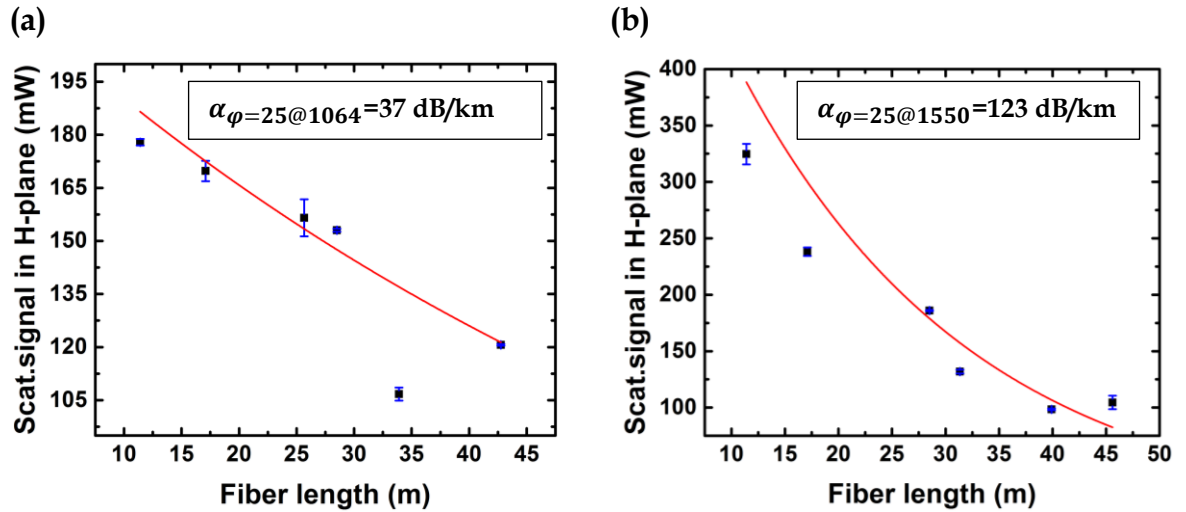


Figure 5-12 Curves fitting of scattering data to deduce decay rate coefficient of scattered signal at (a) 1064 nm and (b) 1550 nm. Red curve shown in the figures represent exponential curve fits.

Scattered signals in H-plane especially at 25 degrees H-plane is dominated by surface roughness. Therefore, to find the decay rate coefficients of the scattered signals with respect to fiber length the following exponential equation is used:

$$y = ae^{(bx)} \quad (5.9)$$

where, y is signal strength, x is fiber length and b gives loss coefficient in per meter which is multiplied by 4,323 to convert into dB/km. As shown in 5-12, the spectra are fitted by the exponential curves shown in red color. Finally, the deduced scattered signal decay rates, $\alpha_{\varphi=25}$ at 1064 and 1550 nm are found as 37.6 and 123 dB/km respectively.

5.6.2 Angular distribution of scattering due to confinement

The collected scattered signal at 90 degrees angle in H-plane (at point N in Figure 5-11) is generally included with components of scattering due to surface roughness and also due to confinement. In order to discriminate contribution of surface scattering on confinement we have investigated their decay coefficients (α_T) in confinement plane (Tr-plane). To do this, PD2 is rotated in Tr- plane about the fiber axis by fixing the detector at point N in H-plane (*i.e.* at $\varphi = 90$).

Figure 5-13 shows of the measured scattered light spectra radial direction (confinement plane) or in Tr-plane of the fiber (show in blue curve). The red and green curves shown in the figure are calculated Poynting vector distributions for both orthogonal (x and y) polarizations for the real fiber. We can see from the figure that spectra of scattered signal are not periodic and not well patterned as in the simulations of ideal fiber. This is due to the imperfection in the symmetry which is inherent to fabrication process that leads to the mixing of radiations of core mode for both polarizations in radial directions. Therefore, the measured

distribution of scattering due to confinement in Tr-plane can be approximated as a combination of Poynting vectors of both polarizations.

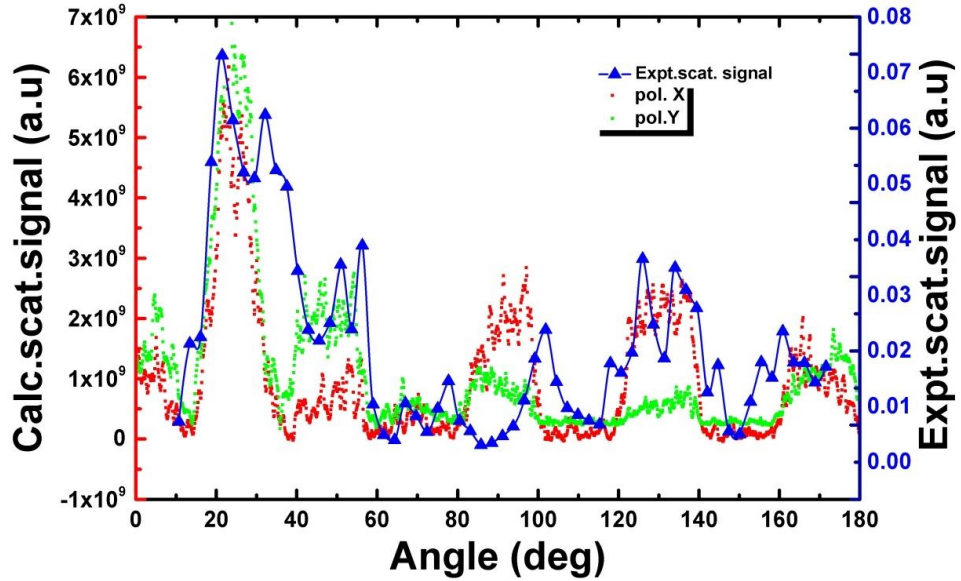


Figure 5-13 Measured scattering distribution (blue triangular curve) due to confinement loss in Tr-plane and comparison with numerical result (red for x – polarization and green for y-polarization).

Apart from symmetry of the structure, scattered signal due to surface roughness affects the radial leakage pattern which is noticed by empirical formula in equation (5.2). Such radial leakage is also affected by multiple interferences at silica/air interfaces of the cladding as light leaks out. However, as we can notice from the Figure 5-13, with optimized our set-up the measured spectra almost match with theoretical simulations. The maximum scattering signal (T_{max}) at 20 deg in Tr-plane is due to the light leakage through tubular gap of the test fiber, whereas the minimum signal (T_{min}) at 43 degrees corresponds light leakage at the tube. These two signals in confinement plane, namely T-max and T-min are used to deduce scattering coefficients $\alpha_{T_{max}}$ and $\alpha_{T_{min}}$ respectively. In order to find these coefficients, we have measured scattered light leakage in Tr-plane at different sections along the fiber length at the wavelengths 1064nm and 1550 nm.



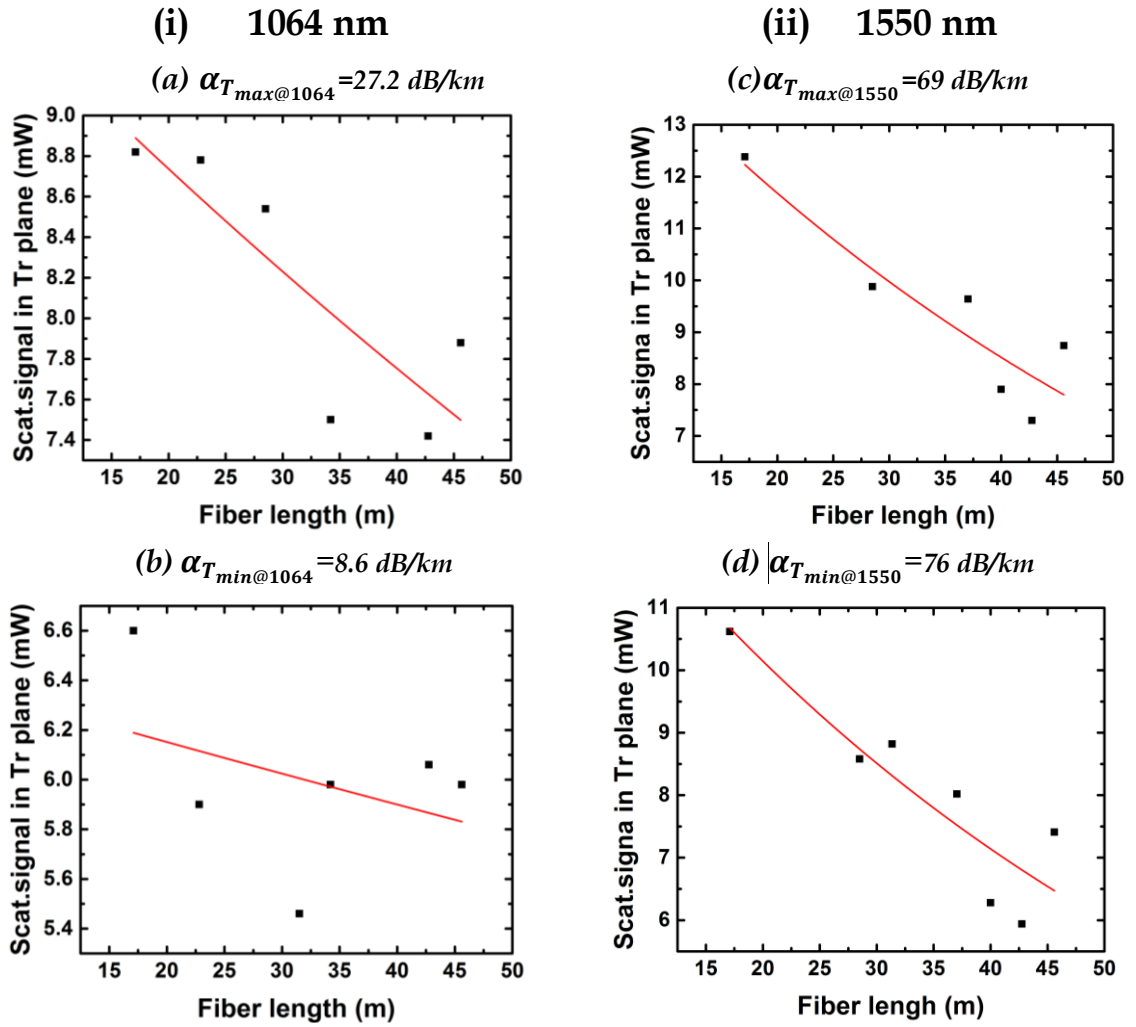


Figure 5-14 (i) Curve fittings of measured scattered signals with fiber length at (i)1064 nm and (ii) 1550 nm in Tr-plane. (a) and (c) represent evolution of maximum signals. Similarly (b) and (d) represent minimum signal evolution.

Analyses of scattered signals in Tr-plane (at $\varphi = 90^\circ$ of H-plane) are summarized in Figure 5-14. The evolutions of T_{max} and T_{min} with fiber length at 1064 nm are shown in Figure 5-14 (i)(a) and (i)(b) are, whereas Figure 5-14 (ii)(a) and (ii)(b) are meant for 1550 nm. All of these curves were fitted with the Equation 5-9 and scattering decay coefficients were found as $\alpha_{T_{max@1064}} = 27.2 \text{ dB/km}$ and $\alpha_{T_{min@1064}} = 8.6 \text{ dB/km}$ at 1064 nm. Similarly for 1550 nm the coefficients are found as $\alpha_{T_{max@1550}} = 69 \text{ dB/km}$ and $\alpha_{T_{min@1550}} = 76 \text{ dB/km}$ at maxima and minima of the scattered signals respectively. The same protocol is repeated also for wavelength

532 nm to find scattered loss coefficient $\varphi = 90$ of H-plane ($\alpha_{\varphi=90}$). Table 5-1 presents all of the experimental results. Finally, Figure 5-15 shows comparison of measured and theoretical loss spectra. The measured spectra of $\alpha_{\varphi=25}$ are then compared with theoretical SSL (red dashed curve) defined by expression:

$$\text{Theo. SSL}(\lambda) = F_{cc}(\lambda) * \varsigma * 10^{-2} \left(\frac{\lambda[nm]}{1700} \right)^{-3} \quad (5.10)$$

where F_{cc} is the power fraction of core mode into cladding defined by equation 5.1, and it is calculated from FEM (COMSOL) simulations and ς is fit parameter related to the surface roughness RMS height.

Wavelength (nm)	Loss coefficients (dB/km)		
	$\alpha_{\varphi=90}$		$\alpha_{\varphi=25}$
	$\alpha_{T_{max}}$	$\alpha_{T_{min}}$	
532	555		
1064	27.2	8.64	37.6
1550	69	76	123

Table 5-1 Summary of measured scattering coefficients in horizontal and transverse planes.

There are several factors for the deviation of experimentally measured scattering coefficients with respect to calculated loss spectra. These uncertainties are mainly due to, position of signal recording, torsion/twists in the fiber during the detector rotation in Tr-plane, length for the fiber segments exposed for the signal collection, interference of scattered signal at air/silica interface of the cladding and even tiny movement of fiber, defector and frame of the rotating arm used for the experiment. In order to avoid these uncertainties, the protocol is repeated several times and average scattering decay rates with error bars are also presented in the Figure 5-15. At 1550 nm the measured $\alpha_{\varphi=25}$ (red circle point) which is supposed due to surface roughness has higher values than theoretical surfaces scattering loss (Theo.SSL). This is due to domination of confinement loss



over surface scattering loss. The decay rates of maxima and minima (blue and green triangles) measured in Tr-planes has the acceptable with respect to calculated CL spectra at 1550 nm. Therefore, at this wavelength, the decay rates α_T can be considered as α_{CL} . At 1064 nm, theoretically SSL dominates CL. Measured $\alpha_{\varphi=25}$ at this wavelength is also seems to have higher values than scattering decay rates α_T in confinement plane for both maxima and minima signals. Among two measured decay rates in Tr-plane, loss coefficient α_{Tmin} (green triangle) is in good agreement with Theo. CL at 1064 nm.

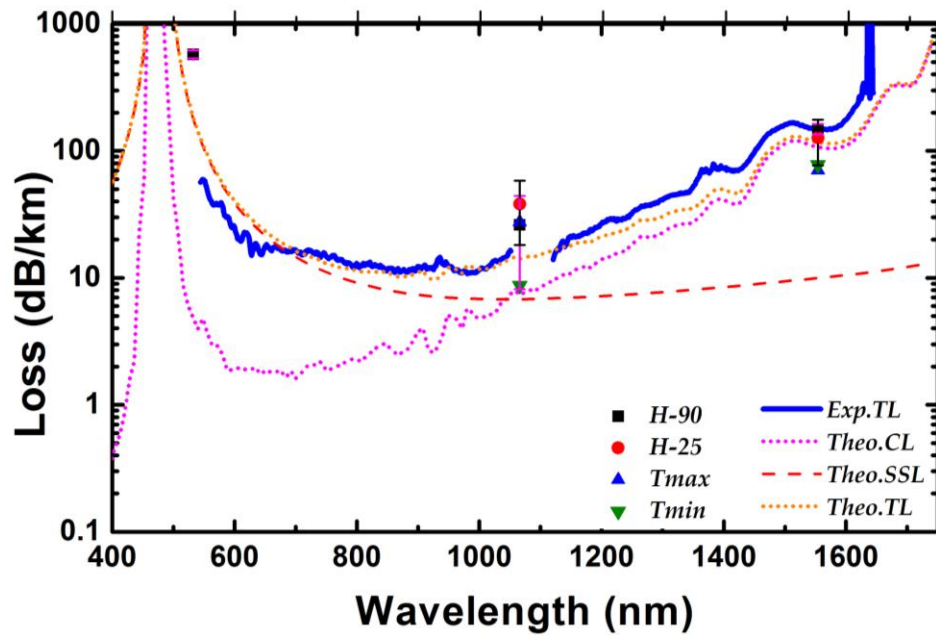


Figure 5-15 Comparison of calculated total loss spectra (orange dashed curve) of the single ring IC HC-PCF and its measured transmission loss spectra (blue solid curve). Red dashed and pink dotted curves are theoretically calculated spectra. Black squares and red circles are measured scattering coefficients in horizontal plane and triangular points are measured scattering coefficients in Tr-plane.

Finally, scattering decay coefficient measured at 532 nm at angle 90 degrees ($\alpha_{\varphi=90}$) shows that at shorter wavelengths, the total loss is mainly due to surface scattering (*i.e.* α_{SSL}) and the confinement loss is negligible as shown in the figure.

5.7 Summary

SR-TL IC HC-PCF has been further investigated of surface roughness induced losses. Sinusoidal roughness profiles with specific period and depth has been theoretically implemented on the core-contour of the fiber designs under consideration in order to mimic the SCW occurring during the fiber fabrication. Then simulations were performed on this real fabricated fiber structures in order to check, its impact on fractional optical overlap with the cladding, CL and leakage of Poynting vectors in radial direction which depends on the wavelength. These numerical results have been realized experimentally with a new optical scheme and finally the angular distribution of scattering induced by surface roughness in the plane of the fiber and its impact on CL along with its angular distribution in transverse plane of the propagation have been studied.

It has been observed that for the case of tubular latticed fiber, the leakage of guided modes in H-plane is comparable with numerical simulations. The strength of the scattered signal in this plane is more dominant in the forward direction by the order of 150 than the signals at the points in Tr-plane. And in the backward direction the leakage strength is more than an order of 10 compared to Tr-plane. Finally, by using newly developed experimental set-up we scattering loss coefficients at 532 nm, 1064 nm and 1550 nm have been investigated. The contributions of major loss sources at specified wavelength have been analysed. In order to further minimize the uncertainties in experimental results and to achieve more accurate results compared to numerical results, the experimental set-up still has to be optimized and hence a further investigation has been recommended to finish this study.





Conclusion

The present thesis reported on theoretical and experimental linear characterization of several Inhibited-coupling (IC) guiding HC-PCFs whose structural parameters have been optimized for both further understanding the guidance mechanism, and improved transmission loss.

Inhibited-Coupling optical guidance contrasts with photonic bandgap (PBG) or total internal reflection guidance by the remarkable co-existence of guided core mode and a continuum of cladding mode at the same effective index-frequency without strongly interacting. In analogy with quantum mechanics or condensed matter physics, the IC guidance relates to quasi-bound or bound state in a continuum, whereby coupling between a guided core mode embedded in a continuum of modes can be dramatically reduced (or suppressed in the case of a proper bound state) if the spatial overlap of the modes is minimized and/or their transverse mismatch (*i.e.* symmetry incompatibility) is enhanced. We reviewed the historical and scientific key principles of the development of IC HC-PCF, with an emphasis on the introduction of hypocycloid core-contour which rendered such fiber transmission performance into a superior alternative to PBG guiding HC-PCF. Within this context of conceptual novelty, we have experimentally demonstrated the nature of quasi-bound state in a continuum of the core guided mode of Kagome IC HC-PCF by unveiling asymmetric Fano profiles in the fiber transmission spectrum. By considering scattering features as a perturbation to the system, numerical simulation on the test fiber explained polarization dependent asymmetric fano features in its confinement loss spectrum. The experimental spectra exhibit the distinctive Fano shape and are highly dependent with the laser input polarization. Such experimental observation has been brought out by the



accurate comparisons of the Fano profiles with theoretical simulations and near field evolution versus the polarization of the input.

The use of IC model as a design tool led to the development of two hypocycloid-like (*i.e.* negative curvature) core-contour IC HC-PCFs with record transmission performances. The first fiber consists of Kagome lattice HC-PCF with a loss figure as low as 8.5 dB/km at 1 μ m, and the second is based on a tubular amorphous lattice cladding which loss is as low as 7.7 dB/km at 750nm. Also, both fiber designs have been scaled, so their fundamental transmission band is as large as possible whilst keeping the transmission loss to an acceptable level. This implies preserving the fiber physical integrity, especially their negative curvature, with cladding silica struts thickness of less than 400 nm. The results show fundamental band transmissions that combine over one-octave wide bandwidth with loss below 30 dB/km. Both fibers present a near-single modedness, with ~20 dB extinction between HE₁₁ fundamental core mode and the strongest first higher-order mode (HOM). The reported fibers not only perform low loss and broadband transmission but also are capable of high power laser delivery due to large mode core areas.

The thesis covers experimentally and theoretically also the limiting sources of the transmission loss of IC HC-PCF. The results show the loss is dominated by light scattering for wavelength shorter than 1 μ m, and by confinement loss (*i.e.* design limit) for longer wavelength.

The thesis results could be exploited to further improve understanding the guidance IC HC-PCF, to design HC-PCF with better transmission loss and to characterize them more accurately. Future work include improving the HC-PCF by reducing the surface roughness of its core-contour, developing a more comprehensive and sensitive modal content analyzer.



Annexure A

Numerical simulations of optimized Kagome IC HC-PCFs

As we have concluded from previous chapters, fabricating Kagome cladding with thinner silica struts in order to achieve broader transmission bands would also rise surface scattering losses at the same time due to capillary waves formation during the fabrication process. Therefore, numerical simulations were performed on fabricated IC HC-PCFs to validate and study the impact of this extra source of loss. Especially, we experimentally notice that the loss level is suddenly increased when the wavelength became shorter than 1 μm which is in contradiction with the theory. The evaluated total losses (TL) will then be a combination of confinement loss (CL) and the surface scattering loss (SSL), and can be simply expressed by:

$$\alpha_{TL} = \alpha_{CL} + \alpha_{SSL} \quad (\text{A.1})$$

Within this context two fabricated Kagome fibers which have been presented in chapter 4 are studied. First section of the annexure deals with simulations of ultra-low loss 7-cell hypocycloid Kagome IC HC-PCF (noted Fiber #1 – section 4.3) which presents record values of 8.5 dB/km at 1030 nm and the second one focus on a fiber (noted Fiber #2 – section 4.4) which demonstrates a broad transmission band with a minimum loss of 30 dB/km at 780 nm. The numerical simulations have been done in collaboration with Luca Vincetti.



A.1 Simulation of fiber #1 and results

Simulations have been performed on the actual fiber structures obtained from its SEM image (see Figure A-1(a)) with an ideal structure (see Figure A-1(b)). The real fiber profile used for FEM simulation is modified according to structural variation from SEM image as shown in Figure A-1(c). The quarter of the extracted fiber profile is considered for FEM simulations in order to reduce the computation time. In the present case, the fiber structure presents a core radius $R_{in} = 30 \mu m$, a negative curvature parameter $b = 0.86$ and a silica strut thickness $t = 835 \text{ nm}$.

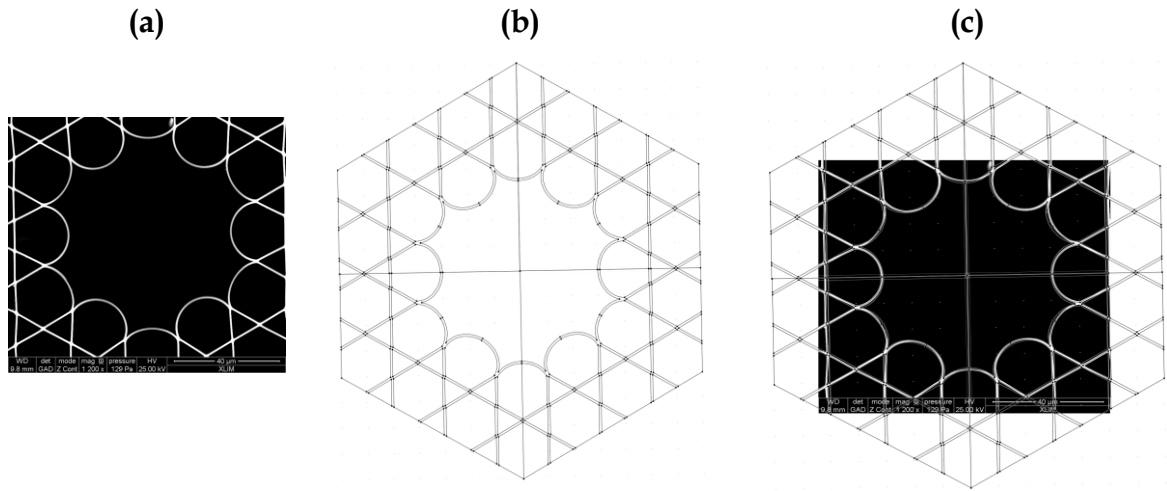


Figure A- 1. (a) SEM image of fiber #1. (b) Ideal Profile created in FEM simulation tool. (c) overlapping of SEM image with FEM profile to create real fiber structure for simulation.

Figure A-2 shows results of measured transmission loss together with numerical simulations performed on the real fiber structure for the spectral range between 900-1350 nm, where fiber present its record transmission loss. Notice that a bend radius of 35 cm is taken into account in order to use the experimental conditions. Finally and very importantly, thickness fluctuations along z-direction of the real fiber have also been considered. Therefore, CL of 11 fibers with different strut thickness varying from 800 nm to 820 nm with a step of 2 nm has been simulated.

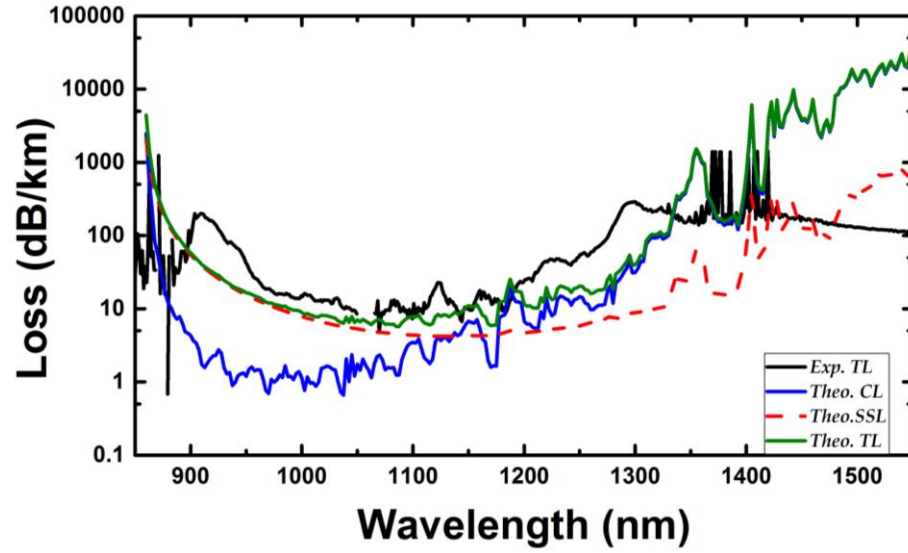


Figure A-2 Comparison of calculated and experimental loss of the fiber #1.

This variation of ± 10 nm is centered with respect to measured thickness value of $t=810$ nm which give over all tolerance not more than $\pm 1.2\%$. Total loss calculated in Figure A-2 is considered empirical formula for SSL mentioned in Chapter 5.

$$SSL(\lambda) = F(\lambda) * \varsigma * 10^{-2} \left(\frac{\lambda[\text{nm}]}{1700} \right)^{-3} \quad (\text{A.2})$$

The parameter F in the equation quantifies the fraction of HE_{11} power overlapped with silica cladding and ς is the fit parameter that depends on fiber drawing parameter and structure of the fiber. For the better fit we considered this fit parameter as 5. However, in both calculations, SSL dominates CL for the wavelengths lower than $1 \mu m$ ($SSL > CL$, at $\lambda < 1 \mu m$) since light propagating along the fiber is more strongly reradiates spherically due local variations in effective index at shorter wavelengths and couples again with guided modes which results in SSL. For wavelengths superior to $1 \mu m$, CL dominates SSL ($CL > SSL$, at $\lambda > 1 \mu m$). Finally the theoretical TL is found in good agreement with experimental observations and confirms that SSL is the main factor that limits the optical performances at shorter wavelength.

A.2 Simulation of fiber #2 and results

This section discusses about theoretical studies of optimized Kagome fiber IC HC-PCF discussed in section 4.3 of Chapter 4. This 7-cell defect Kagome fiber is designed for ultra-broad fundamental band transmission with a minimum value of 30 dB/km at 780 nm. The SEM image of the fiber considered for simulations is presented in Figure A-3 (a) and the same numerical process is followed as explained above. This fiber presents b curvature parameter equal to 0.45, silica struts with a thickness of 300 nm and $R_{in}/R_{out} = 51/57 \mu\text{m}$. From Figure A-3 (b), we can notice the elongate struts around the core and the change in its thickness.

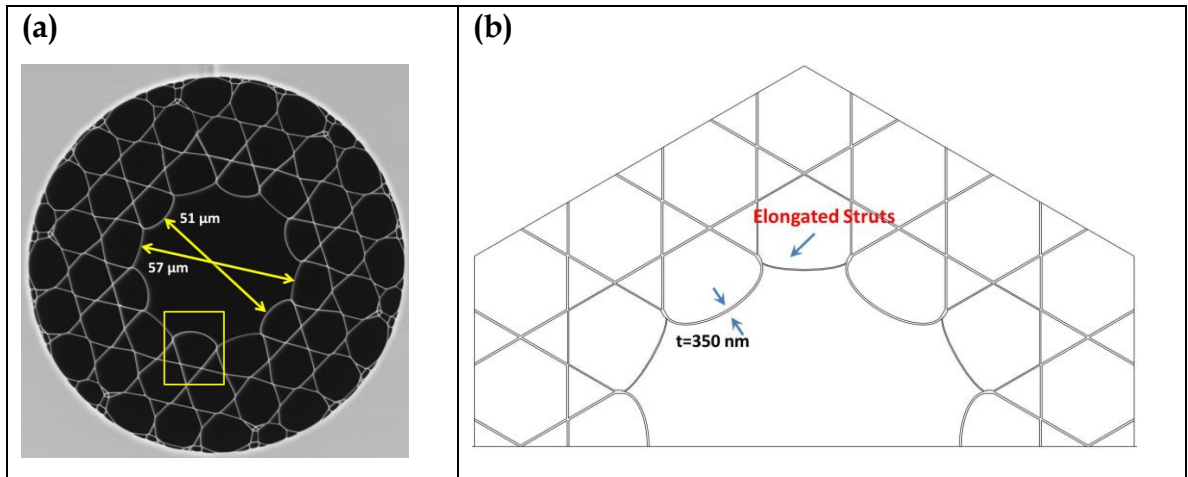


Figure A- 3 (a) SEM image of the 7-cell Hypocycloid Kagome fiber #2. (b) Semi cross section of fiber profile extracted for FEM simulations.

The measured loss spectra are presented in Figure A-4 along with the simulated loss spectra results of CL, SSL and TL (CL+). We can notice that SSL shown in dashed red curve is less dominant over CL (dashed blue curve) at higher wavelengths (SSL < CL at $\lambda > 800 \text{ nm}$) and has negligible impact on TL. At shorter wavelength regions, CL and SSL follow the reversed trends as previously observed.

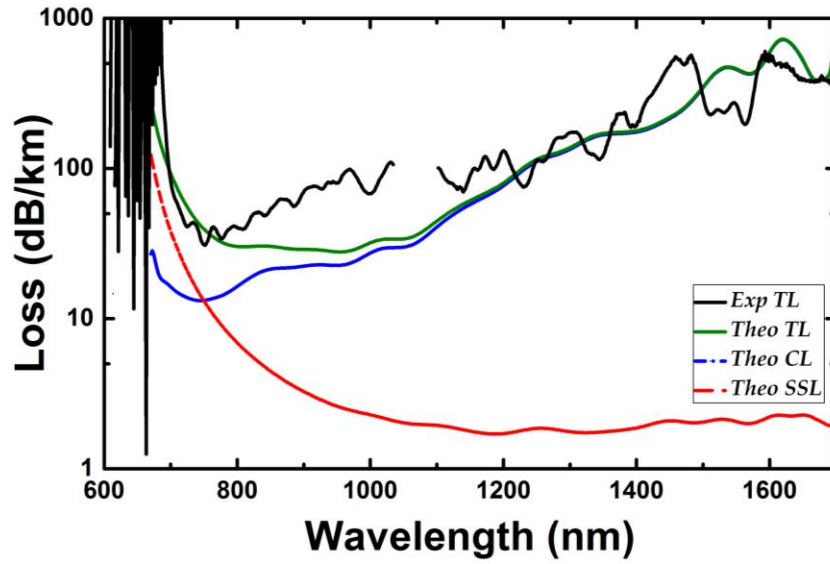


Figure A- 4 Measured and calculate loss spectra of the 7-cell hypocycloid Kagome IC HC-PCF (fiber #2).

A.3 Summary

To conclude, simulations show good agreement between the confinement loss and the experimental loss curves for wavelengths in the infrared region. However, at shorter wavelength regions, the extra source of loss from the surface scattering appears and became the dominant factor. It is also important to note that while calculating SSL for both of fiber cases, we used different coefficient factors of fit parameter. This is because, roughness features and its impact on CL varies with shape of the core and fiber drawing parameters.



Annexure B

Ultra-large core size hypocycloid-shape IC HC-PCFs for high-energy laser beam handling

This annexure presents fabrication and characterization of 19-cell hypocycloid-shape Kagome IC HC-PCF fibers with enlarged core size typically with diameters larger than 100 μm . The optical characterizations supported by theoretical calculations show that this IC design presents low propagation loss (100 dB/km) over broad spectral range combined with low chromatic dispersion and ultra-low power overlap with silica surround. All these performances make them an efficient solution for ultra-high power laser handling and USP laser delivery applications.



B.1 Introduction

Since seminal report of Kagome IC HC-PCF in 2002 [6] and its hypocycloidal core shape in 2010 [16] fibers of this class demonstrated record level broadband transmissions and loss figures down to tens of dB/km in different spectral ranges spanning from visible to mid IR [49] along with dramatic optical overlap reduction by 1000 times and lowered dispersion by 100 times than PBG class. Recent 7-cell hypocycloid core shaped IC HC-PCF designs with loss figure of 40 dB/km filled with air demonstrated compression of 850 fs wide and 105 μ J energy USP down to 300 fs at 1550 nm [52]. In parallel to progressive developments of USP lasers sources with power levels of kW, IC HC-PCFs shall be further optimized to be more robust and efficient to deliver high power USP lasers. One of the possible optimization ways is to enlarge the core size of current 7-cell Kagome record fiber by 19-cell defect to increase fiber performances in two ways. Firstly, the spatial optical overlap with the silica material is decreased. Secondly, by enlarging fiber's core diameter increases ionization threshold of air inside the core. Though replacing air with helium gas can minimize optical nonlinearities, giving the input energies more than 100 μ J m will reach ionization threshold of the filled in gas. Therefore, the ionization thresholds of the gases filled inside the core are shifted to higher values by enlarging the core size.

Within this context this chapter discusses about the design, fabrication and linear characterization of several hypocycloid-core-contour 19-cell Kagome IC HC-PCF in order to assess the fiber suitability to transport ultrafast laser beams. For the first time to our knowledge, hypocycloid-core Kagome HC-PCFs with core diameter that exceed 100 μ m were fabricated to covering all the visible and IR spectral range according to the transmission spectra of each fiber. These fibers exhibit low transmission loss of 100 dB/km (state-of-the-art for a 19-cell design),



low dispersion and ultra-low optical power overlap with silica cladding down to a ppm record level combined with acceptable bending induced transmission loss. All these performances make these 19-cell fibers an excellent platform for high power laser handling, USP delivery with pulse energy that could in theory be as high as 100 mJ, and also open new opportunities as for the recently introduced exotic plasma photonics applications [98]. Table B.1 illustrates some values of characteristics figures (dispersion length, nonlinear length, self-focusing critical power, ionization threshold intensity) which affect USP propagation dynamics in different core size and in gas filled fibers [43].

	He-filled 19-cell fiber	Air-filled 19-cell fiber	He-filled 7-cell fiber	Air-filled 7-cell fiber
Core diameter, R_{in} (μm)	80	80	55	55
Dispersion length, L_d (m)	555	577	28	28
Nonlinear length, L_{NL} (m)	1.9	0.09	0.9	0.04
Self-focusing critical power, P_{cr} (GW)	2026	9.5	2026	9.5
Ionization threshold intensity, I_{it} ($\text{TW}\cdot\text{cm}^{-2}$)	200	40	200	40

Table B.1 Dispersion length, nonlinear length, self-focusing critical power and ionization threshold intensity [99] for different HC-PCF configurations.

B.2 Designing the enlarged hypocycloid 19-cell core

Recent 7-cell hypocycloid Kagome fiber with effective area (A_{eff}) of $1500 \mu\text{m}^2$ filled with helium gas demonstrated its capability as flexible and robust means to deliver USP at peak power of 87 MW and average power 3 W (fiber output of 74 uJ, 850 fs and 40 kHz repetition rate) at 1550 nm [52]. In order to enhance USP delivery capabilities, its effective core size has to be enlarged

(i.e. a core diameter in the range of $100\ \mu\text{m}$ compared to the current $50\text{-}60\ \mu\text{m}$) keeping the other structural parameters almost unchanged. This can be simply done by removing an extra cladding ring to increase the effective core area more than $3000\ \mu\text{m}^2$ than 7-cell designs, and the resultant fiber is called as 19-cell IC HC-PCF.

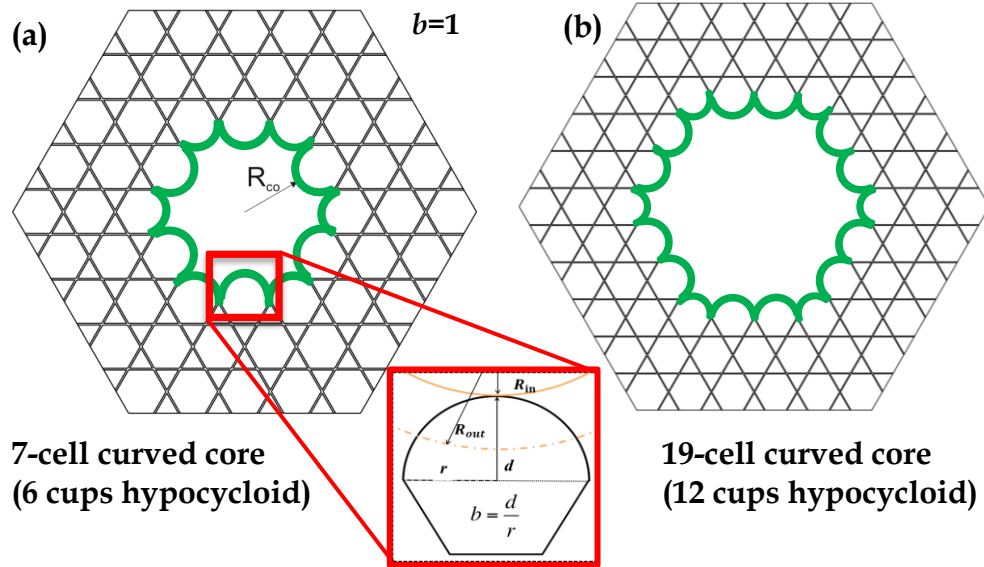


Figure B-1 Process of enlarging hypocycloid core size from (a) 7-cell core to (b) 19-cell along definition of b parameter. Hypocycloid core is highlighted in green color and inset shows the definition of b .

Figure B-1 explains enlarging A_{eff} of core size of Kagome IC HC-PCF from 7-cell to 19-cell and highlights the core contours in green color. Even though, enlarging the core can solve USP laser delivery task, but at the same time it lifts few drawbacks also. Firstly, large hollow-core size allows unwanted multimode propagation. Secondly, as it is evident from the Figure B-1, the number of inner hypocycloid cups are doubled as it is transformed into 19-cell design which potentially will cause the increase of spatial optical power overlap (SPOP) between core mode and silica cladding. Consequently, these 19-cell designs were numerically* investigated in order to check the impact of negative core curvature especially on its confinement loss (CL), modal content, bending sensitivity and

finally investigation of LITD to assess their suitability for high energy applications. Below sections provide numerical simulations and experimental linear characterizations in this regards.

B.2.1 Impact of negative curvature on confinement loss

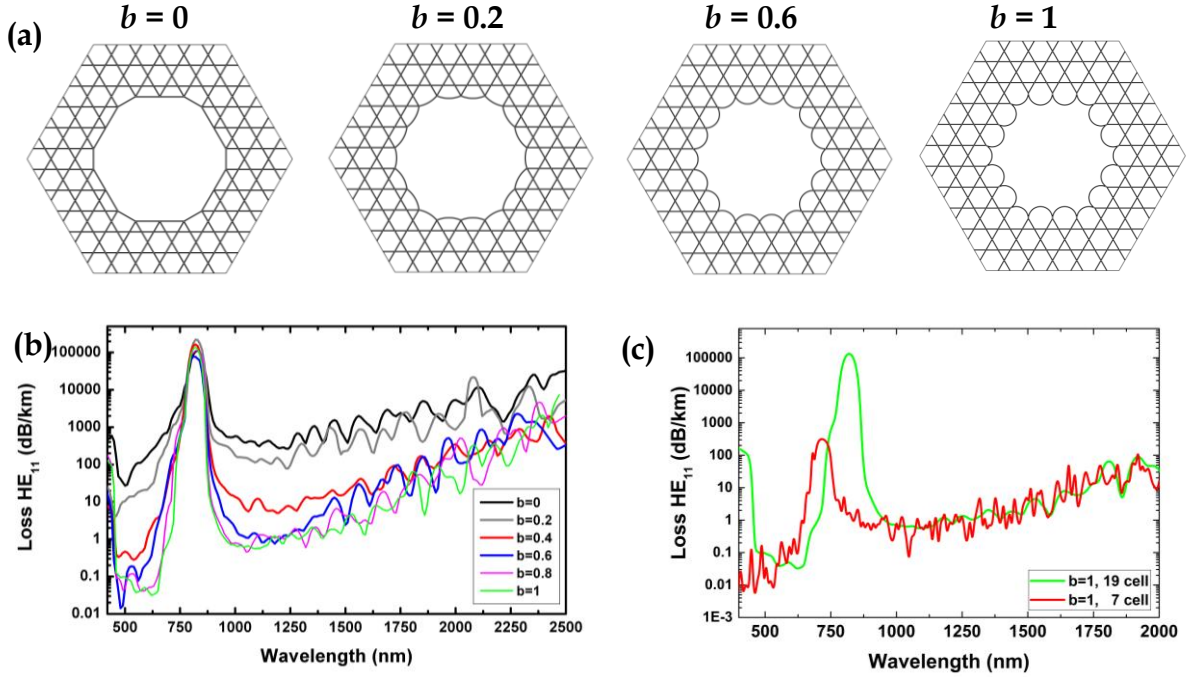


Figure B-2 (a) Enlarged 19-cell three rings Kagome-lattice fiber designs with different b values. (b) Computed loss spectra for the fundamental HE_{11} mode for different arcs curvatures with an inner core diameter of $80\ \mu\text{m}$ and $400\ \text{nm}$ of silica strut. (c) its loss comparison with earlier 7-cell counterpart.

The investigated fiber structures are that of hypocycloid-like core Kagome-lattice IC HC-PCF with different arc curvatures b and a fixed silica strut thickness of $400\ \text{nm}$ and an inner diameter of $80\ \mu\text{m}$ (see Figure B-2 (a)). Based on FEM simulations, the Figure B-2(b) shows spectra of core mode loss for different b parameters ranging from 0 to 1. As anticipated in earlier 7-cell design by our GPPMM group, this 19-cell design have comparable loss trend (see Figure B-2 (c)) with b increase. As demonstrated in a theoretical and experimental systematic study of 7-cell Kagome design [49] [53], a strong influence of the most inwards arcs curvature on the confinement loss is observed with the loss level dropping

from ~ 1000 dB/km in the case of a “quasi” circular core (*i.e.*, $b = 0$) to lower than the dB/km for hypocycloid core with $b = 1$ as shown in Figure B-2(c). According to scaling law reported in [91] [100], CL of Kagome HC-PCF scales as $(\lambda / R_{core})^3$. Here λ operating wavelength and R_{core} is core radius of the fiber. But as we notice from CL spectra in Figure B-2(b), the 19-cell fiber with larger core size instead of showing less CL than 7-cell, it follows almost comparable trend. This relative increment in CL is due to the number of increased cups from 6 in case 7-cell design to 12 in case of 19-cell, which increase optical overlap with HE_{11} mode, thereby results in higher losses. This will be further explained in section B.2.3.

B.2.2 Impact of negative curvature on modal content

Figure B-3 represents numerically computed modal contents of 19-cell design with b equal to 1. Figure B-3(a) shows simulated mode field profiles for both orthogonal polarizations of HE_{11} mode, whereas (b) and (c) show first four high order modes (HOM) profiles.

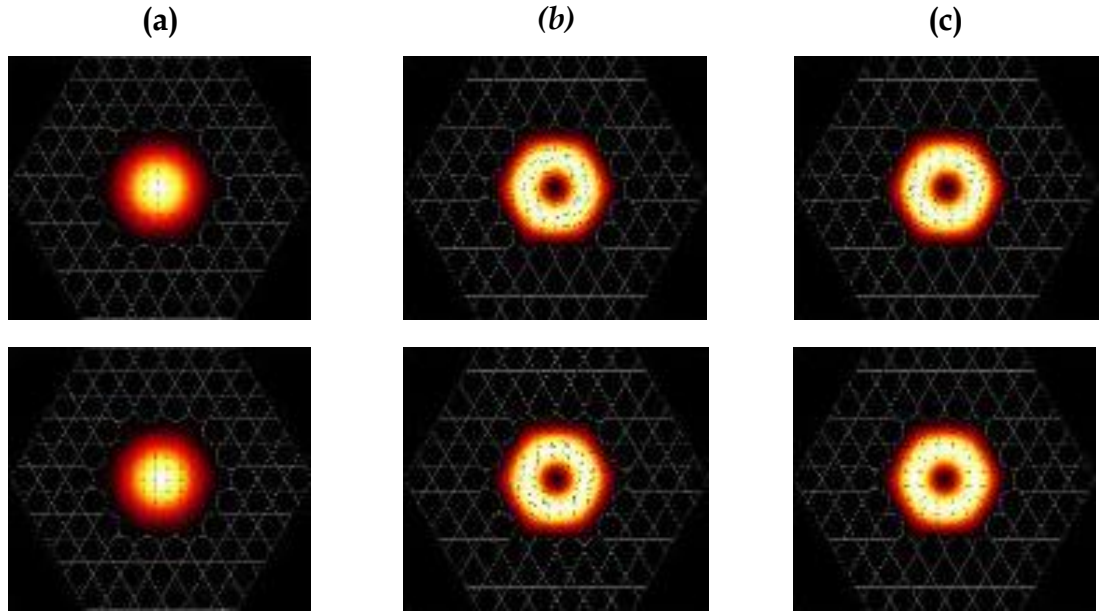


Figure B-3 (a) Computed HE_{11} mode profiles and (b) and (c) first four HOM mode profiles of 19-cell enlarged core with optimum b value.

As we notice from the graphs presented in Figure B-4(a), with increase of b , the loss is reducing and the losses between HE_{11} and the first four HOM at wavelengths of 1 and 2 μm modes differ by 3 times. It is also clear from Figure B-4 (a) and (b) that loss evolution of HE_{11} mode and HOM of 19-cell fiber follows the same trend for all the b values at both wavelengths (1 and 2 μm), and shows discrimination between both modes, whereas for 7-cell fiber design it starts for b values larger than 0.5. In addition, as will be shown in section-B.3, the experimentally investigated modal contents demonstrate multi-mode propagation as expected. However, by carefully launching the light at the fiber input, a selective injection of the fundamental mode is obtained for all the fibers as shown by near field images in Figure B-6 of section-B.3.

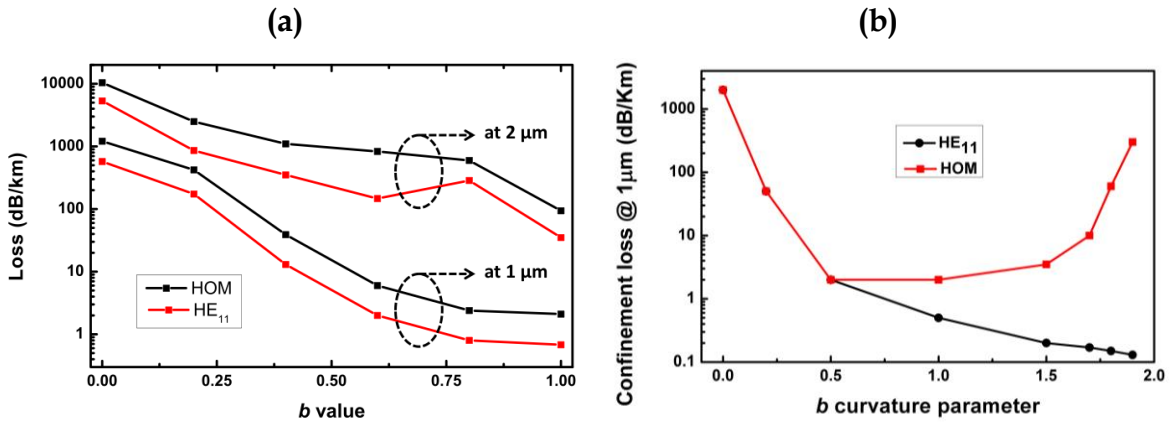


Figure B-4 Impact of negative curvature parameter, b of 19-cell IC HC-PCF on CL at 1 and 2 μm for HE_{11} and HOMs and (b) its comparison with CL of earlier state-of-the-art 7-cell design at 1064 nm.

B.2.3 Impact of negative curvature on optical overlap with cladding

The laser power handling of this type of fibers is presented in Figure B-5. The figure presents the optical power overlap of the HE_{11} core mode with the silica core contour. The results show that this overlap decreases with the increase of b

and reaches to ppm level when $b = 1$ which represents more than three orders of magnitude lower than the one demonstrated with the PBG HC-PCFs.

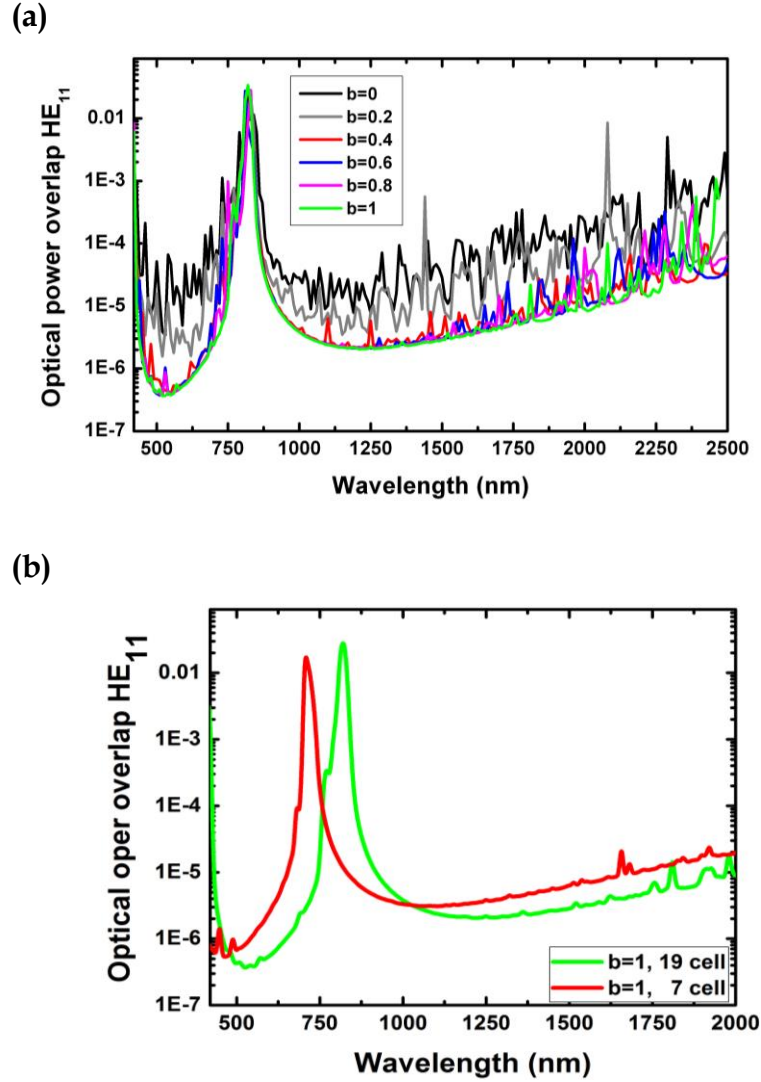


Figure B-5 (a) Evolution of the optical power overlap in 19-cell defect fiber with air-core with the silica cladding structure for different b parameters and (b) compares optical overlap between 7 and 19-cell designs with $b=1$.

As shown in Figure B-5(b), comparable loss figures are same as the 7-cell design and confirm the strong potentiality of this fiber design for high power handling. Here with doubled cups for 19-cell design, there is an increased interaction of the core modes with the silica contour which rises SPOP is the reason for higher losses than theoretically predicted in [50] [91].

B.3 Fabrication and linear characterization

As it has been theoretically demonstrated in [49] [53], ideally hollow-core fiber with core with stronger b parameter as high as 1 would enhance IC guidance and thinner silica struts can provide core guidance with lower loss and larger transmission bandwidth. However, because of rheological limitations during the fabrication process, attaining such large b is extremely challenging with thin silica struts. Consequently, a trade-off between achieving high b and thin struts must be found for optimum performance. In this context, as summarized in Table B.2, four 19-cell fibers have been fabricated with the best compromise between achieving stronger b and thinner silica struts despite of fabrication challenges. These fibers of different geometrical parameters have different silica thickness ranging between 400 to 850 nm, and negative curvature b parameter ranging from 0.46 to 1.

Fiber#	Outer diameter (μm)	b curvature value	HC inner/out diameter (μm)	Mode field diameter (μm)	Silica thickness t (nm)	Pitch (μm)
#1	280	0.46	75/85	52.5	400	15.3
#2	300	0.8	77/91	53.9	600	19
#3	330	0.9	82/98	57.4	700	21
#4	400	1	103/120	72.1	850	26

Table B.2 Geometrical parameters of four fabricated hypocycloid-core 19-cell Kagome latticed IC HCPCFs.

B.3.1 Transmission loss analysis

Figure B-6 shows corresponding optical micrographs, transmission and loss spectra of the different 19-cell Kagome fibers fabricated and along with near field images of HE_{11} modes. In the first case, exhibiting the thinnest strut of 400 nm, Fiber#1 has wide fundamental transmission band (band-I), ranging from a

wavelength near band-I cut-off wavelength of 840 nm to our optical spectrum analyzer (OSA) detection limit of 1750 nm.

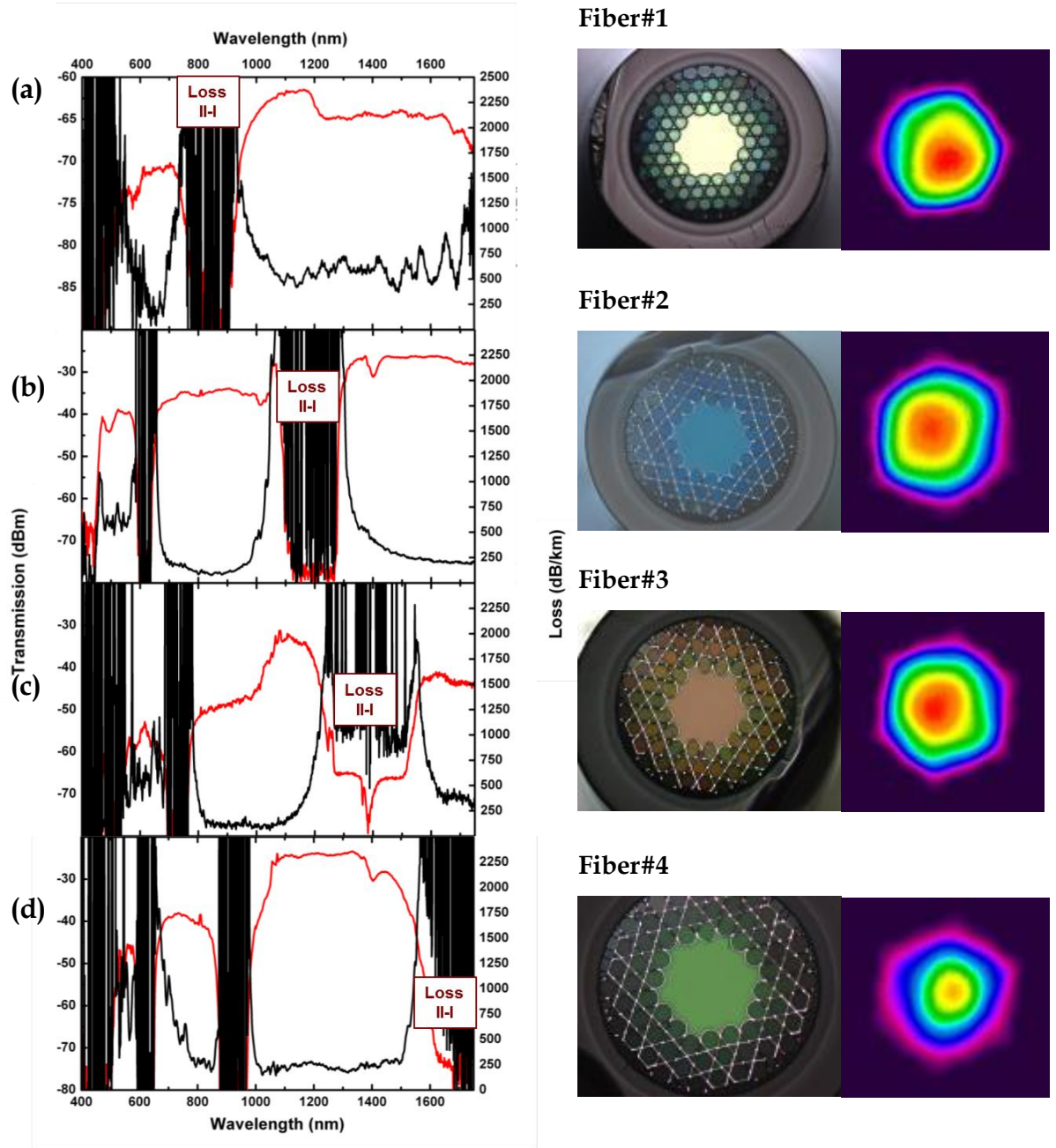


Figure B-6 Transmission after 3 m propagation and loss spectra for a bending diameter of 50 cm of the IC hypocycloid-core 19-cell Kagome-lattice HC-PCFs with core enlarged to (a) 75/85, (b) 77/91, (c) 82/98 and (d) 103/120 μm . The high loss region delimiting the fundamental (I) and the first high-order (II) bands is added. Optical micrographs of the fiber cross section and recorded intensity near-field at 1030 nm are shown for the four IC hypocycloid-core 19-cell Kagome-lattice HC-PCFs for a 3 m-long length.

However, its smaller b -parameter which was set to 0.46 imposes limitation to minimum loss achievable to be less than 500 dB/km in the fundamental band. Due to thicker silica struts of 600 and 700 nm of Fiber #2 and #3 respectively, they present narrower fundamental bands in the fixed analyzed window. Their thicker struts can with stand for b values 0.8 and 0.9 for two fibers (much stronger than Fiber #1). Consequently, they exhibit reduced attenuation with average loss values between 200–150 dB/km, and a cut-off wavelength of 1200 and 1400 nm respectively. Finally for Fiber #4, band-I (*i.e.*, fundamental band) spectral range is outside wavelength range of the OSA. Here, Fiber #2–4 show loss figure-range of 100–200 dB/km, which corresponds to a new record for hollow-core fibers with such larger core size range. For comparison, in case of PBG HC-PCF the core size is limited by 50 μm diameters [101] and further increase in diameter (up to 1000 μm) is possible by capillary fiber using metallic coating. However, the higher loss values and strong multimode behavior (with more than 10,000 guided modes) disqualify this technique for high energy laser delivery [102]. Furthermore, for Fiber #1 a loss figure as low as 200 dB/km was measured around 600–680 nm wavelength range. Interestingly, as we can notice from loss spectra in Figure B-6, all these fabricated fibers exhibit lower loss in the second order transmission band (band-II) compared to band-I. The lower loss in band-II relative to the first one is expected due to lower scattering loss in larger core due to decreased lower optical overlap of the guided mode with the silica core-surround in the case of a larger core size. This is further corroborated by the relatively low measured loss for Fibers #2–4 in the visible range of 400–700 nm, which corresponds to the third-order transmission band (band-III). Finally, we note that Fibers #2–4 band-II transmission windows cover the wavelength of 1 μm , and thus set them as good candidates for high power USP Yb-based lasers, with a core diameter reaching up to 103/120 μm in the case of Fiber #4.



B.3.2 Bending loss analysis

In order to investigate the sensitivity of the different fibers to bend, transmission spectra were measured from the output of 5 m long sections of each fiber for different bend radii. Five bend radii (radius of curvature noted R_c) of 100, 60, 30, 25 and 15 mm were explored. The results obtained from these transmission measurements are reported in Figure B-7. Figure B-7 (a) shows loss spectra of Fiber #1 for the five bend radii. During each spectrum recording, the fiber beam profile was monitored.

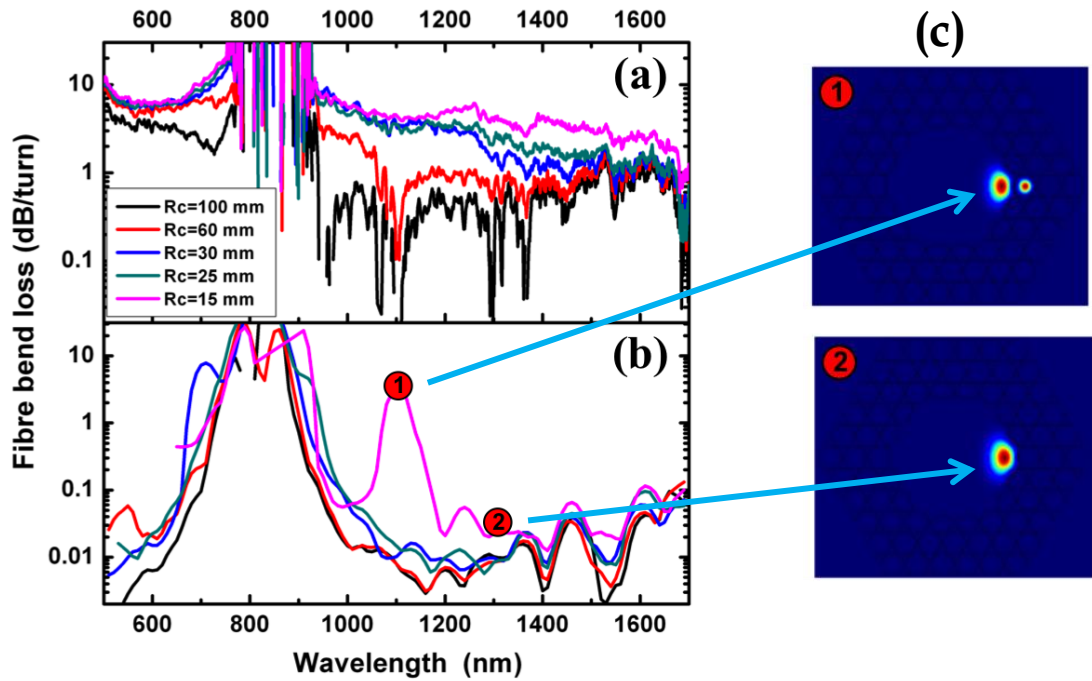


Figure B-7 (a) Fiber #1 measured bend-loss spectra in the visible and NIR bands for five different bend radii and (b) the corresponding calculations. (c) Computed intensity profile of the fundamental core-mode HE_{11} for $R_c = 15$ mm at a resonant coupling wavelength (noted 1) and out of it (noted 2).

The fiber output beam imaging shows that the core-mode remains well confined in the hollow-core even when the bend radius is as small as 15 mm. The spectra show a loss decrease with wavelength increase, except for wavelengths near the band-I-II cut-off wavelength.

Similar to PBG HC-PCF, IC guiding fibers are in principle sensitive to macro-bend [14] [103]. This is illustrated in both the magnitude of the calculated bending loss and its dependence in wavelength as shown in the Figure B-7(b). Micro-bendings are not taken into account in the simulations, explaining thus the discrepancy between experiment and theory. The baseline loss is on average 100 times lower than the experimental one for the fundamental band and up to 1000 times lower for the first higher-order band. Furthermore, the results show a bend loss resonance for bend radius of 15 mm at 1200 nm which are due to resonant coupling between core guided modes with cladding hole modes [44] [103], as confirmed with the computed intensity profiles plotted in Figure B-7(c). Such peaks are not observed experimentally. This is due to the fact that HOMs are bound less tightly to the fiber core than lower order modes and coiling the fiber would results HOMs to radiate out of via cladding, there by vanishing them. This trend in the bend-loss spectrum and the modal properties were found to be similar for all tested IC Kagome HC-PCF.

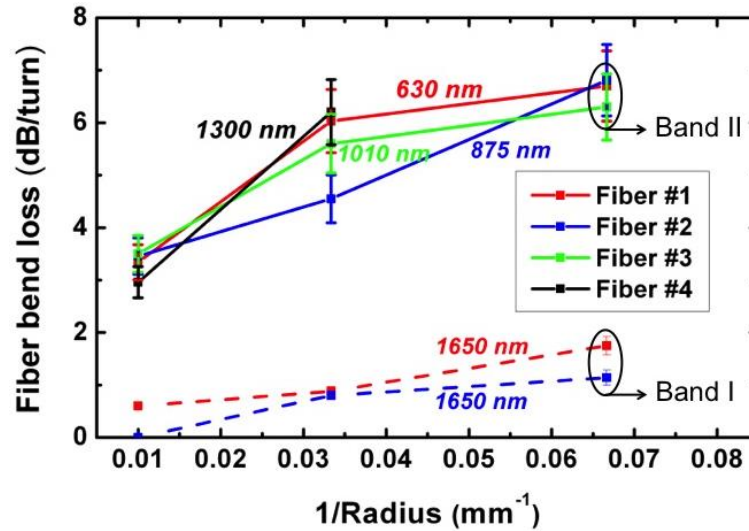


Figure B-8 Bend-loss evolution with bend radius of band-I and II central wavelength (exact values indicated on the plot) for the four fabricated IC Kagome fibers.

Figure B-8 shows the bend loss evolution with the bend radius for band-I and II representative wavelengths. For band-I, the wavelength was chosen to be 1650 nm, and the data set was limited to Fibers #1 and #2 as for the two others fibers band-I is not sufficiently detected due to our detection system limit. For band-II, the chosen wavelengths are 630, 875, 1010 and 1300 nm for Fiber #1, #2, #3 and #4 respectively, and correspond qualitatively to the band central wavelength. Bend-loss in band-I varies little with the bend radius and remains less than 2 dB/turn for the explored radius-range (for example, a bend-loss figure of 1 dB/turn for 3 cm bend-radius). In band-II, the fibers exhibit larger bend-loss figure than in band-I, with 3 dB/turn for 100 mm bend-radius, and 6 dB/turn for fiber-bend radius smaller than 3 cm. These bend-loss figures in the visible region are comparable to conventional SMF28 single mode fiber [104].

B.4 Investigation of high energy USP laser handling

B.4.1 Theoretical investigation of the IC mechanism for power-link potential

To investigate further on the most optimum 19-cell IC Kagome-lattice fiber design for SPOP and power handling capabilities, we performed an additional numerical modeling [49] [53] [105] and results are summarized in Figure B-9. Here, we considered fiber structures with a constant b , which is fixed to 1, and t parameter varying from 400 to 850 nm. The calculated spectrum of the fluence in the silica core contour for injected laser pulse energy of 1 mJ is plotted in Figure B-9 (a), for t equal to 850 nm.



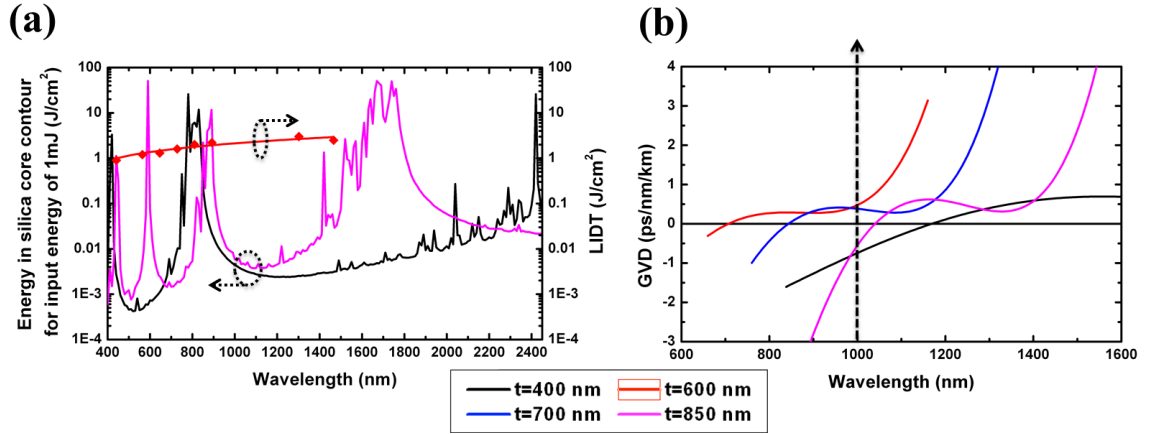


Figure B-9 Computed energy residing in silica core contour compared with the silica LIDT reported in [106]. (b) Evolution of the dispersion curve around 1 μ m for varying silica thickness ($t = 400, 600, 700, 850$ nm) for a typical 19-cell three rings IC Kagome-lattice fibers with an inner hollow-core diameter fixed to 80 μ m and an arc curvature b equal to 1.

We note that in the guidance spectral range, the energy residing in the silica core contour of 10^{-3} J/cm² is three orders of magnitude lower than the silica LIDT with USP [106] (see red curve in Figure B-9 (a)). Consequently, this type of HC-PCF could in principle guide USP with energy as high as several hundreds of mJ. Figure B-9 (b) shows the chromatic dispersion spectra for the different strut thickness, t . For each fiber, the dispersion exhibits a very low level, with values lower than 0.5 ps/nm/km over a large transmission window. This is a similar figure to that of 7-cell hypocycloid-core IC HC-PCF [49] and more than two orders of magnitude lower than the PBG triangular lattice fiber's dispersion. Note, that at ~ 1 μ m wavelength, the transmission windows correspond to the first high order band for all the fibers except for the case of t equal to 400 nm which is referred to the fundamental one. Finally, by simply adjusting the thickness of the silica web, the regime can be easily tuned, at 1 μ m, from anomalous (case of $t = 850$ nm) to anomalous regime (case of $t = 600$ and 700 nm). This point is found particularly attractive to the delivery and compression applications and the more recent high field activities.

B.4.2 Experimental demonstration of high energy USP laser handling at 1 μm .

This section explains first experimental demonstration to prove the high energy capabilities of the fabricated 19-cell Kagome fibers at 1 μm . Among the four fibers, fiber #3 operates at laser wavelength of 1030 μm with 200 dB/km, which is 4 times larger than previous 7-cell fiber which has loss figure around 45 dB/km. As shown in Figure B-10, in terms of power handling this enlarged 19-cell fiber delivers high energies nearly by 2 times more than 7-cell fibers. A laser of 600 fs pulses emitting from an Yb-based at repetition rate of 1 kHz and with maximum of 1 mJ energy is transmitted through a 10 m long piece of 19-cell fiber and also through 7-cell fiber in order to compare their performances with respect to energy handlings. In first run of this experiment, delivery of laser beam has been carried out through air filled fibers. As shown in the Figure B-10 (a), without any noticeable damage at nearly 1 mJ, Fiber #3 demonstrates delivery of pulse energies up to 4 times larger than 7-cell fibers with corresponding maximum input fluence of 32 J/cm². This limit is one order more than the damage threshold of silica with sub-picosecond laser pulses [107]. In the second run, both fibers are filled with He gas at 3 bars pressure. In the case of 19-cell fiber the transmission coefficient reaches 55% and it increases up to 75 % for 3m long piece. But in case of 7-cell fibers, transmission coefficient is still limited to 40% and 50% for both 3 and 10m cases. Therefore, for the 19-cell fiber with air the power handlings capabilities of inside has been increased and are equivalent to that of 7-cell fiber filled with He gas at 4 bars at same 10 m of length. Figure B-10(b) shows the far field images demonstrating the persistence of robust single modenness through of 3 m long of Fiber #3 even at input energy levels of 1 mJ. Also this fiber piece demonstrates 80% transmission with output intensities up to 30 TW/cm².



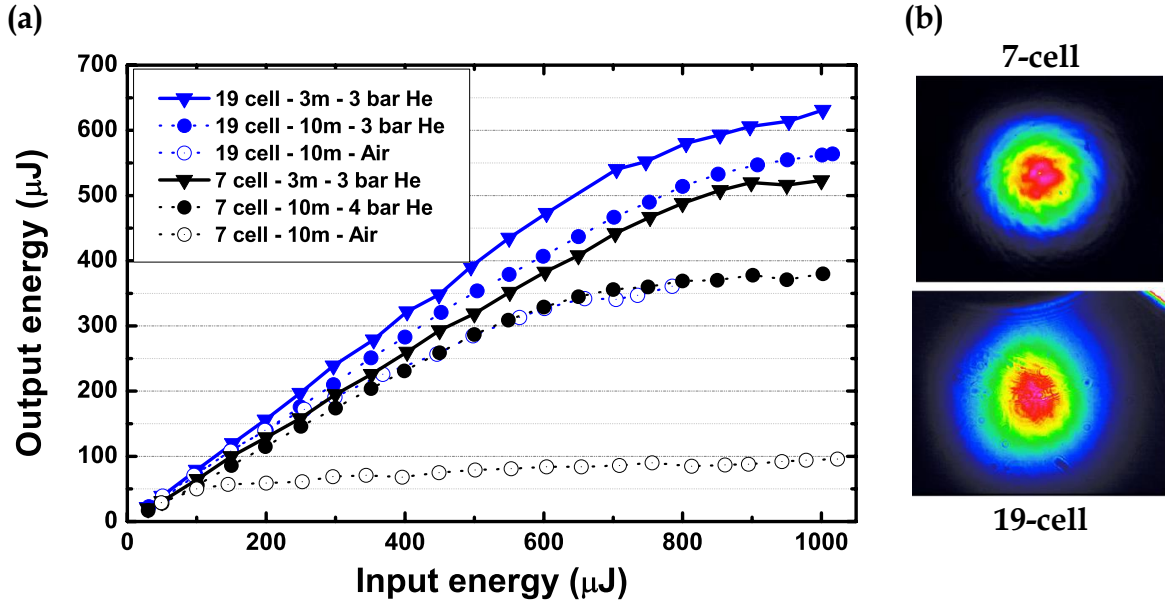


Figure B-10 (a) Measured transmitted energy with input energy at $1\ \mu\text{m}$ for 19-cell fiber (blue color-coded) and 7-cell fiber (black color-coded) for the different cases of fiber-length and gas-filling pressure; (b) Far field beam profiles showing single mode transmissions at $1\ \text{mJ}$ of input energy for both fiber designs

B.4.3 Experimental demonstration of high energy USP laser handling at $780\ \text{nm}$.

Inner core diameter of Fiber #4 has been increased up to $100\ \mu\text{m}$, *i.e.* effective area $4180\ \mu\text{m}^2$ with an aim to increase the level of LIDT and to further capitalize on the very low optical overlap with silica. This fiber offers low-loss guidance at the operative laser wavelength of $780\ \text{nm}$ and can accommodate further high energy lasers than Fiber #3. In order to demonstrate its high energy pulse delivery we used a laser source from Amplitudes Technologies at $800\ \text{nm}$ operating wavelength at a $10\ \text{kHz}$ repetition rate with pulse of $30\ \text{fs}$ and delivering higher energies than the laser used in previous section [43]. Two short pieces of $55\ \text{cm}$ and $35\ \text{cm}$ have been used for this delivery demonstration and their cores have been filled at 3 and 5 bars of monoatomic He gas in order to reduce nonlinearities and solitonic shifting dynamics during the pulse propagation.

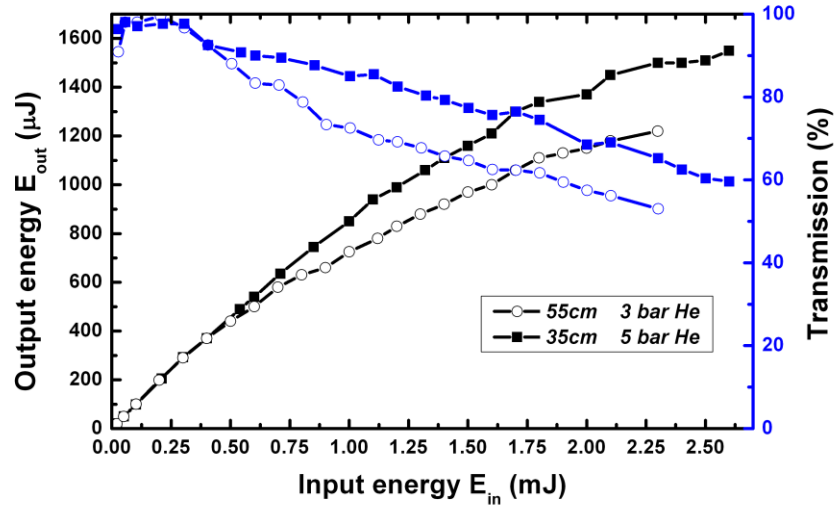


Figure B-11 Evolution of the fiber output energy with the input energy (black curve) and corresponding coefficient transmission curves (blue curve) for 55 and 35 cm long piece of large core HC-PCF filled with He at 3 and 5 bar respectively [43].

The performance of the fiber over high input energies have been summarized in Figure B-11 which confirms the demonstration of two new records. Firstly, enhanced input energy launching abilities up to 2.6 mJ without any structural deformations at input end of the fiber. Secondly, transmittance of such high input power has been reported with 60% efficiency, *i.e.*, 1.5 mJ output energy over 35 cm long piece whereas a 50% transmission coefficient has been measured for 55 cm long piece for a maximum input energy of 2.25 mJ. Therefore, without any optical damage to the newly fabricated 19-cell fiber (Fiber #4), the launching input intensities has been improved by 30 times, *i.e.* up to 1.4 PW/m² and a peak power of 81 GW has been accommodated in the fiber which is 54 times higher than earlier state of the art.

Figure B-12 shows measured output spectra in case of 55 cm long 19-cell fiber filled with He gas at 3 bars and 35 cm long fiber filled with He gas at 5 bars on the left and right side of the figures respectively. We can notice that in the figure, in both fiber cases the output laser spectra shown in red curves does not shift much with respect to the input laser spectrum represented by grey which

confirm the pulse preservation along the high energy laser handlings of the 19-cell Kaogme IC HC-PCF.

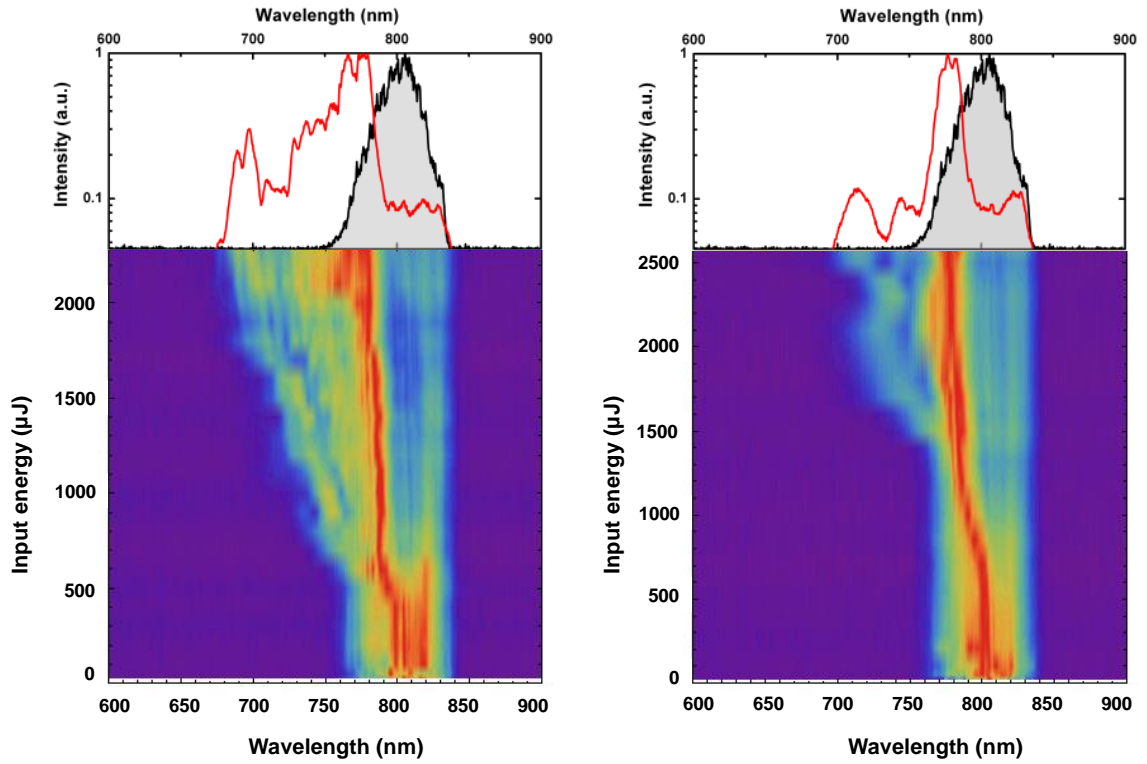


Figure B- 12 Mappings of the measured output spectrum versus input energy for 55 cm long 3 bars He-filled (left) and 35 cm long 5 bars He-filled (right) fiber pieces.

B.5 Summary

This annexure has presented characterization of linear properties of newly designed ultra-large core size (19-cell) ($>100 \mu\text{m}$) hypocycloid-core IC Kagome-lattice HC-PCF, by removing an extra cladding ring of 7-cell fiber. Keeping the structural features undisturbed from negative curvature design, the fabricated 19-cell defect Kagome fiber could achieve low transmission (100 dB/km) and dispersion combined with small bend-loss, making it an excellent candidate to delivery ultrafast laser beams and for the recent plasma photonics applications.



REFERENCES

1. *Strong localization of photons in certain disordered dielectric superlattices.* John, S. 2486–2489, s.l. : Phys. Rev. Lett., 1987, Vols. 58,.
2. *Inhibited spontaneous emission in solid-state physics and electronics.* Yablonovitch, E. 2059–2062, s.l. : Phys. Rev. Lett., 1987, Vols. 58,.
3. *Photonic band-gap structures.* Yablonovitch, E. s.l. : J. Opt. Soc. Am. B, February 1993, Vols. 10, No. 2.
4. *Low loss (1.7 dB/km) hollow core photonic bandgap fiber.* B. J. Mangan, L. Farr, A. Langford, et al. 2004. OFC.
5. *Compact, stable and efficient all-fiber gas cells using hollow-core photonic crystal fibers.* F. Benabid, F. Couny, J. C. Knight. Nature 434, 488-491 : s.n., 2005, Nature, pp. 434, 488-491.
6. *Stimulated Raman Scattering in Hydrogen-filled hollowcore Photonic Crystal Fiber.* F. Benabid, J. C. Knight, G. Antonopoulos, et al. 2002, Science , pp. 298, 399-402 .
7. *Electromagnetically-induced transparency grid in acetylene-filled hollow-core PCF.* F. Benabid, P. S. Light, F. Couny, et al. 2005, Opt. Express , Vol. 5694, p. 13.
8. *Electromagnetically induced transparency and saturable absorption in all-fiber devices based on 12C2H2-filled hollow-core photonic crystal fiber.* F. Couny, P.S. Light, F. Benabid, et al. 2006, Opt. Commun., Vols. 263,, pp. 28-31.
9. *Endlessly single-mode photonic crystal fiber.* Birks, T. A. s.l. : Optics Express, July 1, 1997, Vols. Vol. 22, No. 13.
10. *High-power fiber lasers.* Cesar Jauregui, Jens Limpert & Andreas Tünnermann. s.l. : Nature Photonics, 2013, Vols. 7, 861–867.
11. *High Power Fiber Lasers: A Review.* Codemard, Michalis N. Zervas and Christophe A. s.l. : IEEE, Quantum Electronics, 2014, Vols. 20, NO. 5.



12. *Full 2-D photonic bandgaps in silica/air structures*. Birks T.A, Roberts P.J, Russell P.S.J, Atkin D.M, Shepherd T.J. 1941–1943., s.l. : Electron. Lett., 1995, Vols. 31,.
13. *Low Loss (13 dB/km) Air Core Photonic Band-Gap Fiber*. N. Venkataraman, M.T. Gallagher, Charlene M. Smith, D. Muller, J. A. West, K. W. Koch, J.C. Fajardo. s.l. : IEEE Xplore, October 2002.
14. *Generation and photonic guidance of multi-octave optical-frequency combs*. F. Couny, F. Benabid, P. J. Roberts, P. S. Light, and M. G. Raymer. no. 5853, pp. 1118–21, s.l. : Science, vol., no. 5853, Nov. 2007, Vol. 318.
15. Von Neumann, J. & Wigner, E. no. 465-467, s.l. : Physik. Z, 1929, Vol. 30.
16. *Low loss broadband transmission in optimized core-shape Kagome hollow-core PCF*. Y. Wang, F. Couny, P. J. Roberts, and F. Benabid. s.l. : CLEO, 2010, Vol. p. CPDB4.
17. *Low loss broadband transmission in hypocycloid-core Kagome hollow-core photonic crystal fiber*. Y. Y. Wang, N. V Wheeler, F. Couny, P. J. Roberts, and F. Benabid. s.l. : Opt. Lett., Mar. 2011, Vols. vol. 36, no. 5, pp. 669–71.
18. *Ultra-low-loss (0.1484 dB/km) pure silica core fiber and extension of transmission distance*. K. Nagayama, M. Kakui, M. Matsui, I. Saitoh and Y. Chigusa. s.l. : Electron. Lett., 2002, Vols. 38, 1168-1169.
19. *Singlemode photonic band gap guidance of light in air*. R. F. Cregan, B. J. Mangan, J. C. Knight, T. A. Birks, P. St. J. Russell, P. J. Roberts, and D. C. Allan. 1537–1539, s.l. : Science, 1999, Vol. 285.
20. *Ultimate low loss of hollow-core photonic crystal fibers*. P. J. Roberts, F. Couny, H. Sabert, B. J. Mangan, D. P. Williams, L. Farr, M. W. Mason, T. A. Birks, J. C. Knight and P. St.J. Russell. s.l. : Optical Society of America, 2005, Vols. Vol. 13, No. 1.
21. *Demonstration of a waveguide regime for a silica hollow - core microstructured optical fiber with a negative curvature of the core boundary in the spectral region $\lambda > 3.5$*



- \$\mu\$\$. A. D. Pryamikov, A. S. Biriukov, A. F. Kosolapov, V. G. Plotnichenko, S. L. Semjonov, and E. M. Dianov. s.l. : Opt. Express, , Jan. 2011, Vols. 19, no. 2, pp. 1441–1448.
22. *Identification of Bloch-modes in hollow-core photonic crystal fiber cladding*. F. Couny, et al. s.l. : Optics Express , 2007, Vols. 15(2): p. 325-338.
23. *Particle levitation and guidance in hollowcore photonic crystal fiber*. F. Benabid, J. C. Knight, and P. St. J. Russell. s.l. : Optics Express, 2002, Vols. 10(21):1195–1203.
24. *Particle levitation and guidance in hollow- core photonic crystal fiber*. F. Benabid, G. Antonopoulos, J. C. Knight, and P. St. J. Russell. Paper OP3a.6.4, Cardiff : Photon02 Conference (Structured Optical Materials), 2002, Vol. page 92.
25. *Resonant optical interactions with molecules confined in photonic band-gap fibers*. S. Ghosh, et al. s.l. : Physical Review Letters, 2005, Vol. 94(9). p 093902.
26. *Compact, stable and efficient all-fiber gas cells using hollow-core photonic crystal fibers*. F. Benabid, F. Couny, J. C. Knight, T. A. Birks & P. St J. Russell. s.l. : Nature, 2005, Vol. 434.
27. *Generation of megawatt optical solitons in hollow-core photonic band-gap fibers*. D. G. Ouzounov, et al. s.l. : Science, 2003, Vols. 301(5640): p. 1702-1704.
28. *Photonic crystal fibers: mapping Maxwell's equations onto a Schrödinger equation eigenvalue problem*. Mortensen, Niels Asger. s.l. : Journal of the european optical society, 2006, Vol. 1.
29. Zolla, Frédéric. *Foundations of Photonic Crystal Fibers*. s.l. : Imperial College Press, Jan 2005. ISBN: 978-1-86094-507-6 .
30. *Linear and nonlinear optical properties of hollow core photonic crystal fiber*. F. Benabid, and P. J. Roberts. s.l. : Journal of Modern Optics, 2011, Vols. 58(2): p. 87-124.
31. Russell, P. S. J. s.l. : private papers, 1991.



32. *Hollow-core photonic bandgap fiber: new light guidance for new science and technology.* Benabid, F. s.l. : Philos. Trans. A. Math. Phys. Eng. Sci., Dec. 2006, Vols. 364, no1849, pp. 3439–62.
33. *Double photonic bandgap hollow-core photonic crystal fiber.* Philip S. Light, François Couny, Ying Ying Wang, Natalie V. Wheeler, P. John Roberts. s.l. : OPTICS EXPRESS, Aug. 2009, Vols. Vol. 17, No. 18.
34. *Photonic Solutions towards Optical Waveform Synthesis.* F. Couny et al. s.l. : PhD Thesis, 2008.
35. *High average power, high energy 1.55 μm ultrashort pulse laser beam delivery using large mode area hollow core photonic band-gap fiber.* Xiang Peng, Michael Mielke, and Timothy Booth. s.l. : OPTICS EXPRESS, Jan 2011, Vols. Vol. 19, No. 2, 923.
36. *Optical Properties of Low Loss (70dB/km) Hypocycloid-Core Kagome Hollow Core Photonic Crystal Fiber for Rb and Cs Based Optical Applications.* Thomas D. Bradley, Yingying Wang, Meshaal Alharbi, Benoit Debord, Coralie Fourcade-Dutin, Benoit Beaudou, Frederic Gerome, and Fetah Benabid. s.l. : JLT, Aug. 15, 2013, Vols. 31, NO. 16.
37. *Bound States in the Continuum Realized in the One-Dimensional Two-Particle Hubbard Model with an Impurity.* J. M. Zhang, D. Braak, and M. Kollar. s.l. : Phys. Rev. Lett., Sep. 2012, Vols. 109, no. 11, p. 116405.
38. *Bound states in the continuum.* C. W. Hsu, B. Zhen, A. D. Stone, J. D. Joannopoulos, and M. Soljačić. s.l. : Nat. Rev. Mater., Jul. 2016, Vols. 1, p. 16048.
39. *Observation of trapped light within the radiation continuum.* C. W. Hsu, B. Zhen, J. Lee, S.-L. Chua, S. G. Johnson, J. D. Joannopoulos, and M. Soljagic. s.l. : Nature, Jul. 2013, Vols. vol. 499, no. 7457, pp. 188–191.
40. *Über merkwürdige diskrete Eigenwerte.* Wigner, J. von Neumann and E. s.l. : Physik. Zeitschr, 1929, Vols. 30, 465–467.



41. *Ultrahigh efficiency laser wavelength conversion in a gas-filled hollow core photonic crystal fiber by pure stimulated rotational Raman scattering in molecular hydrogen*. F. Benabid, G. Bouwmans, J. C. Knight, P. S. J. Russell, and F. Couny. s.l. : Phys. Rev. Lett., 2004, Vols. 93(12), 123903.
42. *Over-five octaves wide Raman combs in highpower picosecond-laser pumped H₂-filled inhibited coupling Kagome fiber*. Aurélien Benoit, Benoit Beaudou, Meeshal Alharbi, Benoît Debord, Frederic Gerome, François Salin, and Fetah Benabid. s.l. : Opt. Exp., May 2015, Vols. 23, No. 11.
43. *Multi-meter fiber-delivery and pulse self-compression of milli-Joule femtosecond laser and fiber-aided laser-micromachining*. B. Debord, M. Alharbi, L. Vincetti, A. Husakou, C. Fourcade-Dutin, C. Honninger, E. Mottay, F. Gérôme, and F. Benabid, s.l. : Opt. Exp., 2014, Vols. vol. 22, no. 9, pp. 10735–10746.
44. *Optical Properties of Low Loss (70dB / km) Hypocycloid-Core Kagome Hollow Core Based Optical Applications*. T. D. Bradley, Y. Wang, M. Alharbi, B. Debord, C. Fourcade-dutin, B. pp. 3052–3055, s.l. : J. Lightw. Technol, 2013, Vols. vol. 31, no. 16.
45. *Guidance properties of low-contrast photonic bandgap fibers*. A. Argyros, T. A. Birks, S. G. Leon-Saval, C. M. B. Cordeiro, and P. S. J. Russell. s.l. : Opt. Express, 2005, Vols. vol. 13, no. 7, pp. 2503–2511.
46. *Investigation of coupling between a fiber and an infinite slab*. Marcuse, D. s.l. : JLT, Vols. 7, no. 1. pp. 122–130, 1989.
47. *Large-pitch kagome-structured hollow-core photonic crystal fiber*. F. Couny, F. Benabid, and P. S. Light. s.l. : Opt.Lett., 2006, Vols. 31(24), 3574–3576 .
48. *Square-lattice large-pitch hollow-core photonic crystal fiber*. F. Couny, et al.,. s.l. : Optics Express, 2008, Vols. 16(25): p. 20626-20636.
49. *Hypocycloid-shaped hollow-core photonic crystal fiber Part I: arc curvature effect on confinement loss*. B. Debord, M. Alharbi, T. Bradley, C. Fourcade-Dutin, Y. Y.



- Wang, L. Vincetti, F. Gérôme, and F. Benabid. s.l. : Opt. Express,, Nov. 2013, Vols. 21, no. 23, pp. 28597–608, .
50. *Hollow Metallic and Dielectric Waveguides for Long Distance Optical Transmission and Lasers*. E. A. J. Marcatili and R.A.Schmeltzer. s.l. : Bell Syst. Tech. J., 1964, Vols. 43, no. 4, pp. 1783–1809.
51. *Solid-core fiber with ultra-wide bandwidth transmission window due to inhibited coupling*. T. Grujic, B. T. Kuhlmeiy, A. Argyros, S. Coen, and C. M. de Sterke. s.l. : Opt. Express, Dec. 2010, Vols. vol. 18, no. 25, pp. 25556–66.
52. *Design and fabrication of hollow-core photonic crystal fibers for high-power ultrashort pulse transportation and pulse compression*. Y. Y. Wang, X. Peng, M. Alharbi, C. F. Dutin, T. D. Bradley, F. Gérôme, M. Mielke, T. Booth, and F. Benabid. s.l. : Opt. Lett., Aug. 2012, Vols. 37, no. 15, pp. 3111–3.
53. *Hypocycloid-shaped hollow-core photonic crystal fiber Part II: cladding effect on confinement and bend loss*. M. Alharbi, T. Bradley, B. Debord, C. Fourcade-Dutin, D. Ghosh, L. Vincetti, F. Gérôme, and F. Benabid. s.l. : Opt. Express, Nov. 2013., Vols. vol. 21, no. 23, pp. 28609–16.
54. *Models for guidance in kagome-structured hollow-core photonic crystal fibers*. G. J. Pearce, G. S. Wiederhecker, C. G. Poulton, S. Burger, and P. St J Russell. s.l. : Opt. Express, Oct. 2007, Vols. vol. 15, no. 20, pp. 12680–5.
55. *Numerical Modeling of S-Band EDFA Based on Distributed Fiber Loss*. L. Vincetti, M. Foroni, F. Poli, M. Maini, A. Cucinotta, S. Selleri, S. Member, and M. Zoboli. s.l. : J. Lightw. Technol., 2008, Vols. vol. 26, no. 14, pp. 2168–2174.
56. *Design of single-moded holey fibers with large-mode-area and low bending losses: the significance of the ring-core region*. Y. Tsuchida, K. Saitoh, and M. Koshiba. s.l. : Opt. Express, Mar. 2007, Vols. vol. 15, no. 4, pp. 1794–803.
57. *Flexible tube lattice fibers for terahertz applications*. V. Setti, L. Vincetti, and a Argyros. s.l. : Opt. Express, Mar. 2013, Vols. vol. 21, no. 3, pp. 3388–99.



58. *Waveguiding mechanism in tube lattice fibers*. Vincetti, V. Setti and L. s.l. : Opt. Express, Oct. 2010, Vols. vol. 18, no. 22, pp. 23133–46.
59. *Low loss silica hollow core fibers for 3-4 μm spectral region*. F. Yu, W. J. Wadsworth, and J. C. Knight. s.l. : Opt. Express, May 2012, Vols. vol. 20, no. 10, pp. 11153–8.
60. *Hollow-core fibers for high power pulse delivery*. M. Michieletto, J. K. Lyngsø, C. Jakobsen, J. Lægsgaard, O. Bang, and T. T. Alkeskjold. s.l. : Opt. Express, 2016, Vols. vol. 24, no. 7, pp. 7103–7119.
61. *Antiresonant Hollow Core Fiber with Octave Spanning Bandwidth for Short Haul Data Communications*. J. R. Hayes, et.al., s.l. : CLEO 2016.
62. *Antiresonant reflecting photonic crystal optical waveguides*. N. M. Litchinitser, a K. Abeeluck, C. Headley, and B. J. Eggleton. s.l. : Opt. Lett., Sep. 2002, Vols. vol. 27, no. 18, pp. 1592–4.
63. *Identification of Bloch-modes in hollow-core photonic crystal fiber cladding*. F. Couny, F. Benabid, P. J. Roberts, M. T. Burnett, and S. A. Maier. s.l. : Opt. Express, 2007, Vols. vol. 15, no. 2, pp. 325–338.
64. *Properties of dielectric-tube waveguides*. Kharadly, J. E. Lewis and M. M. Z. s.l. : Proceedings of the Institution of Electrical Engineers, 1969, Vols. vol. 116, no. 2. pp. 214–224.
65. *Antiresonant reflecting optical waveguides in SiO₂-Si multilayer structures*. M. A. Duguay, Y. Kokubun, T. L. Koch, and L. Pfeiffer. s.l. : Appl. Phys. Lett, 1986, Vols. vol. 49, no. 1.
66. *Complex FEM modal solver of optical waveguides with PML boundary conditions*. S. Selleri, L. Vincetti, A. Cucinotta, and M. Zoboli. s.l. : Opt. Quantum Electron., 2001, Opt. Quantum Electron., Vols. 33, no. 4–5, pp. 359–371.



67. *Analysis of curved optical waveguides by conformal transformation.* Harris, M. Heiblum and J. s.l. : Quantum Electronics, IEEE Journal of, 1975, Vols. 11, no. 2. pp. 75–83.
68. *Low Loss Broadband Transmission In Optimized Core-shape Kagome Hollow-core PCF.* Y. Y.Wang, F. Couny, P. J. Roberts, and F. Benabid. 2010. Conference on Lasers and Electro-Optics (CLEO). p. p. CPDB4.
69. *Effects of Configuration Interaction on Intensities and Phase Shifts.* Fano, Ugo. s.l. : Phys.Rev.Lett., 1961, Vols. Vol.124, 1866-1878.
70. *Effects of Configuration Interaction on Intensities tensities and Phase Shifts.* Fano, Ugo. s.l. : Citation Classics 8, 219, 1977.
71. *Bound states in the continuum.* C. W. Hsu, B. Zhen, A. D. Stone, J. D. Joannopoulos, and M. Soljačić. s.l. : Nat. Rev. Mater., Jul. 2016, Vols. vol. 1, p. 16048.
72. *Classical analogy of Fano resonances.* Joe, Y. S., A. M. Satanin and C. S. Kim. s.l. : Phys. Scr., 2006, Vols. 74, 259.
73. *Observation of electronic bound state above a potential well.* F. Capasso et, al. s.l. : Nature, Aug.1992, Vol. 358.
74. *Observation of trapped light within the radiation continuum.* C. W. Hsu, B. Zhen, J. Lee, S.-L. Chua, S. G. Johnson, J. D. Joannopoulos, and M. Soljagic. s.l. : Nature, Jul. 2013, Vols. vol. 499, no. 7457, pp. 188–191.
75. *Generation and photonic guidance of multi-octave optical-frequency combs.* F. Couny, F. Benabid, P. J. Roberts, P. S. Light, and M. G. Raymer. s.l. : Science, Nov. 2007, Vols. 318, no. 5853, pp. 1118–21.
76. *Über Absorptionsserien von Argon, Krypton und Xenon zu Termen zwischen den beiden Ionisierungsgrenzen 2P₂/03 und 2P₂/01.* Beutler, H. s.l. : Z. Phys, 1935, Vols. A 93, 177–196.



77. *Interaction between Configurations with Several Open Shells*. Fano, Ugo. s.l. : Phys. Rev., 1965, Vols. 140, A67–A75.
78. *Sullo spettro di assorbimento dei gas nobili presso il limite dello spettro d'arco*. Fano, Ugo. s.l. : Nuovo Cimento, 1935, Vols. 12, 154–161.
79. *Interfering resonances and bound states in the continuum*. Wintgen, H. Friedrich and D. s.l. : Phys. Rev. A, 1985, Vols. 32, no. 6, pp. 3231–3242.
80. *Controlling multipolar radiation with symmetries for electromagnetic bound states in the continuum*. B, Lepetit T and Kante. s.l. : Phy.Rev.B, 2014, Vol. B 90 241103(R).
81. *Fano Resonances in Polygonal Tube Fibers*. Luca Vincetti, and Valerio Setti. s.l. : JLT, January 1, 2012, Vols. 30, No.1.
82. *Extra loss due to Fano resonances in inhibited coupling fibers based on a lattice of tubes*. V.Setti, L. Vincetti and. s.l. : Optics Express-OSA, Jun 2012, Vols. Vol. 20, No. 13.
83. *Analysis of guided resonances in photonic crystal slabs*. Fan, S. & Joannopoulos, J. D. s.l. : Phys. Rev. , 2002, Vols. B 65, 235112.
84. Haus, H. *WaVes and Fields in Optoelectronics*. NJ : Prentice-Hall: Englewood Cliffs, 1984.
85. *A free electromagnetic solver for layered periodic structures*. Liu, V. & Fan, S. S. s.l. : Comput. Phys. Commun., 2012, Vols. 183, 2233–2244.
86. *Mie scattering as a cascade of Fano resonances*. et.al, Mikhail V. Rybin. s.l. : Optics Express, 2013, Vols. 21, No. 24.
87. *Temporal Coupled-Mode Theory for Fano Resonance in Light Scattering by a Single Obstacle*. et.al, Shanhui Fan. s.l. : Shanhui Fan, 2010, Vols. 114, 7324–7329.
88. *Origins of modal loss of antiresonant hollow-core optical fibers in the ultraviolet*. Alexander Hartung et al. s.l. : Opt.Exp., 2015, Vols. 23, No. 3.



89. *Visible Continuum Generation in Air- Silica Microstructure Optical Fibers with Anomalous Dispersion at 800 Nm.* J. K. Ranka, R. S. Windeler, and A. J. Stentz. s.l. : Opt.Lett., Vols. 25 (2000) 25-27.
90. *Spatially and spectrally resolved imaging of modal content in large-mode-area fibers.* J. W. Nicholson, A. D. Yablon, S. Ramachandran, and S. Ghalmi. s.l. : Opt. Express, 2008, Vols. vol. 16, no. 10, pp. 7233–7243,.
91. *Empirical formulas for calculating loss in hollow core tube lattice fibers.* Vincetti, L. s.l. : Opt. Express, 2016, Vols. 24, no. 10, pp. 10313–10325.
92. *Mise en forme spatiale dans une fiber optique microstructurée pour la réalisation d'amplificateurs lasers tout fibrés pour les pilotes des lasers de puissance.* Calvet, P.
93. *Dipole radiation model for surface roughness scattering in hollow-core fibers.* Eric Numkam, Francesco Poletti and David J. Richardson. s.l. : OSA Technical Digest (Optical Society of America), 2012, Vol. paper JW2A.18.
94. *Nested antiresonant nodeless hollow core fiber.* Poletti, F. s.l. : Opt. Express, Oct. 2014, Vols. 22, no. 20, p. 23807.
95. *Analysis of light scattering from surface roughness in hollow-core photonic bandgap fibers.* Eric Numkam Fokoua, Francesco Poletti, and David J. Richardson. s.l. : Opt.Exp., 14 Aug 2012, Vols. 20, No. 19.
96. *Hypocycloid-core Kagome hollow core photonic crystal fiber for Rb and Cs based optical applications.* T. D. Bradley, Y. Y. Wang, M. Alharbi, and B. Debord. s.l. : J.Light.Tech., 2013, Vols. 31, no.16,pp.1-4.
97. *Leakage properties of photonic crystal fibers.* D. Ferrarini, L. Vincetti, M. Zoboli, A. Cucinotta, and S. Selleri. s.l. : Opt. Express, Nov. 2002, Vols. 10, no. 23, pp. 1314–1319.
98. *Generation and confinement of microwave gas-plasma in photonic dielectric microstructure.* B. Debord, R. Jamier, F. G´erôme, O. Leroy, C. Boisse-Laporte, P. Lep Leprince. vol. 21, pp. 25509–25516, 2013, Vol. Opt. Exp.



99. *Inert gas beam delivery for ultrafast laser micromachining at ambient pressure.* Longtin, J. Sun and J. P. s.l. : J Appl Phys, 2001, Vols. 89, 8219.
100. *Reducing the size of hollow terahertz waveguides.* D. S. Wu, A. Argyros, and S. G. Leon-Saval,. s.l. : J. Lightwave. Tech., 2011, Vols. 29(1), 97–103.
101. *Low-loss and low-bend-sensitivity mid-infrared guidance in a hollowcore– photonic-bandgap fiber.* N. V. Wheeler, A. M. Heidt, N. K. Baddela, E. N. Fokoua, J. R. Hayes, S. R. Sandoghchi, F. Poletti, M. N. Petrovich, and D. J. Richardson. s.l. : Opt. Lett., vol. 39, no. 2, pp. 295–298, 2014.
102. *A review of IR transmitting, hollow waveguides.* Harrington, J. A. 19, no. 3, pp. 211–217, 2000, Vols. Fiber Integr.Opt., vol. .
103. *Macro bending losses in single-cell Kagome-lattice hollow-core photonic crystal fibers.* B. Beaudou, A. Bhardwaj, T. Bradley, M. Alharbi, B. Debord, F. Gerome, and F. Benabid. s.l. : J. Lightw. Technol., Apr 2014, Vols. vol. 32, no. 7,pp. 1370–1373, .
104. *Improved bend loss formula verified for optical fiber by simulation and experiment.* H.Cole, R. T. Schermer and J. s.l. : IEEE J. Quantum Electron, Oct. 2007, Vols. vol. 43, no. 10, pp. 899–909.
105. *Confinement loss in Kagome and tube lattice fibers: Comparison and analysis.* Setti, L. Vincetti and V. s.l. : J. Lightw. Technol, May 2012, Vols. 30, no. 10, pp. 1470–1474.
106. *Ultraviolet-infrared femtosecond laser-induced damage in fused silica and CaF₂ crystals.* T. Q. Jia, H. X. Chen, M. Huang, F. L. Zhao, X. X. Li, S. Z. Xu, H. Y.Sun, D. H. Feng, C. B. Li, X. F. Wang, R. X. Li, Z. Z. Xu, X. K. He, and H. Kuroda. s.l. : Phys. Rev. B, 2006, Vols. 73, no. 5, p. 054105.
107. *Laser Ablation and Micromachining with Ultrashort Laser Pulses.* X. Liu, D. Du, and G. Mourou. s.l. : IEEE J. Quantum Electron, 1997, Vols. 33(10), 1706–1716 .





PUBLICATION LIST

Conference publications

1. A. Amsanpally, B. Debord, M. Alharbi, E. Ilinova, L. Vincetti, F. Gérôme and F. Benabid., *Fano resonance in inhibited coupling Kagome fiber*, CLEO US: OSA, 2015. STu4L.6.
2. Benoît Debord, Abhilash Amsanpally, Meshaal Alharbi, Luca Vincetti, Jean-Marc Blondy, Frédéric Gérôme, Fetah Benabid., *Inhibited coupling Kagome fibers with ultra-large hollow-core size for high energy ultrafast laser applications*, CLEO US: OSA, 2015. SF1G. 3.
3. B. Debord, M. Maurel, A. Amsanpally, M. Adnan, A. Gorse, B. Beaudou, J. M. Blondy, L., *Experimental optimization of curvature and silica thickness core contour of inhibited-coupling Kagome fibers.*, Vincetti, CLEO EU: OSA, 2017.
4. B. Debord, M. Maurel, A. Amsanpally, M. Adnan, B. Beaudou, J.M. Blondy, L. Vincetti, F. Gérôme, F. Benabid., *Ultra-low loss (8.5 dB/km@ Yb-laser wavelength range) inhibited-coupling Kagome HC-PCF for laser beam delivery applications.*, Proc. of SPIE Vol, 2017. Vols. 100941M-1.
5. A. Amsanpally, B. Debord, L. Vincetti, F. Gérôme and F. Benabid., *Manifestation opetique d'un etat lie dans un continuum au sein d'une fiber a cœur creux a couplage inhibe*, JNOG, 2017.
6. M. Chefer, M. Maurel, A. Amsanpally, A.Gorse, B. Beaudou B. Debord, L. Vincetti, F. Gérôme and F. Benabid., *Developpements recents de fibers a cœur creux a couplage inhibe.*, JNOG, 2017.
7. Benoît Debord, Abhilash Amsanpally, Matthieu Chafer, Assaad Baz, Luca Vincetti, Jean-Marc Blondy, Frederic Gerome, Fetah Benabid., *7.7 dB/km losses in inhibited coupling hollow-core photonic crystal fibers.*, CLEO US: OSA, 2016. JTh4C. 8 (post-deadline).
8. B. Debord, A. Amsanpally, M. Chafer, A. Baz, M. Maurel, J.M. Blondy, E. Hugonnot, F. Scol, L. Vincetti, F. Gérôme, F. Benabid., *7.7 dB/km transmission*



loss at 750 nm inhibited-coupling guiding hollow-core photonic crystal fibers., CLEO EU: OSA, 2017.

9. Benoît Debord, **Abhilash Amsanpally**, Jean-Marc Blondy, Frédéric Gérôme, and Fetah Benabid., *Low loss inhibited coupling hollow-core photonic crystal fiber with ultrabroad fundamental band., CLEO US: OSA, 2016. STu4P.2.*

Journal publications

1. Benoit Debord, **Abhilash Amsanpally**, Meshaal Alharbi, Luca Vincetti, Jean-Marc Blondy, Frédéric Gérôme, Fetah Benabid., *Ultra-large core size hypocycloid-shape inhibited coupling kagome fibers for high-energy laser beam handling, Journal of Lightwave Technology-IEEE, 2015, Vol. 33. 3630-3634.*
2. B. Debord, **A. Amsanpally**, M. Chafer, A. Baz, M. Maurel, J.M. Blondy, E. Hugonnot, F. Scol, L. Vincetti, F. Gérôme, F. Benabid., *Ultralow transmission loss in inhibited-coupling guiding hollow fibers., Optica, 2017, Vol. 4. 209-217.*
3. B. Debord, M. Maurel, **A. Amsanpally**, M. Adnan, B. Beaudou, J.M. Blondy, L. Vincetti, F. Scol, E. Hugonnot, F. Gérôme, F. Benabid., *Optimized inhibited-coupling Kagome fibers at Yb-Nd:Yag (8.5 dB/km) and Ti:Sa (30 dB/km) ranges, Optics Letters (submitted), 2017.*
4. **A. Amsanpally**, B. Debord, L. Vincetti, F. Gérôme and F. Benabid., *Experimental photonic manifestation of bound state in continuum in inhibited coupling HC-PCF., Optica (in progress), 2017.*
5. **A. Amsanpally**, B. Debord, L. Vincetti, F. Gérôme and F. Benabid., *Surface scattering loss measurement of inhibited coupling HC-PCF., Optica (in progress), 2017.*



Propriétés linéaires des fibres creuses à cristal photonique à couplage inhibé

[Résumé de la thèse]

Cette thèse a porté sur les principes de guidage, les propriétés linéaires et les outils de conception autour des fibres à cristal photonique à cœur creux (HC-PCF) à couplage inhibé (IC). Le guidage IC a été démontré comme une manifestation photonique de Q-BiC (état quasi lié dans un continuum) en étudiant des profils asymétriques et dépendants en polarisation dit Fano présentant une bande passante spectrale de 30 GHz. En utilisant le concept de IC, nous reportons la caractérisation linéaire de fibres IC HC-PCF supérieures à l'état de l'art. Par une optimisation de la forme du cœur, une fiber Kagome IC HC-PCF a démontré des pertes très faibles de 8,5 dB/km à 1030 nm associées à une bande passante à 3 dB de 225 nm. Une autre conception avec des entretoises de silice amincies à 300 nm a permis d'atteindre des pertes de 30 dB/km à 780 nm avec une bande de transmission fondamentale record décalée à 670 nm et capable de couvrir toutes les gammes spectrales du Ti:Sa, Yb et Er. Nous avons également travaillé sur la conception et la fabrication de IC HC-PCF présentant une gaine dont la structure est un réseau unique de tubes fins isolés. Une de ces fibres a permis de démontrer une transmission jusqu'à 220 nm avec des pertes records de 7,7 dB/km à ~ 750 nm, tandis qu'une seconde réalisation s'est traduit par une bande fondamentale de plus d'une octave allant de 600 à 1200 nm avec des pertes de 10-20 dB/km. Finalement, cette dernière fiber a été étudiée plus en détail pour déterminer les sources à l'origine des pertes due à la rugosité de surface présente à l'interface du contour du cœur.

Mots-clés : Couplage inhibé, Kagome, Q-BiC, resonance Fano, Rugosité de surface

Linear properties of inhibited coupling hollow-core photonic crystal fibers

[Summary of the thesis]

This thesis reported on guiding principles, linear properties and conceptual design tools of inhibited coupling (IC) guiding hollow-core photonic crystal fibers (HC-PCF). IC guidance was proved as photonic manifestation of Q-BiC (quasi bound-state-in-a-continuum) by investigating asymmetric and polarization dependent Fano profiles with bandwidth of 30 GHz in high resolution transmission spectra. By using IC design concept, we reported on linear characterization of state-of-the-art IC HC-PCFs. Based on core shaping optimization, a Kagome IC HC-PCF demonstrated ultra-low loss down to 8.5 km/km at 1030 nm associated with a 225 nm wide 3-dB bandwidth. Another Kagome design with thinner silica struts of 300 nm exhibited lowest loss of 30 dB/km at 780 nm along with record level fundamental bandwidth spreading down to 670 nm and able to cover the entire Ti:Sa, Yb and Er laser spectral ranges. We also reported on design and fabrication of single-ring tubular lattice IC HC-PCFs. One of these fibers demonstrated transmission down to 220 nm with a record transmission loss of 7.7 dB/km at ~750 nm, while the second one exhibited ultra-broad fundamental band with loss range of 10-20 dB/km over one octave spanning from 600 to 1200 nm. Finally, the second tubular fiber was further investigated for fundamental loss sources due to surface roughness around its core-contour.

Keywords : Inhibited coupling, Kagome, Q-BiC, Fano resonance, Surface roughness

